Wellbore Instability Mechanisms in Clays

by

Sherif Adel Akl

Bachelor of Engineering in Civil Engineering
Cairo University, Cairo, Egypt (2003)

Master of Science in Soil Mechanics and Foundations Engineering
Cairo University, Cairo, Egypt (2005)

Submitted to the Department of Civil and Environmental Engineering
in Partial Fulfillment of the Requirements for the Degree of

Doctor of Philosophy in The Field of Geotechnical and Geoenvironmental Engineering

at the

MASSACHUSETTS INSTITUTE OF TECHNOLOGY

February 2011

Signature of Author.....
Department of Civil and Environmental Engineering
October 13, 2010

Certified by.....
Andrew J. Whittle
Professor of Civil and Environmental Engineering
Thesis Supervisor

Accepted by.....
Heidi M. Nepf
Chair, Departmental Committee for Graduate Students

Wellbore Instability Mechanisms in Clays

by

Sherif Adel Akl

Submitted to the Department of Civil and Environmental Engineering on October 13, 2010
in Partial Fulfillment of the Requirements for the Degree of
Doctor of Philosophy in The Field of Geotechnical and Geoenvironmental Engineering

Abstract

This dissertation investigates the stability of wellbores drilled in K_0-consolidated clays using non-linear finite element method (FEM) and effective stress soil models to characterize the behavior of clay and unconsolidated shale formations. Two constitutive models are used: Modified Cam Clay (MCC; Roscoe and Burland, 1968), and MIT-E3 (Whittle and Kavvadas, 1994). These soil models are incorporated in the commercial finite element program ABAQUS^{TM} through user material subroutines (Hashash, 1992). The wellbores are modeled by a quasi-3D finite element model to approximate the far field stresses and plane strain boundary conditions. The constitutive models are calibrated to the behavior of Resedimented Boston Blue Clay (RBBC), an analog shale material which is K_0-consolidated to stress levels ranging from 0.15MPa to 10.0 MPa.

The thesis comprises three major parts. Part one analyzes the short-term wellbore instability during drilling in low permeability formations. The part focuses on the relationship between the mud pressure inside the wellbore and the undrained shear deformations within the formations. The analyses predict critical mud pressure values necessary to maintain wellbore stability at different deviation angles and stress histories. The MIT-E3 model predicted higher deformations at reference mud pressure and estimated higher values of mud pressures than the underbalanced limit to prevent failure in highly deviated wellbores in NC clays.

The second part validates the numerical analyses by comparing model predictions to results of an extensive program of model borehole tests. The lab experiments are performed on high pressure Thick-Walled Cylinder (TWC devices) using RBBC as analog testing material (Abdulhadi, 2009). The MIT-E3 predictions demonstrated a very good match with results from the experiments. The results from the analyses illustrated the effect of the device boundary conditions on specimen behavior and validated approximate analytical methods for interpreting TWC results.

Part three studies the effects of consolidation on long-term wellbore stability. Non-linear coupled consolidation analyses are performed to simulate the post-drilling, time-dependent deformations and pore pressures around the wellbore. The analyses consider two different boundary conditions on seepage at the cavity. The analyses show that consolidation generates extensive volumetric strains around the wellbore and cavity deformations can aggravate stability conditions in highly deviated wellbores.

Thesis Supervisor: Andrew J. Whittle
Title: Professor of Civil and Environmental Engineering

Acknowledgments

My deepest gratitude is to my mentor and thesis advisor Professor Andrew John Whittle. I learned a great deal from him about life and academia. I will spend a life time using what he taught me and for that I will be forever grateful. I am proud beyond words to be one of his students.

I am indebted to the rest of my thesis committee members: Dr. John Germaine for his careful review of my thesis and extremely helpful feedback; and Professor Ruben Juanes for his valuable input and his enlightening discussions. I would like to thank Professor Herbert Einstein for being my professor and sharing his vast knowledge and wisdom; and Dr. Lucy Jen for keeping me in touch with the practical side of research and giving me sincere advice.

I would like to acknowledge BP America Inc., Houston, and BP-MIT Major Projects Program for their financial support of this research. Special thanks to Dr. Steve Willson, the technical monitor for the project for his indispensable assistance. I would like to express my appreciation to the miracle workers who made my life much less difficult than it could have been: Kris Kipp, Sheila Fay, Patty Glidden, Jeanette Marchocki, Andre Dixon, Carolyn Jundzilo-Comer, Patricia Dixon and the staff of the CEE department.

It was an honor and a great pleasure working with my colleagues from the computational geomechanics group, "The Geotechs": Antonios Vytiniotis, Gonzalo Corral, Davoud Ebrahimi, Yixing Yuan, Despina Zymnis, Dimitrios Niarchos, Evanglia Ieronymaki, and Nina Panagiotidou. I would like to thank my colleagues from the experimental research group "The Labrats". Kartal Toker and Eng Sew Aw for being my TAs. Nikolaos Kontopoulos for managing the CEE computer networks. Dr. Naeem Abdulhadi and Safia Moniz for providing valuable laboratory data. Through the years I was blessed with the

greatest officemates, Maria Nikolinakou, Jianyong Pei, Yvonne Moret, Alberto Ortega, Jay Miller, Julia Roberts, Jaehoon Lee, Yun Kim and Amy Adams.

Life in MIT would have been unbearable without my friends whom I will cherish forever. My old gang; Rita Sousa, Anna Agarwal, Bruno Silva, and Catarina Ferreira. My new gang; Amer Deirieh, Muhannad Abuhaikal, and the invincible Mehdi Akbarian. The members of the Egyptian Student Association; especially Tamer Elkholy who has been more than a brother to me and Dr. Tarek Moselhy who treated me like a member of his wonderful family. The members of the Arab Student Organization who trusted me with the newletter Sifr; especially Hussam Busfar, Obaidah Abuhasem, and Dahlia Alkekhia. Sincere thanks go to Dr. Lamia Youseff who has been on the other end of the most sophisticated and wonderful conversations in history.

To my family I owe the most. The unconditional love and tremendous support of my parents, my sister and my brother in law kept me going on this journey during my ups and downs. I would also like to thank Uncle Yosry Nasr and Aunt Hana Nasr who provided a sanctuary for me in New Jersey when I needed it the most.

Finally I would like to thank Allah for his countless blessings and say: ALHAMDOLELAH.

To My Parents,

My Sister, My Brother in law,

And to My Nephew Ali

Table of Contents

List of Tables

List of Figures

1 Introduction

There is no doubt that oil has been one of the most important raw materials since the beginning of the twentieth century. The growing demand for cheaper energy and cutting operating costs has made borehole stability a key issue for the oil industry. Geomechanics has an important role to play in the mechanical simulation of reservoir deformations and the performance of wellbores. Efforts to expand oil resources and explore new territories are vital to sustain energy production in the next few decades. Part of these efforts includes oil production at very shallow depths. One of the major oil companies, BP has a number of development projects where oil reservoirs are located at depths less than 1,000m in both deepwater environments in the Gulf of Mexico and onshore prospects in the North Slope of Alaska. Effective exploitation of such reservoirs relies on a small number of surface drilling locations, with highly deviated wells drilled with complex directional trajectories. The formations encountered at such shallow depths are poorly-lithified and are more properly unconsolidated rocks or stiff clays. The expected strength of these formations is expected to be one-order of magnitude weaker than strength at typical reservoir depths. Such unconsolidated shale formations exhibit highly non-linear deformation properties, are strongly anisotropic and exhibit strain-softening in some states and modes of shearing.

Wellbore stability methods commonly employed in the design of deep wells are based on assumptions appropriate to the strength and deformation characteristics of well-lithified rock formations (shales and mudstones). These materials fail in a quasi-brittle manner (Santarelli and Brown, 1989) creating classic borehole breakout failure patterns. Most wellbores pass vertically through the weaker upper sediments and are usually successfully cased and cemented to mitigate effects of near-surface disturbance. There are currently no methods for evaluating the stability of shallow boreholes in unconsolidated soil formations. These materials are expected to undergo large plastic deformations (borehole squeezing), creating a more extensive zone of disturbance around the borehole. Prior studies (e.g. Yu and Rowe, 1999) are based on simplified constitutive models of soil behavior. Given the highly complex material behavior, reliable predictions

of borehole deformations and stability can only be achieved with relatively sophisticated constitutive models that are able to represent realistically the anisotropic stress-strain-strength properties of the clay (and shale) formations.

The importance of wellbore stability in unconsolidated rocks has motivated a four year research project at MIT, sponsored by BP America. The project comprises an integrated program of experimental measurements and numerical analyses. The laboratory experiments use Resedimented Boston Blue Clay (RBBC) as an analog shale material to enable consistent, repeatable element and model-borehole tests. Abdulhadi (2009) performed a series of 1-D consolidation and undrained triaxial shear tests to evaluate the engineering properties of this analog testing material. Borehole stability was studied using reduced-scale Thick-Walled Cylinder (TWC) tests with independent control of the vertical stress and radial pressure acting on the inner and outer walls of the cylinder. This thesis focuses on numerical analyses of wellbore stability. The behavior of RBBC is modeled by two effective stress constitutive models: Modified Cam Clay (MCC; Roscoe and Burland, 1968) and MIT-E3 (Whittle and Kavvadas, 1994). The MCC model is the most popular and widely used elasto-plastic soil model based on principles of critical state soil mechanics. The MCC predictions serve as a base case for using the more advanced MIT-E3 soil model. MIT-E3 is a significantly more complex elasto-plastic model which describes many aspects of the rate-independent behavior clays, including: a) small-strain non-linearity; b) anisotropic stress-strain-strength; c) post-peak softening. This model has been extensively validated using laboratory element test data and widely used by the offshore oil industry in predicting the performance of pile foundations used to anchor productions platforms such as tension leg platforms (Whittle, 1992).

None of these constitutive models has been applied at the range of consolidation stresses needed for the current project. Previous studies on Resedimented Boston Blue Clay (RBBC) have been based on experiments performed at consolidation stresses; $\sigma'_{vc} \leq 0.5$ MPa. The MAA and MIT-E3 model assume normalized engineering properties of the soil such that the undrained shear strength and stiffness of normally consolidated specimen is proportional to the vertical effective stress at the end of consolidation. The elemental test

program reported by Abdulhadi (2009) shows remarkable reductions in the undrained shear strength and stiffness ratios with consolidation stress level. Hence, model input parameters must be re-calibrated at the consolidation pressures of interest in order to achieve realistic predictions of wellbore stability. The current numerical simulations are based on non-linear finite element analyses that represent coupled flow/seepage and deformations in the formation. This is accomplished using the commercial FE program ABAQUS^{TM}. The complexity of this problem dictated the use of numerical modeling and discretization. The chosen constitutive models are integrated within Finite Element program ABAQUS^{TM} via user material subroutines after Hashash (1992).

Borehole instability during drilling depends on the density of drilling fluid (mud pressure inside borehole cavity). Borehole stability analysis aims at improving methods for controlling the density of the drilling fluid during construction. Even small percentage savings in drilling costs results in large monetary savings. An accurate prediction of required mud pressures in the field is a complex process where parameters are ill-defined or excessively difficult to collect precisely. A more rational goal is to focus on the relationship between mud pressure value and wellbore stability and deformations. The goal of this research is to develop reliable methods of evaluating borehole stability in soils form the results of numerical analysis using the FEM. The data from model borehole tests validates the finite element simulations. This thesis is divided into seven chapters making up three major parts: 1) investigating the relationship between mud pressure and wellbore stability, 2) validation of simulations using results of TWC model borehole tests, and 3) studying the time dependent deformations and pore pressures within the formation due to post-drilling consolidation:

1.1 Undrained Deformations due to Drilling of Wellbore

Wellbore drilling causes stresses within the formation. For wellbores in low permeability clays the process is sufficiently rapid that there is minimal migration of pore fluid within the formation. Hence, the wellbores stability analyses consider stability due to undrained

shearing within the formation. Chapter 2 provides the necessary background to wellbore stability analysis. The chapter describes the categories of wellbore failure and introduces the concepts of wellbore instability analysis. Then, the chapter presents the wellbore unloading problem and summarizes previous solutions using different material models and modeling techniques.

Chapter 3 gives details of the numerical procedures and methods used to simulate effective stresses and pore pressures around deviated wellbores. The chapter describes the finite element models used to simulate wellbores with general orientation in K_0-consolidated clays exhibiting cross-anisotropic behavior. The chapter also describes the effective stress soil models used in this analysis and the calibration of the models' input parameters to RBBC behavior consolidated up to high stress levels (~10MPa).

Chapter 4 describes the prediction of instabilities due to undrained shearing of the clay as a function of the wellbore orientation and stress history of this clay.

1.2 Simulation of Model Borehole Tests

Results from TWC model borehole tests (Abdulhadi, 2009) are used to validate finite element analysis of wellbore stability. Chapter 5 describes briefly the experimental procedures, boundary conditions and key results. The chapter compares the computed and measured cavity pressure-volume relations for the model borehole tests. The chapter also evaluates the analytical methods adopted to interpret lab results and presents a full set of results to understand stress conditions within the TWC device.

1.3 Effect of Consolidation on Borehole Stability

Drilling in low permeability formations can be represented as an undrained shear process which develops pore pressures within the formation. Chapter 6 analyzes the effects of subsequent fluid migration (and coupled consolidation) in the formation on wellbore

stability over the timeframe required for installation of wellbore casings. Numerical analyses of the coupled consolidation processes involve time-dependent deformations and pore pressures. The analyses in this chapter consider different permeability conditions at the cavity wall in which pore pressures in the formation either fully interact with the mud pressure or redistribute around an impermeable cavity. The chapter investigates the deformations generated during consolidation as they may prevent casing settings.

A summary of the analyses procedures and the main conclusions from each part are contained in Chapter 7. The chapter also proposes several recommendations for future research.

2 Background

2.1 Introduction

Wellbore instabilities during drilling cause substantial problems for petroleum engineers in all sorts of geological formations. Problems include incidents such as tight hole, stuck pipe, and lost circulation are often encountered on the rig-floor. There are many possible reasons for such problems; inappropriate hole cleaning, mechanical vibrations of drilling equipment to name a few; but in a majority of the field cases reported, the fundamental reason is mechanical failure of material around the wellbore (Bol et al., 1994; Gazianol et al., 1995). Opinions vary as to the value of lost equipment and time arising directly from wellbore instability, but no one disputes estimates of $500 M per year worldwide (Dusseault, 1994). It is common in the industry that such stability problems amount to typically 5-10% of drilling costs in exploration and production (Fjaer et al., 2008). Better wellbore analysis methods, data retrieval, and use of educated individuals on the rig-floor will save more money than is necessary for data collection, software development, and education.

Inclined wellbores are very beneficial for reducing costs of production drilling, but stability of such wells can be very critical during drilling especially in soft formations. If the production wells can be drilled as deviated holes, the production platform can drain larger areas of the reservoir and decrease the number of platforms required to produce the field. There is a large potential for cost saving here, both with respect to avoiding stability problems of the drilled wells, and also with respect to reducing the required number of wells.

Oil reservoirs are usually encountered thousands of meters below ground surface, where well lithified formations and competent rock reside. Most common wellbore design procedures are based on the assumption that the prevailing material behaves like brittle

rock. However, stability problems are often encountered in shale-like rock layers above the reservoir. Charlez (1997) stated that 80% of the wellbore instability problems occur in soft or ductile formations. The plastic behavior of shale is more difficult to predict. Shallow reservoirs (less than 1000m deep) require wellbore stability in weak rocks or hard soils. The host formations can undergo large plastic deformations with extensive disturbance zones around the wellbore. Deviated wellbores are also very important for shallow reservoirs. To have feasible production rates from shallow reservoirs, networks of inclined wellbores with tortuous trajectories must be planned and employed.

The wellbore stability analysis depends on a proper determination of the drilling fluid density that provides the mud weight inside the cavity of the wellbore. In order to prevent influx of fluid, it is necessary to keep the mud weight above the pore pressure gradient. Conversely, to prevent loss of mud into fractures (lost circulation), it is necessary to keep the mud weight below the fracture gradient. These two constraints constitute the minimum and maximum mud weights associated with stable drilling. This leads to the mud weight window as the key input parameter for well design.

Several factors other than stress conditions affect the mechanical response around the wellbores. The mechanical behavior can be affected by the high temperatures found at such large depths. Hojka et al. (1993) proposed a thermoelastic model to count for the temperature effects on rock behavior. Guenot and Santarelli (1989) investigated the influence of mud temperature on the wellbore behavior, while Zoback (2007) considers chemical effects on wellbore stability when drilling through reactive shale. Reactive shales are identified as those that react chemically with drilling mud in such a way as to weaken the formation leading to wellbore instability. This thesis as well as this background chapter considers wellbore stability as a geotechnical issue: hydraulic and chemical factors are vital, but instability is a function only of stresses (σ), strains (ε), and yield, whatever the causative agents.

For several reasons, stability evaluation is particularly problematic: direct observation is impossible when the drill bit is thousands of meters away; in situ stresses are not measured systematically; and there can be large variations in the material properties. The complexity of the wellbore problem and the abundance of intertwined factors affecting wellbore stability make comprehensive modeling a significant challenge. In complex processes such as these for which parameters are ill-defined or excessively difficult to collect precisely, parametric analyses are a more rational goal than accurate prediction. Thus, exploring the effect of changing mud weight on stability is more beneficial than determining the required mud weight to guarantee stability.

The rest of this chapter is divided into three sections. Section 2.2 categorizes wellbore failures in three different categories; brittle compressive failure, ductile compressive failure, and tensile failure. Each category is discussed in terms of instability mechanism and operational problems. Section 2.3 gives a brief introduction to the general process of wellbore instability analysis. This section focuses on the concept of the safe mud weight window as a key input to the wellbore design procedure. Section 2.4 describes the wellbore unloading problem as assessing the effects of changing mud pressure on wellbore deformations. This section explains the assumptions required to model the mechanical behavior of real wellbores, and the factors affecting the problem solutions. The factors discussed in this section relate to the analysis of brittle and ductile compressive failures. Factors considered in conjunction with brittle failure are the choice of failure criterion, using elastic non-linear modulus, and the interplay between well trajectory and material anisotropy. In conjunction with ductile failure, the discussed factors are the choice of yield criterion and effective stress soil models, deviation of wellbores and anisotropy of far field stresses, and the consolidation around wellbores and associated coupled behavior of the formations.

2.2 Wellbore Instability during Drilling

Wellbore instability during drilling can be evidenced by minor wall sloughing, reduced drilling speed because of inability to clear cuttings, stuck pipe because of mudrings on trips or salt squeeze, large washouts, excessive hole cleaning to reach bottom, out right hole collapse, and even fracturing and fluid loss by internal blowout (Dusseault, 1994).

Bradley (1979) and others (e.g. Santarelli et al., 1986; Yu, 2000) categorized wellbore instabilities into three general types based on the symptoms witnessed in the field:

a) Hole size reduction due to ductile yield of the rock or soil
b) Hole enlargement due to brittle rock fracture or rupture: and
c) Unintentional hydraulic fracturing induced by excessive mud pressure.

On the other hand, Fjaer et al (2008) divided instabilities into two categories of wellbore failures based on the type of mobilized strength, compressive or tensile failure. Compressive failure is caused by an insufficient mud weight leading to stress concentration at the cavity wall higher than the rock strength, while tensile failure is caused by an excessive mudweight compared to the smallest in situ stress. Figure 2.1 shows schematically the two different types of failure.

Compressive failure can be divided into two main types: breakouts and plastic squeeze. Breakouts lead to an increase in wellbore diameter, and normally take place in brittle rocks (type 'b' in Bradley's (1979) classification). In weak or plastic shales, sandstones and salt; these ductile formations undergo plastic deformations and squeeze in reducing the wellbore diameter (type 'a' in Bradley's (1979) classification). Some chalk formations can also show such behavior.

2.2.1 Brittle compressive failure

Formations at a given depth are exposed to compressive stresses, vertically and horizontally, as well as a pore pressure. When a hole is drilled, the surrounding rock mass must re-distribute stresses associated with creation of the borehole. The mud pressure provided by the drilling fluid can carry some of the stress. In a rock which behaves linear elastically, and in zones where the mud pressure is insufficient, this leads to a stress concentration (high hoop stresses) near the well. Breakouts occur when the maximum hoop stress around the hole is large enough to exceed the compressive strength of the rock. This causes the rock around a portion of the wellbore to fail in compression (Bell and Gough, 1983; Zoback and Moos et al., 1985; Bell, 1989). For weaker rocks such as shales, rapid sloughing occurs in zones of low mud pressure. Softening and weakening involves mainly loss of cohesive bonding because of shear distortion and dilation, swelling, and extensional fractures analogous to axial splitting in triaxial testing. (Dusseault and Gray, 1994)

For the simple case of a vertical well, when vertical stress is principal stress, this leads to the occurrence of stress- induced wellbore breakouts that form at the azimuth of the minimum horizontal compressive stress. Breakouts are ubiquitous in oil wells and permit stress orientations to be obtained over a range of depth in an individual well. Detailed studies have shown that these orientations are quite uniform with depth, and independent of lithology and age (e.g., Plumb and Cox, 1987; Castillo and Zoback, 1994). Breakouts occurring in deviated wells are somewhat more complicated to analyze (Peska and Zoback, 1995) but have the potential for providing information about stress orientation and stress magnitude.

When excess breakout formation produces so much failed material from around the wellbore that the total volume of cuttings and failed material in the hole cannot be circulated out by mud circulation, the wellbore enlarges and the velocity of the drilling mud decreases. Reduced cleaning capacity associated with slow mud circulation can cause the cuttings and failed rock to stick to the bottom hole assembly. This is called

wellbore collapse because it seems as if the wellbore has collapsed in on the bottom hole assembly.

Figure 2.2 shows the relationship between breakout width and wellbore failure. Breakout width is the central angle that corresponds to the failed portion of the circumference. Limited breakout width (a), $\theta_b \leq 60^0$ in the shown example, produces a failed zone of limited size. Literally thousands of near-vertical wells have been studied in which breakouts of such size are present but there were no significant wellbore stability problems (Zoback, 2007). In designing a stable wellbore it is only necessary to raise mud weight sufficiently to limit the initial breakout width to an acceptable amount. Empirically, many case studies have shown that designing for maximum breakout widths of $\theta_b \sim 90^0$ in vertical wells is often reasonable, if somewhat conservative criterion for mud weight prediction. However, in critical geological conditions, no damage is permitted by the design especially for near horizontal wellbores ($\theta_b = 0^0$), which is called a gun barrel situation (Willson et al., 2004).

One can see that breakout widths that exceed 90^0 correspond to failure of more than half of the well's circumference. In this case, the well could lack adequate arch support, i.e. sufficient unfailed formation to support the applied forces (Bratli and Risnes 1981). As illustrated in Figure 2.2(b), inadequate arch support could lead to failure all the way around a well and the formation of a washout (the well is enlarged in all directions).

2.2.2 Ductile compressive failure

Rock fragments breaking loose from the wellbore wall, or a minor reduction in the wellbore diameter due to plastic flow do not necessarily create drilling problems. Guenot (1990) pointed out the need for a new failure criterion which can account for these practical aspects. One obvious modification is to account for the post-failure behavior of the rock by incorporating plasticity (and/or nonlinear elasticity). However, one must differentiate clearly between yielding in the plastic behavior and the plastic and ductile

failure of wellbores. Yield is a continuum mechanics term for a change in load-deformation (or stress-strain) response coincident with fundamental physical alteration in the microfabric of the material. On the other hand, failure is a loss of function. For example, yield and non-linear behavior dominate the rock mass surrounding a typical tunnel, but this yield actually stabilizes the tunnel by redistributing stresses away from the wall, thereby reducing chances of catastrophic failure. In wellbores, the stress concentration at cavity wall is greatly reduced in most real materials by non-linear, elastoplastic, and viscous behavior (Nawrocki and Dusseault, 1993, Wang and Dusseault 1991a&b, Bogobowicz et al., 1991; Euverte et al., 1994).

Charlez (1997) proposed that the minimum value for the mud weight should be the Critical Instantaneous Mud Weight (CIMW). The CIMW is defined as the well pressure for which the first point in the formation reaches critical state according to a critical state model. Charlez (1997) used in his work the original Cam-Clay model (Schofield and Wroth, 1968). This mechanical criterion is comparable to defining wellbore stability according to a kinematic criterion of limiting inward deformations (borehole convergence limited to a certain percentage of the initial wellbore diameter). Charlez (1997) argued that due to the random choice of the critical convergence value, the kinematic criterion is much more subjective than the mechanical criterion. These two criteria are discussed more thoroughly when effects of plasticity on wellbore analysis are explained.

2.2.3 Tensile failure

High mud weights reduce the hoop stresses in the surrounding rock, but hydraulic fractures can be created if the circumferential stresses become tensile. If a fracture existed, a significant amount of drilling fluid would seep into the fracture and get lost into the formation. The mud loss may also lead to temporary pressure drop in the well, due to the mud volume intruding into the formation. Fjaer et al. (2008) argued that pore fluid may flow into the well from permeable layers higher up. In the presence of gas, this may lead to a rapid increase in well pressure and a high risk of a blowout. This is potentially

dangerous situation that may result in loss of lives and equipment. (Guenot, 1998) stated that extensional fields with abnormal pressures at depth are more prone to blowout occurrences.

The focus of this thesis is on the lower limits possible for the mud weights in plastic formations; hence, investigating drilling induced tensile fractures are beyond the scope of this study. However, this phenomenon yields useful information about stress orientations (Moos and Zoback, 1990; Brudy and Zoback, 1999). These fractures form in the wall of the wellbore at the azimuth of the maximum horizontal compressive stress. As shown by Wiprut, Zoback et al. (2000), drilling-induced tensile fractures can define stress orientations with great detail and precision. According to Brudy and Zoback (1993) and Peska and Zoback (1995) drilling-induced tensile fractures observed in deviated wells have the potential for providing information about stress orientation and stress magnitude.

2.3 Wellbore Stability Analysis

Wellbore stability problems fall into two general categories: 1) Preventing significant wellbore instability during drilling; and 2) limiting failure of the formations surrounding the wellbore during production. The latter problem is sometimes referred to as sand (or solids) production (Zoback, 2007), as significant formation failure during production results in fragments of the formation being produced from the well along with hydrocarbons. Another aspect of wellbore failure during production is the collapse of well casings due to depletion-induced compaction and/or the shearing of wells by faults through injection- (or depletion-) induced faulting. This thesis and in turn this chapter focuses on the first problem and investigates factors contributing to wellbore instability during the drilling process.

During drilling, the well is filled with mud to prevent flow of pore fluid into the well or rock failure. This mud is also called the drilling fluid. The mud weight is primarily adjusted to prevent flow of pore fluid, while other aspects of rock stability have traditionally received less attention. This represents no problem in competent rocks, but in weak formations it may be the stability of the formation which sets the lower acceptable limit for the mud weight, not the pore pressure. Underbalanced drilling refers to intentionally drilling with mud weights that are less than the pore pressure. This is done to prevent high mud weights from damaging formation permeability, to increase rate-of-penetration (ROP) and to prevent mud losses in permeable intervals. Ottesen, Zheng et al., (1999) and Moos, Peska et al., (2003) introduced the utilization of Quantitative Risk Assessment (QRA) for problems of wellbore instability in the context of underbalanced drilling.

The upper bound of the mud weight is that at which lost circulation occurs due to hydraulic fracturing of the formation. The difference between these two limits is the safe mud weight window. The drilling fluid is also used to transport drill cuttings from the hole to the surface. The mud density controls the well pressure. In this thesis, the analysis of wellbore stability uses the actual stresses and well pressure rather than the actual mud density.

Stability problems are generally larger in a deviated wellbore, since the stress distribution is less favorable. The vertical stress (which is normally the major principal stress) will have an increasing component normal to the wellbore as the deviation angle increases, and the stable range for the mud weight decreases. Also, it is more difficult to clean highly deviated wells (near horizontal or horizontal wells) because gravity causes the cuttings to settle on the bottom of the hole. In some zones it may be inadvisable to drill above a certain angle. These limitations must therefore be considered already in the planning phase of a field. This effect of deviation applies to zones of normal stress gradients. If tectonic stresses dominate, the situation may be reversed, (i.e. increased deviation is more favorable, in a given azimuth direction).

As it is generally not possible to drill the entire section with one mud weight, a casing has to be set to seal off the upper part of the section before continuing with an increased mud weight in the lower part. This illustrates the two main tools available to drill stable wellbores: the mud weight and the casing set points. Figure 2.3 shows a case history by Moos et al. (2003) that demonstrates the importance of basing drilling decisions on a quantitative model of wellbore stability founded on a comprehensive geomechanical model.

Figure 2.3a shows the original well design using pore pressure as the lower bound and the fracture gradient as the upper bound of the mud window. Based on a wellbore stability problem in a previously drilled well, the lower bound of the mud weight pressure was increased at depth, necessitating a number of casing strings and a very small window for the third string of casing (Figure 2.3b). A better arrangement of the case set points as shown in Figure 2.3c allows the upper two casing strings to be deepened, resulting in one less casing string to be used. In the field, the design shown in Figure 2.3b was the one followed, and millions of dollars were spent unnecessarily on an extra casing string.

The work done on wellbore stability is integrated in a general drilling strategy as shown in Figure 2.4 from Charlez (1997). To begin with, the Geologist and Reservoir Engineer define a target to be reached from the surface. According to the location of the starting point, the Directional Engineer proposes a well profile taking into account both the starting point, the target but also the presence of nearby well. According to the well profile, XLOT (the closest extended leak-off test value) and pore pressure data (issued from previous wells) a casing strategy is defined. Meanwhile, the initial stress state (K_0 and σ_v) is estimated as well as the mechanical properties of various rocks to be drilled and subjected to stability problems.

Once all the necessary data joined together, a stability calculation is carried out to estimate the required mud weight. The next step in the engineering tree concerns the choice of the mud (water-based-mud (WBM) or oil-based-mud (OBM) depending on the

chemical reactivity of the drilled formations) and the minimum circulation flow rate to ensure a correct cleaning of the bottom hole. In a final step, taking into account the rig constraints, the bit hydraulic can be optimized and the ECD (equivalent circulating density) calculated. In conclusion, the mud weight plan should always result from an integrated study involving geomechanics, drilling and mud experts, people form drilling manager and operations. However, the stability model should never be considered as a purely deterministic tool and a measured risk is accepted (Charlez 1997).

2.4 The Wellbore Unloading Problem

The axial dimension of a wellbore is characteristically several orders of magnitude larger than the in-plane dimensions (i.e. diameter is O [1m] while depth is O [10^3m]). Hence, it is appropriate to assume plane strain geometry for the wellbore model. Gradients of gravitational forces are small compared to stress changes in the cross-sectional planes of interest, and therefore ignored. These two assumptions lead to the popular plane strain wellbore model shown in Figure 2.5 as presented by Santarelli et al. (1986), Detournay and Cheng (1988); and Charlez and Hugas (1991).

At any point in the Earth's crust a stress state prevails, caused both by the weight of the overlying formations (lithostatic component) and the action of the plates with respect to each other (tectonic component). The geostatic stress state can be locally represented by a tensor σ (x, y, z) such that

$$\sigma = \begin{bmatrix} \sigma_{xx} & \sigma_{xy} & \sigma_{xz} \\ \sigma_{yx} & \sigma_{yy} & \sigma_{yz} \\ \sigma_{zx} & \sigma_{zy} & \sigma_{zz} \end{bmatrix} \qquad (2.1)$$

The stress state appears as a heterogeneous local value as it is defined at any point. However, in the wellbore model, the stress state is considered as a homogeneous boundary condition applied to the periphery of the medium (Far Field Stresses). Within

the medium the stress state is considered homogeneous. In most cases, when topography effects become practically imperceptible, the vertical geostatic component σ_v can be considered as a principal direction. Hence, the geostatic stress is expressed with respect to its principal axes as

$$\sigma = \begin{bmatrix} S_h & 0 & 0 \\ 0 & S_H & 0 \\ 0 & 0 & S_v \end{bmatrix} \tag{2.2}$$

S_H and S_h are the major and minor in-plane stress components respectively. $S_H = p_0$ and $S_h = Kp_0$ as shown in Figure 2.5, where the ratio K can be ≤ 1.

Any geometric disturbance (drilling a well) modifies the initial geostatic stress state. To satisfy equilibrium, the stresses no longer supported by the solid rock skeleton (which has been removed) must necessarily be transferred to the material located on the periphery of the wellbore (cavity wall, r=R). This is described as a stress concentration. The stress state in the medium then becomes heterogeneous and will only return to its original value in the far field (r>>>R). For this reason, geostatic stresses are also known as far field stresses or stresses at infinity. Far field stresses are discussed in more detail in Section 2.4.3.

Knowing the geostatic state of stress, σ, the radius of the cavity, R, as well as the pressure acting inside the cavity, p_w, the most basic model of a wellbore is a linearly elastic plate with a central hole subjected to a bi-axial stress state p_0, Kp_0. This is one of the oldest problems of plane elasticity known as the 'Kirsch Problem'. The stress distribution around the cavity is given as

$$\sigma_r = \frac{p_0}{2}[(1+K)\left(1-\frac{R^2}{r^2}\right) - (1-K)\left(1-4\frac{R^2}{r^2}+\frac{3R^4}{r^4}\right)\cos 2\theta] + \frac{p_w R^2}{r^2} \tag{2.3}$$

$$\sigma_\theta = \frac{p_0}{2}\left[(1+K)\left(1+\frac{R^2}{r^2}\right)+(1-K)\left(1-\frac{3R^4}{r^4}\right)\cos 2\theta\right]-\frac{p_w R^2}{r^2} \tag{2.4}$$

$$\sigma_{r\theta} = \frac{p_0}{2}\left[(1-K)\left(1+2\frac{R^2}{r^2}-\frac{3R^4}{r^4}\right)\sin 2\theta\right]-\frac{p_w R^2}{r^2} \tag{2.5}$$

For a value of K=1, the problem is reduced to an infinite hollow cylinder loaded on its external boundary by an isotropic stress p_0. This simple plane elasticity problem is the 'Lamé Problem'. The stress distribution becomes

$$\sigma_r = p_0\left[1-\frac{R^2}{r^2}\right]+\frac{p_w R^2}{r^2} \tag{2.6}$$

$$\sigma_\theta = p_0\left[1+\frac{R^2}{r^2}\right]-\frac{p_w R^2}{r^2} \tag{2.7}$$

$$\sigma_{r\theta} = 0 \tag{2.8}$$

According to the given stress distribution, the most critical stress state is found at the cavity wall.

$$\sigma_r = p_w \tag{2.9}$$

$$\sigma_\theta = 2p_0 - p_w \tag{2.10}$$

The inward radial deformations, δ_r

$$\delta_r = \frac{\frac{p_0 - p_w}{2G} R^2}{r} \tag{2.11}$$

where G is the elastic shear modulus of the formation.

Wellbore unloading refers to the decrease in fluid pressure inside the cavity. The cavity wall of a wellbore subjected to isotropic far field stresses will converge inwards with a uniform radial displacement. This special case of the wellbore unloading problem is referred to as a 'cavity contraction' problem. The solution of the cavity contraction problem presented above is a simple linear elastic solution. The same problem can be solved using numerous elastic and elastoplastic constitutive relations. It is worth noting the difference between the cavity contraction problem and cavity expansion problem that are encountered in geotechnical problems including pressure meter testing (Aubeny et al., 1998), pile driving (Whittle, 1987) and cone penetration (Levadoux, 1980). Cavity expansion is a large strain problem where cavity radius increases from zero to R, while wellbore cavity contraction entails relatively small changes in cavity radius (small strain problem). However, the cavity expansion problem gives very similar and interchangeable results with the cavity contraction when used to simulate an incremental increase in cavity radius. Cavity contraction problems are commonly encountered in problems involving stress changes around tunnels (Lo et al., 1984; Ogawa and Lo, 1987), provided that the tunnel cross-section is a simple circular cavity (and prior to tunnel lining construction). In particular, Yu and Rowe (1999) modeled tunneling using the cavity contraction problem with elastoplastic models.

The following subsections describe different factors affecting the analysis of brittle compressive failure (failure criterion, material non linearity, well deviation, and cross anisotropy). Factors affecting the analysis of ductile compressive failure are also

discussed (yield surface, flow rule, effective stress analysis, consolidation, and coupled analysis of hydraulic diffusion around wellbores).

2.4.1 Effect of formation shear strength

This part focuses on the instability associated with hole enlargement due to brittle rock failure around the wellbore. This instability mechanism relates to type 'b' from Bradley's (1979) classification of wellbore failures. The wellbore is regarded as unstable when the elastic stress field around the wellbore satisfies the chosen failure criterion for the rock. In this section, three failure criteria are presented; the Mohr-Coulomb, the Hoek-Brown, and the Drucker-Prager criterion. The influence of the axial stress acting normal to the plane of the wellbore cavity is also discussed. In this section, only total stresses are considered

Mohr-Coulomb (MC) failure criterion

The MC criterion most commonly used for soils assumes that the radial and tangential stresses are the minor and major principal stresses respectively. For the purposes of the wellbore stability problem using the MC failure criterion only the σ_r and σ_θ are the stresses inducing failure, if this equation is satisfied

$$\sigma_\theta - \alpha\sigma_r = Y \tag{2.12}$$

where;

$$\alpha = \frac{1+\sin\phi}{1-\sin\phi} \text{ and } Y = \frac{2C\cos\phi}{1-\sin\phi} \tag{2.13}$$

and ϕ and C are the friction angle and cohesion respectively. If the expressions for σ_r and σ_θ at r=R from equation 2.3 and 2.4 respectively are introduced in this failure criterion in (equation 2.12), the minimum value of well pressure that will initiate compressive rock failure is:

$$p_w < \frac{[(1+K)+2(1-K)\cos 2\theta]p_0 - Y}{1+\alpha} \tag{2.14}$$

Hoek-Brown failure criterion

The Hoek-Brown failure criterion most commonly used for rock mass behavior can be expressed as follows

$$\sigma_\theta = \sigma_r + \sqrt{mq_c\sigma_r + sq_c^2} \tag{2.15}$$

where q_c is the uniaxial compressive strength of the intact rock material and m and s are constants depending on the nature of the rock mass and the extent to which it has been broken. The Hoek-Brown criterion may be better suited for predicting the imitation of shear failure in the jointed rock mass (Yu, 2000). Similar to the procedure followed using the MC failure criterion, the minimum well pressure possible without initiating failure is

$$p_w < \frac{d}{2}p_0 - \left[\frac{1}{8}\sqrt{m^2 + \frac{8dmp_0}{q_c} - 16s} - \frac{m}{8}\right]q_c \tag{2.16}$$

where $$d = 1 + K + 2(1-K)\cos 2\theta \tag{2.17}$$

Effect of the axial stress

In the previous subsections only the in-plane stresses (σ_θ and σ_r) are considered to initiate failure. Solutions which incorporate the axial stress are few and specialized (e.g. Florence and Schwer, 1978; Risnes et al., 1982). According to plane strain elasticity the axial stress is easily calculated based on a specific Poisson's ratio, μ and the initial axial stress

σ_v from equation 2.2. Following the solution of the Kirsch Problem the axial stress becomes

$$\sigma_z = \sigma_v - \mu\frac{4R^2}{r^2}p_0\left[\frac{1-K}{2}\right]\cos 2\theta \qquad (2.19)$$

Ewy (1991) used the Mohr-Coulomb failure criterion to estimate the minimum well pressure needed before failure is initiated at the cavity wall of a wellbore subjected to axisymmetric loading ($S_H = S_h = \sigma_h$) as shown in Figure 2.6. The wellbore is subjected to different initial geostatic stress states in this analysis, and for each case the minimum safe value of p_w is recorded (elastic limit). However, Ewy (1991) also used the major and minor principal stresses from the full principal stress tensor (σ_r, σ_θ, σ_z; 3D analysis) and not just the in-plane stresses (σ_r and σ_θ; 2D analysis). Hence, equation 2.12 becomes

$$\sigma_1 - \alpha\sigma_3 = Y \qquad (2.20)$$

A 3D stress analysis using MC gives the same result for K_0 values greater than ~0.6, but for values less than this, the results diverge as shown in Figure 2.6. This is because the axial stress, σ_z, is the major principal stress at the wellbore for low K_0 values. The 2D stress analysis underpredicts the value of p_w when σ_z is not the intermediate principal stress.

To investigate the effects of the intermediate principal stress on the calculated values of the elastic limit, a different shear strength criterion must be used. Several studies have proposed 3D shear strength criteria to solve the wellbore unloading problem (e.g. McLean and Addis (1990) and Ewy (1991)). To demonstrate the influence of the axial stress, the linear extended von Mises criterion, or Drucker-Prager (DP) (Drucker and Prager, 1952) is the most common choice:

$$q = d + p\tan B \qquad (2.21)$$

This criterion uses two stress invariants:

$$q = \frac{1}{\sqrt{2}}\sqrt{(\sigma_1 - \sigma_2)^2 + (\sigma_1 - \sigma_3)^2 + (\sigma_2 - \sigma_3)^2} \tag{2.22}$$

$$p = \frac{(\sigma_1 + \sigma_2 + \sigma_3)}{3} \tag{2.23}$$

where d and B are material parameters define the intercept and frictional coefficient in p-q space. The values of d and B depend on how the DP criterion is fitted to laboratory strength measurements. If standard triaxial compression tests are run to obtain the strength envelope, then the DP and MC parameters can be related by

$$d = c\frac{6\cos\phi}{3 - \sin\phi} \tag{2.24}$$

and

$$\tan B = \frac{6\sin\phi}{3 - \sin\phi} \tag{2.25}$$

If standard triaxial extension tests are run to obtain the strength envelope, then the relationship between the parameters of the two models becomes

$$d = c\frac{6\cos\phi}{3 + \sin\phi} \tag{2.26}$$

$$\tan B = \frac{6\sin\phi}{3 + \sin\phi} \tag{2.27}$$

The DP analysis predicts less conservative support requirements (elastic limit for p_w) than the MC 3D analysis, for nearly all K_0 values when the triaxial compression parameters are used as shown in Figure 2.6. The two criteria agree only at the points which correspond to triaxial compression at the wellbore (K_0 = 0.23, 1.83). When the triaxial

extension parameters are used, the predicted support requirements can be either greater or less than those predicted by the MC criterion. This difference is directly due to the fact that DP includes a strengthening effect from the intermediate principal stress.

2.4.2 Effect of material non-linearity on elastic stress distribution

The prediction of wellbore instability by assuming linear elasticity with constant elastic parameters may be in error. It has been established that the pre-yield and pre-peak stress strain properties of some rocks are non-linear and the elastic properties are pressure dependent (Kullhawy, 1975).

Santarelli et al. (1986) presented a numerical study on the analysis of wellbore stresses using a non-linear elastic model with a simple pressure-dependent Young's modulus. Based on the experimental data obtained for dry carboniferous sandstone, Santarelli et al. (1986) assumed that Young's modulus depends on the minor principal stress σ_3 in the following way

$$E = E_0(1 + 0.043\sigma_3^{0.78}) \tag{2.28}$$

where E_0 = 17.49 GPa for the carboniferous sandstone, σ_3 is in MPa and E is in GPa.

Using this non-linear elastic modulus, it is no longer possible to obtain a closed form solution for the elastic stress distribution around a wellbore. Santarelli et al. (1986) used the finite difference technique to solve the Lamé Problem described above, and calculate the stress distribution in a thick cylinder subjected to internal pressure, p_w, and external pressure p_0. The results are shown in Figure 2.7.

Figure 2.7 indicates that close to the cavity wall, the tangential stress derived from a non-linear elastic model is considerably smaller than that from a linear model with constant

stiffness. The non-linear elasticity results suggest that the maximum tangential stress does not necessarily develop at the cavity wall as suggested by linear elasticity. Larger volumes of rock are influenced by the wellbore cavity being drilled. This phenomenon agrees with observations of fracture being initiated within the surrounding wellbore and the production of discrete and largely intact rock chips. Several researchers used other pressure dependent models and produced similar results to that shown in Figure 2.7 (e.g. McLean , 1987; and Nawrocki and Dusseault, 1994).

2.4.3 Interplay between well trajectory and anisotropy

This section considers the effects of material anisotropy and anisotropic far field stresses. One specific type of material anisotropy, the transverse anisotropy or cross-anisotropy is considered in this section. Transversely isotropic materials have one plane of isotropic mechanical properties, with complete rotational symmetry in this privileged plane. Within planes perpendicular to this direction, the mechanical behavior is isotropic. Privileged planes are readily linked to weak bedding planes in shaley rocks. Their orientation with respect to the applied stresses affects the rock strength. This is illustrated in Figure 2.8, for strength tests with bedding planes whose normal is at an angle, β, to the applied maximum stress (Zoback, 2007). To be more quantitative, one could view a rock as having two strengths (illustrated in the Mohr diagram in Figure 2.8b). The intact rock would have its normal strength which would control failure when slip on bedding planes did not occur and a lower strength defined cohesion S_w and internal friction μ_w of the weak bedding planes which would apply when slip occurs along the pre-existing bedding planes.

Mathematically, Zoback (2007) described how to estimate the degree to which bedding planes lower rock strength using a theory developed by Donath (1966) and Jaeger and Cook (1979). The maximum stress, at which failure will occur, σ_1, will depend on σ_3, S_w, and μ_w by

$$\sigma_1 = \sigma_3 + \frac{2(S_w + \mu_w\sigma_3)}{(1 - \mu_w cot\beta_w)sin2\beta} \quad (2.29)$$

where $tan2\beta_w = \frac{1}{\mu_w}$. This is shown in Figure 2.8c, where at high and low values of β the intact rock strength is unaffected by the presence of the weak planes; and at $\beta=\beta_w=60^0$, the strength is markedly lower.

There have been long standing efforts of characterizing the failure strength and failure modes with theoretical models that are more sophisticated and generalized than the basic method described above. Duveau et al. (1998) classified the widely used anisotropic failure criteria into three categories: the mathematical continuous criteria, the empirical continuous criteria, and the weakness plane criteria. The empirical approaches are based purely on the observation of anisotropic strength of rocks in conventional triaxial tests. The continuous criteria describe failure with a continuous failure surface in the stress space. A continuous criterion is usually constructed using tensor representation theory. The critical plane approach assumes that failure occurs through planes, and a failure function is assumed for planes at different orientations. This is a brief description of the anisotropic failure criteria, but more information can be found at Duveau et al (1998) or Pei (2008). Pei (2008) proposed a new failure criterion for transversely isotropic rocks under true triaxial stress states. The new model has the ability to describe the coupling between material orientation (weak bedding planes) and principal stress orientation (Far field stresses).

Far field stresses are usually described in terms of the principal stresses. The principal coordinate system is the one in which shear stresses vanish and three principal stresses, $\sigma_1 \geq \sigma_2 \geq \sigma_3$ fully describe the stress field. At the earth's surface, no shear tractions can be supported, and hence, this surface is a principal plane, and one principal stress is generally normal to the earth's surface with the other two principal stresses acting in an approximately horizontal plane. According to Zoback and Zoback (1980, 1989) and

Zoback (1992), this orientation is generally true to the depth of the brittle-ductile transition in the upper crust at depths of 15-20 km. Therefore, geostatic stresses are defined by four components; vertical stress S_v, maximum principal horizontal stress S_H, the minimum principal horizontal stress S_h, and the azimuth of S_H to define the stress orientation. Regimes with anisotropic geostatic stresses is classified according to the E. M. Anderson scheme into three categories; normal, strike-slip, and reverse faulting regimes as shown in Figure 2.9.

Wellbore stability is affected by its orientation relative to the frames of reference that define the bedding planes (i.e. planes of isotropic material properties) and the far-field stresses. Three different coordinate systems are involved in the stability of a deviated well in a transversely isotropic medium (Pei, 2008): 1) the global coordinate system XYZ, where the far field stresses are defined for simplicity, 2) the local wellbore frame xyz, and 3) the material coordinate system STN as shown in Figure 2.10. Peska and Zoback (1995) utilized tensor transformation to evaluate stress in the wellbore system.

$$[\sigma_{local}] = [R]^T[\sigma_{global}][R] \tag{2.30}$$

where,

$$[R] = \begin{bmatrix} -\cos\gamma\cos\omega & -\sin\gamma\cos\omega & \sin\omega \\ \sin\gamma & -\cos\gamma & 0 \\ \cos\gamma\sin\omega & \sin\gamma\sin\omega & \cos\omega \end{bmatrix} \tag{2.31}$$

Where γ is the well azimuth and ω is the deviation angle. To evaluate the stability of wells of any orientation, a lower hemisphere diagram is used as shown in Figure 2.11. Each point represents a different wellbore with a specific orientation. Vertical wells correspond to a pint in the center; horizontal wells correspond to a point on the periphery at the appropriate azimuth, and deviated wells are plotted at the appropriate azimuth and radial distance.

Figure 2.12 shows the relative stability of wells for various orientations for normal, strike-slip and reverse faulting environments. The shown stress magnitudes and pore pressures correspond to a depth of 3.2 km and hydrostatic pore pressures. The mud weights, also stated in the figure, are assumed to be equal to the pore pressure, for simplicity. The color shown in each figure represents the rock strength required to prevent the initiation of breakouts according to the Mohr-Coulomb failure criterion previously mentioned in subsection 2.4.1. Red colors represent relatively unstable well orientations as higher rock strength is required to prevent breakout initiation whereas dark blue represents relatively stable well orientations as failure is prevented by much lower rock strength.

In normal faulting environments, breakout initiation is more likely to occur in wells that are highly deviated in the direction of S_H than for vertical wells; and wells that are highly deviated in the S_h direction are more stable than vertical wells. This is attributed to the stress concentration at the cavity wall. For a horizontal well parallel to S_H, for example, the greatest principal stress S_v is pushing down on the well and the minimum principal stress S_h is acting in a horizontal direction normal to the well path which yields the maximum stress concentration at the wellbore wall. In the case of strike-slip faulting, vertical wells are most likely to fail whereas horizontal wells drilled parallel to S_H are most stable. In the case of reverse faulting, sub-horizontal wells drilled parallel S_h are most unstable.

Figure 2.13 illustrates how weak bedding planes can affect wellbore stability. Zoback (2007) considered a drilling case in steeply dipping shales in the Andean foothills of Colombia. Willson et al. (1999) described the case and emphasized the significance of the prevailing material anisotropy. A near-vertical well experienced severe mechanical failures accompanied by large increases in well diameter in a particularly problematic shale section. When a fault was crossed by the well, the dip of the bedding changed dramatically, and no longer affected the degree of wellbore failure. Figure 2.13 shows the mud weight required to limit breakout width to 60^0 using the Donath (1996) method

explained above. The upper figure is for the formation above the fault where the bedding is dipping 60^0 to the SW. It shows that relatively low mud weights (less than 10ppg) could be used only when drilling wells deviated more than 30^0 to the NW or horizontal wells to the SE. this is because when drilling nearly orthogonal to bedding (the pole to the bedding planes is shown by the red dot), the weak bedding planes do not affect failure. The lower figure shows the bedding dipping 30^0 to the west below the fault. For this situation, a near vertical well is in a relatively stable direction because the nearly horizontal bedding planes did not affect wellbore stability.

Effect of Rock Anisotropy on elastic stress distribution

The problem of an anisotropic homogenous body bounded internally by a cylindrical surface of arbitrary cross-section has been discussed by Lekhnitskii (1963) and Amadei (1983). General solutions were provided on the distribution of stresses, strains, and displacements around the cylindrical surface for a variety of loading conditions. To demonstrate the effect of material anisotropy on the stress distribution derived from the theory of elasticity, the solution for a cylinder with both internal and external pressures is summarized in this section from Wu et al. (1991) which is a special case from the Lekhnitskii (1963) solutions. The cylinder has an internal radius 'a' and external radius 'b'. This analytical solution of the special case is used when one of the local axes rzθ may be treated as axis of symmetry.

The general stress-strain relationship for a plane strain problem in a cross-anisotropic elastic material can be written as follows (Lekhnitskii (1963), Van Cauwelaert (1977)

$$\epsilon_r = \beta_{11}\sigma_r + \beta_{12}\sigma_\theta \qquad (2.32)$$

$$\epsilon_\theta = \beta_{12}\sigma_r + \beta_{22}\sigma_\theta \qquad (2.33)$$

where β_{ij} are coefficients that can be expressed as simple functions of Young's moduli and Poison's ratios. For the cylindrical cavity, the compatibility and equilibrium equations become respectively as follows

$$\epsilon_r = \frac{d}{dr}(r\epsilon_\theta) \tag{2.34}$$

$$r\frac{d\sigma_r}{dr} + (\sigma_r - \sigma_\theta) \tag{2.35}$$

The above equations can be solved to give the following general solution for the radial stress

$$\sigma_r = Ar^{n-1} + \frac{B}{r^{n+1}} \tag{2.36}$$

in which n is $\sqrt{\frac{\beta_{11}}{\beta_{22}}}$. Using the boundary conditions: $\sigma_r = p_w$ at 'r=a', and $\sigma_r = p_0$ at 'r=b'; then the integration constants A and B can be derived. The final solutions for the stresses are:

$$\sigma_r = \frac{p_0 - p_w\left(\frac{a}{b}\right)^{n+1}}{1-\left(\frac{a}{b}\right)^{2n}}\left(\frac{r}{b}\right)^{n-1} + \frac{\left(p_w - p_0\left(\frac{a}{b}\right)^{n-1}\right)}{1-\left(\frac{a}{b}\right)^{2n}}\left(\frac{a}{r}\right)^{n+1} \tag{2.37}$$

$$\sigma_\theta = n\frac{p_0 - p_w\left(\frac{a}{b}\right)^{n+1}}{1-\left(\frac{a}{b}\right)^{2n}}\left(\frac{r}{b}\right)^{n-1} - \frac{n\left(p_w - p_0\left(\frac{a}{b}\right)^{n-1}\right)}{1-\left(\frac{a}{b}\right)^{2n}}\left(\frac{a}{r}\right)^{n+1} \tag{2.38}$$

For a value of n=1, the above solutions reduce to the basic solution of a hollow cylinder in an elastic isotropic material. Figure 2.14 shows the elastic stress distribution in both isotropic and anisotropic elastic materials. This comparison suggests that assuming cylindrical anisotropy affects the stress distribution significantly, especially the distribution of tangential stresses provided that the Young's modulus in the tangential direction is lower than that in the radial direction. This indicates that the rock around the cavity would appear stronger because the difference between radial and tangential stresses is lower. These findings are consistent with the investigation carried out by Wu and Hudson (1991) on the effects of stress-induced anisotropy on wellbore stability.

2.4.4 Effect of plasticity

In Subsection 2.4.1, the instability is assumed to occur when the chosen failure criterion is satisfied by the stress state at any point on the cavity wall of the wellbore. If a certain breakout width is permitted (θ_b $<60^0$ for example), then all points on the associated circumference may reach the stress state of the failure criterion. The corresponding mud weight 'p_w' to the stress state at the cavity wall is regarded as the elastic limit (Bradley, 1979). Using the elastic limit as guide lines for stability is an appropriate measure against hole enlargement failure types (type 'b' according to Bradley's (1979) classification). Further reduction in p_w causes a zone of yielded rock to grow around the cavity hole. The failure criteria are treated as yield loci (i.e. the onset of plastic behavior rather than the onset of failure). This approach is preferred for a ductile material which is prone to hole reduction rather than brittle breakouts as in shales and unlithified mudstones (type 'a' from Bradley's (1979) classification of wellbores failure). Each incremental reduction in p_w causes: 1) an outward movement of the elastic-plastic boundary, $r=R_p$, 2) elastic hole closure, and 3) additional closure due to plastic displacements.

Post-yield behavior is modeled in the elasto-plastic constitutive relations using two concepts; 1) the plastic flow rule, and 2) the stain hardening modulus, H. The plastic flow

rule states that the plastic strain increments are perpendicular to the plastic potential surface, g. The strain hardening modulus allows the calculation of the magnitude of plastic strain increments as follows:

$$d\epsilon^p = \frac{1}{H} QPd\sigma \tag{2.39}$$

where $Q = \frac{\partial f}{\partial \sigma}$ and $P = \frac{\partial g}{\partial \sigma}$.

As plastic deformations progress, energy is stored in the material. Strain hardening or softening correspond to a change in the stored energy and characterize the current position of the yield surface. An increase in the stored energy corresponds to an expansion of the yield surface. The quality of the material is improved or 'hardened' because the range of stresses within which behavior remains purely elastic is widened. Similarly, a decrease in the stored energy softens the material and contracts the yield surface. A perfectly plastic material is defined by the absence of any strain hardening process. All irrecoverable energy is plastically dissipated. For a perfectly plastic material, the yield surface is fixed within the stress space and the strain hardening modulus, H = 0. In this subsection wellbore stability is investigated using the Mohr-Coulomb criterion and the Drucker-Prager criterion as yield surfaces. First, these yield surfaces are used for perfectly plastic models, then a plastically dilating model is used for non associated Mohr-Coulomb material, and finally a strain hardening model is used with the Drucker-Prager yield surface.

Results using perfectly plastic models

Ewy (1991) used the Mohr-Coulomb failure criteria (MC, using only in-plane stresses in the analysis) and the Drucker-Prager failure criteria (DP, fitted to triaxial compression parameters) as yield surfaces as explained in Section 2.4.1; and decreased the well pressure in the cavity beyond the elastic limits shown in Figure 2.6. The rock around the wellbore is modeled as elastic perfectly plastic with the same parameters associated with

the results in Figure 2.6. Two cases of wellbores subjected to axisymmetric far field stresses are discussed in this subsection. The normalized hole closure and normalized plastic radius curves from these two cases are shown in Figure 2.15.

In the first case (Figure 2.15 left), the well pressure p_w is decreased from σ_h=4000 psi till the elastic limit is reached and then decreased further till zero, while σ_v = 5000 psi. The MC predicted an elastic limit of ~1700 psi. As p_w decreased further, MC predicts an expanding plastic zone and accelerating hole closure (these results are obtained analytically following Detournay, 1986). The DP predicted an elastic limit of ~800 psi. At p_w = 0, DP predicted smaller size of plastic zone and hole closure value than those predicted by MC (these results are obtained using the finite elements method).

The second case (Figure 2.15 right) is chosen because both MC and DP models predict similar elastic limits (p_w = 2370 psi). However, the DP model predicts less increase in yielding with further support reduction. At p_w = 0, the DP predicted less hole closure and smaller plastic zone. Including the axial stress 'σ_z' strengthens the rock when the DP model is used, while the MC model overestimates hole closure and size of the plastic zones.

Results using plastic dilation with Mohr-Coulomb

Yu and Rowe (1999) solved the cavity contraction problem using non-associated Mohr-Coulomb material. The cavity contraction problem as explained earlier is decreasing the well pressure inside the cavity subjected to axisymmetric far-field stresses, p_0. The chosen yield surface is defined by the Mohr-Coulomb criterion assuming the radial stress is the minor principal and the hoop stress is the major principal.

The well pressure is decreased beyond the elastic limit stated in Equation 2.14 to zero. A circular plastic zone is created around the cavity and expands with further decrease in well pressure. The radius to the elastic-plastic interface, r_p is derived from solving the equilibrium equations and maintaining continuity of stresses at the interface

$$r_p = R_0 T^{\frac{1}{1-\alpha}} \tag{2.40}$$

where
$$T = \frac{(\alpha+1)[(\alpha-1)p_w + Y]}{(2[(\alpha-1)p_0 + Y])} \tag{2.41}$$

while α and Y are the MC parameters (Equation 2.12).

Following Davis (1968), the soil is assumed to dilate plastically at a constant rate. This non-associated flow rule with the Mohr-Coulomb yield criterion has been widely used in geotechnical engineering for modeling cohesive-frictional soil behavior. The use of a fixed angle of dilation is a simplification and it is more realistic to consider angles of friction and dilation as functions of density and stress level. However, a constant dilation angles enables a complete analytical solution.

$$\frac{\dot{\epsilon}_r^p}{\dot{\epsilon}_\theta^p} = -\beta \tag{2.42}$$

where
$$\beta = \frac{1+\sin\psi}{1-\sin\psi} \tag{2.43}$$

and ψ is the dilation angle.

Figure 2.16 shows some selected results from the Yu and Rowe (1999) analyses. The effect of soil dilatancy on the predicted soil behavior around tunnels is studied by using three dilation angles of 0^0, 20^0 and 40^0. These dilation angles are much higher than the practical range but this variation illustrates the maximum possible effects of soil strength

and dilatancy on the behavior around the cavity. In Figure 2.16 the inward deformation at the cavity wall is plotted against the normalized value of well pressure. These curves are referred to as cavity contraction curves by Yu and Rowe (1999) or ground response curves by Brown et al. (1983).

Yu and Rowe (1999) compared between results using logarithmic and small strain formulations. The differences between both solutions are concluded to be negligible and the small strain solutions would be adequate for practical purposes. The soil displacements induced by tunneling increase with increasing dilation angle. Also the size of plastic zone increases when the value of dilation angle is increased. The ground response curves are found to be very sensitive to soil stiffness. Increasing stiffness index $G/p_0 = 10 \sim 50$ leads to reduction by a factor 5 in soil displacements due to tunneling.

Results using strain hardening with Drucker-Prager

Ewy (1993) used a nonlinear strain-hardening constitutive model to represent the behavior of weak sedimentary rocks observed in the laboratory. The initial yield surface expands as plastic strain accumulates until it becomes coincident with the failure surface that defines the ultimate strength ($\sigma_Y = \sigma_{Yult}$). The yield surface is the Drucker-Prager type explained in Subsection 2.4.1, but the yield criterion takes this form

$$q - p \tan B = \sigma_Y(\epsilon^p) \tag{2.44}$$

where $\sigma_Y(\epsilon^p)$ defines the size of the yield surface as a function of the work equivalent plastic strain defined as

$$\epsilon^p = \int \sqrt{\frac{2}{3}(d\epsilon_1^p d\epsilon_1^p + d\epsilon_2^p d\epsilon_2^p + d\epsilon_3^p d\epsilon_3^p)} \tag{2.45}$$

and $d\epsilon_1^p, d\epsilon_2^p, d\epsilon_3^p$ are incremental principal plastic strains related by non associated flow rule.

Ewy (1993) simulated wells at different orientations in different stress regimes using the finite element program ABAQUS^{TM}. To correctly calculate all far field stresses and displacements including the concentration of out-of-plane shear stresses near the wellbore cavity, a single slice of 3D finite elements are used. The two planar surfaces of the slice are constrained to have parallel displacements, but these displacements are allowed in all three dimensional directions. This ensures that the slice maintains constant thickness, yet allows it to warp, or become non-planar. The slice model has been also used by Zervos et al. (1996) to simulate directional wellbores using elastoplastic constitutive models with similar results.

Ewy (1993) and Zervos et al. (1996) recorded yield distribution and hole closure of vertical and inclined wells. As the hole deviation from vertical increases, yielding becomes less axisymmetric and more concentrated around the local x axis of the wellbore that corresponds to a horizontal line in the earth. The most extreme concentration of yielding occurs for a horizontal ($\omega=90^0$) well, and the severity increases with increasing difference between the vertical and horizontal stress. If the horizontal stresses are not equal then the azimuth (γ) of a non-vertical well becomes important.

Hole closures are determined mainly by the far field stresses acting orthogonally to the hole. Figure 2.17 plots radial hole closures for wells at $\omega=0^0$ (vertical), 45^0, and 90^0 (horizontal) subject to equal horizontal stresses with respect to the global frame of reference. The closure in the x direction (δ_{rx}) represents radial deformation at the sides of the cavity looking down on the well. The closure in the y direction (δ_{ry}) represents radial deformation at the top and bottom of the cavity. As the well is increasingly deviated from vertical it deforms more strongly into an elliptical type shape as shown by the difference between δ_{rx} and δ_{ry} in Figure 2.17. Hole closures in all directions are greater with lower support pressure in the hole. On the other hand, for a well that is not parallel to a

principal in situ stress, the displacements around the hole are actually three dimensional. The top of the wellbore cavity warps down and the bottom warps up.

Figure 2.18 shows the required well pressure to prevent failure in wellbores with different inclinations using three different design criteria and the same rock properties shown in Figure 2.17. Highest well pressures are mandated by linear elastic limit analysis using the Drucker-Prager criterion as shown in Subsection 2.4.1. The required support in the well cavity increases nonlinearly with the deviation of the well from vertical because the difference between the horizontal and vertical stresses in the cavity plane increases with well inclination. Also in Figure 2.18, the well pressure at which the rock at the wellbore reaches ultimate strength using nonlinear finite element analysis and the constitutive model described above. Nonlinear behavior of the rock reduces the stress concentration at the cavity wall compared to linear elastic analyses, so a lower support pressure is required for the same strength criterion. Another important consideration for drilling operations is the amount by which the hole closes after it is created (borehole convergence) because it determines clearances around the drilling tools. If no strain softening occurred after attaining ultimate strength, then lower support pressure than given by ultimate strength limit could be used. In Figure 2.18, the well pressure needed at which the smallest diameter is 2% less than the initial hole diameter.

2.4.5 Effective stress soil models

The time frame for wellbore drilling is shorter than the time frame for diffusion of pore water within the ductile formations around the cavity. Hence, plastic shearing and deformation assumed to involve undrained shearing in low permeability formations i.e. the soil skeleton deforms with no fluid flux or volume strain.

For undrained problems a more accurate approach is to use an effective stress analysis in conjunction with critical state soil models. Such an effective stress approach was used by

Randolph et al. (1979) and Whittle (1992) to predict soil behavior around driven piles. Collins and Yu (1996) have developed analytical solutions for cavity expansion in critical state soils. Yu and Rowe (1999) used the finite element method incorporating effective stress soil models to study soil behavior around tunnels. These studies are applicable to the wellbore unloading problem because of the similarities discussed earlier.

The effective stress analysis accounts for observed features of the mechanical behavior of ductile formations in undrained shear conditions that otherwise would not be included in total stress analysis. These features include: 1) the effect of stress history (OCR) on the soil behavior, 2) the variation of soil stiffness with stress level and void ratio, and 3) the effects of soil strain-hardening/softening.

The analysis of undrained problems is done by maintaining constant volume conditions in the soil around the cavity. This condition gives the following relationship between the current radius of a material element, r (initial radius, r_0) and the current radius of the cavity, R (initial radius, R_0).

$$R_0^2 - R^2 = r_0^2 - r^2 \tag{2.46}$$

Yu and Rowe (1999) used Equation 2.46 to derive a finite Lagrangean form of shear strain from the kinematics of cavity unloading.

$$\epsilon_{sh} = \epsilon_r - \epsilon_\theta = 2 \ln\left(\frac{r}{r_0}\right) \tag{2.47}$$

while

$$\epsilon_{vol} = \epsilon_r + \epsilon_\theta \tag{2.48}$$

Yu and Rowe (1999) followed closely the cavity expansion analysis in Collin and Yu (1996) and used the following deviator and mean effective stresses for the formulation.

$$q = \sigma_r' - \sigma_\theta' \tag{2.49}$$

$$p' = \frac{\sigma_r' + \sigma_\theta'}{2} \tag{2.50}$$

Using the p' and q parameters, the yield condition and plastic flow rule can be written in the form

$$q = f(p') \tag{2.51}$$

$$\frac{\dot{\epsilon}_{vol}^{p}}{\dot{\epsilon}_{sh}^{p}} = g(p') \tag{2.52}$$

The radial distribution of the pore pressure u(r) can be calculated from the quasi-static radial equilibrium equation in terms of total stresses so that the non dimensional pore pressure gradient is given by

$$\frac{du}{dr} = -\frac{dp'}{dr} - \frac{1}{2}\left(\frac{dq}{dr}\right) - \frac{q}{r} \tag{2.53}$$

Equation 2.53 can be integrated in the elastic and plastic regions using the constitutive relations of the chosen model; and hence, the distribution of excess pore pressures is deduced.

Yu and Rowe (1999) used three different critical state soil plasticity models. The first model is the original Cam-Clay model for both normally and overconsolidated clays.

This model was proposed by Schofield and Wroth (1968) to describe the stress strain behavior of clays. The yield surface of this model for cavity contraction problems is

$$q = f(p') = \frac{M}{\Lambda} p' \ln p' \tag{2.54}$$

where the stresses have been non-dimensionalized by the equivalent consolidation pressure at the same specific volume, $\nu = (1+e)$

$$p'_e = \exp\left(\frac{N-\nu}{\lambda}\right) \tag{2.55}$$

The constant $\Lambda = 1 - \kappa/\lambda$, where κ, λ are the slopes of the elastic swelling line and normal consolidation line respectively, in $\ln(p') - \nu$ space and N is the value of ν on the normal consolidation line when p' is = 1kPa. The final critical state constant M is the slope of the critical state line in p'-q space. The ratio of the plastic volumetric and shear strain rates calculated from the normal flow rule is

$$g(p') = -\frac{M}{2\Lambda}(\Lambda + lnp') \tag{2.56}$$

The second model is the Hvorslev yield surface for heavily overconsolidated clays. It is well established that the original Cam-Clay yield surface over-predicts the soil strength significantly for heavily overconsolidated clays. In this case, the Hvorslev surface has often been used as the yield function. The Hvorslev yield surface is a straight line p'-q space with a slope, h.

$$q = -hp' - (M-h)\exp(-\Lambda) \tag{2.57}$$

The third model is the modified Cam-Clay model proposed by Roscoe and Burland (1968) to improve the performance of the original Cam-Clay model for normally

consolidated clays. The modified Cam-Clay yield surface for cavity unloading problems is

$$q = f(p') = -Mp'\sqrt{p'^{\left(-\frac{1}{\Lambda}\right)} - 1} \tag{2.58}$$

The ratio of the plastic volumetric and shear strain rates calculated from the normal flow rule is

$$g(p') = \frac{1}{2}\left(\frac{M^2 - \eta^2}{2\eta}\right) \tag{2.59}$$

where $\eta = q/p'$.

Figure 2.19 shows the effects of using different yield surfaces on the predicted soil behavior of normally consolidated and heavily overconsolidated clays according to the results from Yu and Rowe (1999). The figure shows the cavity contraction curves including both the cavity pressure, p_w, and the pore pressure change using the original and modified Cam-Clay for normally consolidated clays, and using the original Cam-Clay and the Hvorslev yield surface for overconsolidated clays (OCR = 10). All results are normalized by the undrained shear strength, s_u, computed in an elemental triaxial compression test.

For normally consolidated clays, when the cavity pressure is reduced the pore pressure increases initially before eventually decreasing to a much lower value. On the other hand, the pore pressure remains constant during the elastic unloading before starting to decrease when unloading becomes plastic in overconsolidated clays. The soil displacement induced by tunneling decrease with increasing value of the overconsolidation ratio.

For the comparison shown in Figure 2.19, it is noted that the choice of a particular critical state model has a very important effect on the predicted soil behavior around the cavity. In general, the use of more realistic soil models such as the Hvorslev criterion for heavily

overconsolidated clays and the Modified Cam-Clay, MCC, model for normally consolidated clays tends to predict smaller displacements around tunnels.

Charlez (1997) proposed a method to assess wellbore stability for a given mud weight based on analysis using critical state soil models. Under undrained conditions, the extension of the zone reaching critical state for a given mud weight is called the critical instantaneous zone. The critical zone reflects the distribution of stresses and pore pressure around the wellbore. Charlez (1997) used the original Cam-Clay model to define the Critical Instantaneous Mud Weight (CIMW). The CIMW is the weight for which a single point reaches the critical state considering the ratio C such that

$$Cr = \frac{\frac{q}{p'} - M}{M} \tag{2.60}$$

The CIMW corresponds to the well pressure for which Cr becomes null at a single point of the structure.

2.4.6 Effect of Consolidation

The solutions presented in the previous subsections assume that the rock behaves as a single phase material and hence the solutions obtained are relevant only to the short term (undrained or constant volume) conditions or the long term (fully drained) conditions. However, the displacements and stress changes around a wellbore are time-dependent. This time dependence is due to the two phase nature of a saturated material. Volume change takes place only as fluid is expelled from the voids between the solid particles. Movement of fluid through the soil or rock cannot occur instantaneously and so any deformations which involve a change in volume require a finite time to occur. Assuming a two phase material, Carter and Booker (1982) presented a semi-analytical solution for

the displacements and stress changes around a long circular opening in a saturated rock material.

The initial conditions of the problem are similar to that of the wellbore unloading problem described at the beginning of this section. It is also assumed that the initial pore water pressure is hydrostatic with a constant magnitude of u_0 in the considered cross-section. Carter and Booker (1982) considered two extreme hydraulic boundary conditions at the wellbore wall. The first case is for a permeable wellbore surface, which is defined by the following boundary condition on pore pressure

$$u = 0 \tag{2.61}$$

The other extreme case that was considered is an impermeable wellbore, which would give the following boundary condition at $r = R_0$.

$$\frac{\partial u}{\partial r} = 0 \tag{2.62}$$

To simplify the analysis, Carter and Booker (1982) solved the problem as the superposition of three different modes of loading for (a) the permeable wellbore and two modes for (b) the impermeable wellbore.

Mode Ia

The removal of the volumetric component of the total radial stress on the wellbore surface

$$\Delta\sigma_r = -\sigma_m = -\frac{1}{2}(K+1)p_0 \tag{2.63}$$

Mode IIa

The removal of the initial pore water pressure on the wellbore surface

$$u = -u_0 \tag{2.64}$$

Mode IIIa

The removal of the deviatoric components of total radial stress and shear stress on the wellbore surface

$$\Delta\sigma_r = -\sigma_d \cos 2\theta = -\frac{1}{2}(K-1)p_0 \cos 2\theta \tag{2.65}$$

$$\Delta\sigma_{r\theta} = \sigma_d \sin 2\theta = \frac{1}{2}(K-1)p_0 \tag{2.66}$$

On the other hand, for an impermeable wellbore only loading modes Ib and IIIb exist.

The solution by Carter and Booker (1982) outlined above is based on the assumption that both pore fluid and particles are incompressible. This is particularly applicable to soil mechanics problems. For application to wellbore stability, it is necessary to extend the Carter and Booker (1982) solution to include the compressibility of pore fluid and particles.

2.4.7 Coupled behavior of soft formations

Detournay and Cheng (1988) followed Biot's theory of consolidation to simulate the formations around the wellbore as poroelastic material with compressible constituents. This solution reveals the effects of coupling between changes in total stresses and changes in pore pressures. However, in the solution of Detournay and Cheng (1988), only a permeable wellbore is considered. This state of drainage relates to a few cases in the field when mud pressure penetrates the formation and is no longer sealing the pores on the cavity wall. Special measures are needed to prevent the drilling fluid from dissipating into the formations especially in fractured formations (Labenski et al., 2003).

Charlez (1997) studied the effect of drainage on stability assuming a perfect mud cake in the cavity and an impermeable cavity wall. The effects of hydraulic diffusion are analyzed within the time after the drilling and before setting the casing and cementing which could take several hours to several days. Especially when the wall is drilled in an anisotropic stress field the undrained pressure distribution will re-equilibrate through time according to the permeability of the formation. Charlez (1997) monitored the change in the stability criterion Cr explained in the previous subsection with time to conclude if the current mud pressure ensures stability versus time. Using the original Cam-Clay model, Charlez (1997) simulated the formation around the wellbore as poroplastic material.

2.4.7.1 Poroelasticity

As discussed by Detournay and Cheng (1988, 1993), a set of five bulk material constants are needed to provide a full description of an isotropic rock-fluid system. These include: two elastic constants G and μ (shear modulus and drained Poisson's ratio); two poroelastic coefficients B (ratio of the induced pore pressure to the variation of confining pressure under undrained condition, i.e. Skempton's coefficient) and μ_u (undrained Poisson's ratio); and the parameter χ which, for the case of incompressible fluid and solids, is related to the permeability coefficient k by $\chi = k/\gamma_w$. Based on these definitions, Detournay and Cheng (1988) defined a generalized consolidation coefficient as

$$c = \frac{2\chi B^2 G(1-\mu)(1+\mu_u)^2}{9(1-\mu_u)(\mu_u-\mu)} \tag{2.67}$$

Charlez (1997) used the Detournay and Cheng (1988) solution and produced the results shown in Figure 2.20 for a wellbore subjected to anisotropic far field stresses. The initial pore pressure distribution (Figure 2.20a) corresponds to the undrained conditions except at the wellbore wall where there is an incompatibility between the undrained value and the boundary condition imposed at the well (u = 0). To ensure continuity, the pressure

exhibits a maximum close to the wall but located inside the formation then finally joins the undrained curve. This peak moves with time towards the exterior of the formation but decreases in intensity. The undrained pore pressure configuration evolves into a purely radial flow through time.

Since the drainage of the rock occurs at the wall, the rock at this point is almost instantaneously characterized by its drained elastic constants. However, inside the formation, the rock is characterized by its stiffer undrained elastic constants. Due to the contrast in stiffness, the stresses relax in the softer drained region and a maximum hoop stress is observed in the interior of the formation as shown in Figure 2.20b. Detournay and Cheng (1988) reported that failure occurs away from the wall at a distance ranging from 5% to 10% of the wellbore radius.

2.4.7.2 Poroplasticity

Charlez (1997) derived the undrained poroplastic response as the sum of Skempton's effect and a contribution related to the plastic volumetric stain. In this case of an elastically and plastically incompressible matrix the variation in pore pressure with respect to the virgin pore pressure is such that

$$\Delta u = B\left(\frac{\Delta\sigma_{oct}}{3}\right) + BK_B\epsilon_{vol}^{p} \tag{2.68}$$

where K_B is the drained bulk modulus.

Charlez (1997) concluded that in case of a horizontal well (anisotropic far field stresses), the undrained pore pressure values are generally larger than that observed for a poroelastic model in the direction of minor geostatic stress. The maximum pore pressure value can be located at the wellbore wall (low B values as in sands) or inside the formation (high B values as in claystones).

In order to assess the effect of time on the stability of the wellbore, Charlez (1997) performed a two phase calculation. First, an undrained unloading of pressure at the wellbore wall is stopped slightly higher than the CIMW. Then, the well pressure is kept constant and time is incremented to simulate the hydraulic diffusion process. As shown in Figure 2.21, the pore pressure in the minor stress direction gradually flattens by diffusion but it remains inside the formation because the wellbore wall is assumed impermeable. The critical parameter Cr is then plotted versus time as shown in Figure 2.22. The criterion becomes slightly positive with early time increments which shows that time in this case is slightly unfavorable to well stability.

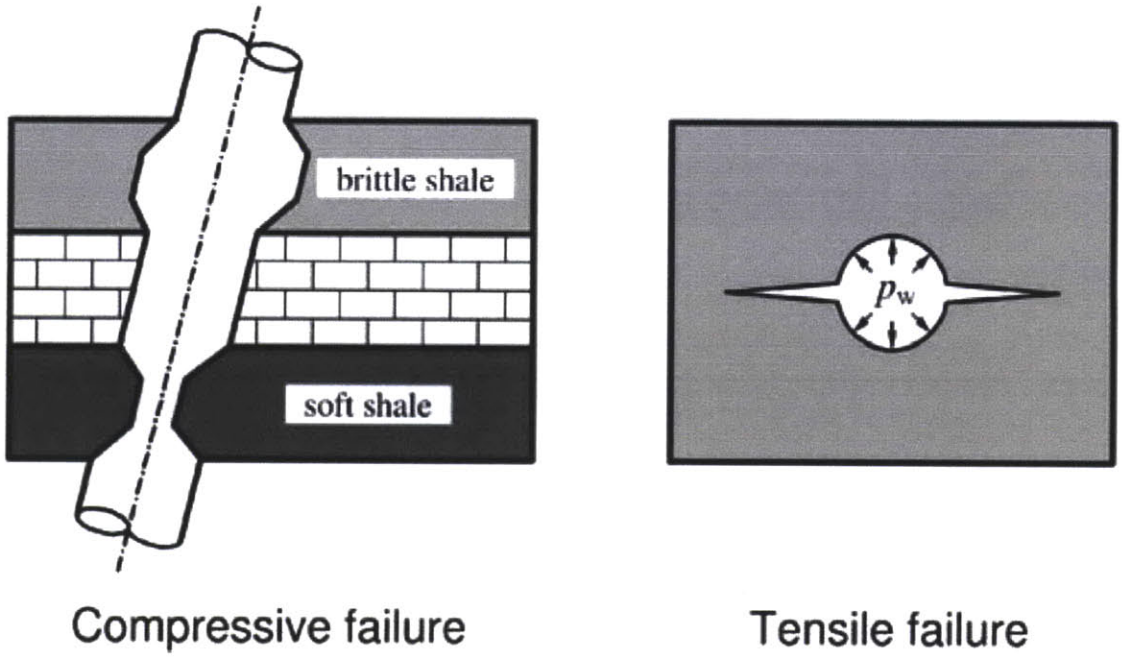

Figure 2.1 Types of Wellbore failure according to Fjaer et al (2008) after Bradley (1979).

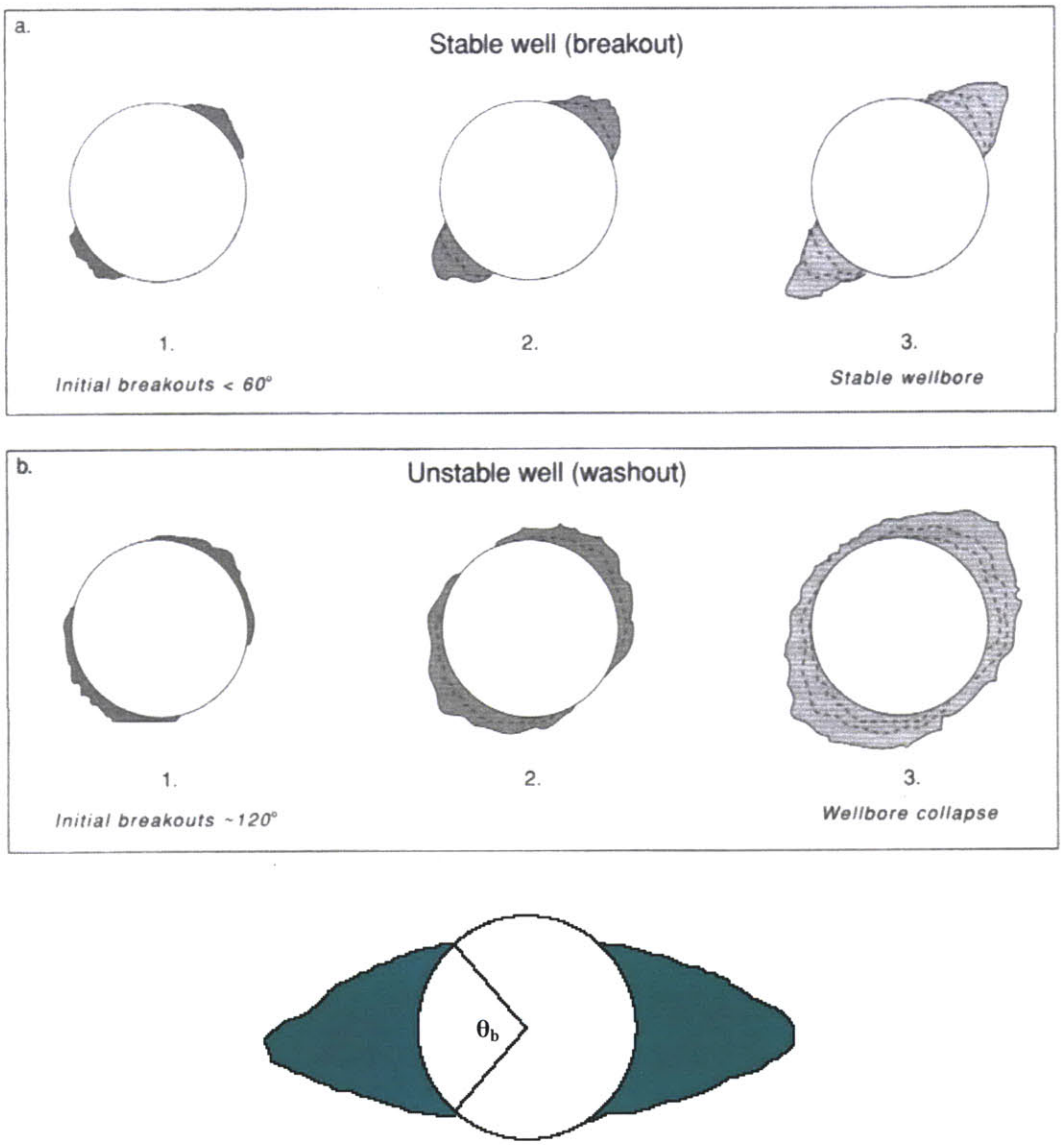

Figure 2.2 Schematic representation of breakout growth (a) when the initial breakout size is relatively small ($\theta_b < 60^0$) and (B) when it is relatively large ($\theta_b > 120^0$) (Zoback, 2007). The definition of breakout width (θ_b) is also described in the accompanied sketch as the central angle corresponding to the damaged part of the circumference.

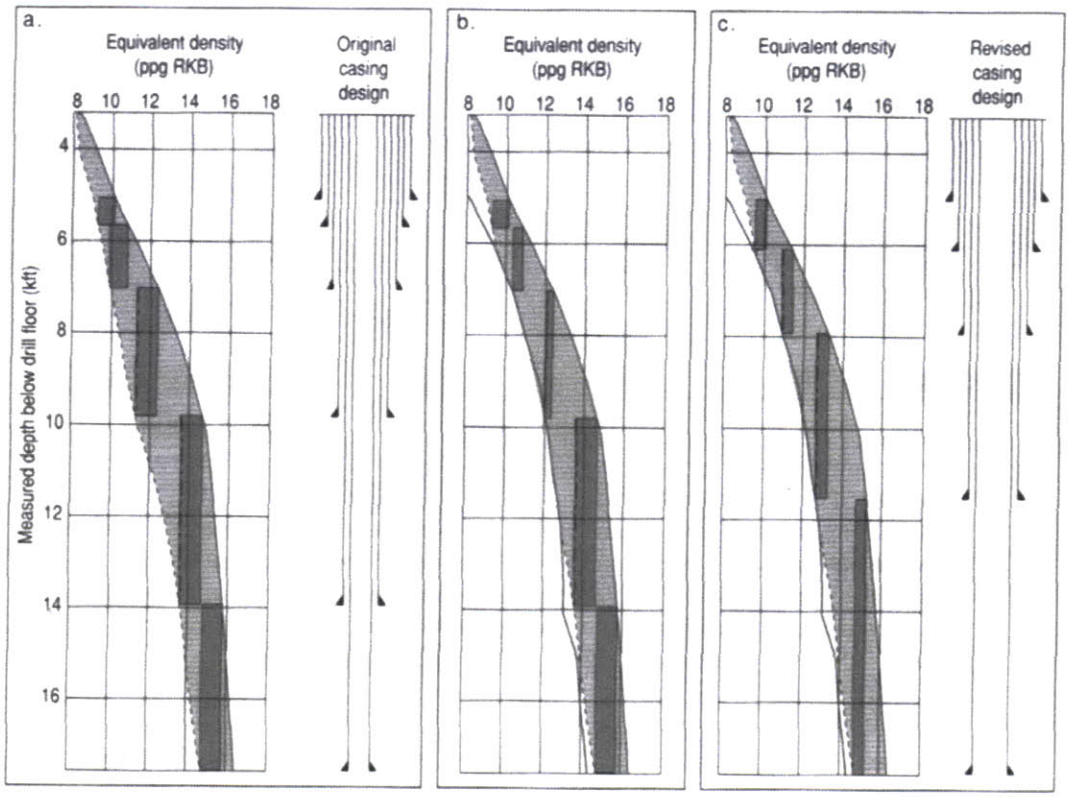

Figure 2.3 (a) A pre-drill well design, made by assuming that the pore pressure and the fracture gradient limit the mud window. (b) An illustration of the impact of considering the collapse pressure on the pre-drill design. (c) A design made utilizing a comprehensive geomechanical model, which adjusts the positions of the first two casings. (Moos et al., 2003)

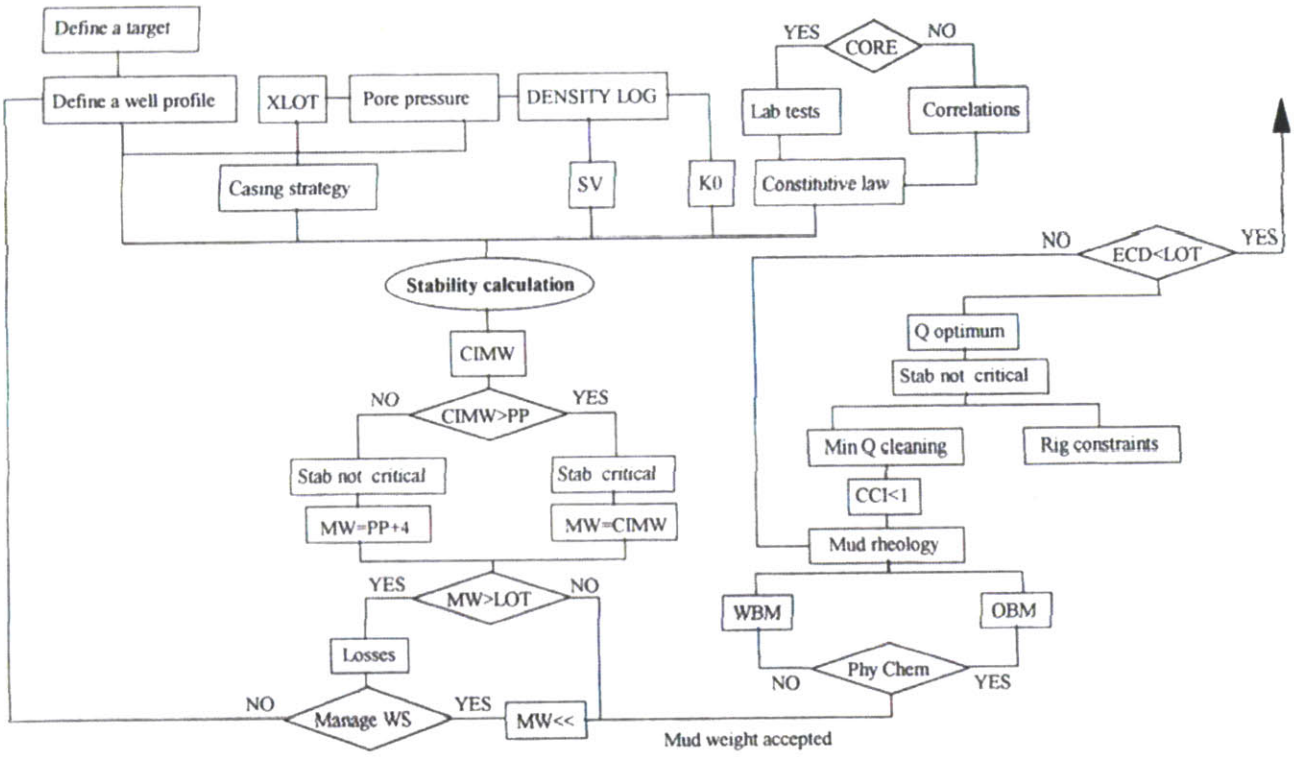

Figure 2.4 Well design decision tree (Charlez, 1997)

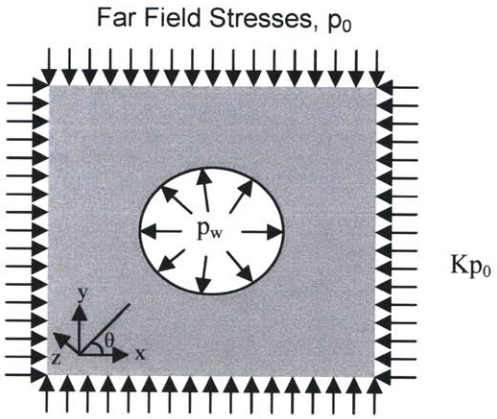

Figure 2.5 A schematic of the wellbore unloading problem.

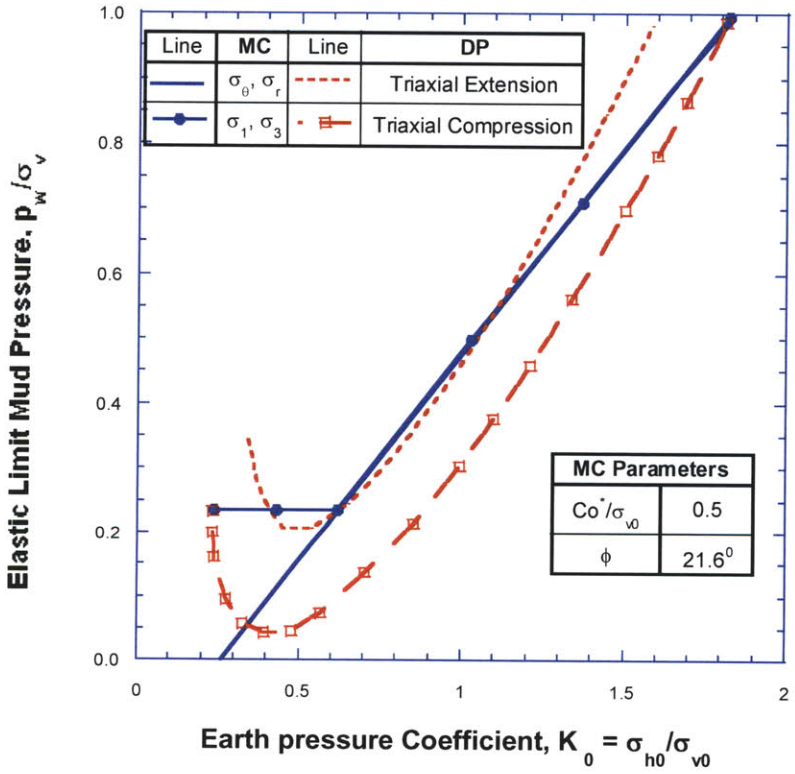

Figure 2.6 Minimum well pressure required without initiating failure at the cavity wall of the wellbore model for different values of K_0 (Ewy, 1991). The elastic parameters are the Young's modulus E= 5E+5 psi and μ=0.3.

*Co = 2C cosϕ/(1-sinϕ)

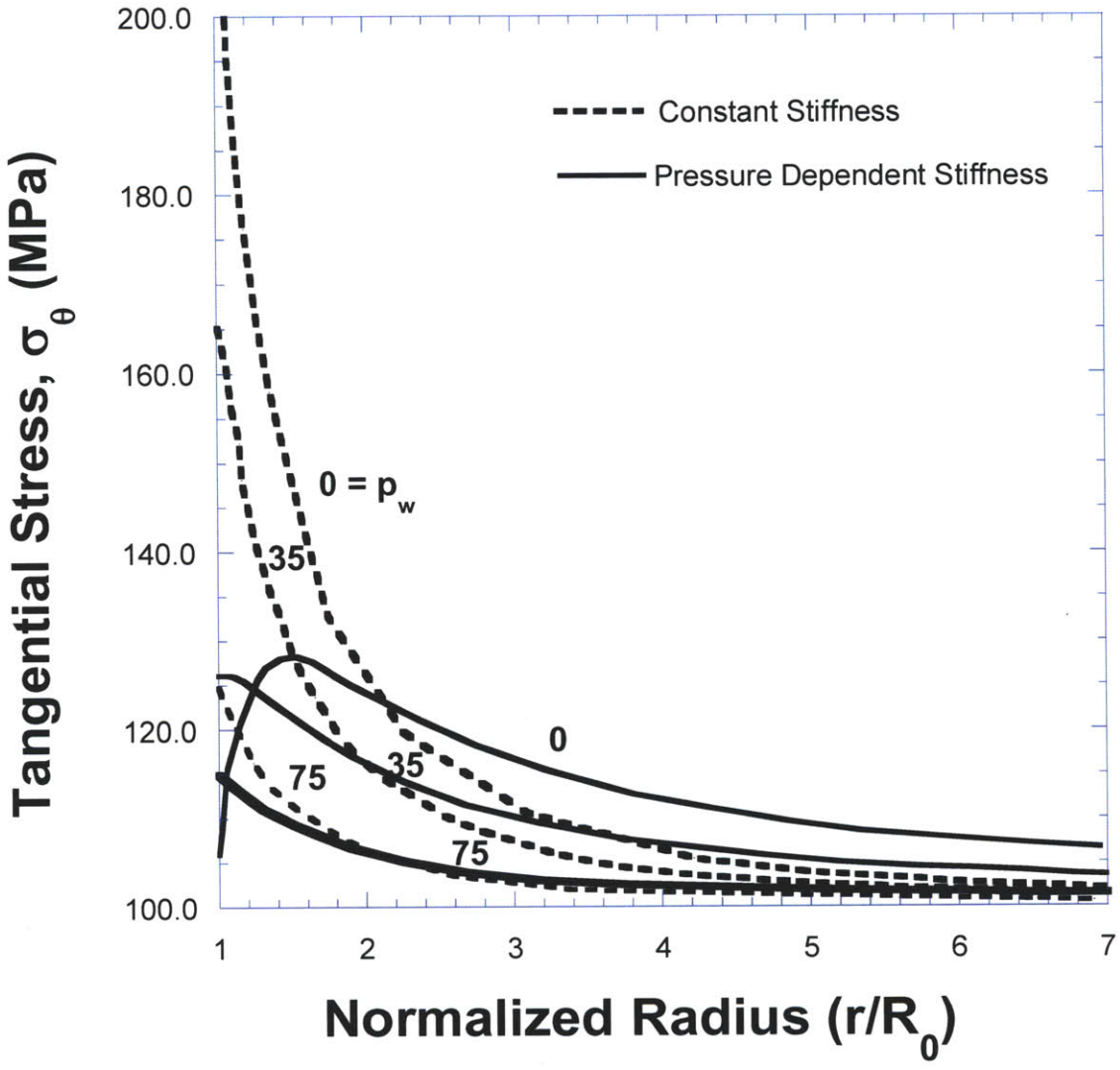

Figure 2.7 Distribution of tangential stresses along the thickness of thick hollow cylinder subjected to uniform outer stresses p_0 = 100 MPa. The stress distribution is calculated using both constant and pressure dependent Young's modulus. Each curve is calculated for a certain internal pressure p_w indicated on the curve. (Santarelli et al. 1986)

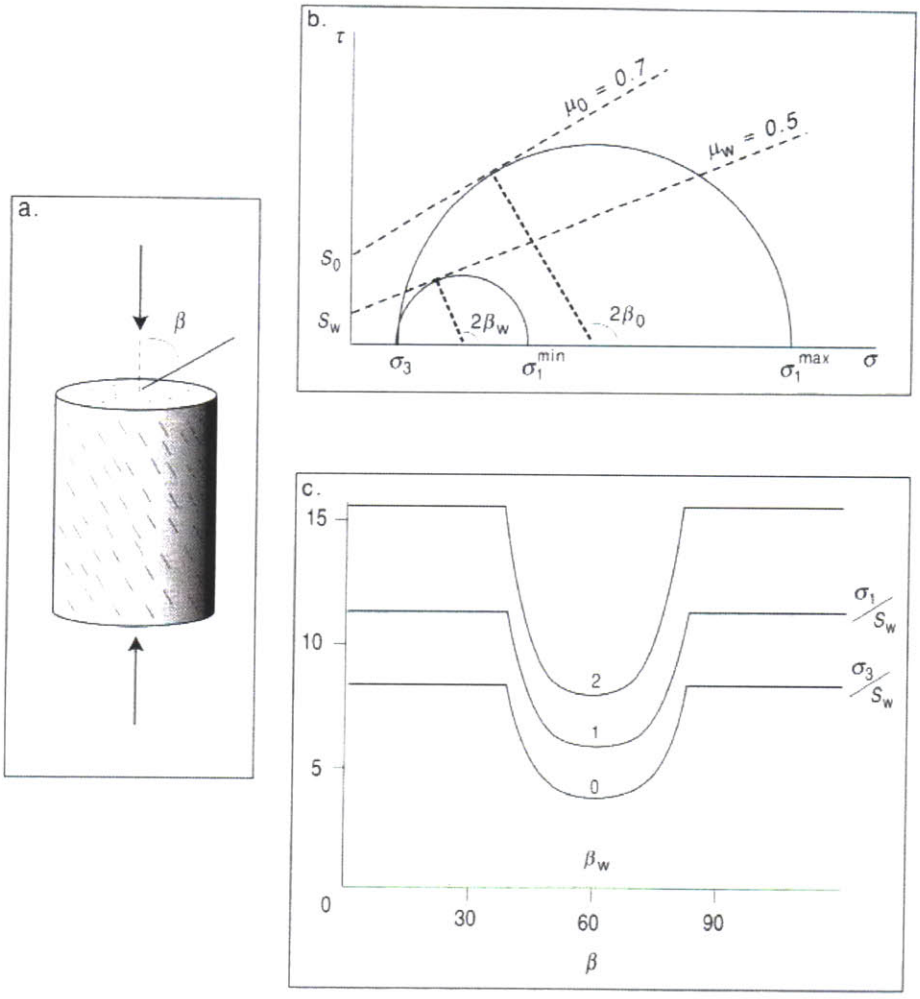

Figure 2.8 Dependence of rock strength on the angle of weak bedding planes. (a) Rock samples can be tested with the orientation of the weak planes at different angles, β, to the maximum principal stress σ_1. (b) The strength can be defined in terms of the intact rock strength (when the weak planes do not affect failure and the strength of the weak planes. (c) Prediction of rock strength (normalized by the cohesion of bedding planes) as function of β. (Zoback (2007) after Donath (1966), and Jaeger and Cook (1979)).

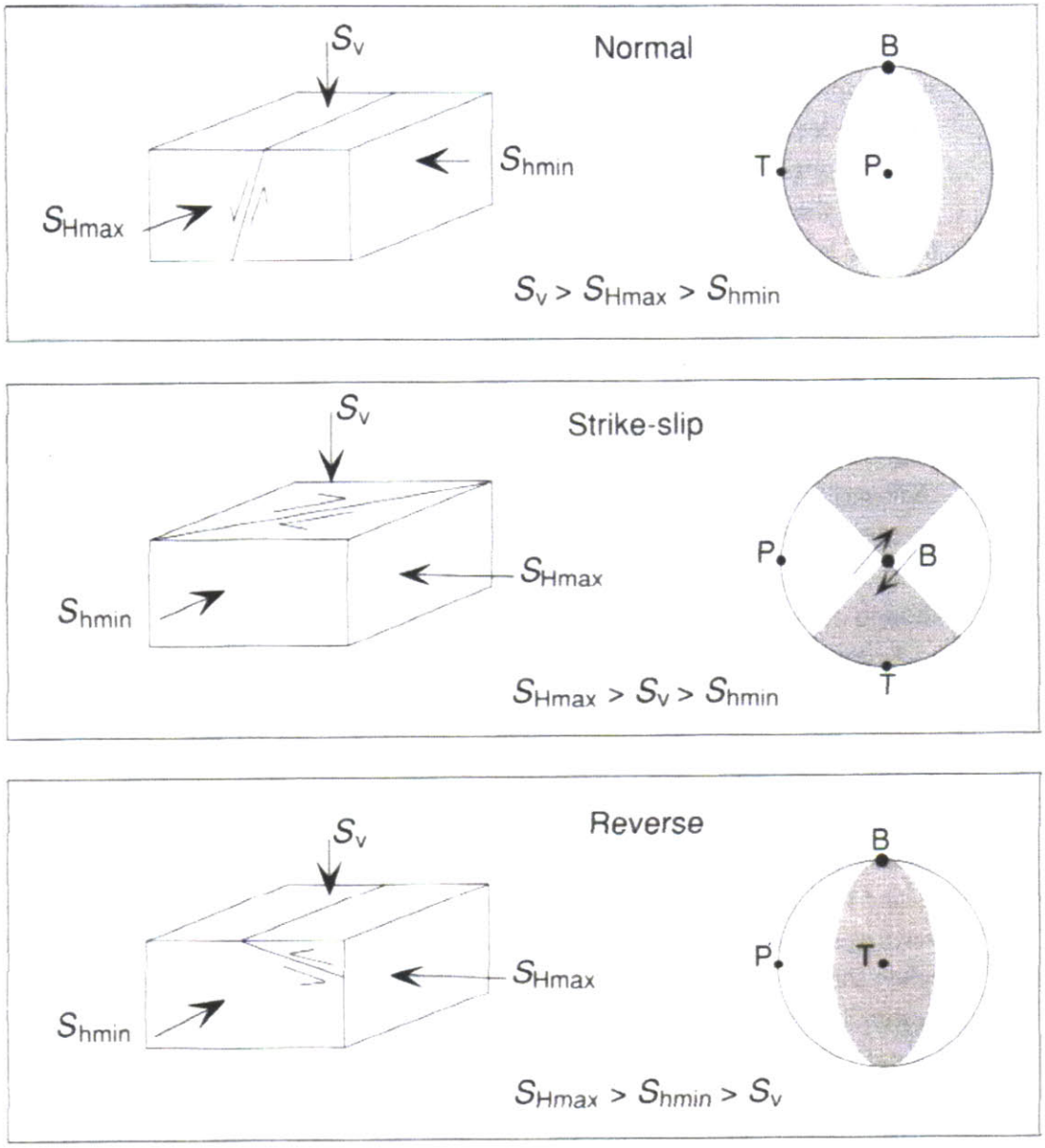

Figure 2.9 E. M. Anderson's classification scheme for relative stress magnitudes in normal, strike-slip and reverse faulting regimes. The beach balls on the right are the earthquake focal mechanisms as identified by Zoback (2007).

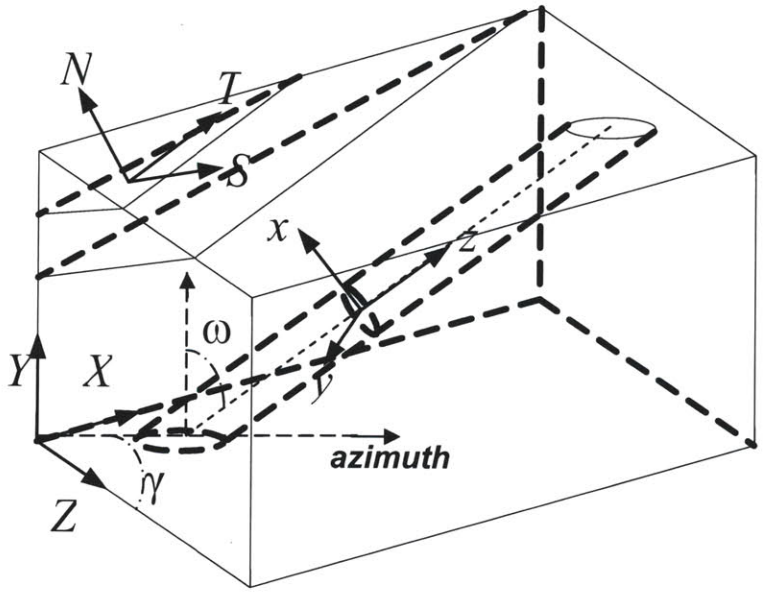

Figure 2.10 A schematic diagram showing the global frame of reference X, Y, Z (The principal stresses can be considered as aligned with the global frame of reference to simplify the mathematical efforts needed for stress tensor transformation from the principal frame of reference to the geographic frame of reference); and the local frame of reference aligned with the drilling axis x, y, z. Also, the frame of reference aligned with the bedding planes N, T, S. (Modified from Pei (2008)). Angles γ and ω are the azimuth and deviation angles of the well respectively.

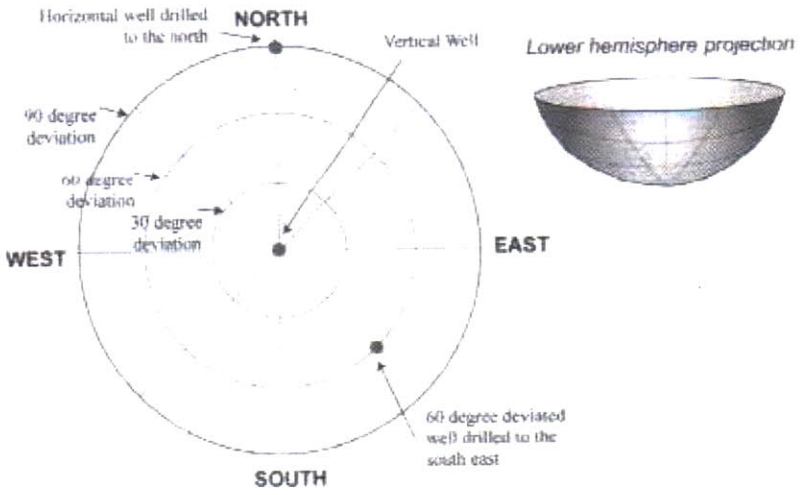

Figure 2.11 Lower hemisphere projection used to display relative stability of wells with different deviations and azimuth. (Zoback (2007) after Peska and Zoback (1995)).

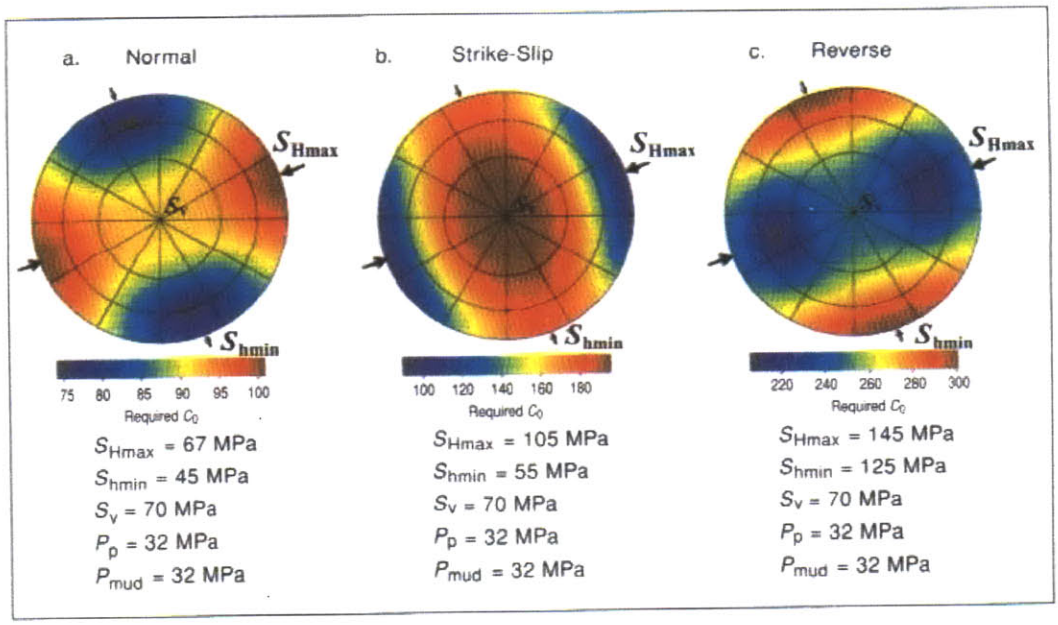

Figure 2.12 The tendency for the initial of wellbore breakouts in wells of different orientation for normal, strike-slip and reverse faulting regimes (Zoback (2007) after Peska and Zoback (1995)).

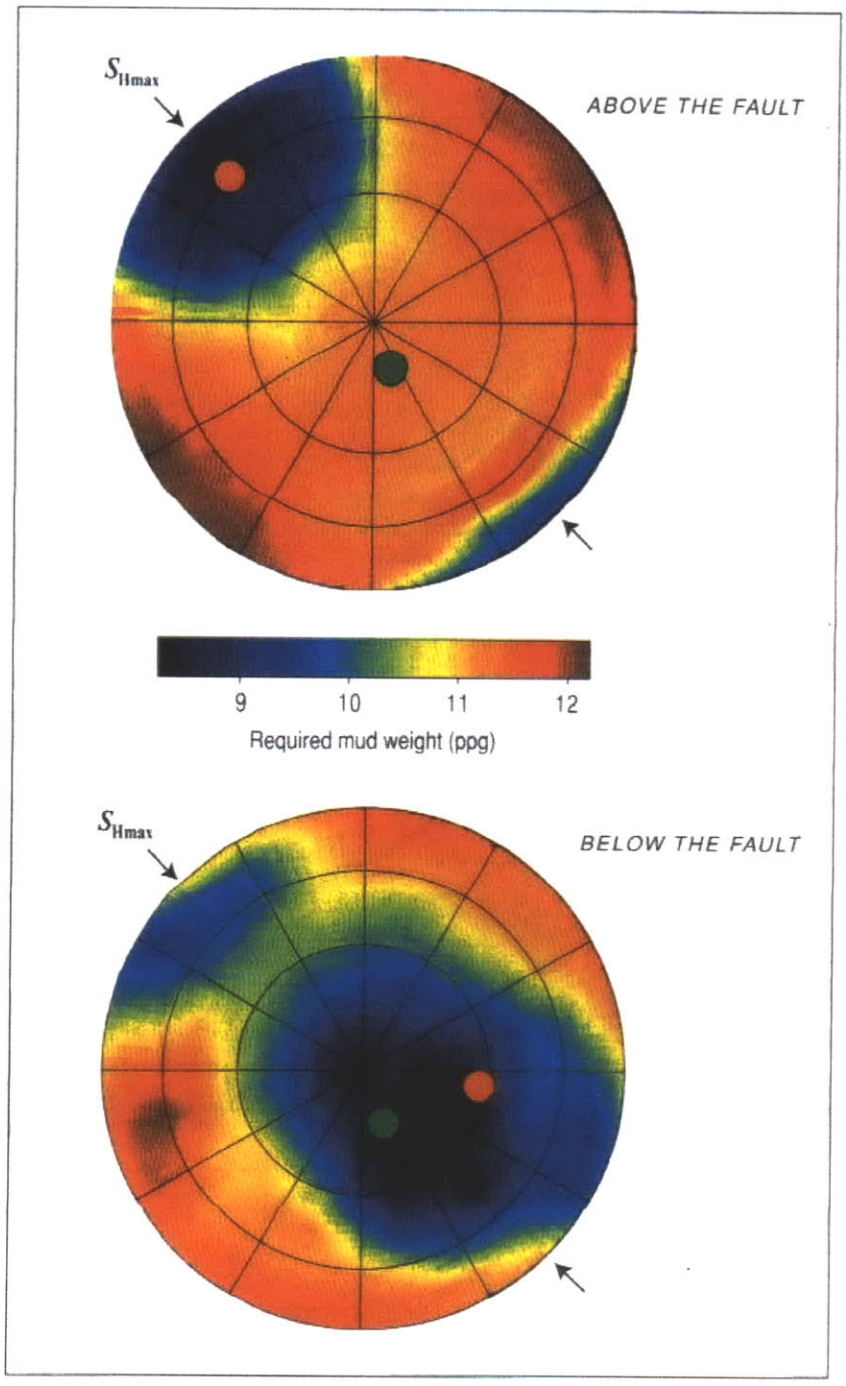

Figure 2.13 Effect of bedding planes orientation (indicated by red dot) on the stability of a near vertical wellbore (indicated by green dot). (a) Wellbore stability diagram for the case above a fault. (b) Below the fault in the Andean foothills of Colombia (Zoback (2007) after Willson et al. (1999)).

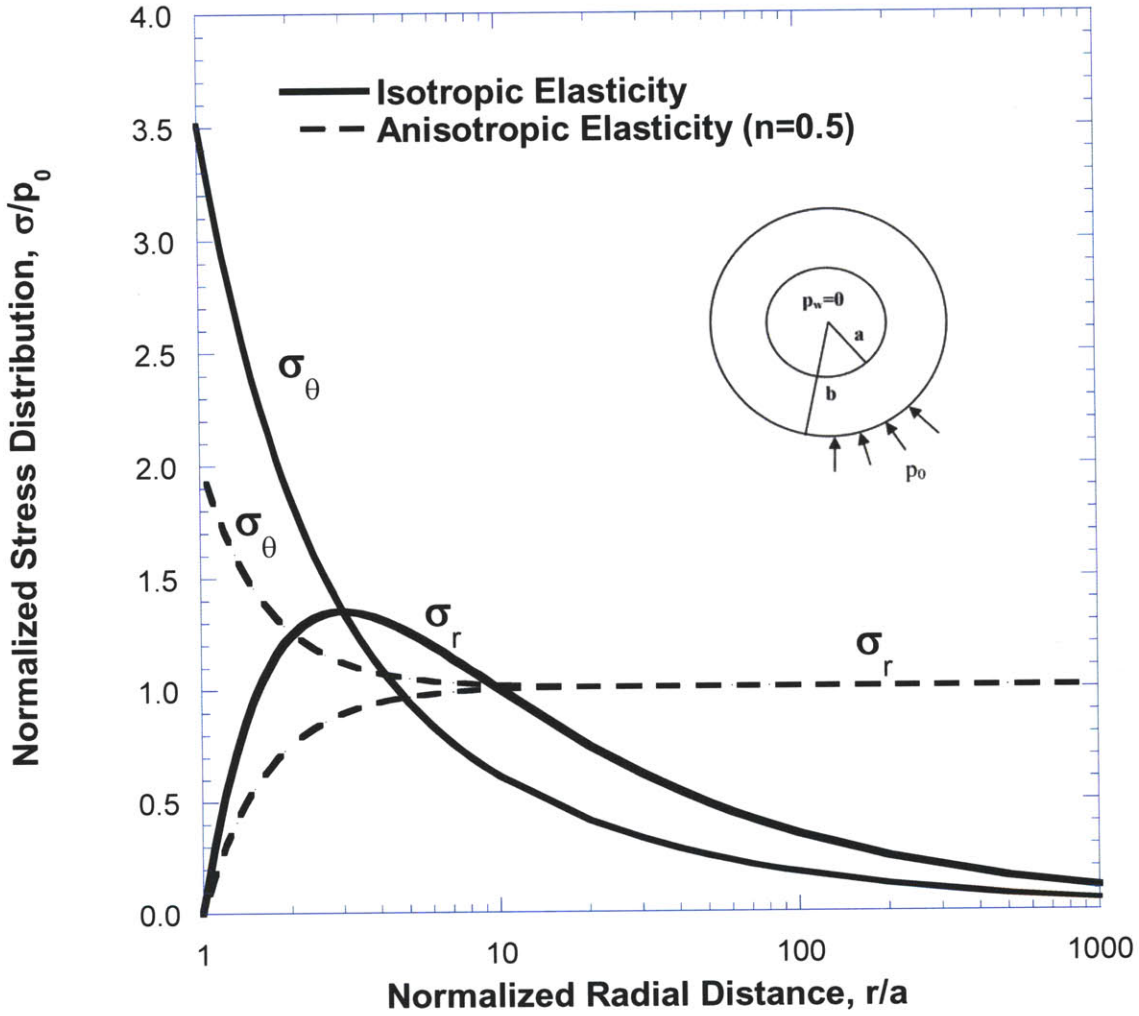

Figure 2.14 Effect of material anisotropy on the distribution of elastic stresses around a hollow cylinder bounded by internal and external pressure. The details of the problem are shown in the accompanied sketch. The results shown are for a value of n=0.5 where tangential Young's modulus is higher than radial Young's modulus.

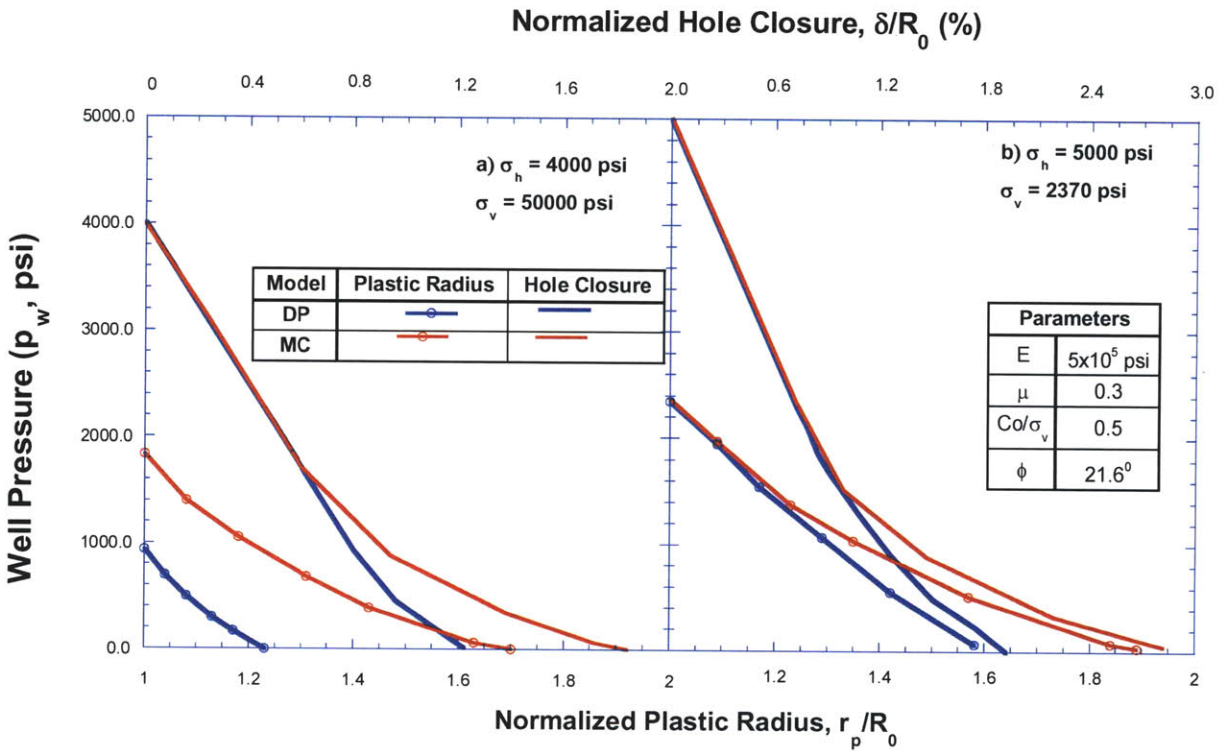

Figure 2.15 Normalized hole closure curves and normalized plastic radius curves for wellbores subjected to two different initial geostatic stress conditions using the Mohr Coulomb yield criterion and the Drucker Prager yield criterion. (modified from Ewy, 1991).

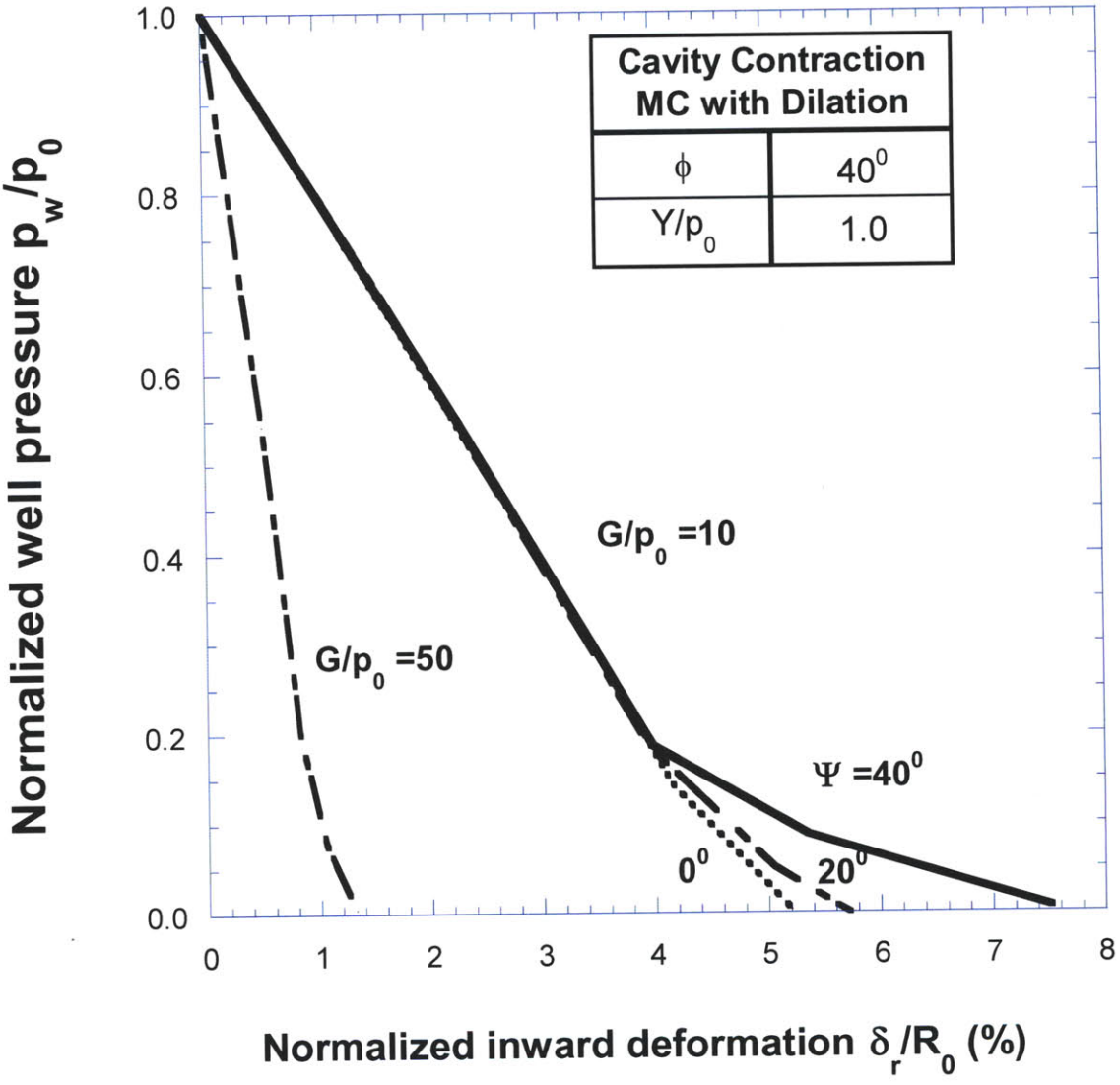

Figure 2.16 Cavity contraction curves of a wellbore subjected to isotropic geostatic stresses using non-associative Mohr Coulomb constitutive relations. The results show the effect of variation in dilation angle and stiffness index (modified from Yu and Rowe (1999)).

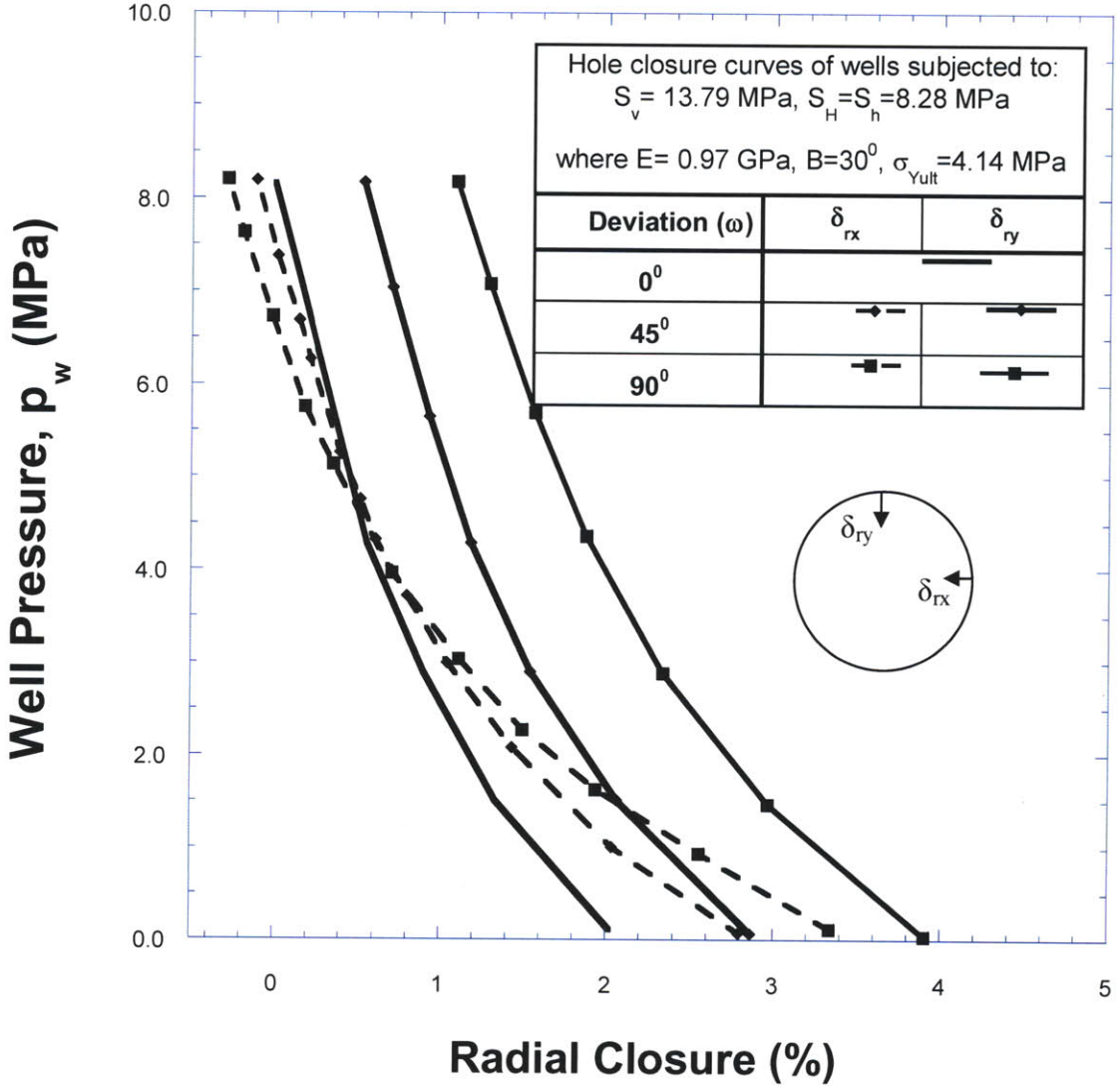

Figure 2.17 Hole Closure curves using non-linear strain-hardening constitutive model with expanding Drucker Prager yield criterion. Inward radial deformations at sides (δ_{rx} at $\theta=0^0$) and at top and bottom (δ_{ry} at $\theta=90^0$) are plotted for different angles of deviation (Ewy, 1993).

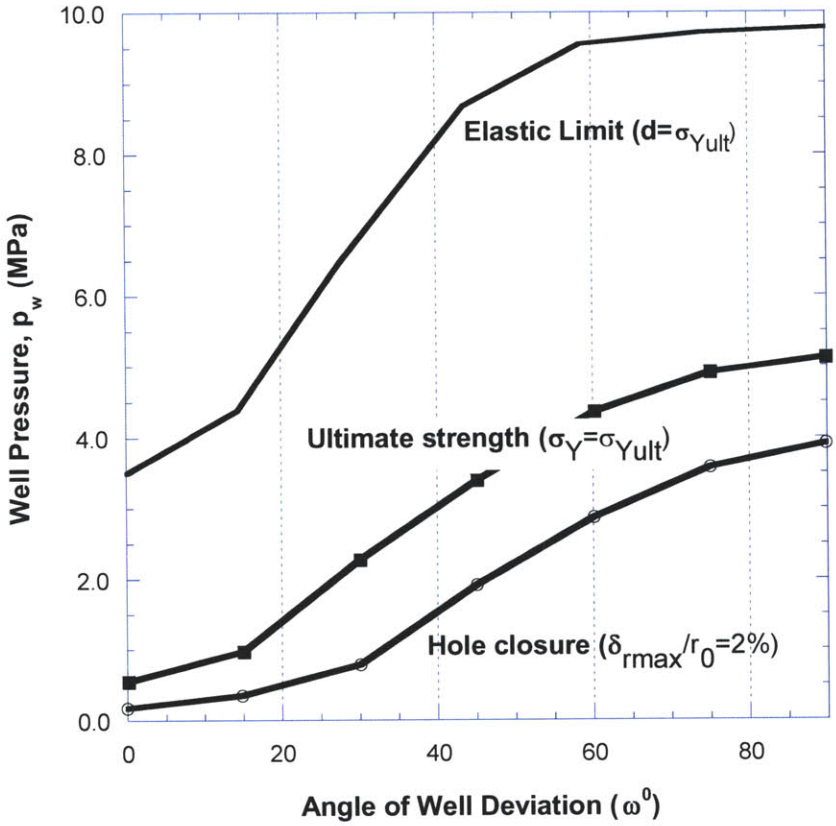

Figure 2.18 The well pressure needed for wellbore stability at different deviation angles according to three criteria of stability analysis; (1) Using Drucker-Prager failure criterion with isotropic elastic constitutive relations, (2) Using Drucker-Prager yield criterion with non-linear strain hardening model, (3) Using maximum limit on permitted hole closure (Ewy, 1993).

(a)

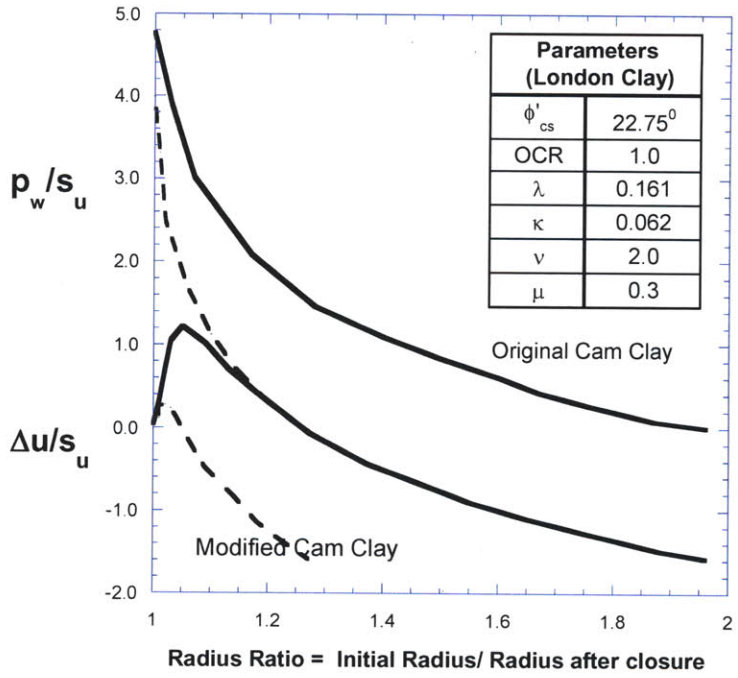

(b)

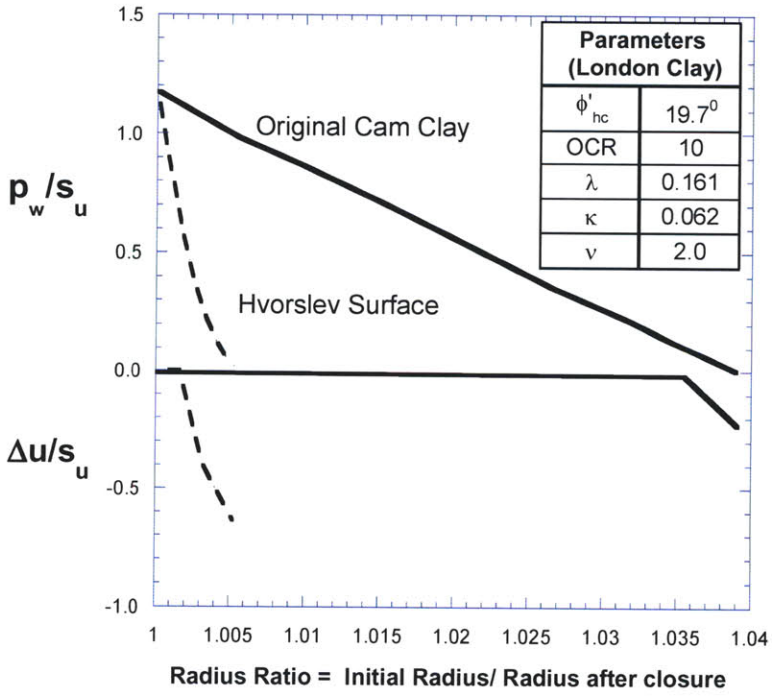

Figure 2.19 Cavity contraction curves plotted against well pressure and pore pressure change using different critical state soil models. (modified from Yu and Rowe (1999)).

(a)

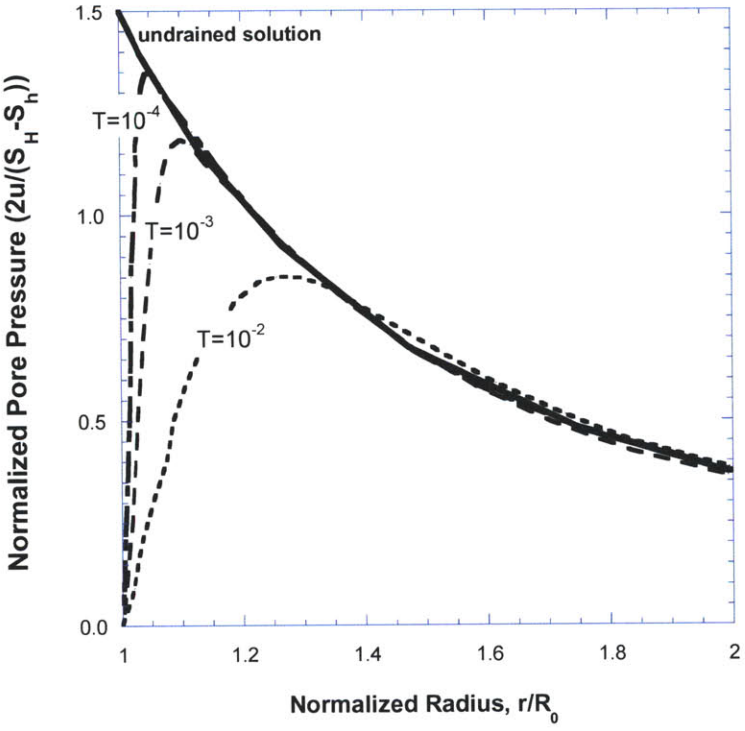

(b)

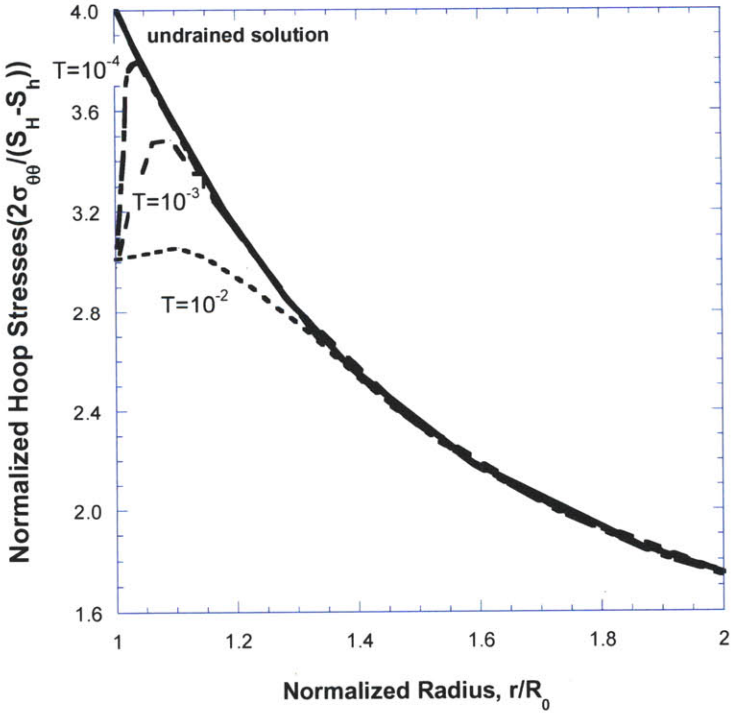

Figure 2.20 Normalized distributions of pore pressure and hoop stresses along the normalized radial distance on the x axis of the wellbore at different values of the dimensionless time factor $T=ct/R_0^2$ (from Charlez (1997) after Detournay and Cheng (1988)).

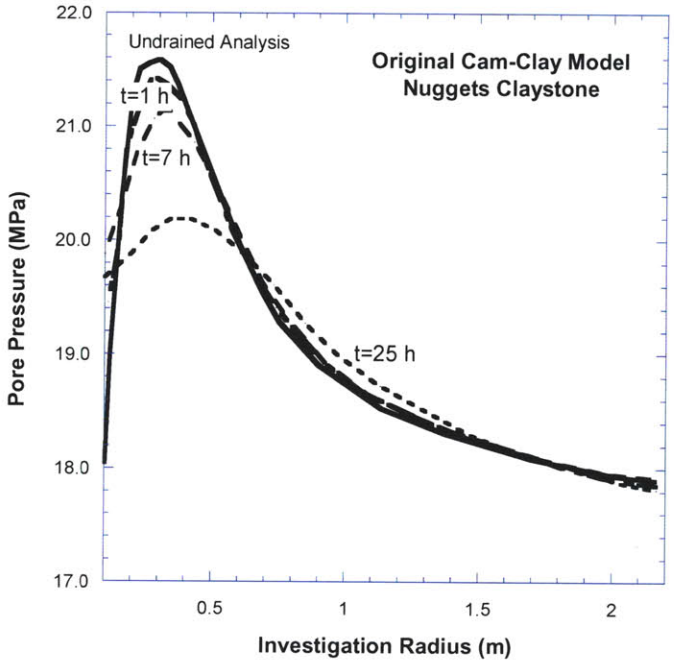

Figure 2.21 Pore pressure distribution in the radial direction of the minor principal stress through time (Charlez, 1997).

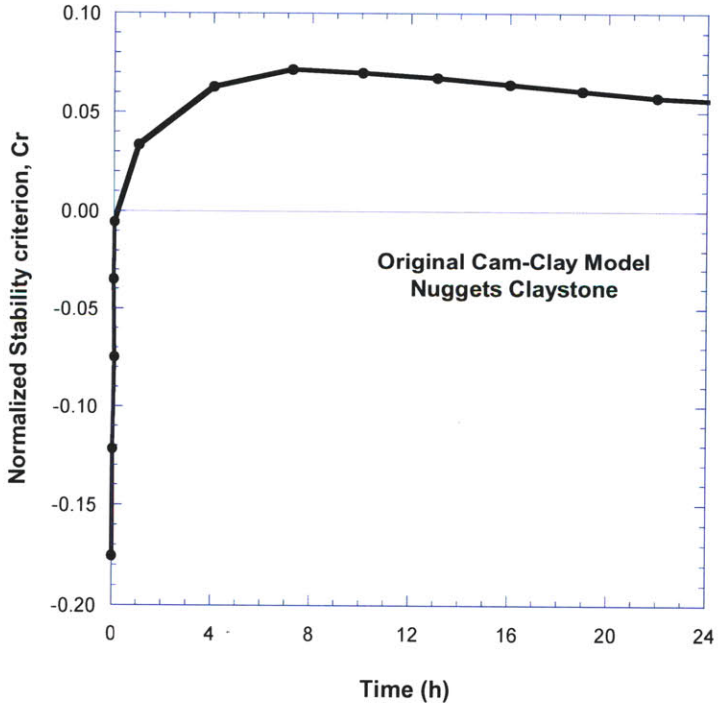

Figure 2.22 Change in the value of the normalized stability criterion with time to assess the effect of hydraulic diffusion around a on its stability (Charlez, 1997).

3 Numerical Modeling of Wellbore Deformations and Stability

3.1 Introduction

From the previous chapter, the mechanical model of the wellbore (wellbore unloading problem) is formed by taking a plane strain section orthogonal to the wellbore axis. The formation around the wellbore cavity is modeled as a saturated porous medium with engineering properties described by effective stress soil models. This model is implemented in the Finite Element program ABAQUS^{TM} and simulates coupled flow and deformation within the formation.

The wellbore unloading problem is fully defined by a slice model. The slice model only represents half of the space around the wellbore cavity due to symmetry and is of a finite thickness to accommodate out-of-plane traction forces. Plane strain conditions are imposed by preventing any out-of-plane deformations. Far field stresses are determined by transforming geostatic stresses in the rock mass into the analysis plane. Drilling is simulated by reducing a set of stresses around the wellbore cavity to a hydrostatic condition defined by the weight of the drilling mud.

Two types of analyses are performed in this research, undrained analyses and consolidation analyses. Undrained analyses are used to simulate drilling of wellbores and to examine critical mud pressures at which failure during drilling occurs. The basic assumption is that drilling takes place in a short time frame such that there is no migration of pore water within the surrounding formation and hence, the low permeability clay/shale is sheared under undrained (nearly incompressible) conditions. Consolidation analysis is used to monitor the effect of time on the wellbore stability when an adequate mud pressure is present. This type of analysis is more complex involving non-linear soil behavior and coupling between fluid flow and total stress changes during

the consolidation phase. Two types of fluid are present: water in the formation and slurry in the wellbore. The analyses consider two different conditions where there is no seepage into or out of the medium, or cases where seepage does occur.

The Finite Element implementation uses 3D mesh to represent the slice model in ABAQUS^{TM}. The mesh used mixed interpolation elements (displacement and pore pressure degrees of freedom) to perform the analysis. Two effective stress soil models are used to define the behavior of the formation, Modified Cam Clay (MCC, Roscoe and Burland, 1968) and MIT-E3 (Whittle and Kavvadas, 1994). These constitutive models are numerically integrated into the program by means of user material subroutines (UMAT; Hashash, 1992).

This chapter gives details of the numerical procedures and methods used in the analyses. Section 3.2 describes the simulation procedures of a wellbore with general orientation in cross-anisotropic formation. The section explains modeling the wellbore unloading problem and the far field stresses using the slice model. Then, the section details the stages of undrained and consolidation analysis.

Section 3.3 describes the effective stress models used in this analysis and the mathematical formulations of these models. Then, the section explains the calibration of these models to capture the behavior of the analog material, the Resedimented Boston Blue Clay (RBBC). The section presents the results of investigating the effects of high consolidation pressures associated with depths of wellbores (~2,000ft) on the behavior of the analog testing material and how the models are re-calibrated to capture these effects. Section 3.4 describes the implementation of the slice model in the FE program ABAQUS. The section illustrates the meshes and different types of elements used in the analysis. The issues of incompressibility associated with undrained analysis and integrating non-linear constitutive models are discussed in this section.

3.2 Wellbore simulation procedures

3.2.1 Problem Description

The current analyses make the key assumption that the formation comprises 1-D consolidated sediments, such that far field stresses, in the global frame of reference, are fully defined by the effective vertical overburden stress, σ'_{v0}, and the lateral earth pressure ratio, K_0, associated with the consolidation stress history. Stress conditions in the horizontal plane are isotropic, $\sigma'_{xx} = \sigma'_{yy} = K_0\sigma'_{v0}$. Mechanical (deformation and strength) properties of the formation are also expected to be isotropic in the horizontal plane (i.e. material will be cross-anisotropic) under these formation conditions. In practice, K_0-formation conditions are typically with horizontal stratification (horizontal layering of sediments) and level ground surface.

The wellbore orientation is defined by the deviation angle, ω, and the azimuth angle, γ, as discussed in Chapter 2. For wellbores installed in K_0-consolidated formations, behavior is fully defined by the deviation angle. Figure 3.1 sketches a wellbore of general orientation in cross-anisotropic formation (with an arbitrary deviation angle, ω) with respect to the global frame of reference (X, Y, Z). The figure also illustrates a cross-section perpendicular to the wellbore axis and shows the far field stresses with respect to the local frame of reference (x, y, z).

Wellbore inclination results in an out of plane shear component, σ_{yz}. Figure 3.2 shows the slice model used to approximate the far field stresses and plane strain boundary conditions in a half space cross-section orthogonal to the wellbore axis (z), where the y-axis is an axis of symmetry (approximating complementary shear stresses in the axis of the wellbore). The slice model has a limited thickness in the z-direction where only a single layer of 3D elements is required to accommodate out-of-plane shear components of geostatic stress tensor. The thickness of the model is chosen as unit length for normalization. The mesh is discussed in details in Section 3.4.

The quasi-3D problem geometry reverts to a 2D case only for special cases correspond to $\omega = 0^0$ (vertical wellbore) and $\omega=90^0$ (horizontal wellbore). For these 2D situations the wellbore stability can be analyzed using a plane strain analysis of the quarter plane model as shown in Figure 3.3. For the vertical wellbore $\sigma'_{yy} = \sigma'_{xx} = \sigma'_{h0} = K_0\sigma'_{v0}$, and for the horizontal wellbore, there are far field deviatoric stress conditions such that $\sigma'_{yy} = \sigma'_{v0}$ and $\sigma'_{xx} = K_0\sigma'_{v0} = \sigma'_{h0}$.

Far field stress components shown in Figures 3.1, 3.2, and 3.3 are obtained by standard transformation of the geostatic stress tensor under frame rotation:

$$[\sigma_{local}] = [R]^T[\sigma_{global}][R] \tag{3.1}$$

where:

$$[\sigma_{global}] = \begin{bmatrix} \sigma'_{XX} & \sigma'_{XY} & \sigma'_{XZ} \\ \sigma'_{XY} & \sigma'_{YY} & \sigma'_{YZ} \\ \sigma'_{XZ} & \sigma'_{YZ} & \sigma'_{ZZ} \end{bmatrix} = \begin{bmatrix} K_0\sigma'_{v0} & 0 & 0 \\ 0 & \sigma'_{v0} & 0 \\ 0 & 0 & K_0\sigma'_{v0} \end{bmatrix}$$

$$[R] = \begin{bmatrix} 1 & 0 & 0 \\ 0 & cos\omega & sin\omega \\ 0 & sin\omega & cos\omega \end{bmatrix}$$

$$[\sigma_{local}] = \begin{bmatrix} \sigma'_{xx} & \sigma'_{xy} & \sigma'_{xz} \\ \sigma'_{xy} & \sigma'_{yy} & \sigma'_{yz} \\ \sigma'_{xz} & \sigma'_{yz} & \sigma'_{zz} \end{bmatrix}$$

3.2.2 Analysis Stages

The most realistic depiction of the actual drilling process is the real time analysis of unloading; however, this approach, while adding to the complexity of the numerical

analysis, did not add significantly to the understanding of the wellbore creation[1]. This complexity is expected to increase when wellbore inclination and deviatoric stresses are considered.

The wellbore unloading problem can be simplified without compromising the quality of the solution by considering it as two separate problems in series: an undrained unloading problem and a consolidation problem. The decrease in well pressure that represents the creation of the cavity is accomplished under undrained conditions. Typical drilling rates (30m/hr, Willson, pers. comm.) are sufficiently rapid that there is little time for migration of pore fluid within the low permeability formation. Then the soil around the cavity is allowed to consolidate for an extended time period. The current analyses consider a reference of 30 days to represent a base case for delay in casing installation. Figure 3.4 illustrates the 4 stages of wellbore unloading; the first three stages are performed under undrained conditions and the formation around the wellbore is allowed to consolidate in the fourth stage.

Undrained Analysis

Figure 3.4a describes the initial conditions of the analysis. The initial stresses are defined in Stage I, when the deformations at the cavity wall are prevented (drilling did not start). Then, the deviatoric component of stresses at the cavity wall is relieved. Stage II is established when pressure on cavity wall is only radial as shown in Figure 3.4b. The radial pressures are then reduced to define the relationship between wellbore deformations and mud pressure. Critical mud pressures (radial pressures) are reached when severe element distortions are encountered in the analysis and failure is initiated. Stage III is achieved by reaching failure mud pressures as shown in Figure 3.4c.

Consolidation Analysis

As an alternative to stage III, mud pressures are reduced to a reference value (that corresponds to a stable condition) as shown in Figure 3.4d. Stage IV simulates the effect

[1] Real time analysis of wellbore unloading is discussed in details in Chapter 6.

of time on wellbore stability at a specific design mud pressure. The consolidation analyses couples between the effect of pore flow and total stress changes.

Whittle (1992) and Aubeny (1992) have introduced non-linear consolidation analyses around piles and penetrometers installed in clay. These analyses were also performed numerically by non-linear finite element methods with effective stress-strain-strength properties described by the MCC and MIT-E3 models. Whittle et al. (2001) describe these coupled non-linear analyses as E-C consolidation.

The pore water flow in the soil during consolidation is controlled by D'Arcy's Law with constant hydraulic conductivity; hence, the non-linearity is controlled exclusively by stiffness changes of the soil skeleton. Given these assumptions, there is no unique definition of the time factor. Instead, Whittle et al. (2001) selected a dimensionless time factor in order to normalize predictions of set-up times and proposed two different definitions of the time factor:

$$T = \frac{\sigma' kt}{\gamma_w R^2} \tag{3.2}$$

$$T = \frac{\sigma'_p kt}{\gamma_w R^2} \tag{3.3}$$

where t is the time after undrained unloading occurred, σ' is the in-situ mean effective stress, σ'_p is the vertical pre-consolidation pressure, k is the hydraulic conductivity, R is the cavity radius, and γ_w is the unit weight of water. The two definitions are interchangeable for normally consolidated clays, but only the second is used in this chapter for convenience.

For a well in the field, the drilling fluid creates a filter cake that seals the pores at the cavity wall to prevent pore water from flowing into the well. If this filter cake is well formed, it provides a very low permeability barrier and pore pressures will redistribute within the formations

At r = R:

$$q = 0 \tag{3.4}$$

where q is the pore water flow.

If the filter cake is less effective, it will have hydraulic conductivity comparable to or higher than the formation's. In this case the cavity becomes fully drained and formation pore pressures must equilibrate with mud pressures inside the wellbore:

At r = R:

$$u_{cavity} = p_{design} \tag{3.5}$$

3.3 Constitutive Models

Prior research on related analyses of cavity contraction problems in elasto-plastic soils show that the predictions are strongly related to the constitutive behavior and stress-strain properties of the soils. The mechanical response of low permeability clays is highly complex and involves non-linear and inelastic behavior even at small levels of shear strain (as small as 10^{-3}%), while anisotropic stress-strain-strength properties are previously observed due to 1-D consolidation stress history.

There are a wide range of generalized effective stress models that have been proposed to describe these material properties. Most are based on the theoretical framework of elasto-plasticity and have evolved from the original formulations of critical state soil models such as Modified Cam Clay (Roscoe and Burland, 1968). Prior research at MIT has led to

more sophisticated formulations that deal with the anisotropic behavior of clays such as MIT-E3 (Whittle and Kavvadas, 1994).

The current research compares predictions of stress conditions around wellbores using the MCC and MIT-E3 models. The results using the MCC are considered a reference case, and are amenable to simplified interpretation due to assumptions of isotropy. MIT-E3 is a more realistic model that provides more accurate representation of the non-linear and anisotropic stress-strain properties observed in laboratory element tests. It is therefore considered more realistic for predictions of wellbore stability.

The description of the MCC and MIT-E3 model formulations uses general tensorial spaces: the effective stress space (σ', S), the strain space (ϵ, E), the gradient of the yield surface Q, the plastic flow direction P, and the anisotropy tensor β. Kavvadas (1982) introduced a set of transformed variables for these tensorial quantities. Each transformed variable involves six components: one isotropic component (namely σ', ϵ, Q, P, 1, respectively) and five deviatoric components (e.g. S_1, S_2, S_3, S_4, and S_5 are the transformed deviatoric components of stress). Table 3.1 shows the transformed variables for the stress and strain tensors which will be used in the description of the constitutive relations in this chapter and the analysis results in later chapters.

All tensor relations can be written in terms of transformed variables in a form completely analogous to their tensorial form. Moreover, most practical problems can be solved in convenient subspaces involving a reduced number of variables (Kavvadas, 1982). For example:

1- Any triaxial test can be represented in the (σ', S_1) two-dimensional stress space; and $S_2 = S_3 = S_4 = S_5 = 0$.
2- Any plane strain or cavity contraction/expansion problem can be represented in the (σ', S_1, S_2) three-dimensional space; and $S_3 = S_4 = S_5 = 0$.
3- Any DSC test can be represented in the (σ', S_1, S_2, S_3) four-dimensional space; with $S_4 = S_5 = 0$.

4- The wellbore unloading problem considered in this thesis can be represented in the (σ', S_1, S_2, S_4) four-dimensional space; with $S_3 = S_5 = 0$.

3.3.1 Modified Cam-Clay

The MCC model (Roscoe and Burland, 1968) describes an idealized behavior of soils which is characterized by the framework of Critical State Soil Mechanics around two major observations of soil behavior:

1. It unifies observations of volumetric behavior and shear behavior. Normally consolidated stress states of soil form an ellipsoidal yield surface ($f = 0$; Figure 3.5) beyond which the soil undergoes large irrecoverable plastic strains (following an associated flow rule). Any stress state within the yield surface ($f < 0$) is an overconsolidated state and is characterized by elastic behavior.
2. When soils are subjected to shearing, they tend asymptotically to a critical state where continuous shear distortions can occur at constant effective stress and void ratio.

The generalized constitutive equations of the MCC model can be summarized as follows:

1- The yield function has the form of an ellipsoid:

$$f = S_i S_i - c^2 \sigma'(2\alpha' - \sigma') = 0 \tag{3.6}$$

where α' is a hardening parameter describing the maximum hydrostatic pressure, and c the slope of the critical state line. The version of MCC in this thesis assumes extended Von Mises generalization of the yield surface and critical state failure criterion (Whittle, 1987). The constant c is calculated from large strain frictional angle in triaxial compression shear tests, ϕ'_{TC}:

$$c = \sqrt{\frac{2}{3}} M = \frac{\sqrt{\frac{2}{3}}(6 \sin\phi'_{TC})}{3 - \sin\phi'_{TC}} \tag{3.7}$$

2- The plastic strains follow an associated flow rule:

$$P = Q = \frac{\partial f}{\partial \sigma'} = 2c^2(\sigma' - \alpha') \tag{3.8}$$

$$P_i' = Q_i' = \frac{\partial f}{\partial S_i} = 2S_i$$

3- The elastic moduli are estimated from the slope of a 1-D swelling line, κ, in e-$\log_e\sigma$ space:

$$K = \frac{\dot{\sigma}'}{\dot{\epsilon}} = (\frac{v_0}{\kappa})\sigma' \tag{3.9}$$

where $v_0 = (1+e_0)$ is the initial specific volume. In this version of the model, a constant Poisson's ratio, μ', is used and hence, $\frac{2G}{K} = \frac{3(1-2\mu')}{1+\mu'} = \text{constant}$.

4- The yield surface exhibits density hardening which is proportional to the rate of plastic volumetric strain $\dot{\epsilon^p}$:

$$\dot{\alpha}' = \left(\frac{v_0}{\lambda - \kappa}\right)\dot{\Lambda}P \tag{3.10}$$

where λ is the measured slope of the virgin consolidation line (VCL) in e-$\log_e\sigma'$ space.

3.3.2 MIT-E3

The MIT-E3 formulation (Whittle and Kavvadas, 1994) is based on the theory of incrementally linearized elasto-plasticity and consists of three distinct components: a) an elasto-plastic model for normally consolidated clays; b) a perfectly hysteretic formulation and c) bounding surface plasticity. The model describes a number of important aspects of soil behavior which have been observed in laboratory tests on K_0-normally consolidated clays including: 1) anisotropic stress-strain-strength properties associated with 1-D consolidation history and subsequent straining; 2) post-peak, strain softening in

undrained shear tests in certain modes of shearing on normally and lightly overconsolidated clays; 3) small strain non-linearity following a reversal of load direction; 4) hysteretic behavior during unload-reload cycles of loading; 5) occurrence of irrecoverable plastic strains during cyclic loading and shearing of overconsolidated clays.

The mechanical behavior of soil elements normally consolidated along radial effective stress paths (S/σ' = constant) is described by a yield surface which is initially oriented along the direction of consolidation. The yield function is written by Kavvadas (1982):

$$f = (S - \sigma' b) : (S - \sigma' b) - c^2 \sigma' (2\alpha' - \sigma') = 0 \tag{3.11}$$

where, α' controls the size of the yield surface, b is a second order tensor describing the orientation of the yield surface in effective stress space (σ', S) and c is the ratio of the semi-axes of the ellipsoid (Figure 3.6). For the case when b=0, the yield surface reduces to the same form as that used in the MCC (Roscoe and Burland, 1968).

Failure conditions are represented by an anisotropic failure criterion. It is assumed that the orientation of the failure criterion is fully defined by the friction angles measured in triaxial compression and extension tests (ϕ'_{TC} and ϕ'_{TE}, respectively) at large strain conditions (typically ϵ_a = 10% in undrained shear tests). The failure condition can then be written using the transformed variables:

$$h = S_i S_i - 2 S_1 \sigma' \xi_1 + \sigma'^2 (\xi_1^2 - k^2) = 0 \tag{3.12}$$

where $\xi_1 = \frac{1}{2}(C_c - C_e)$ and $k = \frac{1}{2}(C_c + C_e)$

$C_c = \frac{\sqrt{\frac{2}{3}}(6\sin\phi_{TC})}{3-\sin\phi_{TC}}$ and $C_e = \frac{\sqrt{\frac{2}{3}}(6\sin\phi_{TE})}{3+\sin\phi_{TE}}$

The model assumes two hardening rules to describe changes in the size and orientation of the yield surface respectively

$$\dot{\alpha}' = \dot{\alpha}'\zeta\dot{\epsilon}^p \tag{3.13}$$

$$\dot{b} = \psi_0\langle r_x\rangle\left(\frac{1}{\alpha'}\right)(S - \sigma' b)\dot{\epsilon}^p \tag{3.14}$$

where ζ is dimensionless function of the state variables which is obtained by invoking the consistency requirement ($\dot{f} = 0$), $\psi_0$is a material constant controlling the rate of rotation of the yield surface, and r_x is a scalar which describes the relative orientation of the yield surface to the critical state cone.

A non-associated flow rule is used in order to generate: a) critical state failure conditions; and b) K_0 conditions for 'virgin normally consolidated clay' (K_{0NC}). The flow rule is defined as follows:

$$\begin{aligned} P &= 2c^2\alpha' r_c \\ P' &= c^2 x(Q' + \langle r_c\rangle S \end{aligned} \tag{3.15}$$

where x is a constant which defines the K_{0NC} condition:

$$x = \left(\frac{\lambda}{\lambda - \kappa}\right)\left\{\frac{1 + 2K_{0NC}}{3(1 - K_{0NC})} - \left(\frac{K}{2G}\right)\left(\frac{\kappa}{\lambda}\right)\right\} \tag{3.16}$$

and the parameter r_c is a scalar variable which describes the location of the current state relative to the failure surface.

The elasto-plastic modulus, H, is defined by detailed consideration of the behavior of K_0-normally consolidated clays. The functional form of H is selected in order to describe: a)virgin consolidation lines (VCL) with slope λ in e-$\log_e\sigma'$ space for all radial consolidation paths in effective stress (σ', S) space; and b) stain hardening, peak

strength, strain softening and critical state conditions for undrained shearing of K_0-normally consolidated clays:

$$H = 2c^2\left(\frac{\kappa}{\lambda-\kappa}\right)K\{\alpha' P - S_t 2c^2 x\langle r_c\rangle(Q':b)\} \tag{3.17}$$

where S_t is a material constant.

For the overconsolidated soil behavior, the model formulation sub-divides the observed behavior into:

1. A closed symmetric, hysteresis loop Figure 3.7a, which matches the observed behavior during unloading.
2. For reloading, plastic strains are assumed to develop as the Virgin Consolidation Line (VCL) is approached Figure 3.7b. The magnitude of plastic strains is determined by the proximity of the current stress state to the VCL. Thus, plasticity is conveniently described using a bounding surface (Dafalias and Hermann, 1980).

The volumetric response during unloading is described by a tangential bulk modulus:

$$K = \frac{1+e_0}{(1+\delta)\kappa_0}\sigma' \tag{3.18}$$

where $\delta = Cn(\log_e \xi + \xi_s)^{n-1}$, e_0 is the void ratio, κ_0 defines the initial unloading slope in e-$\log_e\sigma'$ space, C and n are material constants to describe non-linearity at small strain levels, and ξ and ξ_s are dimensionless distances in stress space which relate the current stress state to the stress reversal state:

$$\xi = \begin{cases} \dfrac{\sigma'}{\sigma'_{rev}} \; if \; \sigma' > \sigma'_{rev} \\ \dfrac{\sigma'_{rev}}{\sigma'} \; if \; \sigma' < \sigma'_{rev} \end{cases} \tag{3.19}$$

$$\xi_s = (\overline{\eta_i}\overline{\eta_i})^{\frac{1}{2}}$$

where σ'_{rev} is the mean effective stress at the stress reversal point, and $\overline{\eta_i} = \omega_i \times \eta_i = \omega_i(\frac{S_i}{\sigma'} - \frac{S_{i,rev}}{\sigma'_{rev}})$ is the change in shear stress ratio from the last stress reversal state. The parameters ω_i are material constants. For K_0-normally consolidated clays, values of ω_i can be obtained from triaxial shear data assuming that $\omega_1=\omega$, $\omega_2=\omega_3=\omega_4=\omega_5=10\omega$.

During reloading, the bounding surface model (Dafalias and Hermann, 1980) relates the plastic strains of overconsolidated clays to the plastic behavior previously defined for the normally consolidate material. A radial mapping rule is used to define a unique image point in the bounding surface. Functions are developed to relate the elasto-plastic modulus, H, and flow direction, P, to the corresponding values at the current image point, H_I and P_I. The MIT-E3 model introduces separate mapping rules for the elasto-plastic modulus and the flow direction which can be expressed in general form:

$$\begin{aligned} P &= P_I + P_0 g_1 \\ H &= H_I + H_0 g_2 \end{aligned} \tag{3.20}$$

where P_0, H_0 are the values of P and H at the first loading for stress states within the bounding surface (first yield); and g_1, g_2 are mapping functions described by the relative position of the current stress and image stress states. The following expressions are adopted for H_0, P_0, g_1 and g_2:

$$P_0 = -\{2c^2\alpha' r_c + (\eta_I : Q'_I)\} \tag{3.21}$$

$$g_1 = \left(\frac{\alpha' - \alpha'_0}{\alpha' - \alpha'_{0i}}\right)^{\gamma}$$

$$H_0 = \frac{1}{K_0}(1 + e_0)\{(\alpha' - \alpha'_0)h|Q_I||P_I|\}$$

$$g_2 = \left(\frac{\alpha' - \alpha'_0}{\alpha' - \alpha'_{0i}}\right)$$

In these equations, h, g are dimensionless material constants which are established from parametric studies; α'_{0i} is the size of the load surface at first yield.

The model also has a number of key restrictions: 1) it uses a rate independent formulation and hence, cannot model creep, relaxation or other strain rate dependent properties of the soil skeleton; and 2) it assumes normalized soil properties (e.g., the strength and stiffness are proportional to the confining pressure at a given overconsolidation ratio, OCR) and hence, does not describe complex aspects of soil behavior associated with cementation; and 3) its predictions become progressively less reliable for OCR>4~8.

Table 3.4 summarizes the input parameters used by the MIT-E3 model together with their physical significance and proposed laboratory tests from which these properties can be determined (Whittle and Kavvadas, 1994). In addition to these 15 material constants, the MIT-E3 model uses the following state variables:

1- The effective stress tensor (σ', S).
2- The size and orientation of the bounding surface (α', b).
3- Effective stresses at the most recent reversal state (σ'_{rev}, S_{rev}).
4- The strains accumulated since the last reversal state (Δl_ϵ, Δl_E).
5- The size of the bounding surface at the last reversal state, α'_{rev}; and the size of the load surface at first yield, α'_{0i}.

At the start of a wellbore unloading problem in K_0-normally consolidated clays, the initial values used in this analysis must be specified. The effective stress tensor (σ', S_1, S_2, S_4) is computed from standard tensor transformation as discussed earlier. The rest of the state variables can be defined as:

$$\alpha' = \frac{(S_1 - \sigma' b_1)^2 + (S_2 - \sigma' b_2)^2 + (S_4 - \sigma' b_4)^2}{2c^2\sigma'} + \frac{\sigma'}{2} \tag{3.22}$$

$$b_1 = \frac{\frac{3}{\sqrt{6}}\left((2\cos^2\omega - \sin^2\omega) + K_0(2\sin^2\omega - \cos^2\omega - 1)\right)}{1 + 2K_0}$$

$$b_2 = \frac{\frac{3}{\sqrt{2}}\left(\sin^2\omega + K_0(\cos^2\omega - 1)\right)}{1 + 2K_0}$$

$$b_4 = \frac{3\sqrt{2}\left((\cos\omega \sin\omega) + K_0(\sin\omega \cos\omega)\right)}{1 + 2K_0}$$

$$\sigma'_{rev} = \sigma', S_{rev} = S$$

$$\Delta l_\epsilon = \Delta l_E = 0$$

$$\alpha'_{rev} = \alpha'_{0i} = \alpha'$$

3.3.3 Modeling of Resedimented Boston Blue Clay (RBBC) behavior

The previously described effective stress models are calibrated to results of a standardized suite of laboratory experiments on the analog soil, RBBC. The analog clay is a soil resedimented in the laboratory from the natural Boston Blue Clay, an illitic glacio-marine clay of low to medium sensitivity. RBBC is used for the following reasons: 1) procedures for manufacturing uniform samples of RBBC are well-established (Germaine, 1982); 2) The engineering properties of RBBC are well-established from extensive studies at the Massachusetts Institute of Technology; 3) Input parameters for the MCC and MIT-E3 models have been selected and validated (e.g. Whittle et al., 1994); 4) the engineering behavior of RBBC is typical of natural, uncemented clay deposits with similar index properties. These reasons made this soil an ideal research material to investigate fundamental aspects of soil behavior without having to take into account the variability of natural soils.

Previous studies of RBBC have established normalized engineering properties of soil (following the SHANSEP framework; Ladd and Foott, 1974) such that the undrained shear strength and stiffness of K_0-normally consolidated clay are proportional to the

vertical effective stress at the end of consolidation. However, Abdulhadi (2009) has found that there are significant differences in the effective stress-strain-strength properties at high confining stresses. These results cannot be simulated directly by constitutive models that are based on assumptions of normalized clay behavior, including elasto-plastic models such as MCC and MIT-E3. Prior studies have focused on the behavior of RBBC at effective consolidation stresses in the range of 0.1~0.4 MPa (low pressure). One way to reconcile the situation is to reconstruct a new set of model input parameters for each model, so that the predicted behavior becomes representative of RBBC properties consolidated at pressures within the range of 1~10 MPa (high pressure), that are of principle interest for wellbore stability. This section, first presents the low pressure MCC and MIT-E3 calibrations (Whittle et al., 1994); and discusses the prediction capabilities of both models for plane strain behavior of RBBC. Then, the section summarizes the engineering properties of the RBBC from the high pressure test program (Table 3.2; Abdulhadi, 2009) and the calibration of model parameters from these tests (Abdulhadi et al., 2009). Tables 3.3 and 3.4 compare between input parameter for low and high pressure calibrations of MCC and MIT-E3 models respectively.

RBBC behavior under low consolidation pressures

Abdulhadi et al. (2008) gave a comparison between the predictive capabilities of MCC and MIT-E3 models for the behavior of RBBC consolidation under low pressures (0.1~0.4MPa). The input parameters of the MCC model are chosen by Whittle et al. (1994) based on lab experiments by Ladd and Varllalyay (1965) and Sheahan (1991). The measured lateral effective stress ratio for the virgin normally consolidated clay ranges from K_{0NC} = 0.47 to 0.53 for the tests reported in Figure 3.8. The friction angle, ϕ'_{TC} = 33.4^0 is well defined from effective stress measurements at axial strain levels, ϵ_a = 10% in CK_0UC tests at OCR =1. The equivalent friction angle in the extension mode, ϕ'_{TE}, is much more difficult to estimate due to geometric nonuniformities (necking) observed in the tests. Recent data (Sheahan and Germaine, 1992) suggest that the selected friction angle ϕ'_{TE} = 45.9^0 is about 10^0 too high. This is revised when the MIT-E3 model is recalibrated for behavior under high pressure consolidation.

Figure 3.8 compares typical MCC predictions of the elemental undrained stress-strain response of K_0-normally consolidated Boston Blue Clay (RBBC) in triaxial compression and extension modes of shearing with measured data for RBBC[2]. The stress-strain properties predicted by MCC are strongly conditioned by the assumption of an isotropic yield surface. In triaxial extension, elastic behavior prevails inside the isotropic yield surface and hence, there are initially no shear-induced pore pressures ($\Delta\sigma' = 0$), and the yield point is clearly distinguished by the change in direction of the stress path. In compression, positive shear-induced pore pressures occur throughout shearing. In both modes, the undrained shear strength is only mobilized at large, strain critical state conditions. The model predicts a unique undrained shear strength ratio in both triaxial compression and extension shear modes, $s_u/\sigma'_{vc} = 0.32$. As a result, the model grossly overestimates the undrained shear strength in the extension modes. It also underestimates significantly the measured shear stiffness in both modes of shearing.

Figure 3.9 illustrates typical MIT-E3 predictions of the elemental undrained stress-strain response of normally consolidated clays in plane strain compression and extension modes of shearing. These data illustrate clearly the capabilities of the model to capture complex mechanical response such as non-linear stress strain behavior and post-peak softening in the compression mode of shearing. The MIT-E3 predictions match closely the measured undrained shear strengths in both modes of shearing (model strength ratios are $s_{uTC}/\sigma'_{vc} = 0.32$ and $s_{uTE}/\sigma'_{vc} = 0.16$ in compression and extension, respectively), as well as the axial strain at peak shear resistance (ε_{ap}=0.3%). Also, the anisotropic yield surface and hardening rules allow a non-unique effective stress state failure that depends on consolidation history. Moreover, the shear-induced pore pressure is calculated for stress states inside as well as on the yield surface as shown in the non-linearity of the shown stress paths due to bounding surface plasticity.

---

[2] The MCC predictions are in better agreement with data from hydrostatically consolidated ($K_0 = 1$) sheared samples of BBC.

Model predictions of undrained shear behavior measured in laboratory plane strain tests provide a useful framework for interpreting the subsequent cavity contraction analyses around inclined wellbores. The DSC (Arthur et al., 1977) is a plane strain, stress-controlled device that is able to apply both normal and shear forces to four faces of a cubical sample and hence can control principal stress directions in the plane of loading. Figure 3.10 illustrates an idealized test procedure for using the DSC to evaluate the anisotropic stress-strain properties of clay in undrained shearing that develop due to a one-dimensional consolidation stress history. Soil specimens are first consolidated under K_0-conditions to the prescribed OCR (i.e., with no lateral strains in the x-z plane) and are then sheared by imposing principal stress increments oriented at angle, δ_{inc}, to the original direction of deposition. Tests performed at $\delta_{inc} = 0°$ and 90° correspond to conventional undrained plane strain active and passive modes of shearing, while those at intermediate values of δ_{inc} involve rotation of principal stress directions.

Figure 3.11a and b compares MCC and MIT-E3 predictions with effective stress paths measured in a series of laboratory undrained plane strain Directional Shear Cell (DSC) tests on K_0-normally consolidated BBC (Seah, 1990). Material properties for the two models are chosen using other laboratory data (triaxial and oedometer tests). Therefore, the comparisons are true predictions of the models' responses in this mode of shearing. The figure shows the three in-plane stress components (σ'_h, σ'_v, τ) in two 2D planes ($p' = \frac{1}{2}(\sigma'_v + \sigma'_h)$, $q = \frac{1}{2}(\sigma'_v - \sigma'_h)$) and ($\tau$, q). Stress paths in the (p', q) space describe the shear-induced pore pressures in these tests, while reference friction angles, $\phi' =$ 42.3°, 35.7° represent the large strain (critical state conditions) predicted in the active and passive modes of shearing, respectively (Whittle et al., 1994). The undrained shear strength, $s_u = \max \sqrt{q^2 + \tau^2}$ can be described as a function of the major principal stress direction, δ, in the (τ, q) space.

The results highlight some of the key limitations of the MCC model. The MCC model describes a unique undrained shear strength ($s_u/\sigma'_{vc} = 0.37$) which is mobilized at critical state conditions (i.e., unique effective stress state at failure) and is independent of the direction of the applied principal stresses. As a result, the model greatly overestimates

(by up to 100%) the measured strengths for $\delta > 0^0$. The predicted effective stress paths are controlled by isotropic elastic behavior for stress states inside the yield surface (and are characterized by $\Delta p'=0$). This condition does not correspond with the measured data which show the development of positive shear induced pore pressures for all directions of undrained shearing. Also in this figure, all directions of shearing produce a unique amount of shear-induced pore pressure for shearing to critical state ($\Delta u_s/\sigma'_{v0} = 0.77 - 0.48 = 0.29$).

The MIT-E3 predictions are generally in very good agreement with the measured effective stress paths but tend to underestimate changes in the average, p', at high values of δ_{inc}. The predicted locus of undrained shear strengths $s_u(\delta)$, which range from $s_u/\sigma'_{vc} = 0.34\sim0.18$, are in excellent agreement with the measured data, with a maximum difference of about 10%.

Effect of high consolidation pressure

Table 3.2 compares some of the key normalized engineering properties measured in undrained shear tests at $\sigma'_{vc} = 0.15$ MPa and the averages of measurements at higher range of consolidation stresses 1~10 MPa (Abdulhadi et al., 2009). The tests performed at higher pressure have much lower Undrained Strength Ratio (USR= $s_{uTC}/\sigma'_{vc} = 0.28$ vs 0.33 at $\sigma'_{vc} = 0.15$ MPa), there is also a significant reduction in the stiffness ratio, E_{uMAX}/σ'_{vc}, and an increase in the axial strain required to mobilize the peak shear ($\varepsilon_{ap} = 1.0\%$ vs 0.2% at $\sigma'_{vc} = 0.15$ MPa). There is also a surprising decrease in the friction angle measure at large strain, i.e. critical state conditions ($\phi'_{TC} = 31.5^0$ and 33.7^0 for $\sigma'_{vc} = 1\sim10$ MPa and 0.15 respectively). Figures 3.12 to 3.15 (Abdulhadi, 2009) illustrate these results in more detail.

Figure 3.12 shows the significant effect of consolidation pressure on the normalized stress strain curves in undrained triaxial compression shear tests. There is a marked decrease in undrained brittleness at higher confining effective stresses. However, there

are only small differences in shear resistance at large strains (q/σ'_{vc} = 0.23~0.24 at ε_a = 12%) for σ'_{vc} ranging from 0.33 to 9.7 MPa.

Figure 3.13 shows the degradation curves of the normalized undrained secant Young's modulus, E_u/σ'_{vc}, with axial strain level. These results show that the consolidation effective stress has a major effect on the maximum stiffness ratio at small strains (E_{uMAX}/σ'_{vc}, Table 3.2). However, effects of the confining stress become less pronounced in the post-peak strain range.

Figures 3.14 a and b compare the normalized effective stress paths for two sets of triaxial compression tests that were pre-consolidated to σ'_{vm}=0.19 MPa and 9.74 MPa, respectively. Each group shows three normalized effective stress paths for RBBC at OCR = 1.0, 2.0, and 4.0. In each case the large strain shear strength conditions can be represented by a Mohr-Coulomb envelope with dimensionless parameters c'/σ'_{vm} and ϕ'. The results show a small difference in the apparent cohesion ratio at higher pre-consolidation pressures (c'/σ'_{vm} = 0.032 vs. 0.018) and a much larger reduction in the friction angle (ϕ' = 26.8^0 vs. 33.7^0).

Figure 3.15 shows that the vertical hydraulic conductivity (k_v) decreases with decreasing void ratio (i.e., with increasing consolidation stress). The considered range of consolidation stress (1~10 MPa) is associated with overburden stresses at depths of shallow oil reservoirs. The corresponding reference void ratio is chosen 0.65 (σ'_{v0} = 4MPa) and the permeability is 1.44 $x10^{-7}$ m/hr as opposed to the reference void ratio at low consolidation pressures, e_0 = 1.12, and the corresponding permeability coefficient, k = 2.52 x 10^{-6} m/hr. The permeability throughout the analysis is assumed to be isotropic and fully defined by the chosen value.

Less experimental data is available for behavior of RBBC K_0-normally consolidated to high pressures and sheared in undrained extension triaxial tests (CK_0UE). Moniz (2009) performed CK_0UE experiments after K_0-consolidation to vertical effective stress, σ'_{vc} = 0.15~2 MPa. Figure 3.16 shows the effect of stress level on the normalized shear stress-strain behavior and confirms the decreasing trend of the undrained strength ratio with

increasing consolidation stresses. The value of s_{uTE}/σ'_{vc} reduces from 0.173 at σ'_{vc} = 0.14MPa to 0.153 at σ'_{vc} = 2MPa. Figure 3.17 shows the normalized effective stress paths from the CK_0UE tests. The values of ϕ'_{TE} reduces from 43.1^0 at σ'_{vc} = 0.14 MPa to 31.2^0 at σ'_{vc} = 2MPa. The variation of stress states at failure demonstrates that the failure envelope in triaxial extension mode is also influenced by high consolidation pressures.

The experimental results show that the consolidation pressure influences three main areas of behavior; ductility, strength, and critical state friction angle. Table 3.2 shows average values of measured engineering properties at high consolidation pressures (σ'_{vc} = 1~10MPa). These values are used to calibrate new parameters of the MCC and MIT-E3 constitutive models to represent the behavior of RBBC under high consolidation pressures as shown in Tables 3.3 and 3.4, respectively. Figure 3.18 illustrates the selection of the proposed MCC parameters. The figure shows (a) effective stress path and (b) shear stress-strain curves.

For the MIT-E3 input parameters, those controlling ductility are modified first, based on 1D compression experiments (oedometer experiments) and monitoring the degradation of the undrained secant Young's Modulus in undrained triaxial compression tests. Then, the size and orientation of the critical state cone in the model formulation are changed based on the values of the critical state friction angle. The most important part is to match the measure undrained strength ratio. This is possible by manipulating key model parameters that control the effective stress paths and shear stress-strain behavior.

Figure 3.19 shows the results of 1-D Constant Rate of Strain (CRS) consolidation tests on RBBC (Abdulhadi, 2009). To a first approximation these data confirm that compression behavior can be described by a virgin compression line, VCL, with slope C_c in e – $\log_{10}\sigma'_v$ space[3]. The figure shows that the higher pressure data are well described by a VCL with C_c = 0.3 (λ = 0.13) and e_0 = 0.65 at σ'_{vc} = 4 MPa. These parameters are also used for the MCC model.

[3] The compressibility parameter used by both MCC and MIT-E3 is $\lambda = de/d\log_e\sigma'_v = 0.434C_c$.

The small strain shear stiffness in MIT-E3 is controlled by the model input parameter, κ_0[4], which controls the compressibility upon load reversal. Assuming that Poisson's ratio is not affected by the consolidation stress (μ=0.277 was used in previous calibrations), then the value of κ_0 depends on the chosen value of E/σ'_v.

$$\frac{E}{\sigma'_v} = \frac{K}{\sigma'_v}\left(\frac{1}{3}\right)\left(\frac{1}{1-2\mu'}\right) = \frac{1+e_0}{\kappa_0}\left(\frac{1}{3}\right)\left(\frac{1}{1-2\mu'}\right)\left(\frac{1}{3}\right)(1+2K_{0NC}) \qquad (3.23)$$

Figure 3.20 shows the degradation of the undrained secant Young's Modulus curves with axial strain in undrained triaxial compression tests. The figure also shows the proposed re-calibration of the MIT-E3 using high pressure test data. The new calibration captures the measured changes in stress strain properties. From the figure E/σ'_v is estimated to be 150, and hence for e_0=0.65 and K_{0NC} = 0.55, the new value of κ_0 = 0.006.

Ductility is governed in the formulation with the parameters controlling the non-linear volumetric swelling behavior (n and C) as well as κ_0 that describe 1D behavior. In Figure 3.21, swelling curves show less axial strains during unloading than expected from prior knowledge of behavior under low consolidation pressure. The prior (low pressure) calibration overestimates axial strains. By changing the values of n and C the model gives much better agreement to swelling data observed at high effective consolidation stress.

The proposed high pressure calibration uses a ϕ'_{TC} = 31.5^0. This corresponds to an average value measured for specimens consolidated at stresses in the range σ'_{vc} = 1~10 MPa. The MIT-E3 model also requires a critical state friction angle in the extension shear mode, ϕ'_{TE} which is chosen to be 34.5^0 based on the value recommended by Sheahan and Germaine (1992). This value is close to recent measured values of ϕ'_{TE} for RBBC K_0-consolidated up to 2 MPa (Moniz, 2009)[5].

---

[4] The small strain elastic bulk modulus is given by $K_{max}/\sigma'_v = (1+e_0)/\kappa_0 * (1/3)(1+2K_{0NC})$.

[5] The re-calibration of MIT-E3 model to accommodate the influence of high consolidation pressures was performed prior to data from CK_0UE became available.

The rest of the parameters are determined from two triaxial tests at OCR=1.0 one each in compression and extension, while a third triaxial compression is needed at OCR =1.5~2.0. Figure 3.22 shows the measured results of these experiments from Abdulhadi (2009) and Moniz (2009). Among this group of parameters two (c, γ) are derived from the measured effective stress paths and two from the shear stress-strain curves (pre-peak, ω; and post-peak, S_t). Parameter (h) corresponds to irrecoverable plastic strain during reloading. In the absence of data for unload reload consolidation cycles at high consolidation pressures, parameter (h) is chosen to be consistent with the rest of the chosen parameters. Figure 3.25 illustrates the calibration of these model parameters. The figure shows good agreement between computed and measured (a) effective stress paths in both compression and extension modes, and (b) the shear stress-strain curves on a logarithmic scale.

3.4 Finite Element Implementation

The finite element method has long been recognized as a very useful tool for the solution of boundary value problems in soil mechanics. However, most commercial Finite Element computer programs were developed mainly for applications in solid mechanics and thus, either cannot be used in Soil Mechanics problems or lack many features required in soil mechanics applications. More specifically, the application of standard finite element codes in the analysis of problems involving common loading problems in soil mechanics such as undrained loading and consolidation, frequently produces inaccurate results and occasionally the algorithms do not even converge (in the case of non-linear material response).

Many of these problems arise from the incompressible, or nearly incompressible, response of soils under undrained and consolidation loading. The incompressibility requirement imposes significant kinematic constraints on the (low-order) finite element used in most Finite Element programs and in many occasions results in overconstrained mesh, "locking" of the elements and significant errors in the predicted response. Several

researchers in MIT have investigated these problems (e.g. Kavvadas, 1993; Legaspi, 1996). In general, these problems can be mitigated by ensuring adequate degrees of freedom (DOF) within each finite element.

The ABAQUS^{TM} program is chosen for the finite element implementation of this research because it consists of large library of different types of finite elements including high order elements. Moreover, ABAQUS is capable of performing analyses of coupled flow and deformation and can accommodate user-defined material models. The constitutive models discussed in Section 3.3 are integrated within the ABAQUS program (Hashash, 1992) in the form of user material subroutines (UMATs). The UMAT subroutine is a FORTRAN code that performs two tasks: 1) it updates the stresses and state-dependent variables at the end of each increment; 2) it calculates the material stiffness matrix (J on a single gauss point level and K on the global level). In Section 3.4.1 the finite element model used to represent the wellbore is discussed and the different types of finite elements used in this thesis are presented. Also, this section describes the meshes and a numerical experiment to verify the adequacy of numerical simulations using these meshes where incompressibility is important. For a base case of a vertical wellbore, 1-D model can be used (FE custom program CAVEXP; Whittle, 1992) to provide a useful check on 2D and quasi 3D problems. In Section 3.4.2, the numerical integration of MCC and MIT-E3 within ABAQUS is explained.

3.4.1 Finite Element Model

A porous medium is modeled in ABAQUS by the conventional approach that considers the medium as a multiphase material and adopts an effective stress principle to describe its behavior. The porous medium modeling provided considers the presence of two fluids in the medium. One is the "wetting liquid," which is assumed to be relatively (but not entirely) incompressible. When the medium is fully saturated, the voids are completely filled with the wetting liquid.

In these formulations, the material model describes the response of the soil skeleton and thus, incompressibility constraints need not be imposed on the material model since the soil skeleton is compressible. Incompressibility is caused by the fluid filling the pore space and is numerically imposed by introducing a new independent variable, the pore pressure (u), which is such that the effective stresses corresponding to the externally applied total stresses cause zero volumetric. Such a value of the pore pressure can always be computed by:

$$\Delta u = \frac{I : \mathbf{S} : \Delta\sigma}{I : \mathbf{S} : I} \tag{3.24}$$

where **S** is the tangent flexibility of the soil skeleton, I is the identity matrix, and Δu is the pore pressure increment corresponding to a total stress increment $\Delta\sigma$.

In these effective stress formulations, the displacements (δ) and the pore pressure (u) are independent variables in four independent governing field equations (3 equilibrium equations and 1 mass conservation equation). In this way the problem is formulated as time-dependent consolidation. Undrained conditions can be simulated by applying the loads at a rate sufficiently fast not allowing dissipation of the generated pore pressures (see Small et al., 1976 and Carter et al., 1979)[6].

The governing field equations can be discretized in a finite element matrix equation of the form:

---

[6] Δt used in the undrained analysis is 10^{-12} hours for $k=1.44 \times 10^{-7}$ m/hr.

$$\begin{bmatrix} \underline{K} & -\underline{L} \\ \underline{L} & -\Delta t\,\underline{H} \end{bmatrix} \begin{bmatrix} \underline{\delta} \\ \underline{U} \end{bmatrix} = \begin{bmatrix} R_\delta \\ R_u \end{bmatrix} \tag{3.25}$$

where

$\underline{\delta}$ and $\underline{U}$ are the nodal values of the field variables: displacement, δ, and pore pressures, u.

$K = \int_V B^T C B dV$ is the stiffness matrix

B is given by $\epsilon = B\underline{\delta}$ which is a derivative of the shape function for displacements, N ($\delta = N\underline{\delta}$), $B = \underline{L}N$

$\underline{L}$ is a differential operator: $\epsilon = \underline{L}\delta$

$\underline{H} = \frac{1}{\gamma_w}\int_V M^T k M dV$, k is the permeability tensor

M is defined by $\Delta u = M\underline{U} = (\Delta A)\underline{U}$, A is the shape function for pore pressures ($u = A\underline{U}$)

R_δ and R_u are load vectors.

Element type and mesh description

Finite element analyses were performed using mixed elements (displacement and pore pressure degrees of freedom) in two different meshes. First, Figure 3.22 shows the finite element mesh for the quarter space 2D problem. The mesh uses 829 quadrilateral elements and 2618 nodes. The quadrilateral elements (8 displacement and 4 pore water pressure degrees of freedom) use isoparametric quadratic expansions of the displacement field and bi-linear expansion of the pore pressure field.

Bi-linear pore pressure interpolation:

$$u = \sum_{i=1}^{4} A_i(x,y)\underline{U} \tag{3.26}$$

where A_i is a linear polynomial.

Quadratic displacement interpolation:

$$\delta = \sum_{i=1}^{8} N_i(x, y, xy, x^2, y^2)\,\underline{\delta} \tag{3.27}$$

where N_i is a quadratic polynomial.

Hughes (2000) described this type of element as continuous pressure elements where displacements and pore pressure results are continuous across element boundaries. Hughes (2000) stated that this element may not satisfy the Babuska-Brezzi[7] conditions for convergence while maintaining incompressibility conditions in some of the cases (ill-stated problems). However, Hashash (1992) and Jen (1998) successfully used these elements for undrained plane strain analysis of excavations in association with non-linear material models (MCC and MIT-E3).

Second, Figure 3.23a shows the finite element mesh for the slice quasi-3D problem. The mesh uses one layer of 1658 brick elements and 12029 nodes. The brick elements uses similar interpolation functions to the ones used by the quadrilateral elements but over 20 displacement nodes and 8 pore pressure nodes (in all 3 dimensions: x, y, z). Figure 3.23b shows the boundary conditions and traction forces imposed on the FE slice model.

Adequacy of numerical simulations

The problems, discussed earlier in this section, associated with undrained analysis of the wellbore in a finite element program can be avoided in a well set problem using an adequate mesh. To prove numerical accuracy, the results for a base case of a vertical wellbore drilled through a K_0-normally consolidated deposit of RBBC are compared to that of a custom FE program (CAVEXP; Whittle, 1992). The mesh used in CAVEXP is one-dimensional; therefore, there are no volume or incompressibility issues.

In the base case, the cavity undergoes uniform outward deformation (cavity expansion) under undrained conditions. Based on Levadoux's (1980) work on cone penetration

[7] The reader is referred to Oden and Carey (1984) for detailed presentation of the mathematics of the Babuska-Brezzi conditions or stability condition of finite elements in incompressible medium.

analysis, strain fields are analytically derived for a finite increase in cavity radius and zero volume change. Then, the program solves the field equilibrium equations for the radial and tangential stresses and pore pressures knowing the constitutive relations of the chosen effective stress model. Distribution of strains along the radial directions is computed as:

$$\epsilon_r = -\epsilon_\theta = -\frac{1}{2}\ln\left(\frac{R^2 - R_0^2}{r^2}\right) \tag{3.28}$$

For the purposes of this numerical experiment, the MCC model described earlier is chosen to define the RBBC behavior in this base case. The radius of the cavity is increased by 5%. Figure 3.25 compares between CAVEXP results and that computed by 2D and quasi-3D meshes in ABAQUS. Figure 3.25a shows the distribution of the pore pressures and radial stresses along the radial direction. Figure 3.25b shows the in-plane shear stress computed as a function of the radial strain at the cavity wall. The results from the 2D mesh are in perfect agreement with CAVEXP results, while the results from the approximate quasi-3D are acceptable (difference < 1%).

3.4.2 Integration of constitutive models

The constitutive relations described in Section 3.3 describe the path dependent elasto-plastic material response for infinitesimal increments of strain. In finite element analyses, global load steps or changes in configuration control the deformation increments experienced at the individual Gauss points. The material response must then be found for finite strain increments $\Delta\epsilon = (\epsilon^{n+1} - \epsilon^n)$, where ϵ^{n+1} and ϵ^n are the strains at times t_{n+1} and t_n respectively.

The constitutive equations are integrated in User Material Subroutines and incorporated in the finite element program ABAQUS™ (Hashash, 1992)[8]. Different algorithms are

[8] Initialization of state variables is modified by the author to accommodate the wellbore unloading problem requirements described in Section 3.3.

used for integrating MCC and MIT-E3 models. An explicit algorithm (Nayak and Zienkiewicz, 1972; and Potts and Gens, 1985) is used for integrating the MIT-E3 equations which is first order accurate and can become unstable for large strain increments. However, the complexity of the MIT-E3 model limited the options of adequate numerical integration to explicit algorithm. The following approximation of the elasto-plastic equations is used:

$$\epsilon_{n+1}^{p} = \epsilon_{n}^{p} + \dot{\Lambda} P_n \tag{3.29}$$

where P_n is the flow direction evaluated at t_n, and $\dot{\Lambda}$ is the plastic multiplier obtained from the loading criterion through the definition of the yield surface.

An implicit integration scheme is used for the MCC formulations. The principal advantage of the implicit integration schemes is that they are unconditionally stable and hence, generally more robust in numerical computations than first order explicit integration schemes. However, it is important to emphasize that the step size ($\Delta\epsilon$) generally controls the numerical accuracy of the analysis for two reasons: 1) the numerical integration linearizes the non-linear constitutive equations over the imposed strain step; 2) the strain step linearizes the non-linear the load-displacement behavior at the global level. Hashash (1992) used the General Closest Point Projection Algorithm proposed by Simo and Hughes (1987) as the implicit integration algorithm for the MCC model.

The updated stress and state variables at time t_{n+1} are calculated using either implicit or explicit algorithms, knowing the initial state and the applies strain increment. The updated stresses are used directly in the global equilibrium calculations (Equation 3.25) and solved by full Newton iteration procedure. On the other hand, the incremental global stiffness matrix K^{n+1} is assembled from the local tangent stiffness or 'Jacobian' ($J = \frac{\partial \sigma}{\partial \epsilon}$) evaluated at the Gauss points of the elements.

For infinitesimal strain steps, $\Delta\epsilon/\Delta t \rightarrow \dot{\epsilon}$, the Jacobian is defined from the rate constitutive equations and consistency condition ($J_c = \frac{\partial \sigma'_{ij}}{\partial \epsilon_{ij}}$, "continuum Jacobian"). For finite load steps, the continuum Jacobian is not uniquely defined, as it can be evaluated at any point along the integration path. Furthermore, Nagtegaal (1982) and Simo and Taylor (1985) show that the use of the continuum Jacobian causes a deterioration in the convergence rate of the global Newton iteration scheme. These authors introduced the concept of the consistent Jacobian ($J = \frac{\partial \Delta\sigma}{\partial \Delta\epsilon}$) to ensure that the global iteration scheme converges quadratically.

Implicit Integration of the MCC model

An elastic predictor gives the first estimate for the updated stress, (σ'_{n+1}, $S_{i,n+1}$) and internal variables at t_{n+1}. If the trial stress state is located outside the yield surface (i.e. f>0) then plastic strains occur. The plastic corrector imposes the flow and hardening rules together with the consistency requirement using an implicit Euler integration scheme with full Newton iteration[9]. Hashash (1992) used a tangent stiffness matrix which is consistent with the integration algorithm for Newton iteration scheme. This stiffness matrix is the previously mentioned consistent Jacobian, J:

$$J = \begin{bmatrix} \frac{\partial \Delta\sigma'}{\partial \Delta\epsilon} & \frac{\partial \Delta\sigma'}{\partial \Delta E_i} \\ \frac{\partial \Delta S_i}{\partial \Delta\epsilon} & \frac{\partial \Delta S_i}{\partial \Delta E_i} \end{bmatrix} \tag{3.30}$$

Hashash (1992) derived analytical expressions for the components of the consistent Jacobian in the user material subroutine used for the MCC model in ABAQUS™.

[9] For more information on implicit integration of the MCC model in non-linear FE analysis, refer to Hashash and Whittle (1992).

Explicit integration of the MIT-E3 model

Implicit integration scheme, although more robust and stable, cannot be used for the MIT-E3 model due to the following reason: 1) The hypo-elastic effective stress-strain equations are complex functions which cannot be integrated analytically because they involve coupling between non-linear volumetric and shear behavior; and 2) The scalar parameters r_c and r_x used in the flow and hardening rules are functions of the current stress state which must be evaluated numerically[10]. Thus, it is not possible to derive closed-form expressions for the coefficients in a consistent Jacobian.

The explicit integration scheme achieves numerically accurate solution (i.e. within prescribed tolerance) by integration over m sub-steps, $d\epsilon$, where $\Delta\epsilon = m d\epsilon$ (e.g. Hermann et al., 1987; Pasternack and Timmermann, 1987; Faruque and Desai, 1985). In the user material subroutine for the MIT-E3 model, the maximum substep size, $d\epsilon_{max}$=0.001%. A radial return drift correction is applied at the end of each sub-step to ensure that plastic consistency is satisfied. Hashash (1992) used an approximate expression for the consistent Jacobian in terms of the continuum Jacobian at each sub-step:

$$J = \frac{1}{m}\sum_{i=1}^{m} C_i J_{c,i} \tag{3.31}$$

where C_i are the drift correction factors at each sub-step.

[10] For more details of numerical evaluation of r_c and r_x, refer to Appendix A in Hashash (1992).

Table 3.1Transformed variables for the stress and strain tensors (Kavvadas, 1982).

Stress (σ, s)	Strain (ε, e)
$\sigma = \frac{\sigma_x + \sigma_y + \sigma_z}{3}$	$\varepsilon = \varepsilon_x + \varepsilon_y + \varepsilon_z$
$S_1 = \frac{2\sigma_y - \sigma_x - \sigma_z}{\sqrt{6}}$	$E_1 = \frac{2\varepsilon_y - \varepsilon_x - \varepsilon_z}{\sqrt{6}}$
$S_2 = \frac{\sigma_z - \sigma_x}{\sqrt{2}}$	$E_2 = \frac{\varepsilon_z - \varepsilon_x}{\sqrt{2}}$
$S_3 = \sqrt{2}\,\sigma_{xy}$	$E_3 = \sqrt{2}\,\varepsilon_{xy}$
$S_4 = \sqrt{2}\,\sigma_{yz}$	$E_4 = \sqrt{2}\,\varepsilon_{yz}$
$S_5 = \sqrt{2}\,\sigma_{zx}$	$E_5 = \sqrt{2}\,\varepsilon_{zx}$

Table 3.2 Effect of consolidation stress on engineering properties of K_0-normally consolidated RBBC.

Parameter	Consolidation Stress, σ'_{vc} (MPa)	
	0.15	**1~10**
S_{uTC}/σ'_{vc}	0.33	0.28
ε_{ap} (%)	0.2	1.0
E_u/σ'_{vc}	450	150
ϕ'_{TC} (°)	38.0	31.5
K_{0NC}	0.48~0.52	0.55

Table 3.3 Input parameters for the MCC model based on low pressure calibration (Whittle et al., 1994) and high pressure calibration.

Laboratory Test	Description	Parameter	Low Pressure	High Pressure
One-dimensional Compression	Reference Void Ratio on VCL	e_0	1.12	0.65
	Normally Consolidated Compression	λ	0.184	0.1302
	Swelling Behavior	κ	0.034	0.01
	Poisson's Ratio	2G/K	1.05	
Undrained Triaxial	Critical State Friction Angle	φ'_{TC}	33.4^0	31.5^0

Table 3.4 Input parameters for the MIT-E3 model based on low pressure calibration (Whittle et al., 1994) and high pressure calibration.

Laboratory Test	Description	Parameter	Low Pressure	High Pressure
One-dimensional Compression	Reference Void Ratio on VCL	e_0	1.12	0.65
	Normally Consolidated Compression	λ	0.184	0.1302
	Non-linear Volumetric Swelling Behavior	C	22.0	1.0
		n	1.6	1.05
	Irrecoverable Plastic Strain	h	0.2	0.5
K_0 –oedometer or K_0 -Triaxial	K_0 for virgin normally consolidated clay	K_{0NC}	0.48	0.55
	Poisson's Ratio	2G/K	1.05	
Undrained Triaxial Shear Tests OCR=1; CK_0UC	Critical State Friction Angles in Triaxial Compression and Extension	φ'_{TC}	33.4^0	31.5^0
		φ'_{TE}	45.9^0	34.5^0
	Undrained Shear Strength (geometry of bounding surface)	c	0.86	0.7
OCR=1; CK_0UE	Amount of Post-peak Strain Softening in Undrained Triaxial Compression	s_t	4.5	3.4
	Non-linearity at Small Strains in Undrained Shear	ω	0.07	0.7
OCR=2; CK_0UC	Shear Induced Pore Pressures for OC Clay	γ	0.5	
Shear Wave Velocity	Small strain compressibility at load Reversal	κ_0	0.001	0.006
Drained Triaxial	Rate of Evolution of Anisotropy (rotation of bounding surface)	Ψ_0	100.0	

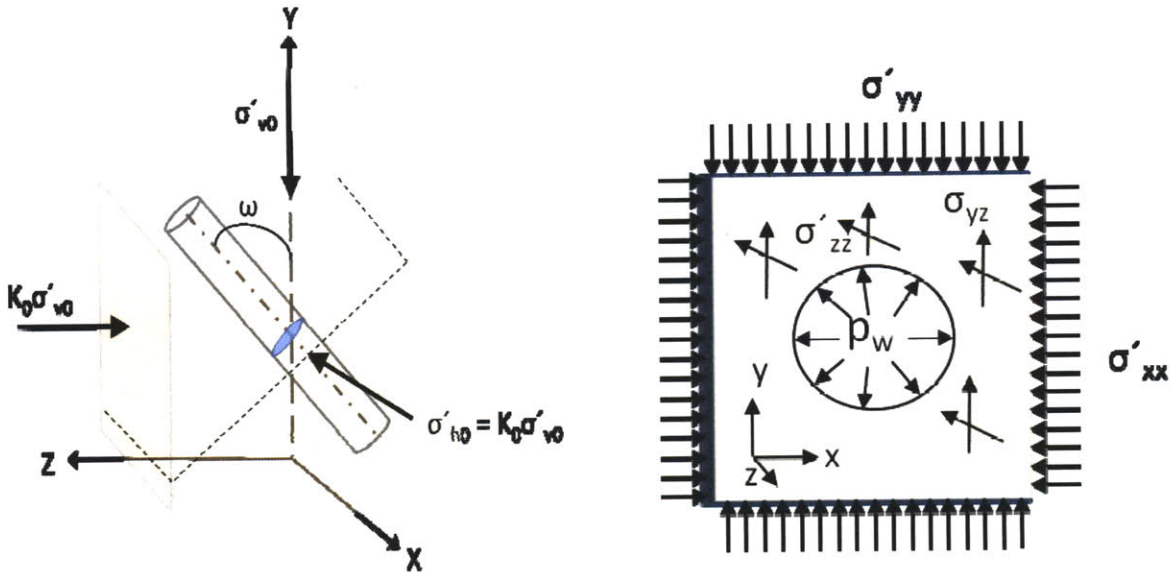

Figure 3.1 Schematic diagram showing the wellbore unloading problems with respect to the global (X, Y, Z) and local (x, y, z) frames of reference.

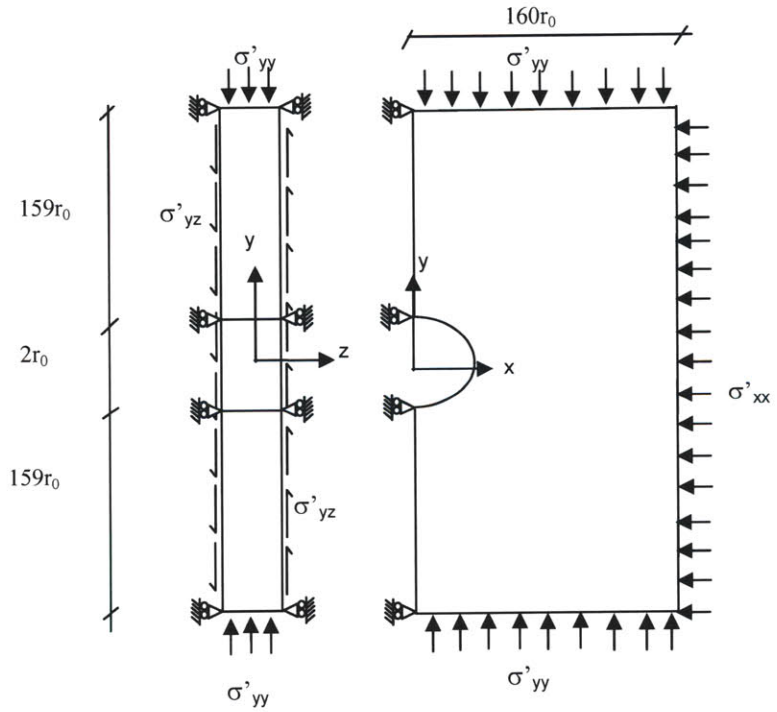

Figure 3.2 A schematic diagram showing the far field stresses for the general case of an inclined wellbore in the plane of analysis orthogonal to the wellbore axis, z.

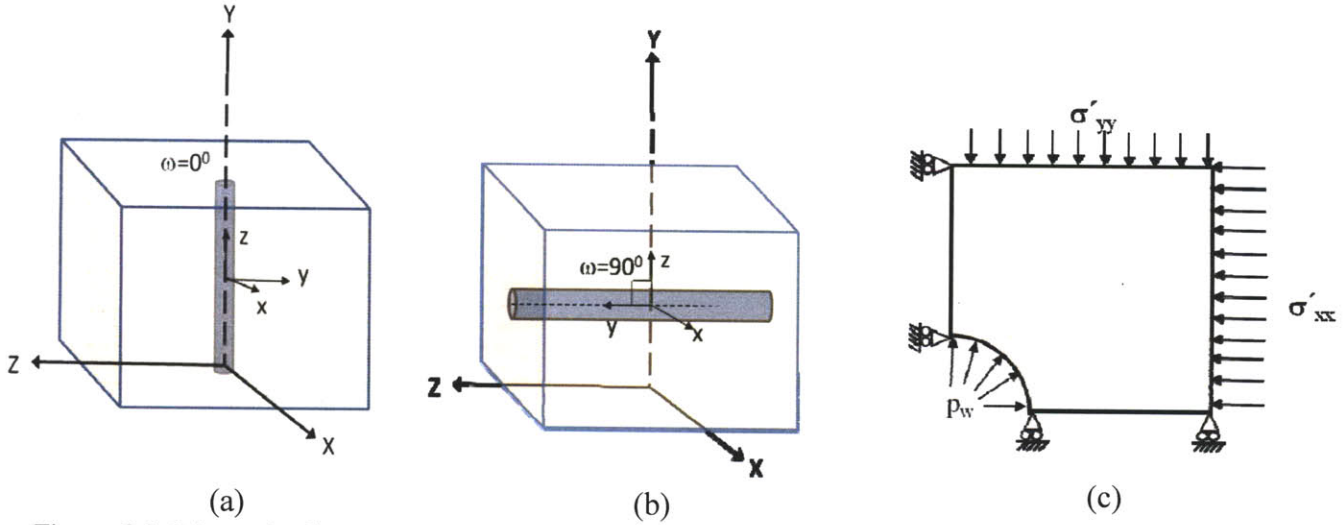

Figure 3.3 Schematic diagrams showing the orientation of (a) vertical wellbores, (b) horizontal wellbores, and (c) 2D wellbore unloading problems for vertical ($\sigma'_{xx} = \sigma'_{yy} = K_0\sigma'_{v0}$) and horizontal ($\sigma'_{xx} = K_0\sigma'_{v0}$; $\sigma'_{yy} = \sigma'_{v0}$) wellbores.

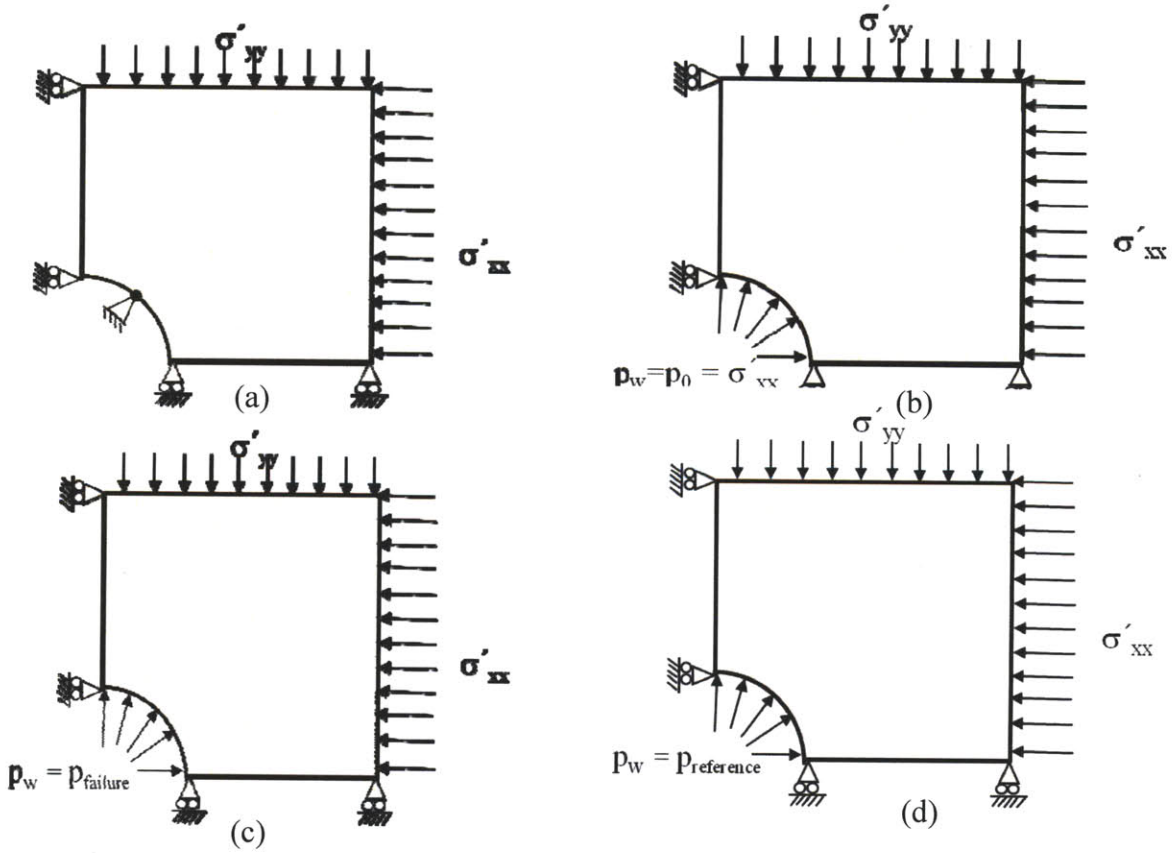

Figure 3.4 Schematic diagrams showing the analysis stages for the wellbore unloading problem: a) establishing initial conditions, b) relieving deviatoric component of stresses at cavity, c) decreasing radial pressure to failure, or d) decreasing radial pressure to a design value and monitoring effect of time on wellbore stability.

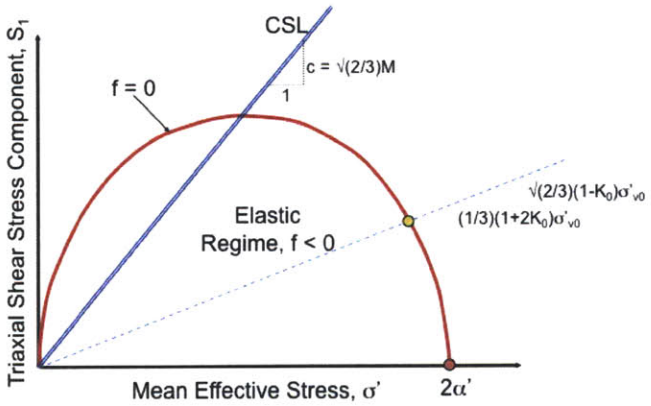

Figure 3.5 Yield surface of MCC model (Roscoe and Burland, 1968) in triaxial stress space. S_1 is the deviatoric stress component (see Table 3.1), and f= .

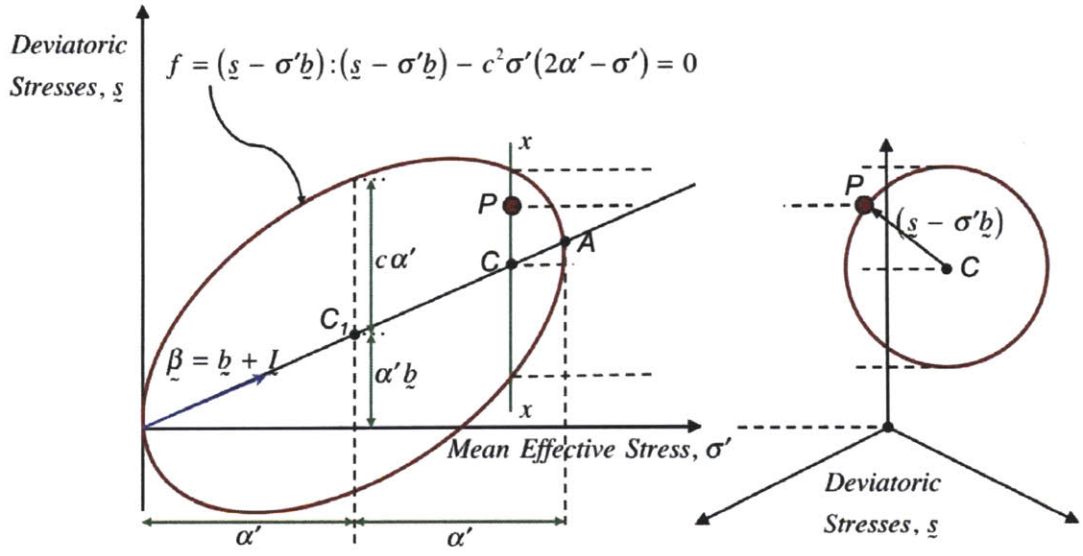

Figure 3.6 Yield surface of the MIT-E3 model (Whittle and Kavvadas, 1994).

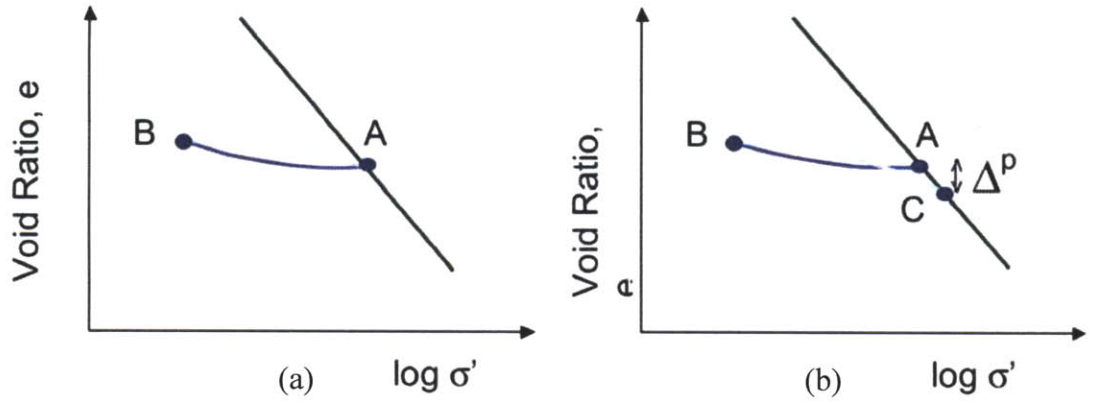

Figure 3.7 Schematic diagram showing the unload-reload behavior in MIT-E3 (Whittle and Kavvadas, 1994).

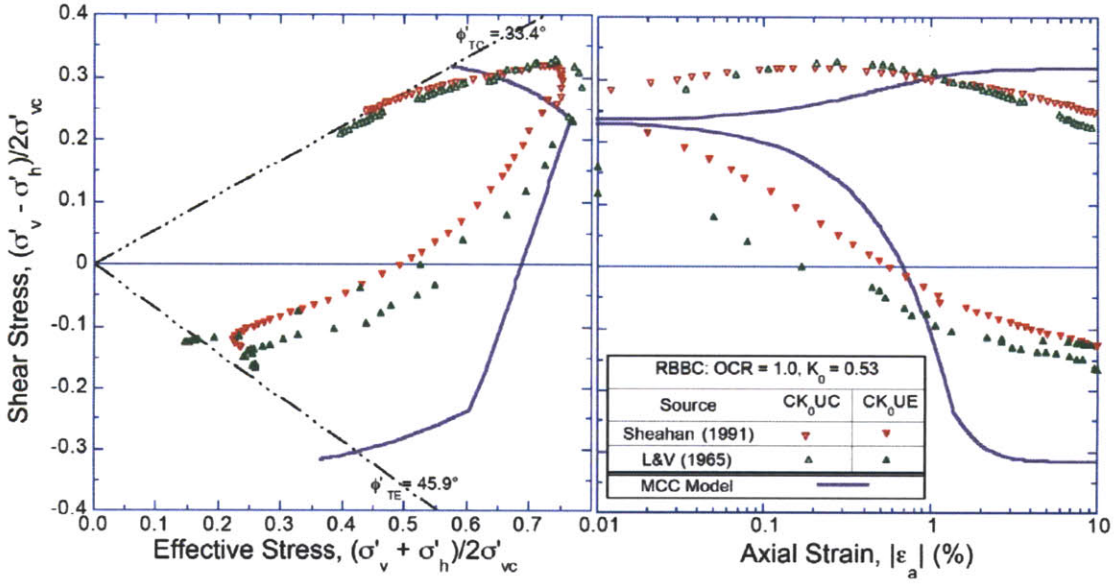

Figure 3.8 Typical undrained shear behavior described by MCC model for normally consolidated RBBC (σ'_{vc}= 0.1~0.4 MPa).

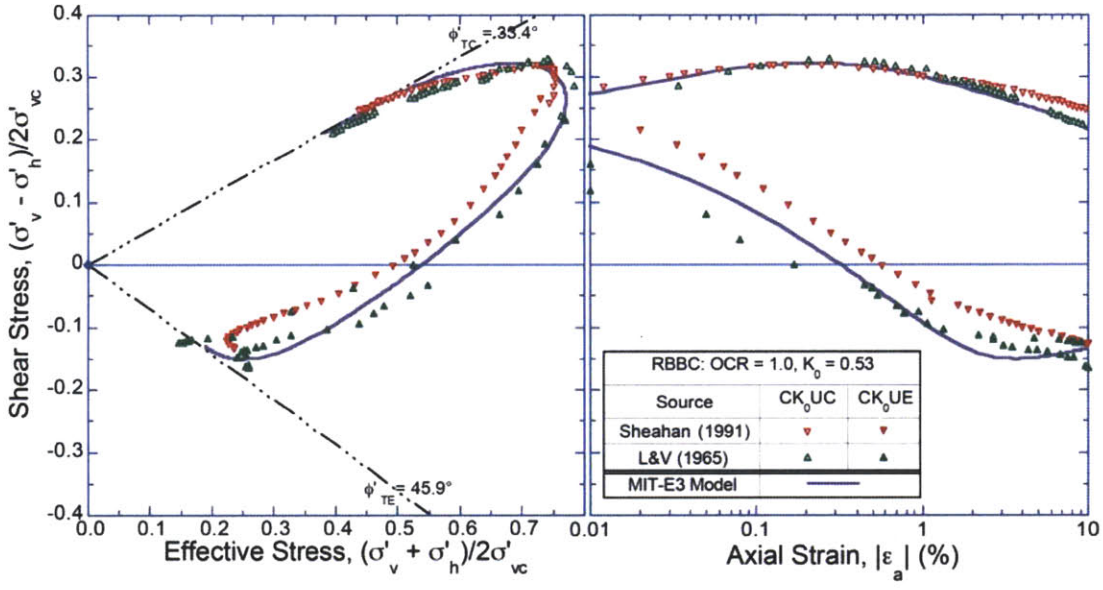

Figure 3.9 Comparison of calibrated MIT-E3 predictions and measured data from k_0-normally consolidated undrained triaxial shear tests of resedimented Boston blue clay (σ'_{vc}= 0.1~0.4MPa).

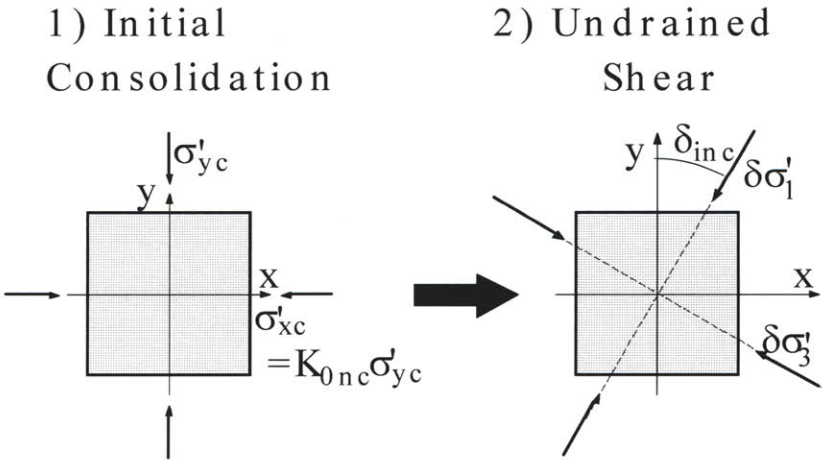

Figure 3.10 Schematic diagram of test procedure for undrained shearing in DSC apparatus (Whittle et al., 1994)

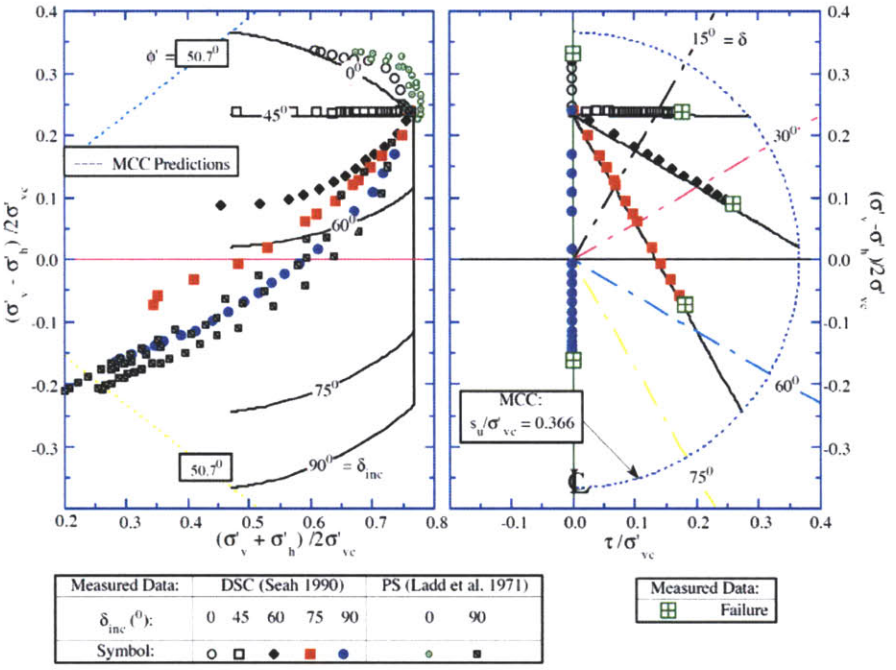

(a)

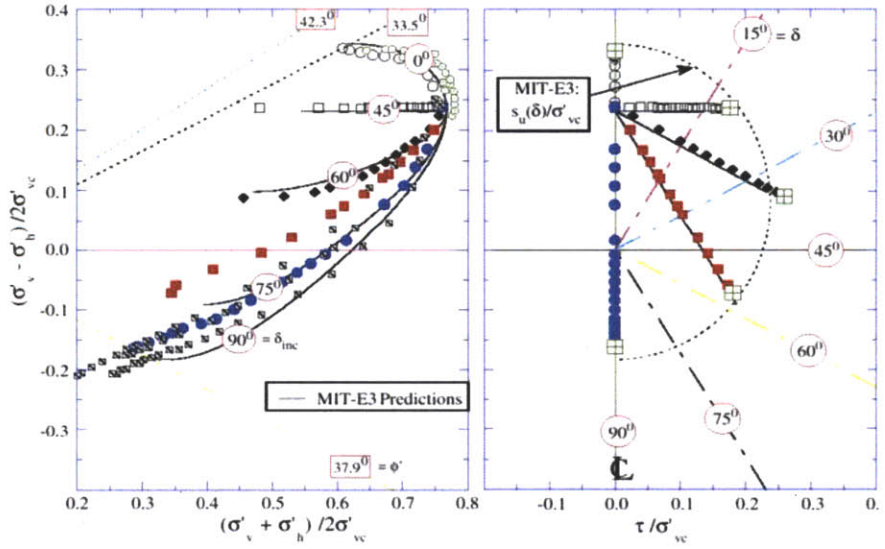

(b)

Figure 3.11 Comparison of measured data from undrained plane strain DSC shear tests and (a) MCC predictions, (b) MIT-E3 predictions for K_0-normally consolidated Resedimented Boston Clay (RBBC) (Whittle et al., 1994).

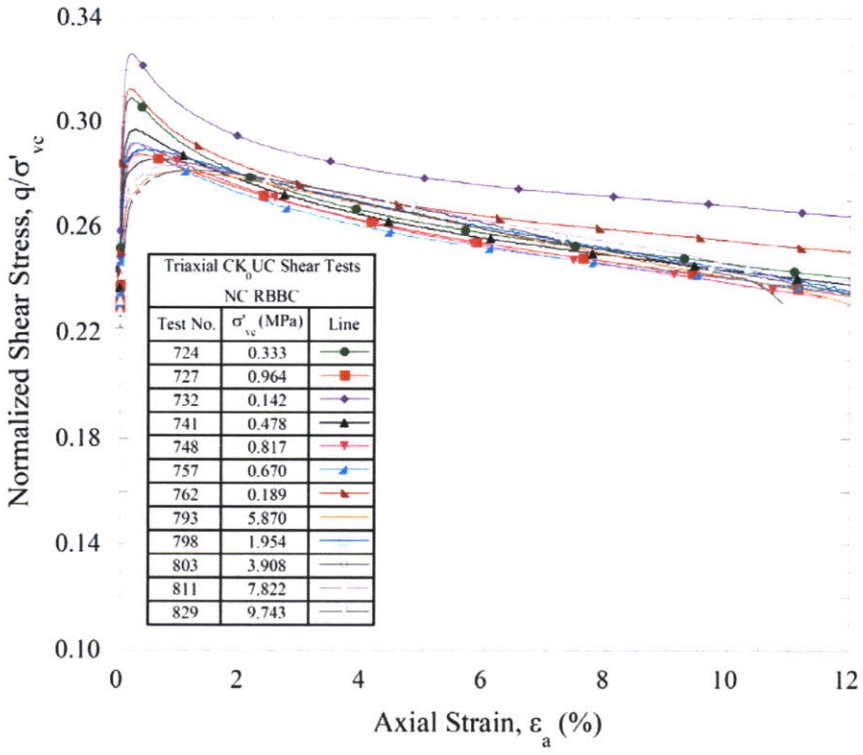

Figure 3.12 Effect of consolidation stress on normalized shear stress strain curves in undrained triaxial compression on K_0-normally consolidated RBBC (Abdulhadi, 2009).

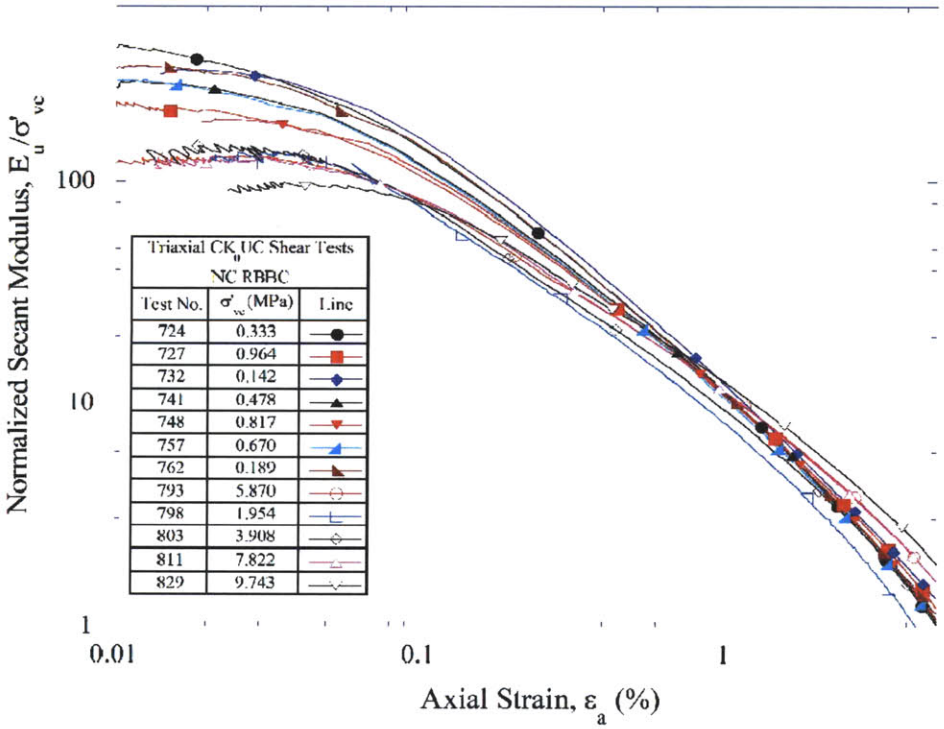

Figure 3.13 Normalized Secant modulus versus axial strain for K_0-normally consolidated RBBC from high pressure triaxial tests (Abdulhadi, 2009).

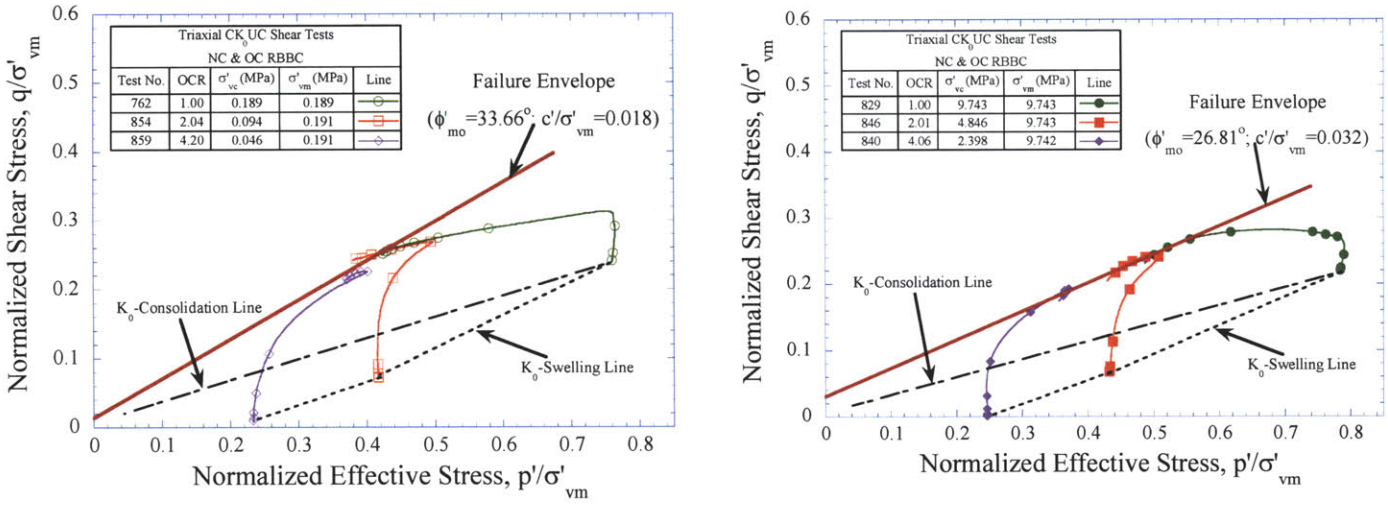

(a) $\sigma'_p = 0.1$ MPa

(b) $\sigma'_p = 9.74$ MPa

Figure 3.14 Normalized effective stress paths from undrained triaxial compression tests on K_0-normally consolidated RBBC at OCR = 1.0, 2.0, and 4.0 (Abdulhadi, 2009).

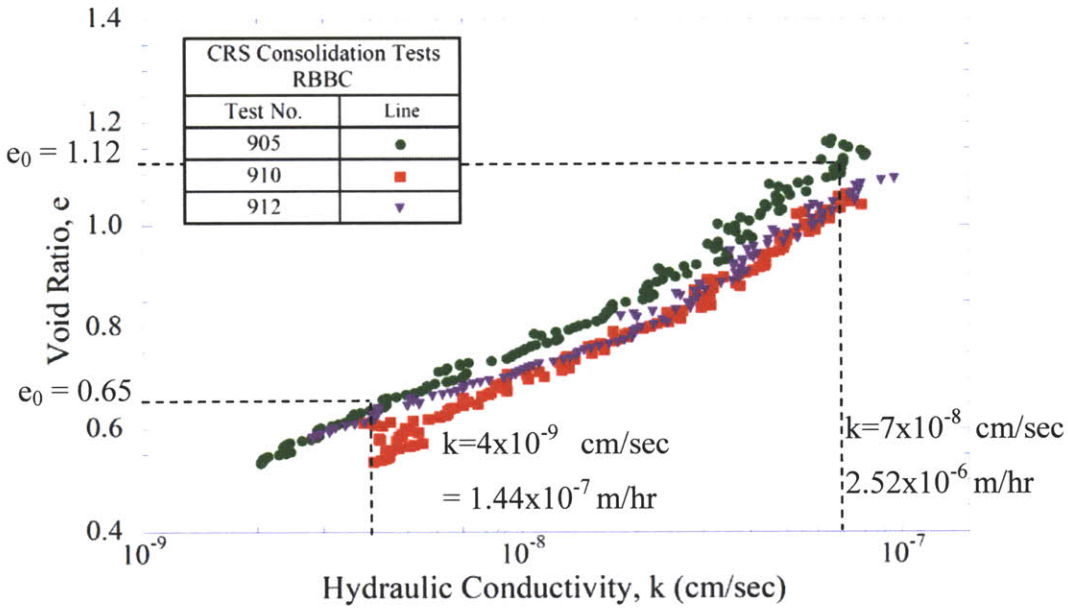

Figure 3.15 Void ratio versus hydraulic conductivity for RBBC from CRS tests (Abdulhadi, 2009).

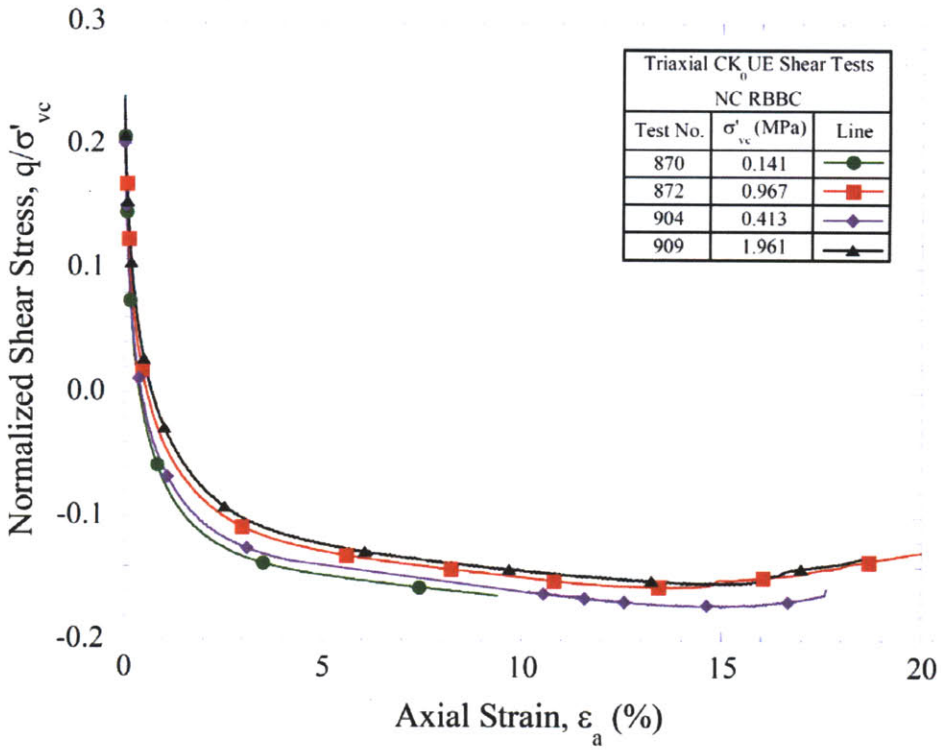

Figure 3.16 Normalized shear stress strain curves from triaxial extension tests on K_0-normally consolidated RBBC (Moniz, 2009).

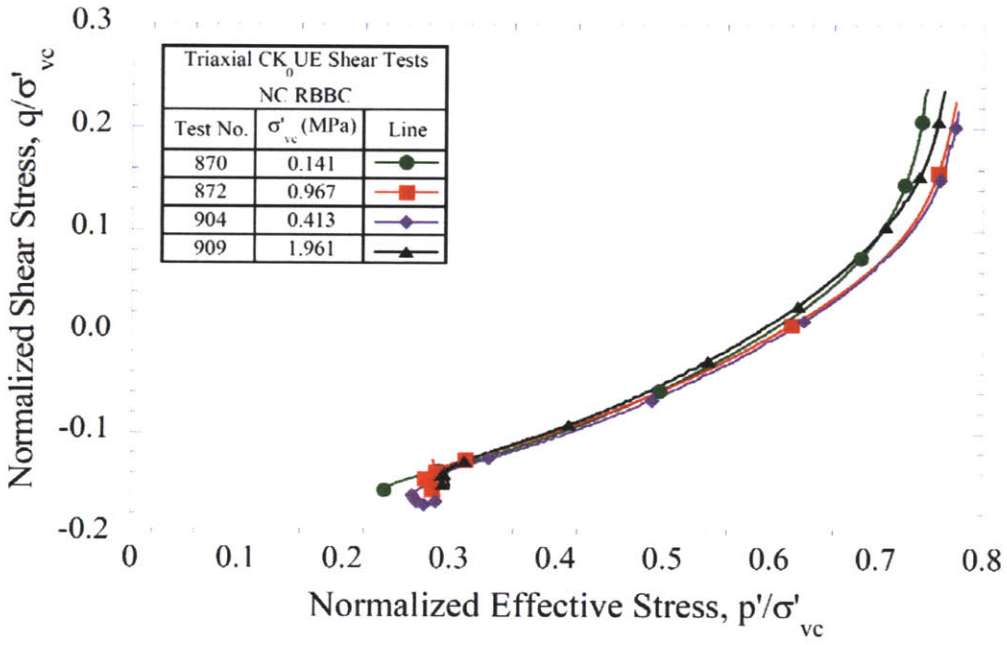

Figure 3.17 Normalized effective stress paths from triaxial extension tests on K_0-normally consolidated RBBC (Moniz, 2009).

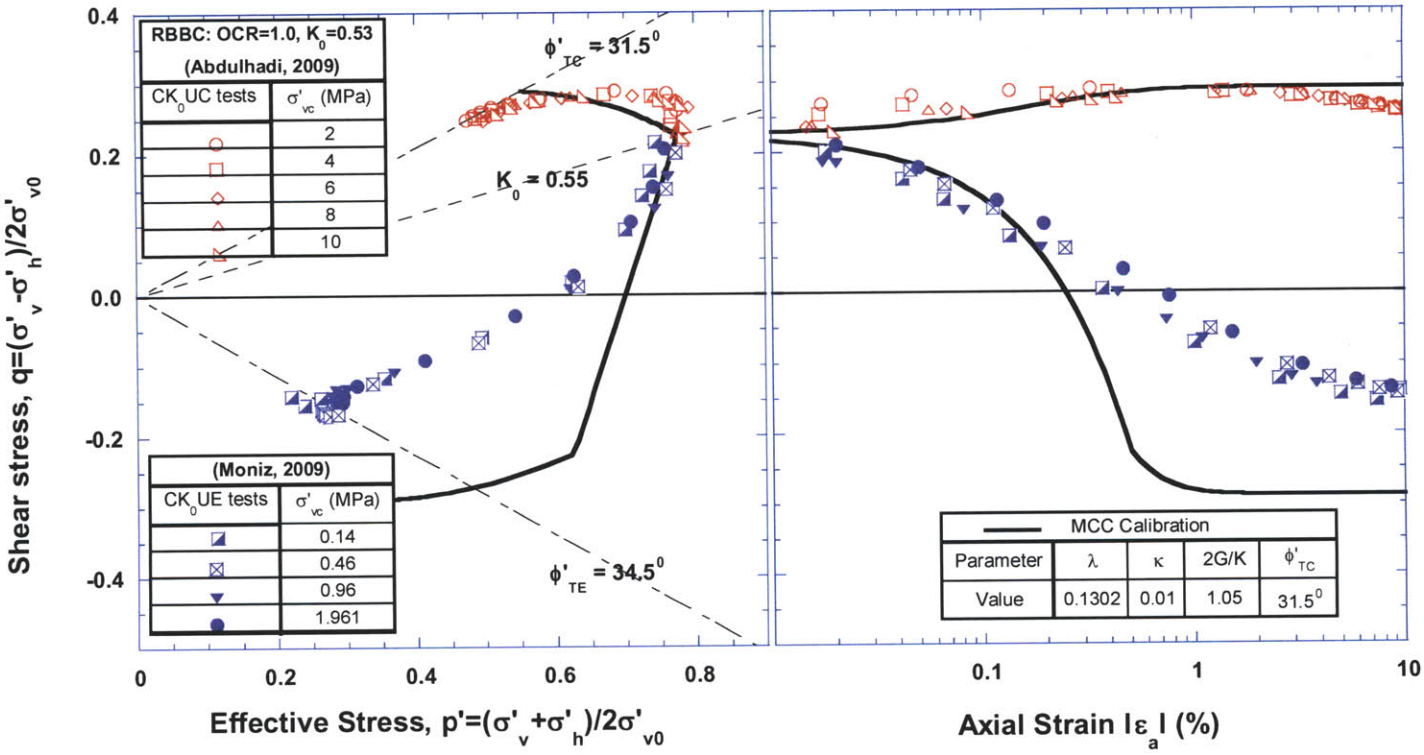

Figure 3.18 Comparison of computed and measured undrained triaxial shear behavior of K_0-normally consolidated RBBC using proposed MCC model calibration.

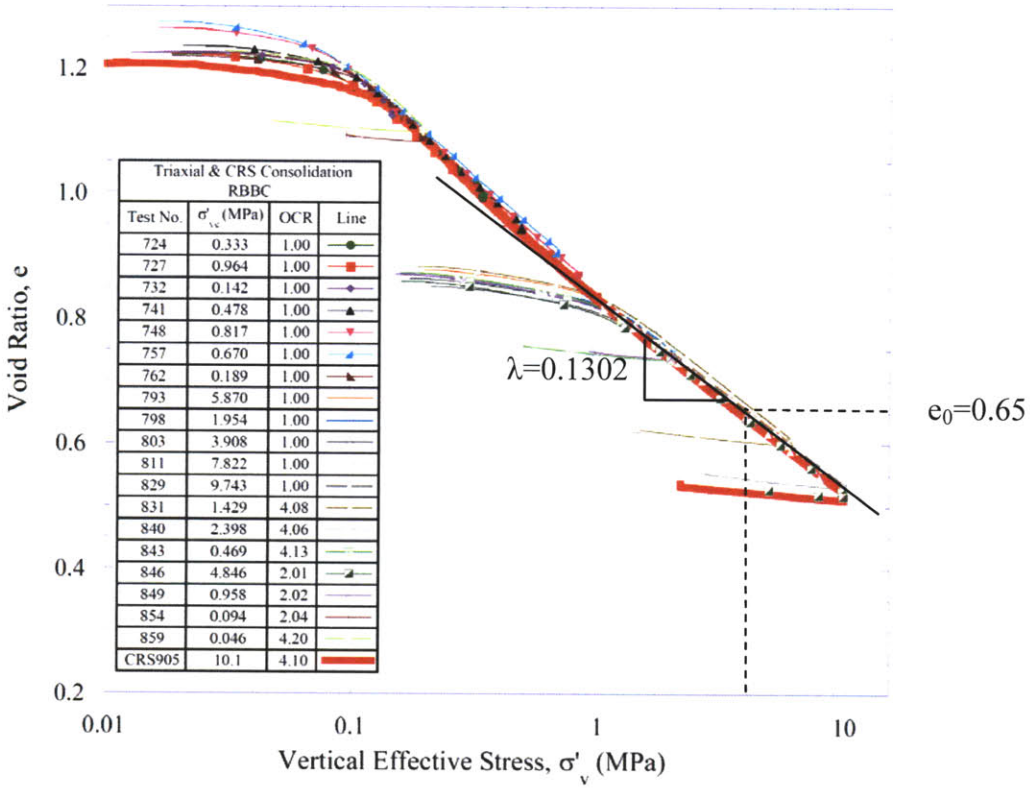

Figure 3.19 1D compression behavior from CRS and triaxial experiments on RBBC (Abdulhadi, 2009). Values of $\lambda = 0.1302$ and $e_0 = 0.65$ are chosen for reference pressure $\sigma'_{v0} = 4$ MPa.

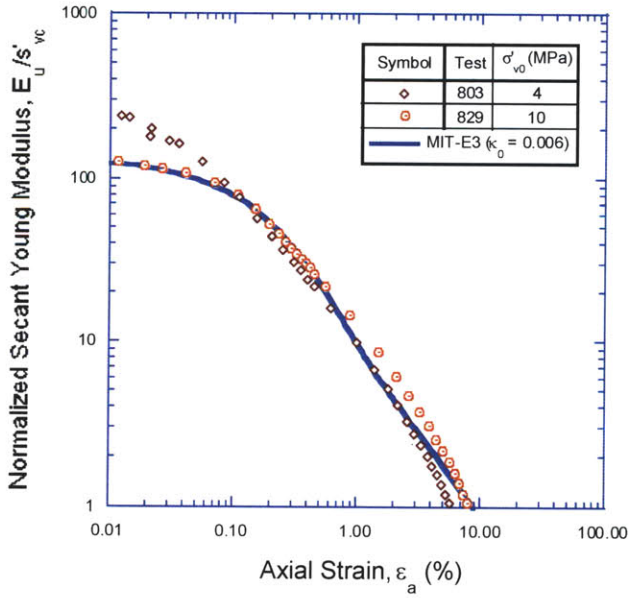

Figure 3.20 MIT-E3 model calibration for undrained stiffness in triaxial shear tests from Abdulhadi (2009).

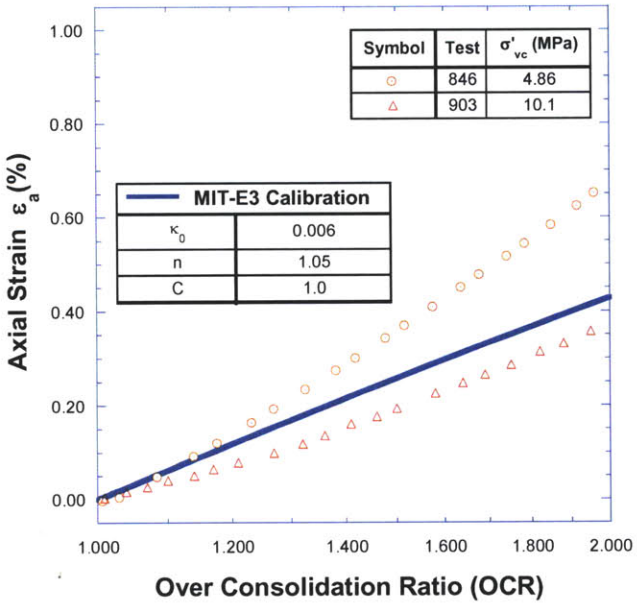

Figure 3.21 MIT-E3 model calibration for 1D swelling behavior in CRS and triaxial tests from Abdulhadi (2009).

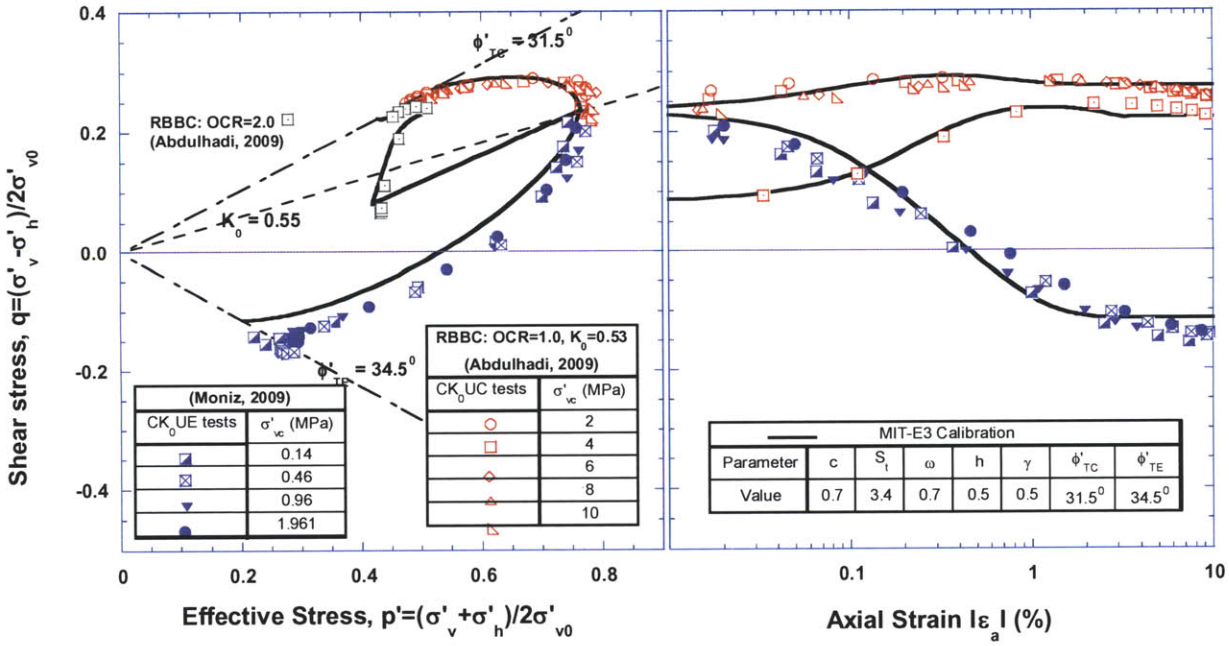

(a) Shear stress-strain behavior (b) Effective Stress Paths

Figure 3.22Comparison of computed and measured undrained triaxial shear behavior of K_0-normally consolidated RBBC (Abdulhadi, 2009) using proposed MIT-E3 model calibration

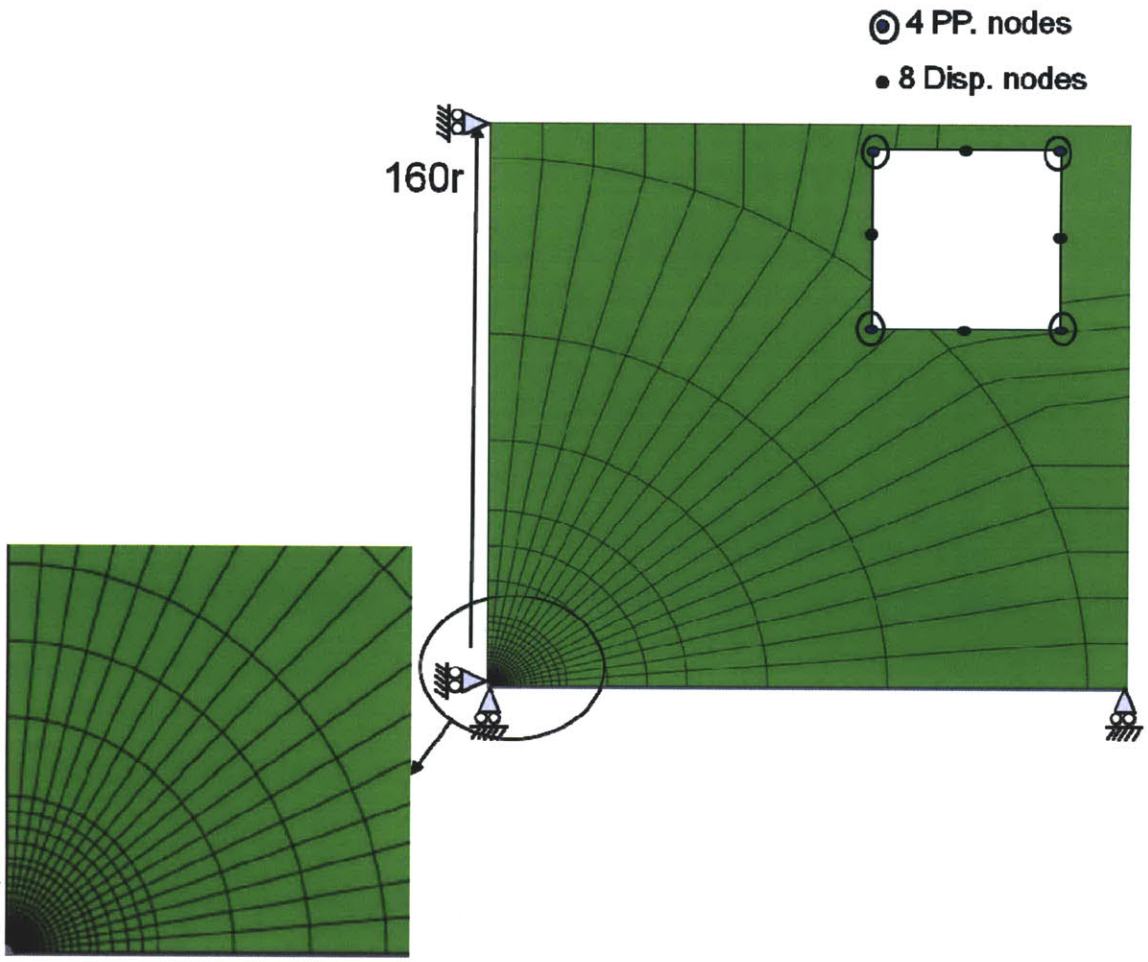

Figure 3.23 The 2D mesh used for simulating horizontal and vertical wellbores. A schematic diagram of the rectangular elements used in the analysis is at the top right corner.

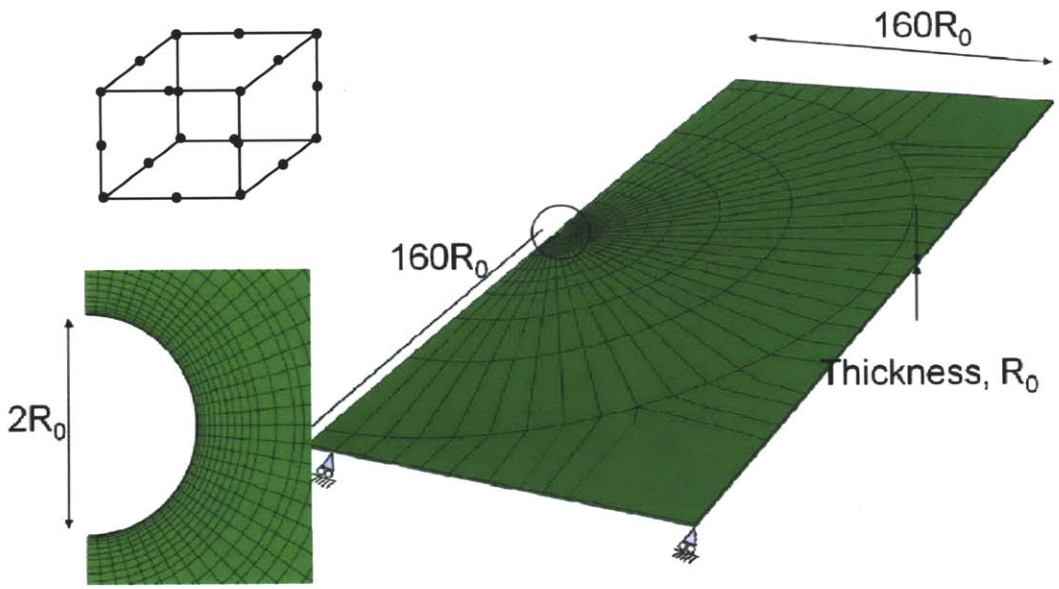

(a)

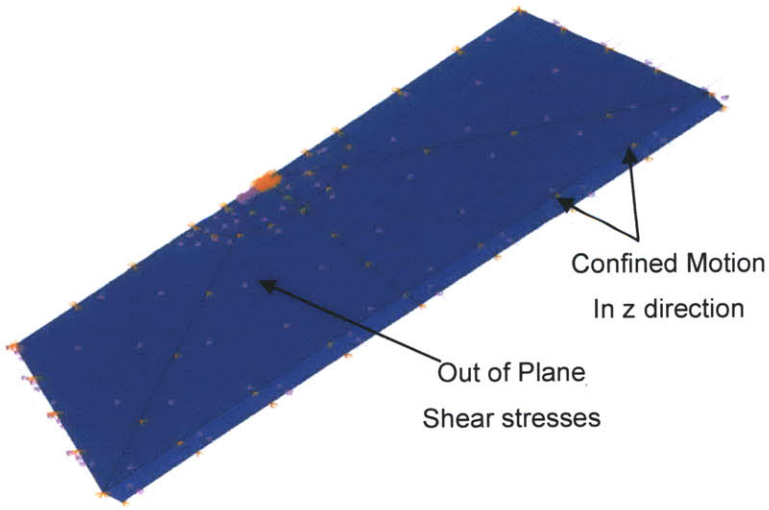

(b)

Figure 3.24 Schematic diagrams showing (a) the finite element mesh used for the quasi 3D wellbore unloading problem and a sketch of the 3D brick elements used in the mesh, and (b) the boundary conditions and surface tractions applied to the slice model in ABAQUS.

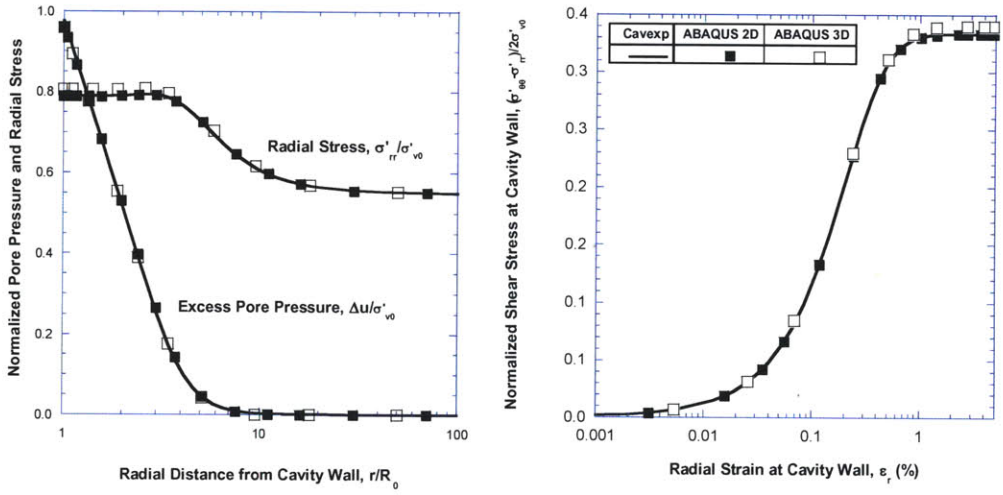

(a) Comparison of radial stresses and pore pressures with prior CAVEXP solutions at 5% cavity expansion.

(b) Comparison of shear stresses computes at cavity wall.

Figure 3.25 Results of base FE analyses for vertical wellbore in K_0-normally consolidates BBC using MCC predictions.

4 Undrained Analysis of Wellbores

4.1 Introduction

Numerical simulations of wellbore drilling in low permeability shales are carried out in four steps: 1) The initial state variables and geostatic stresses are assigned according to the wellbore deviation relative to the K_0-stress field (Stage I); 2) Deviatoric stresses are relieved by reducing stresses around the wellbore cavity to a hydrostatic condition defined by the weight of the drilling mud (Stage II); 3) The mud pressures (radial pressures on cavity wall) are reduced to a specified target value. That corresponds to either the critical mud pressure (at which failure is initiated) or a reference mud pressure that maintains wellbore stability and reasonable inward deformations at the cavity wall (Stage III); 4) For the reference mud pressure conditions, Chapter 6 analyzes long-term stability of the wellbore to coupled flow and deformation within the surrounding formation (non-linear coupled consolidation; stage IV).

Steps two and three in the analysis represent the drilling of the wellbore. In the field, drilling of wellbores usually occurs at a rate from 20 to 60 m/hr (Willson, pers. comm.). For low permeability clay formations[1] drilling is assumed to occur under undrained conditions because drilling time (unit depth is drilled in 0.05 hours) corresponds to very small dimensionless time factors[2].

The goal of this chapter is to identify critical mud pressures at which failure occurs due to undrained shearing in the formation, and to predict the relationship between mud pressure and wellbore deformations. Wellbore collapse is described by deformations and shear

---

[1] The recent data for RBBC (Abdulhadi, 2009) show permeabilities ranging from k = 5.4 x 10^{-6} m/hr at in-situ effective stress, σ'_{v0} = 1.5 MPa to k = 7.2 x 10^{-8} m/hr at in-situ effective stress, σ'_{v0} = 10 MPa. Therefore, it is reasonable to assume negligible migration of pore fluid within the formation during drilling.

[2] $T = \sigma' \frac{kt}{\gamma_w R^2}$, for k= 1.44 x 10^{-7} m/hr at in-situ effective stress, σ'_{v0} = 4 MPa, and R=0.25 m, T = 1.44 E-4.

strains around the wellbore cavity. The effect of stress history and wellbore deviation are investigated by simulating wellbores deviated by a range of angles and simulating horizontal wellbores in formations with different stress histories.

The chapter also considers the deformations and pore pressure fields around the wellbore at the reference mud pressure. The analysis examines how the predicted wellbore behavior is related to the chosen constitutive model and calibration parameters. Analyses are preformed using the effective stress soil models MCC and MIT-E3. The input parameters for these models are previously determined by calibrating with laboratory data for Resedimented Boston Blue Clay (RBBC) at low consolidation pressure (Whittle et al., 1994) and at high consolidation pressure (see Section 3.3.3).

This rest of this chapter is divided into two main sections. Section 4.2 starts by describing the two criteria used to interpret wellbore failure. The section considers the relationship between well pressure and inward deformations for five different deviation angles: 0^0, 30^0, 45^0, 60^0, and 90^0 focusing on the strain fields within the formation. Stress paths at critical positions around the cavity of the wellbore and the effects of stress history on the value of critical mud pressure are also presented.

Section 4.3 describes the soil behavior around wellbores at design mud pressures. The section describes deformations, pore pressures and effective stress paths around the wellbore. The results contrast MIT-E3 predictions to that of the MCC model and using low pressure calibration parameter to using high pressure calibration parameters.

4.2 Failure at critical mud pressures

This section presents results from stage III analyses of the wellbore unloading problem. Two different criteria are chosen to define failure in a wellbore and the corresponding critical mud pressure at which failure occurs. The first criterion defines failure by an

increase in inward deformations and shear strains locally at the cavity wall. The second criterion is a limit on large uniform cavity deformations up to $0.1R_0$ at a reference point. Figure 4.1 shows inward deformations of the wellbore as a function of the net total radial stress ratio, $(\sigma_{rr}-u_0)/\sigma'_{v0}$, where u_0 and σ'_{v0} are the initial hydrostatic pore pressure within the formation and the initial vertical effective stress, respectively. The cavity deformations are plotted for vertical ($\omega = 0^0$) and horizontal ($\omega=90^0$) wells. The presented results are computed at the reference point on the cavity where the angular coordinate, $\theta = 90^0$. This point corresponds to the crown point ($x = 0$, $y = R$) in the FE model. The reference point is chosen at the crown because this is initially where the maximum inward deformations occur (at the end of Stage II); i.e. when there is no remaining deviator stress at the wellbore[3].

Figure 4.1 marks clearly the occurrence of failure as predicted by the MCC and MIT-E3 soil models based on reference properties of K_0- normally consolidated RBBC up to 10MPa reported by Abdulhadi (2009) (as shown in Section 3.3.3). The MIT-E3 model predicts failure in horizontal wells according to the first criterion. The crown point in the horizontal wellbore deforms inwardly by $0.07R_0$ at the end of stage II where the net total radial stress ratio, $(\sigma_{rr}-u_0)/\sigma'_{v0} = K_0 = 0.55$. This ratio corresponds to the maximum uniform radial stresses acting on the cavity wall (mud pressure). When $\delta_{cr}/R_0 = 2.8\%$, failure occurs when excessive shear strains develop locally at the wellbore at $(\sigma_{rr}-u_0)/\sigma'_{v0} = 0.18$. This is considered as the onset of localized wellbore collapse. The reference mud pressure is chosen as $0.2\sigma'_{v0}$ to be slightly higher than the critical mud pressure predicted by the MIT-E3 model for the horizontal wellbore (i.e. most unstable case). This mud pressure is chosen as a reference value to study the behavior around wellbores at different wellbore deviations. MCC predictions for the horizontal wellbore show no comparable behavior, and pressures can be reduced far below the underbalanced drilling limit ($\sigma_{rr}-u_0/\sigma'_{v0} = -0.7$) with large plastic deformations in the formation. In these cases, failure is defined according to the second criterion when inward deformations at the crown reach maximum limit at $\delta_{cr}/R_0 = 10\%$. The MIT-E3 and MCC models predicted large plastic

[3] Deformations at other points can exceed that at the crown when failure approaches (see Section 4.2.1).

deformations and interpreted failure according to the second criterion at very low mud pressures, $-0.32\sigma'_{v0}$ and $-0.95\sigma'_{v0}$, respectively.

Figure 4.2 summerizes the relationship between net total radial stress ratio, $(\sigma_{rr}-u_0)/\sigma'_{v0}$ and inward deformations for 5 different deviated wellbores. The deviation angles are 0^0 (vertical), 30^0, 45^0, 60^0, and 90^0 (horizontal). Only the vertical wellbore fails due to excessive cavity deformations (δ_{cr}/R_0 = 10%). The critical mud pressure increases with the increase in deviation angle. Wellbores deviated by 30^0, 45^0, 60^0, 90^0 fail at mud pressures ratios equal to -0.177, -0.013, 0.055, and 0.18, respectively. All deviated wellbores fail due to large shear strains and exhibit tendencies for localized failure but only wellbores deviated at 30^0 and 45^0 reach the underbalanced range of mud pressures. Inward deformations at the crown point at failure decrease with deviation angle. For wellbores deviated by 30^0, 45^0, 60^0, 90^0, the inward deformations are 7.9%, 3.8%, 3.6%, and 2.1% respectively.

The MCC predicts the relationship between net total radial stress ratio, $(\sigma_{rr}-u_0)/\sigma'_{v0}$ and inward deformations as shown in Figure 4.3. Wellbores at all 5 deviation angles fail due to excessive deformations (δ_{cr}/R_0 = 10%) and reach the underbalanced range of mud pressures. Critical mud pressure ratios for wellbores deviated at $\omega = 0^0$, 30^0, 45^0, 60^0, and 90^0 are -0.96, -0.91, -0.86, -0.80, and -0.68, respectively. The MCC simulations do not generate any tendency for localized failure and predicts lower values of the critical mud pressures than MIT-E3.

4.2.1 Deformations and Strains around wellbore cavity

Deformations at the crown point are useful indicators of the critical mud pressure and how the relationship between mud pressures and wellbore deformations is affected by wellbore deviation. However, more data is necessary to understand how failure happens and describe the kinematic behavior around wellbores. This section interprets previous results using the deformations and shear strains around the cavity of the wellbore.

For the vertical wellbore the far field stress conditions are isotropic, and hence the wellbores deform uniformly inwards during unloading. Non-uniformity of inward deformations and cavity distortions increase with the deviatoric component of far field stresses. Initially, the circular cavity takes a regular oval shape, elongated along the local x-axis (see Figure 3.2). Cavity distortion or ovalization can be defined by the ratio of the radial deformations at the springline (y=0, x=R, $\theta=0^0$) to that at the crown (y=R, x=0, $\theta=90^0$), δ_{sp}/δ_{cr}. As failure progresses, the cavity distorts irregularly and the direction of cavity elongation changes.

Figure 4.4 describes the shapes of wellbore cavities at failure using the undeformed shape of the cavity as a datum. The inward deformations are scaled to the plotted size of undeformed cavity by 5:1. The figure shows (a) MIT-E3 predictions and (b) MCC predictions of cavity deformation for vertical and deviated wellbores, with $\omega = 30^0$, 45^0, 60^0 and 90^0. The MIT-E3 model predicts irregular shapes for cavities of deviated wellbores at failure, while the vertical wellbore deforms uniformly inwards up to 10% of initial radius as shown in Figure 4.4a. The wellbore with $\omega = 30^0$ has larger deformations at crown (8%) and springline (9.8%). For $\omega = 45^0$ and 60^0 the largest deformations occur at the springline (4.5%). The inward deformation for 90^0 wellbore (horizontal wellbore) at the crown point reaches 2.8% but the maximum deformations occurs locally at $\theta=15^0$, where δ_r =3.1%.

The MCC model predicts regular oval-shaped cavity for inclined wellbores elongated along the local y-axis as shown in Figure 4.4b. The inward deformation at Crown Point is 10% at failure for all wellbores according to the second failure criterion. The inward deformation at Springline increases with deviation angle. The distortion ratios for wellbores at $\omega = 30^0$, 45^0, 60^0 and 90^0 are δ_{sp}/δ_{cr} = 1.09, 1.17, 1.23, and 1.3, respectively.

The radial deformations at the cavity wall are consistent with shear strains around the cavity. Contours of octahedral shear strains (the second invariant of the deviatoric strain

tensor[4], |E|) describe the state of shear strains around the cavity of a wellbore and provide a clearer indication of the failure mechanism. Figures 4.5 and 4.6 show the distribution of the octahedral shear strains around vertical and deviated wells predicted by the MIT-E3 while Figure 4.7 show those predicted by the MCC model. The figures contrast the state of strains at design mud pressures and critical mud pressures to show the progress of failure with decreasing mud pressure (unloading wellbore) inside the cavity.

The MIT-E3 predictions of shear strain distributions show that the earlier failure occurs, zones of high shear strains (>10%) extend less into the formations. However, the presence of small and isolated zones of high shear strains lead to local increase in deformations at cavity wall and collapse. For the vertical wellbore, the shear strains at design mud pressure are concentric hoops around the cavity with magnitude <1% at cavity wall (Figure 4.5a). The zone of influence (|E|>0.1%) continue to expand and the magnitude continue to increase at cavity wall with decreasing mud pressure. At failure, high shear strains (|E|>10%) are reached all around cavity wall with no localized zones of increased strains (Figure 4.5b).

At reference mud pressure ratio (p_w-u_0/σ'_{v0} = 0.2), shear strains increase at cavity wall with the deviation angle; and the zone of influence extends further in a radial direction. For $\omega=30^0$, shear strain lobes extend radially at $\theta=45^0$ (Figure 4.5c). For $\omega=45^0$ and 60^0, shear strain lobes rotate towards the Crown Point and extend at $\theta=53^0$ (Figure 4.5e) and 60^0 (Figure 4.5g), respectively. Shear strain continue to increase and extend around the 30^0 deviated well at angle, $\theta=45^0$ with decrease in mud pressure. Failure occurs when shear strains increase at the Crown Point and Springline (Figure 4.5d). The small zones of high shear strains at $\theta=0^0$ and 90^0 are linked to the excessive local deformations presented in Figure 4.4a. The shear strains around the 45^0 (Figure 4.5f) and 60^0 (Figure 4.5h) deviated wells increase at the cavity wall within the range of $\theta=0^0$ to 20^0 with decrease in mud pressure. When zones of high shear strains are formed at the Springline point;

[4] $|E|=\sqrt{E_1^2+E_2^2+E_3^2+E_4^2}$, the second invariant of the deviatoric strain tensor in the transformed space (Whittle and Kavvadas, 1994).

distortions and excessive inward deformations lead to failure. Figures 4.6 a and b show the octahedral shear strains around the horizontal wellbore at reference mud pressure ratio (0.2) and critical mud pressure ratio (0.18), respectively. High shear strains up to 27% develop at $\theta=15^0$ where local increase in inward deformations occurs as shown in Figure 4.4a.

The shear strain distributions predicted by the MCC show no localized zones of high shear strains at failure. Magnitudes of octahedral shear strains are generally higher than that predicted by the MIT-E3 model, hence significant shear strains are chosen to be > 1%. The vertical and 30^0 deviated well show no significant shear strains at design mud pressure ratio. Figure 4.7 a and b show the distribution of octahedral shear strains around the vertical and 30^0 deviated wellbores at critical mud pressures, respectively. The 45^0, 60^0 and 90^0 deviated wells exhibit small zones of significant shear strains within the range of $\theta=0^0$ to 45^0 at reference mud pressure as shown in Figure 4.7 c, e, and g, respectively. With further decrease of mud pressure, magnitudes of shear strains at cavity wall increase, and high shear strains (>30%) extend further in the formation with higher deviation angles. The octahedral shear strains around the vertical wellbore form concentric hoops, while lobes of high shear strains are oriented along radial line at $\theta=45^0$ of deviated wellbores at the critical mud pressure.

4.2.2 Failure in horizontal wells

Horizontal wellbores have the highest critical mud pressures (most unstable). This is consistent with literature described in Chapter 2. The critical mud pressure increases with deviatoric component of far field stresses acting in the plane of the wellbore. The local axes of horizontal wellbores are aligned with global frame of reference as shown in Chapter 3 (see Figure 3.3). The geostatic stresses are not transformed to local axes of horizontal wellbores, and the deviatoric stresses resulting from K_0-consolidation of RBBC are fully acting on the horizontal wellbore. Initially, the state of stresses are uniform everywhere in the model; but with decreasing mud pressure, state of stresses at

each point on the cavity wall changes differently depending on it position (defined by angular coordinate, θ).

Figures 4.8 a and b show the initial stress state of elements near to the crown point and to the springline of horizontal wellbores, respectively. The two cases are separated at angular coordinate $\theta=45^0$. The intermediate principal stress acts perpendicular to the plane of the wellbore. The direction of wellbore unloading is aligned with minor principal stress at $\theta<45^0$, and with the major principal stress at $\theta>45^0$. Decreasing mud pressure in wellbore cavity leads to a decrease in the radial stresses (extension), and an increase in the hoop or tangential stresses (compression).

The effective stress paths of different points on the cavity wall show the effect of wellbore unloading on elements at different positions (different values of θ). Figure 4.9 plots the MIT-E3 predictions of effective stress paths at 5 points on the cavity wall of a horizontal wellbore at $\theta=0^0$, 15^0, 45^0, 75^0, 90^0. The effective stress paths are plotted in three subspaces of the transformed variables (σ', S; Whittle and Kavvadas, 1994). The space (σ', S_1) illustrates the effect of triaxial shearing, while (σ', S_2) considers the effect of intermediate stress, and (σ', S_3) shows the simple shearing in-plane. This state of stresses can not be fully defined by the norm of the deviatoric stress tensor $|S|$, because the critical state conditions are not isotropic and depend on the direction and mode of shearing. The figure also contrasts the behavior during Stage II (release of deviatoric stress) and Stage III (decreasing radial pressure). The behavior is clearly changing for points at $0^0 <\theta< 90^0$ and more shear induced pore pressures are generated at these points than at the crown point or the springline.

In Figure 4.9, S_1 increases for points at $\theta=0^0$and 15^0 (compression), and decreases for points at $\theta=45^0$, 75^0, and 90^0 (extension). Positive S_2 is generated during Stage II where unloading is aligned with minor stresses ($\theta=0^0$ and 15^0), and negative S_2 is generated where unloading is aligned with major stresses ($\theta=45^0$, 75^0 and 90^0). Maximum simple shear (S_3) is found at $\theta=45^0$ and decreases at points closer to the crown or the springline.

The previous results indicated excessive deformations and maximum octahedral shear strains at $\theta=15^0$. Stress paths shown in Figure 4.9 indicate an increase in S_1 and S_3 components of the deviatoric stress tensor at this position leading to failure initiation.

Effect of stress history

The stress history is described by the overconsolidation ratio ($OCR=\sigma'_{vc}/\sigma'_{v0}$). Undrained strength ratio and normalized secant stiffness modulus increase with overconsolidation ratio of RBBC as shown in many element shear tests in the lab (e.g Ladd and Varallyay, 1965; Sheahan, 1991). MIT-E3 predictions of wellbore unloading performed on horizontal well in RBBC under different values of OCR illustrates the effect of stress history on wellbore stability and deformations. MIT-E3 model predicts early failure in horizontal wells in normally consolidated RBBC ($[\sigma_{rr} - u_0]/\sigma'_{v0} = 0.12$ using low pressure calibration parameters as shown in Figure 4.10); however, an increase in the value of pre-consolidation pressure (σ'_{vc}) improves strength and increases stiffness around the wellbore.

Figure 4.10 shows the relationship between inward cavity deformations and total radial stresses at the crown point of the horizontal wellbore for OCR= 1.0, 1.5, 2.0 and 4.0. The MIT-E3 predictions use input parameters from Whittle et al. (1994) calibrated to the behavior of RBBC at low consolidation pressure. A slight increase in the OCR allows the mud pressure to be reduced below the underbalanced drilling limit. At higher OCR values the required mud pressure ratio to prevent failure (net critical mud pressure ratio) decreases to $-0.22\sigma'_{v0}$ and $-0.52\sigma'_{v0}$ for OCR=1.5 and 2.0 respectively. However, failure occurs due to local increase in deformations and high shear strains (Criterion 1) as in the case of normally consolidated clays but at larger deformations at $\delta_{cr}/R_0 = 3.1\%$ and 4.2% for OCR=1.5 and 2.0, respectively. At OCR=4.0, no comparable behavior is encountered and wellbores exhibit large plastic deformations, $\delta_{cr}/R_0 = 10\%$ at net mud pressure ratio= -1.5.

The behavior around wellbores becomes stiffer with higher OCR values. The inward deformations at Crown Point decrease with higher OCR at design mud pressure. This can be attributed to the absence of shear induced pore pressure during shearing as well as the general effect of OCR on strength and stiffness. Figure 4.11 shows the effective stress paths at the springline of horizontal wellbore in RBBC for OCR=1.0, 1.5, 2.0, and 4.0 in σ'-S_1 space and S_2-S_1 space. For OCR>1.0, the effective stress paths show initial elastic behavior. Positive shear induced pore pressure are generated with further decrease in mud pressure until failure occurs and the critical state condition is achieved. For OCR=4.0, the large uniform deformations occur before the critical state condition is achieved.

4.3 Wellbore behavior at design mud pressures

The reference mud pressure ratio is chosen to compare behavior around wellbores deviated by different angles using different soil models and calibration parameters at the same well pressure. The reference mud pressure ratio is chosen to maintain stability of wellbores in all the considered cases. The most unstable case is the horizontal wellbore using The MIT-E3 soil model at high pressure calibration parameters. This section presents results for a similar set of simulations for wellbores deviated at 0^0, 30^0, 45^0, 60^0 and 90^0 in K_0-normally consolidated RBBC using the MCC and MIT-E3 soil models.

The wellbore behavior around the cavity is described by plotting cavity wall deformations and pore pressures within the formation. Stress conditions around the wellbore can be represented by the mean effective stress, σ', and series of transformed deviatoric shear components, S_i (Whittle and Kavvadas, 1994) with respect to the global frame of reference (X, Y, Z). These results also describe the state of wellbore before consolidation (Stage IV analysis). The effect of time and consolidation on wellbore stability is discussed in detail in Chapter 6.

4.3.1 Deformations

MIT-E3 and MCC model predictions agree that wellbore deformations increase with deviation angle at low or high consolidation pressures. Cavity distortion into oval shapes can be described by the inverse of distortion ratio used in Section 4.2.1, δ_{cr}/δ_{sp}. The inverse of distortion ratio increases with deviation because at the reference mud pressure ratio, the inward deformations at Crown Point are generally higher than at the Springline. However, distortion is also affected by the state of stability of highly deviated wellbores ($\omega=60^0$ and 90^0 using MIT-E3 model).

Figure 4.12 a, and b show MIT-E3 and MCC predictions of deformations around wellbores, respectively. In Figure 4.12a, the vertical wellbore cavity deforms uniformly inwards to $\delta/R_0 = 0.55$. The 30^0 and 45^0 deviated wellbores deform into regular oval shapes with $\delta_{cr}/\delta_{sp} = 1.17$ and 1.20, respectively. For the 60^0 and 90^0 deviated wellbores, the reference mud pressure ratio is relatively close to the critical mud pressure ratio. The deformed shape of the cavity is irregular and shows local increase in inward deformations at $\theta=0^0$ and 15^0 for 60^0 and 90^0 deviation angles, respectively. The MCC predictions in Figure 4.12b show less deformation than that of MIT-E3. The deformed shape of the cavity is practically circular with negligible ovalization.

Figures 4.13 and 4.14 illustrate the numerical analyses of deformations of the wellbore cavity for vertical and deviated ($\omega = 0^0$, 30^0, 45^0, 60^0 and 90^0) wellbores in K_0-normally consolidated RBBC at low consolidation pressure (0.1MPa) using MIT-E3 and MCC models, respectively. The mud pressure is reduced to the underbalanced drilling limit (unless 1st criterion failure occurs at higher mud pressures). For low consolidation pressures, stability conditions of highly deviated wellbores are better. The MIT-E3 model predicts lower critical mud pressure ratios for 60^0 and 90^0 deviated wellbores (0.1 and 0.12, respectively).

MIT-E3 predicts highly non-linear relationship between wellbore deformations and mud pressures. However, the model predicts smaller deformations at low consolidation pressures than high. This indicates more ductile behavior and less stiffness at high

consolidation pressures. The MCC predicts a nearly linear relationship between wellbore deformations and mud pressure above underbalanced drilling limit using low pressure calibration parameters. Figure 4.14a shows that MCC predicts larger deformations than MIT-E3. MCC predictions under low consolidation pressure overestimate deformations all around the cavity. Values of the inverse of distortion ratio (δ_{cr}/δ_{sp}) predicted by MIT-E3 (up to 1.9 for $\omega=90^0$) are higher than those predicted by MCC (up to 1.4 for $\omega=90^0$) because MCC predicts higher deformations at springline relative to that at Crown Point. Generally, using low pressure calibration parameters generate more ovalization and distortion in cavities. The MIT-E3 predicts tendency for localized excessive deformations in horizontal wellbores similar to results using high calibration parameters. Similarly, the failure is initiated at a point on cavity wall at $\theta=15^0$.

4.3.2 Pore pressure distribution around cavity

This section presents the distribution of normalized excess pore pressures ($\Delta u/\sigma'_{v0}$) at reference mud pressure ratio ($p_w-u_0/\sigma'_{v0} = 0.2$) around wellbores deviated at 0^0, 30^0, 45^0, 60^0 and 90^0. Undrained analyses generate positive and negative excess pore pressures to maintain constant volume constraints. Consolidation analyses in Chapter 6 compute the redistribution of these pore pressures around wellbores through time. The magnitudes and distributions of excess pore pressures depend on the chosen constitutive model and calibration parameters. Figure 4.15 shows the pore pressure distribution around vertical and horizontal wells using the MIT-E3 model at low and high consolidation pressures. Figure 4.16 shows similar set of results for deviated wellbores. Figure 4.17 show pore pressure distribution around all wellbores using MCC model at high consolidation pressure.

Magnitudes of positive and negative pore pressures increase with wellbore deviation angle. In vertical wellbores, pore pressures of low magnitudes ($-0.01<\Delta u/\sigma'_{v0}<0.1$, Figure 4.15c) are uniformly distributed around the wellbore cavity. At low consolidation pressure, higher negative pore pressure values develop around the vertical wellbore

($\Delta u/\sigma'_{v0}$ <-0.01, Figure 4.15d). In horizontal wellbores, negative pore pressures are generated around the crown point ($\theta=90^0$). At low consolidation pressure higher negative pore pressures develop ($\Delta u/\sigma'_{v0}$ <-0.2, Figure 4.15b) than at high consolidation pressures (-0.2<$\Delta u/\sigma'_{v0}$ <-0.1; Figure 4.15a) at the Crown Point. High positive pore pressures ($\Delta u/\sigma'_{v0}$ >0.2) are irregularly distributed in the area around the springline because at high consolidation pressure critical mud pressure is higher. At low consolidation pressure, lower positive excess pore pressures develop near the springline ($\Delta u/\sigma'_{v0}$ <0.2), as shown in Figure 4.15b.

Figure 4.16 show similar trends of pore pressure distributions in deviated wellbores to that in horizontal wellbores. The zones of significant excess pore pressures (>$0.1\sigma'_{v0}$) increase with deviation angle. At low consolidation pressure, smaller zones of positive excess pore pressure (>$0.1\sigma'_{v0}$) develop and larger zones of negative excess pore pressures (<$-0.2\sigma'_{v0}$; Figures 4.15 b, d, and f). The MCC model also predicts higher magnitudes of positive and negative excess pore pressures with increasing deviation angle. Figure 4.17 show MCC predictions at high consolidation pressure. Compared to MIT-E3 predictions, the MCC model generates higher magnitudes of excess positive and negative pore pressure at the crown point and around the springline. These high pore pressure magnitudes lead to higher pore flow gradients during consolidation.

4.3.3 Stress paths at cavity wall

This section compares between MIT-E3 and MCC predictions of effective stress paths around the cavity. Figures 4.18 and 4.19 plot the stress paths at the crown points and springlines, respectively. Stresses are computed due to the reduction of mud pressure to the reference value in stages I, II, and III with respect to global frame of reference.

Figures 4.18 and 4.19 illustrate the effective stress paths in three subspaces (σ'-S_1), (S_2-S_1) and (S_4-S_1) of the transformed variables (σ', S). S_4 is the component corresponding to simple shearing mode out-of-plane, and is needed for deviated wellbores i.e. $\omega \neq 0^0$ or 90^0. For vertical and horizontal wellbores, there are only two deviatoric stress

components (S_1, S_2). The yield surface of the MCC model presents a clear separation between elastoplastic and elastic strains where no shear induced pore pressures are produced. The stress paths at the crown show pure elastic behavior until the tangential stresses become major principal, and only then shear induced pore pressures are produced (in vertical and 30^0 deviated wellbores) and well defined yield points are generated as shown in Figure 4.18a. On the other hand, plastic strains and shear induced pore pressures are generated at the springline at the beginning of shearing as shown in Figure 4.19a.

The MIT-E3 model incorporates bounding surface plasticity in the formulation. Shear induced pore pressures and plastic strains are generated during shearing at both crown (Figure 4.18b) and springline points (Figure 4.19b). This leads to a higher decrease in the octahedral stresses in MIT-E3 results than in that of MCC at the crown point. The MIT-E3 predicts smaller S_2 and S_4 shear stress components than MCC at reference mud pressure ratio; however, MIT-E3 predicts larger S_1 components at springline.

4.4 Summary and Conclusions

Wellbore failure is defined by two different criteria: 1) the onset of localized failure due to local increase in inward deformations and high octahedral shear strains, and 2) large cavity deformations up to $0.1R_0$ at crown point. The MCC did not predict failure according to the first criterion and thus overestimates wellbore stability. MIT-E3 predicted local increase in inward deformations at the cavity wall of deviated wellbores where zones of localized high octahedral shear strains developed.

The MIT-E3 predicts the highest critical state mud pressure ratio for the horizontal wellbore. The reference mud pressure ratio value is chosen slightly higher than the highest critical state mud pressure ratio. Stability of horizontal wellbores is improved in overconsolidated clays. Critical mud pressures ratio decrease and stiffness increases with OCR values.

At reference mud pressure, wellbore deformations and magnitudes of excess pore pressures increase with deviation angle. At low consolidation pressures, MCC predicts larger deformations than MIT-E3. However, when models are adjusted to behavior at high consolidation pressures, MIT-E3 predict larger deformations and positive pore pressures around springline. In general, MCC predict larger magnitudes of positive excess pore pressures around springline and negative excess pore pressures at the crown which affects results of consolidation analyses.

Although effective stress paths computed by MIT-E3 and MCC are relatively similar, MIT-E3 is capable of predicting the onset of localized failure. The bounding surface plasticity and anisotropic yield surface and hardening laws enable the MIT-E3 model of a more realistic depiction of behavior around wellbores and accurate estimates of wellbore stability.

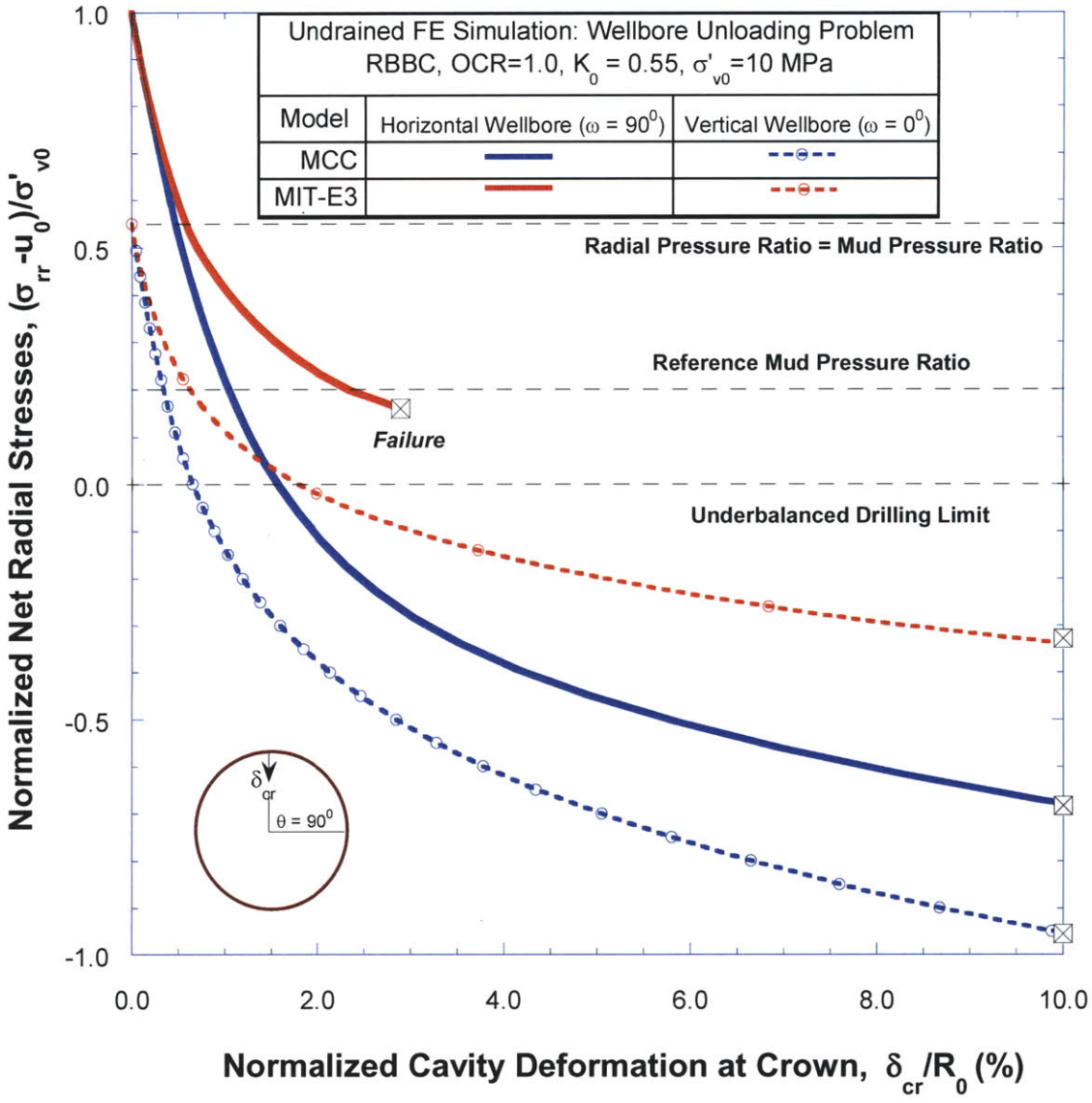

Figure 4.1 Relationship between total radial stresses and cavity deformations at Crown Point ($\theta=90^0$) for vertical and horizontal wellbores in K_0-normally consolidated RBBC using the MCC and MIT-E3 soil models (δ positive for inward deformations).

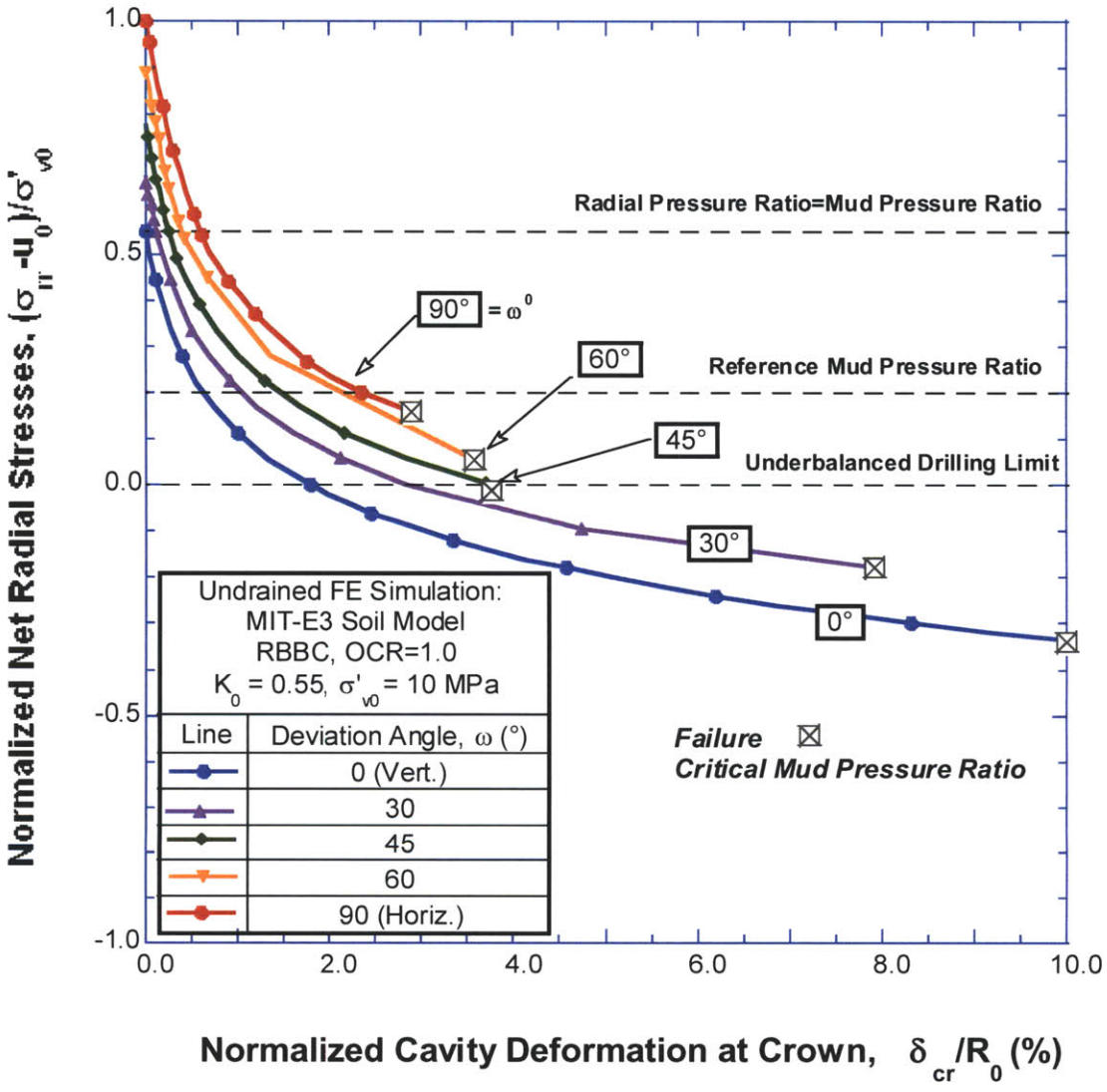

Figure 4.2 The relationship between radial stress at cavity wall and cavity deformations for vertical, inclined, and horizontal wellbores in K_0-normally consolidated RBBC using the MIT-E3 soil model.

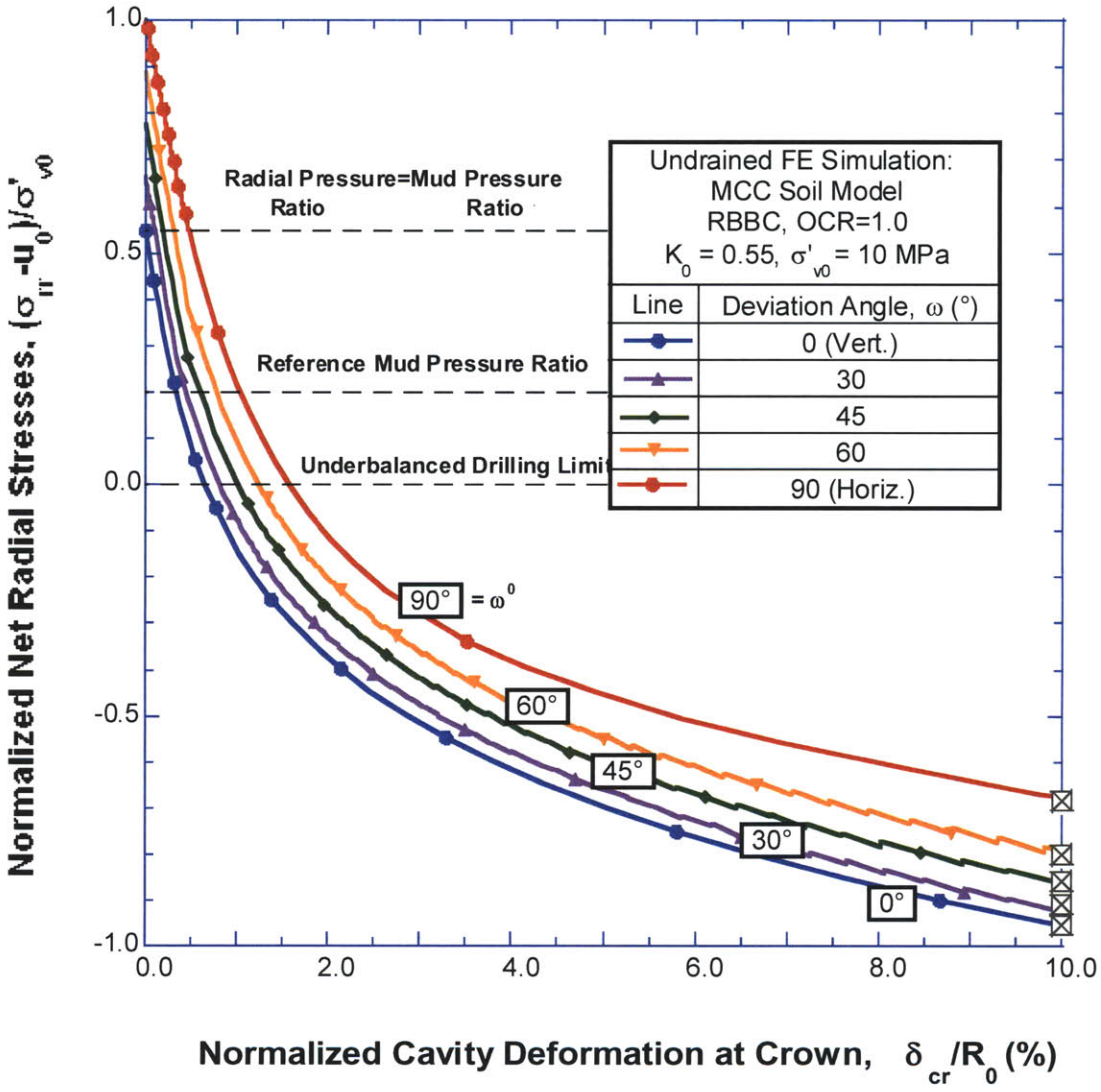

Figure 4.3 MCC predictions of the relationship between radial stress at cavity wall and cavity deformations for vertical, inclined, and horizontal wellbores in K_0-normally consolidated RBBC.

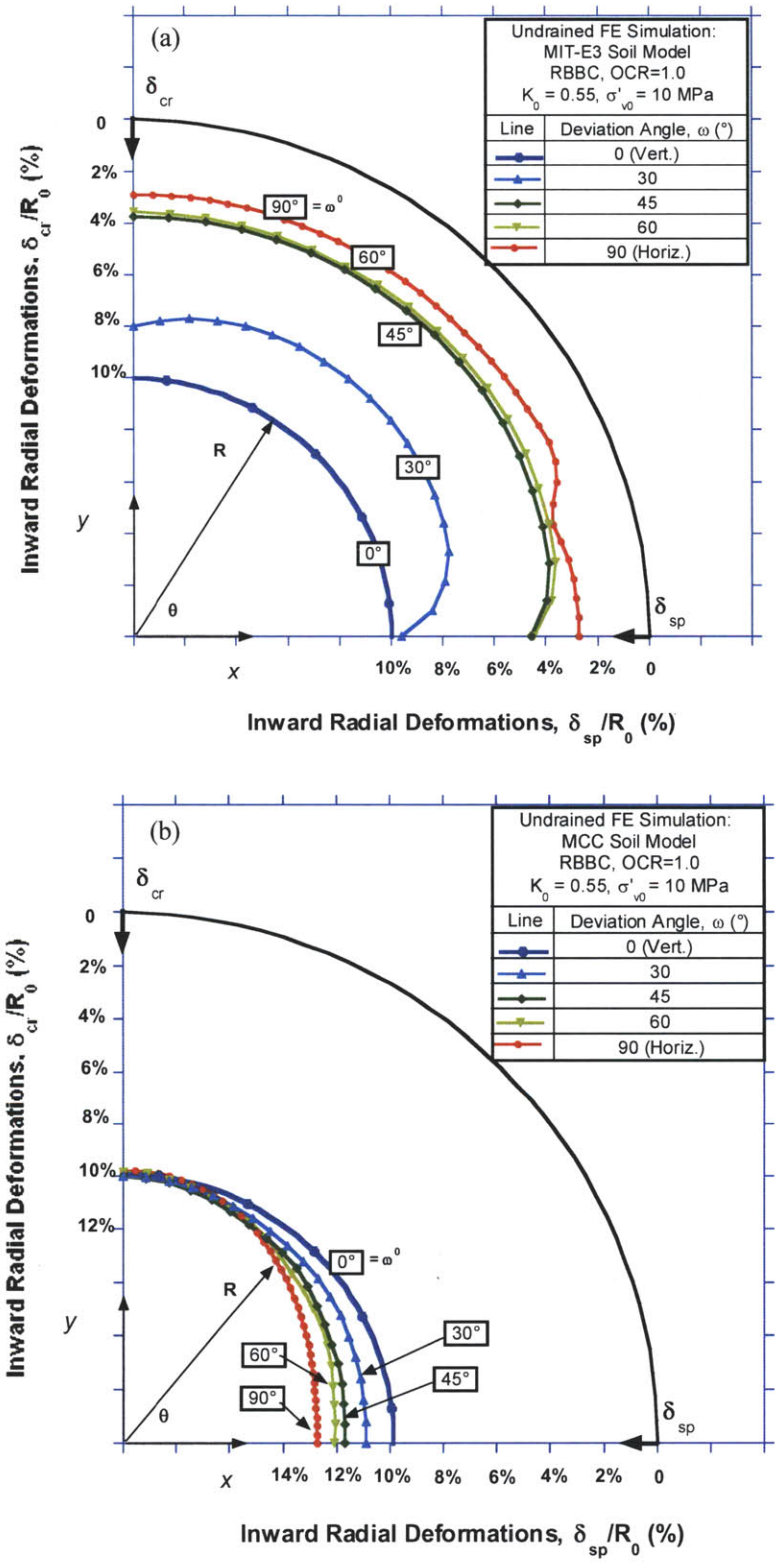

Figure 4.4 Radial deformations at critical mud pressures as predicted by (a) MIT-E3 and (b) MCC models at cavity wall for vertical and deviated wellbores. (Deformations are scaled 5:1)

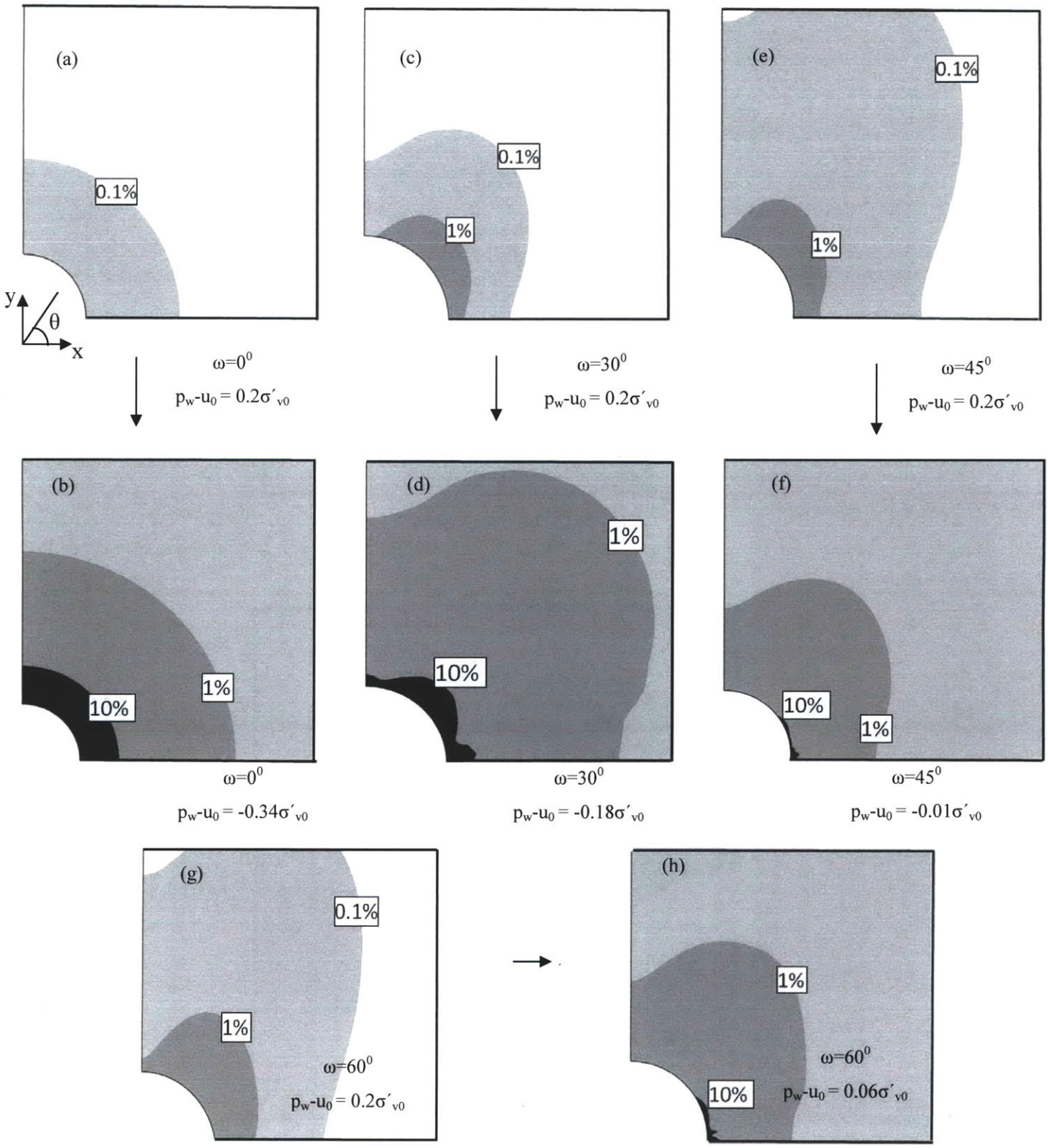

Figure 4.5 Octahedral shear strain contours computed by the MIT-E3 model for vertical and deviated wellbores at $\omega = 30^0, 45^0, 60^0$ and 90^0 at design mud pressures and critical mud pressures.

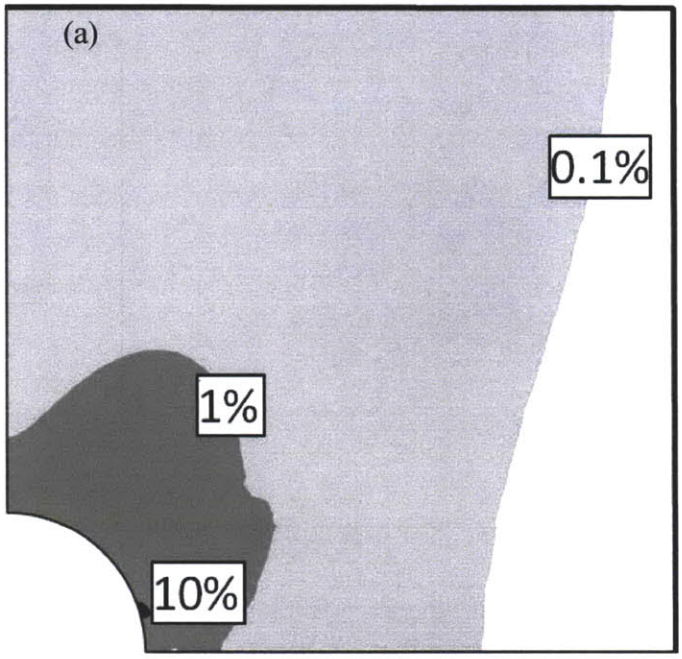

$p_w - u_0 = 0.20\ \sigma'_{v0}$

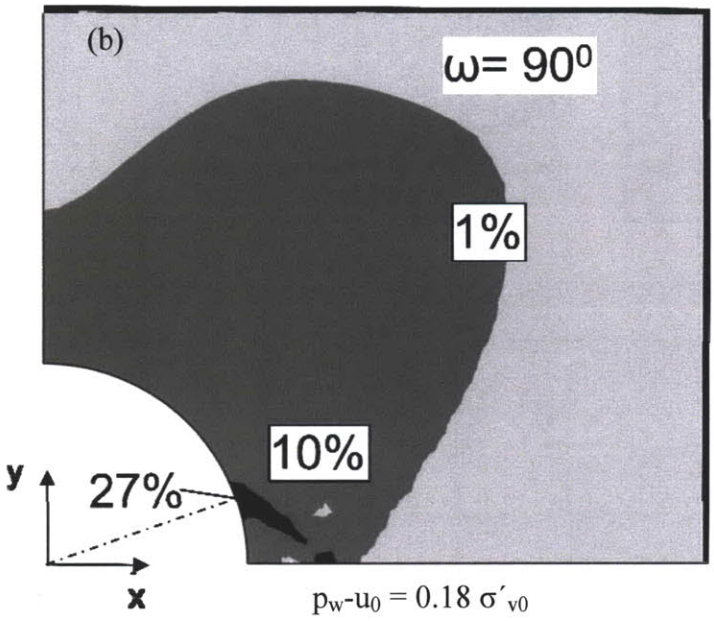

$p_w - u_0 = 0.18\ \sigma'_{v0}$

Figure 4.6 Octahedral shear strain contours computed by the MIT-E3 model for the horizontal at design mud pressures and critical mud pressures.

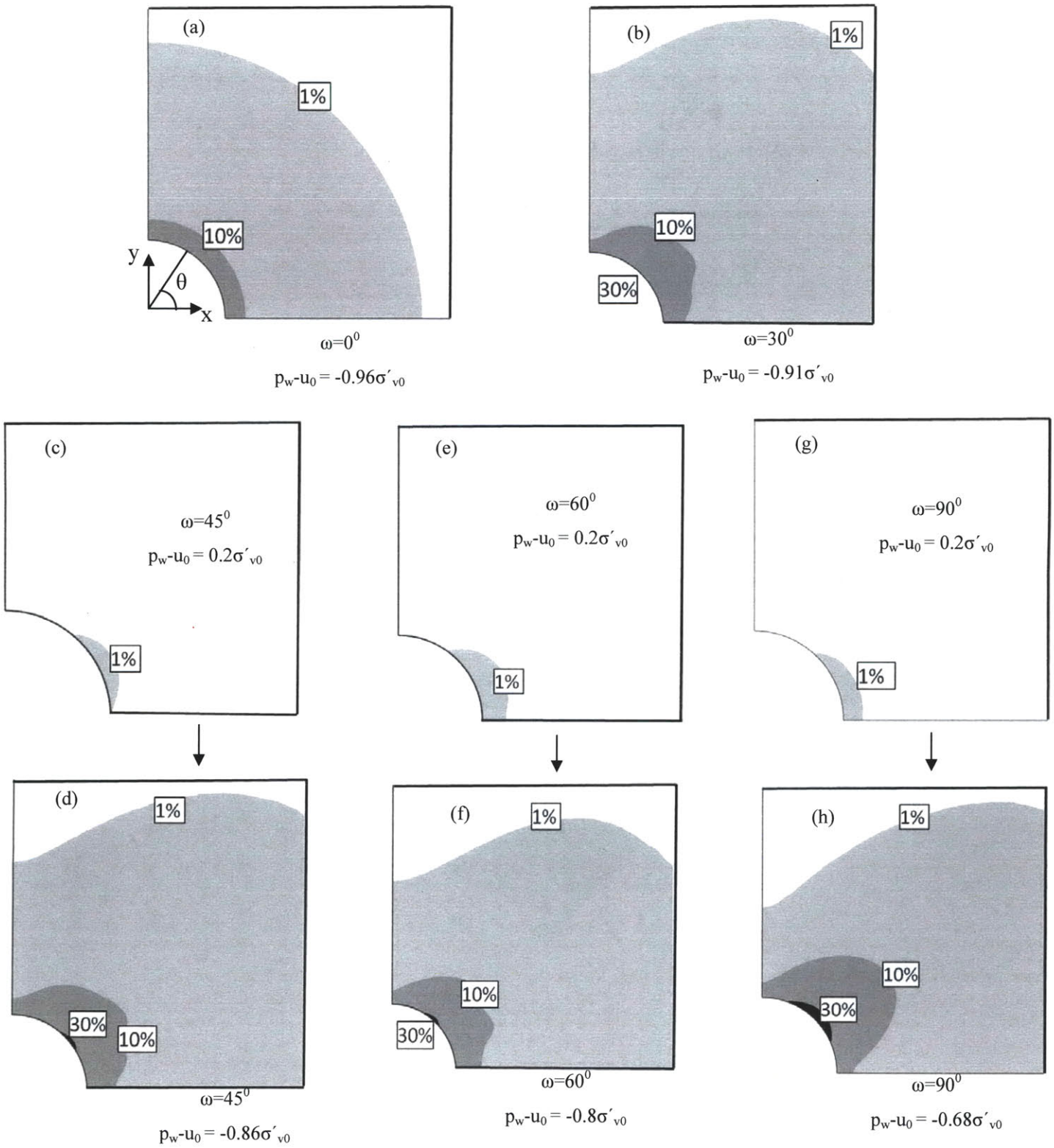

Figure 4.7 Octahedral shear strain contours computed by the MCC model for vertical and deviated wellbores at $\omega = 30^0$, 45^0, 60^0 and 90^0 at design mud pressures and critical mud pressures.

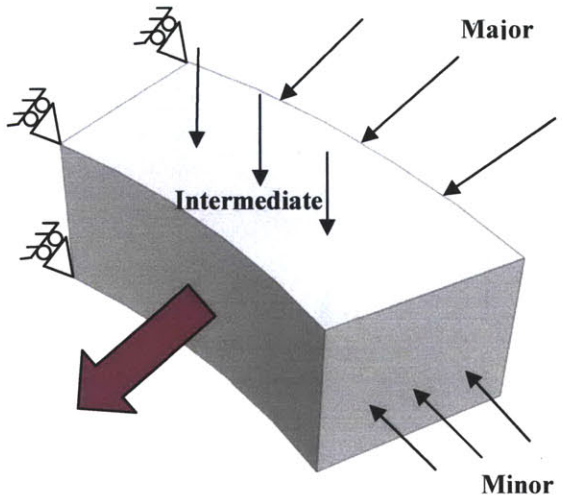

(a)

Stress State near Crown

"$45^0 \leq \theta \leq 90^0$"

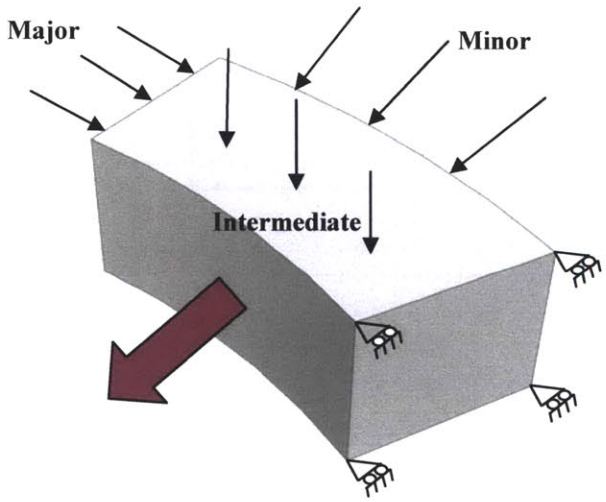

(b)

Stress State near Springline

"$0^0 \leq \theta \leq 45^0$"

Figure 4.8 Initial Stress States near Crown and Springline of a horizontal wellbore before drilling and unloading.

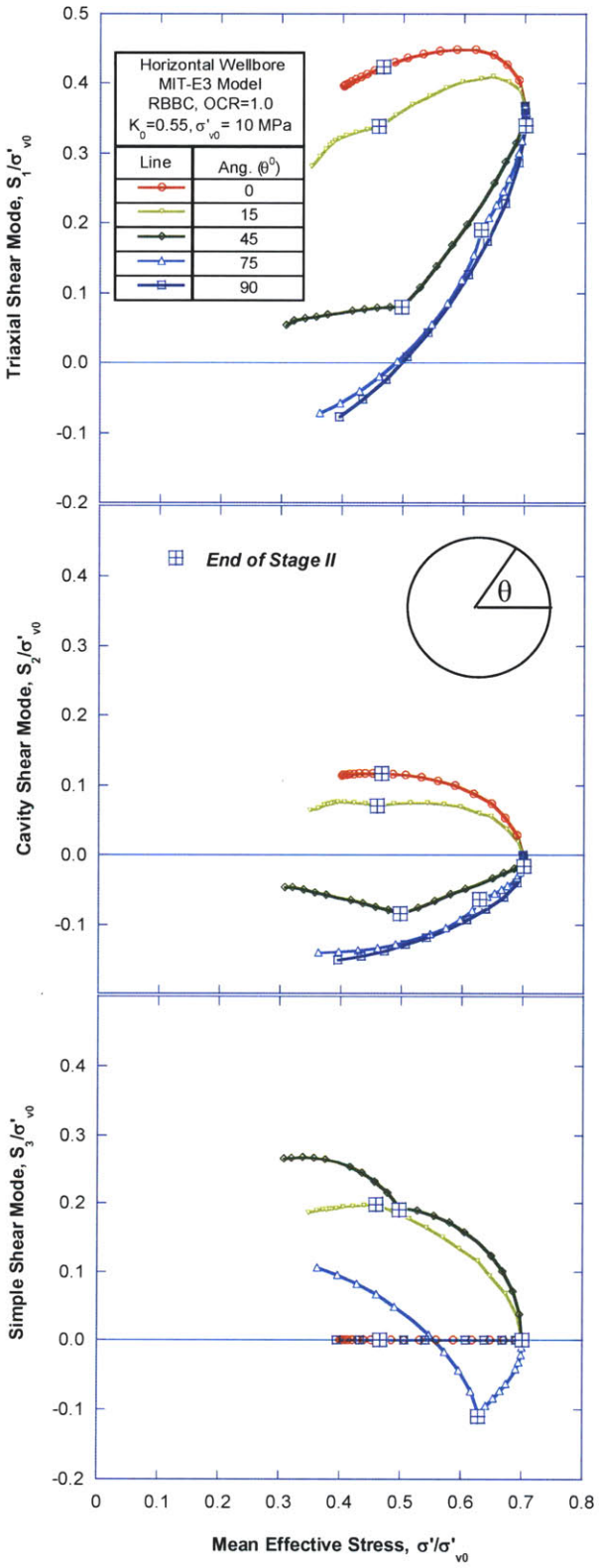

Figure 4.9 Effective stress paths at different points around a horizontal wellbore, using the MIT-E3 model.

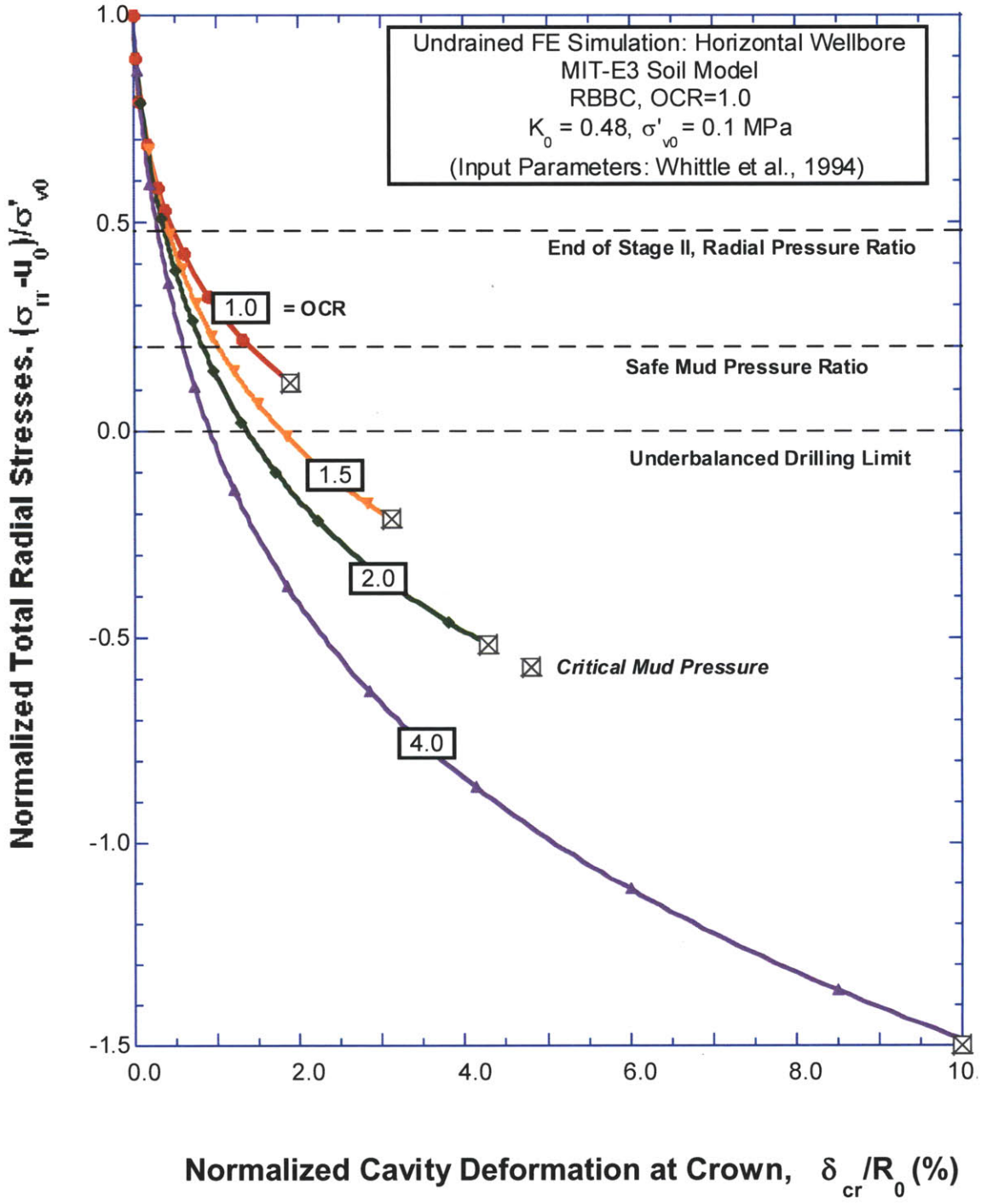

Figure 4.10 Effect of stress history on relationship between wellbore deformations and radial stresses at cavity wall of a horizontal wellbore in K_0-consolidated RBBC modeled by the MIT-E3 model.

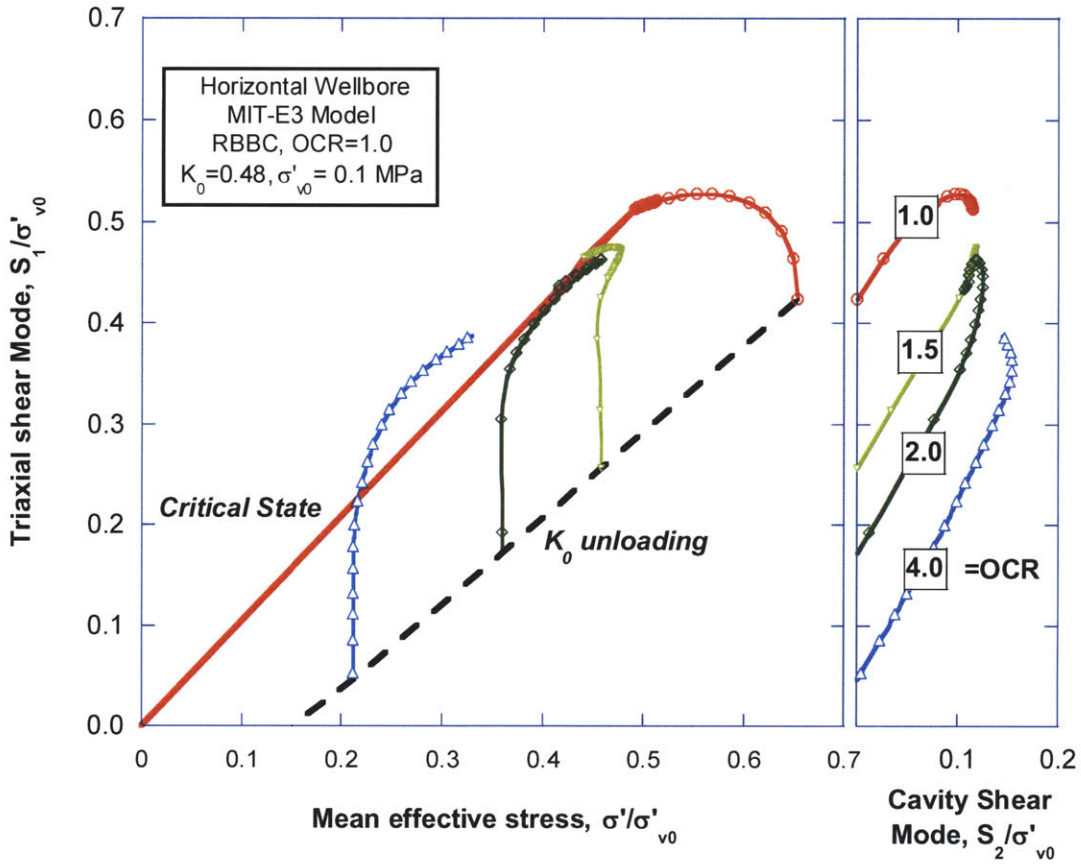

Figure 4.11 Effective stress paths at Springline of horizontal wellbore in K_0-consolidated RBBC at PCR = 1.0, 1.5, 2.0, and 4.0 predicted by the MIT-E3 model.

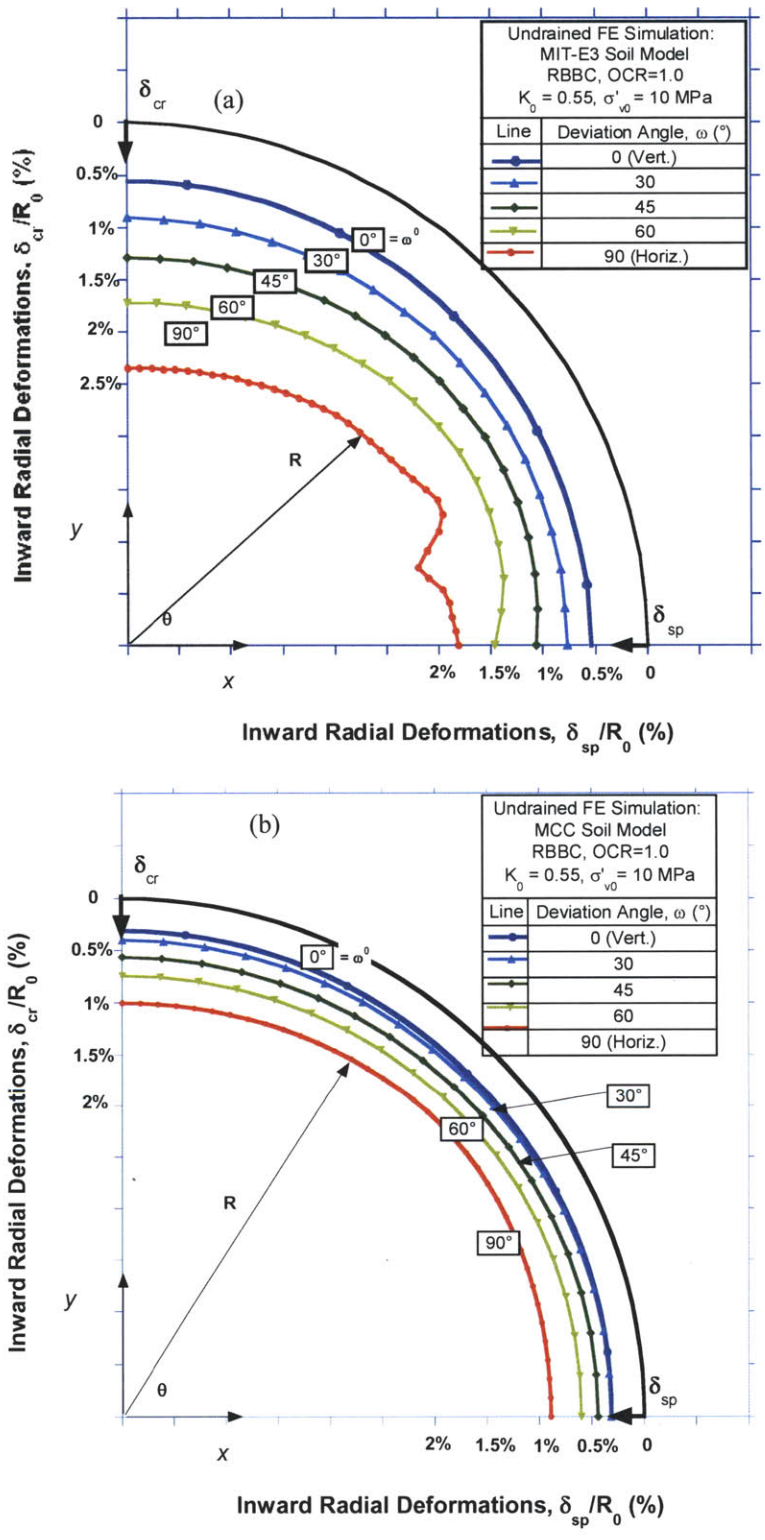

Figure 4.12 Radial deformations at design mud pressures as predicted by (a) MIT-E3 and (b) MCC models at cavity wall for vertical and deviated wellbores. (Deformations are scaled 20:1)

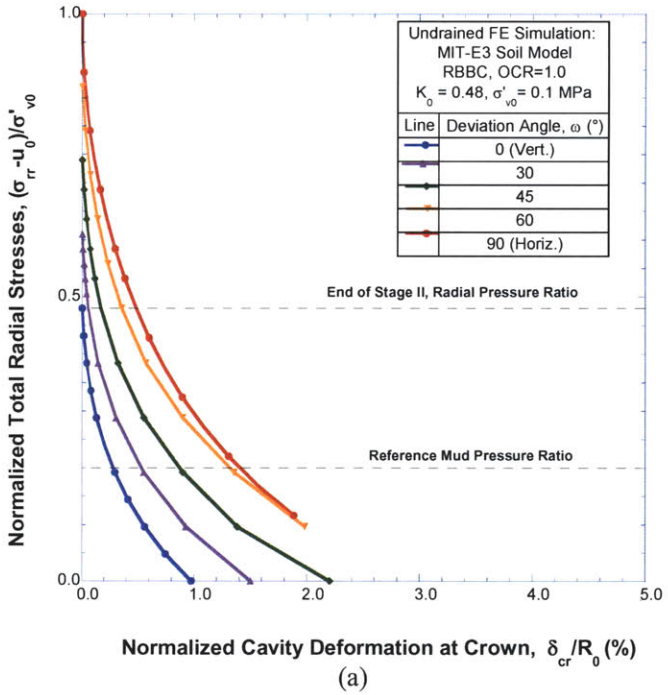

(a)

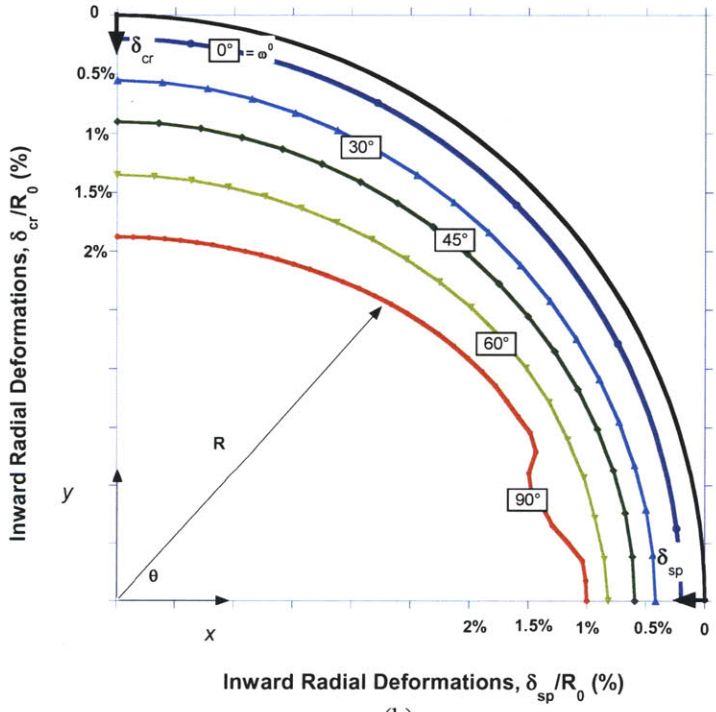

(b)

Figure 4.13 MIT-E3 predictions of (a) relationship between radial pressure and inward deformations at Crown Point and (b) radial deformations around cavity wall for vertical and deviated wellbores in K_0-consolidated RBBC under 0.1 MPa.

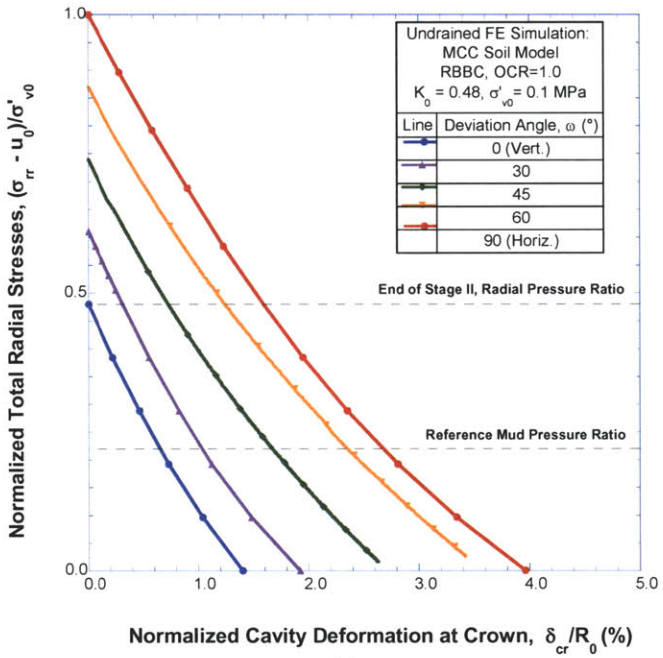

(a)

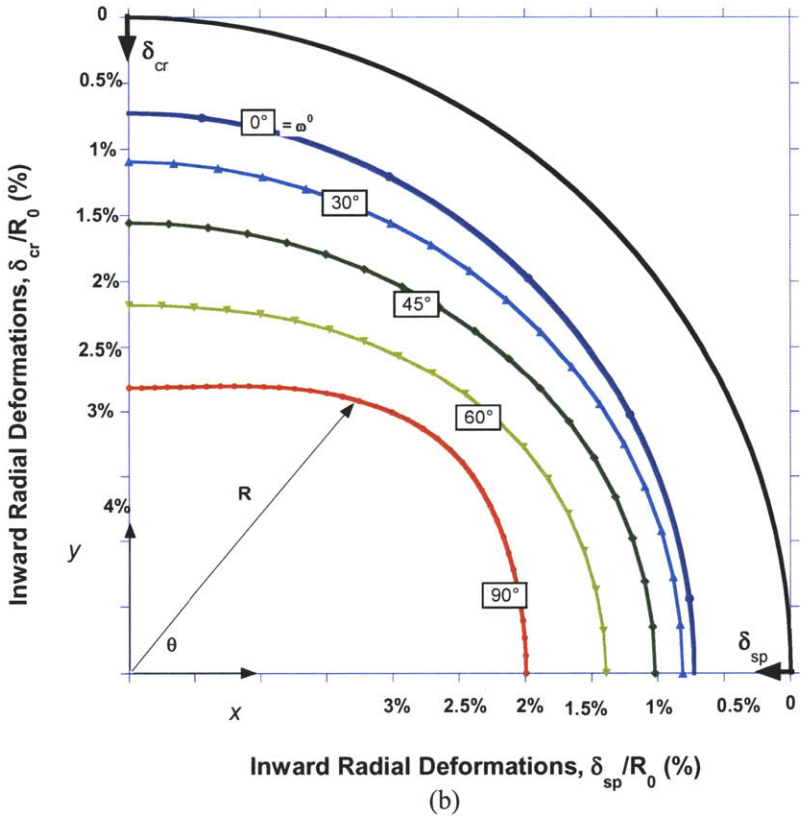

(b)

Figure 4.14 MCC predictions of (a) relationship between radial pressure and inward deformations at Crown Point and (b) radial deformations around cavity wall for vertical and deviated wellbores in K_0-consolidated RBBC under 0.1 MPa.

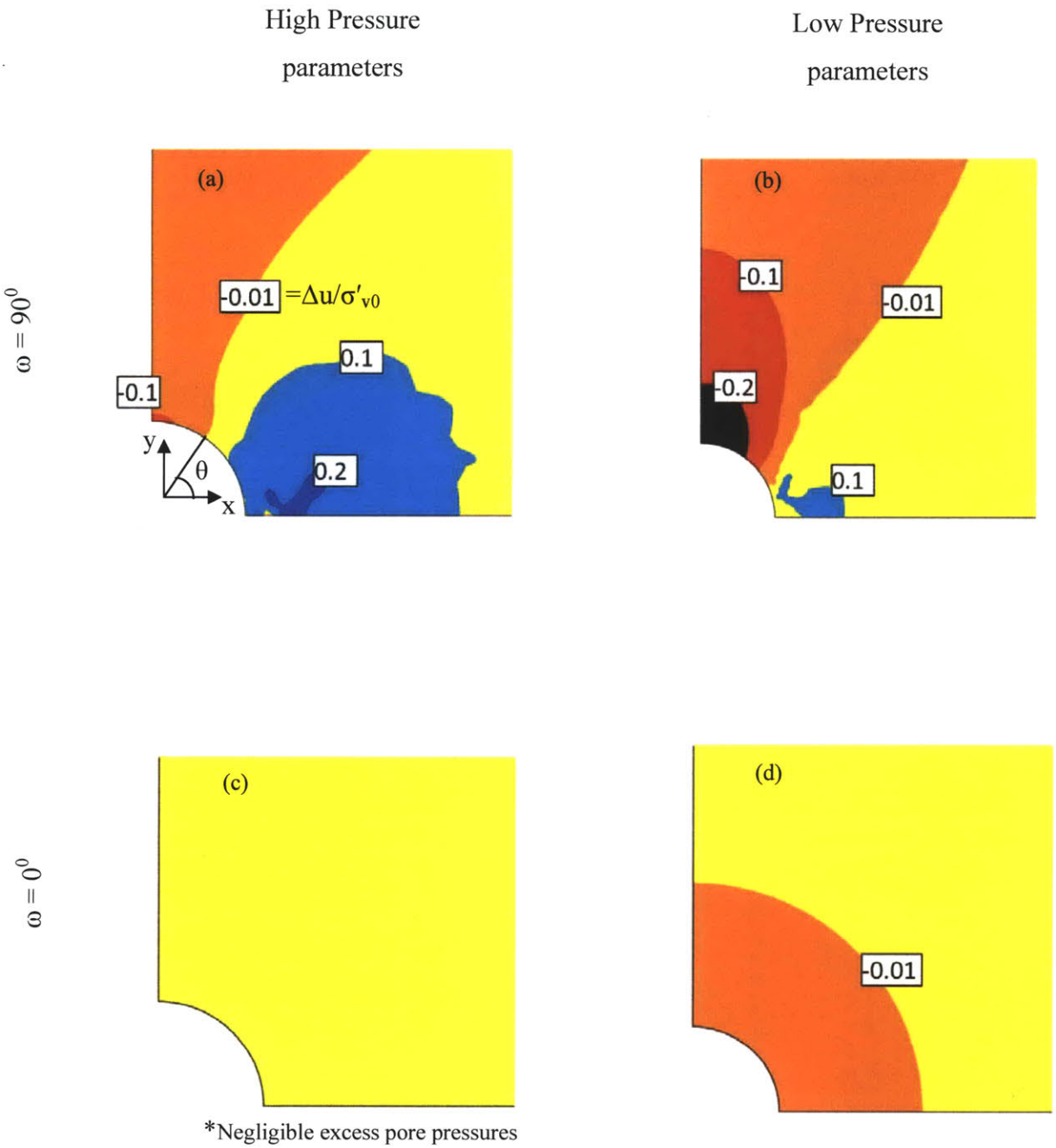

Figure 4.15 MIT-E3 predictions of normalized excess pore pressure distribution around vertical and horizontal wellbores at design mud pressures.

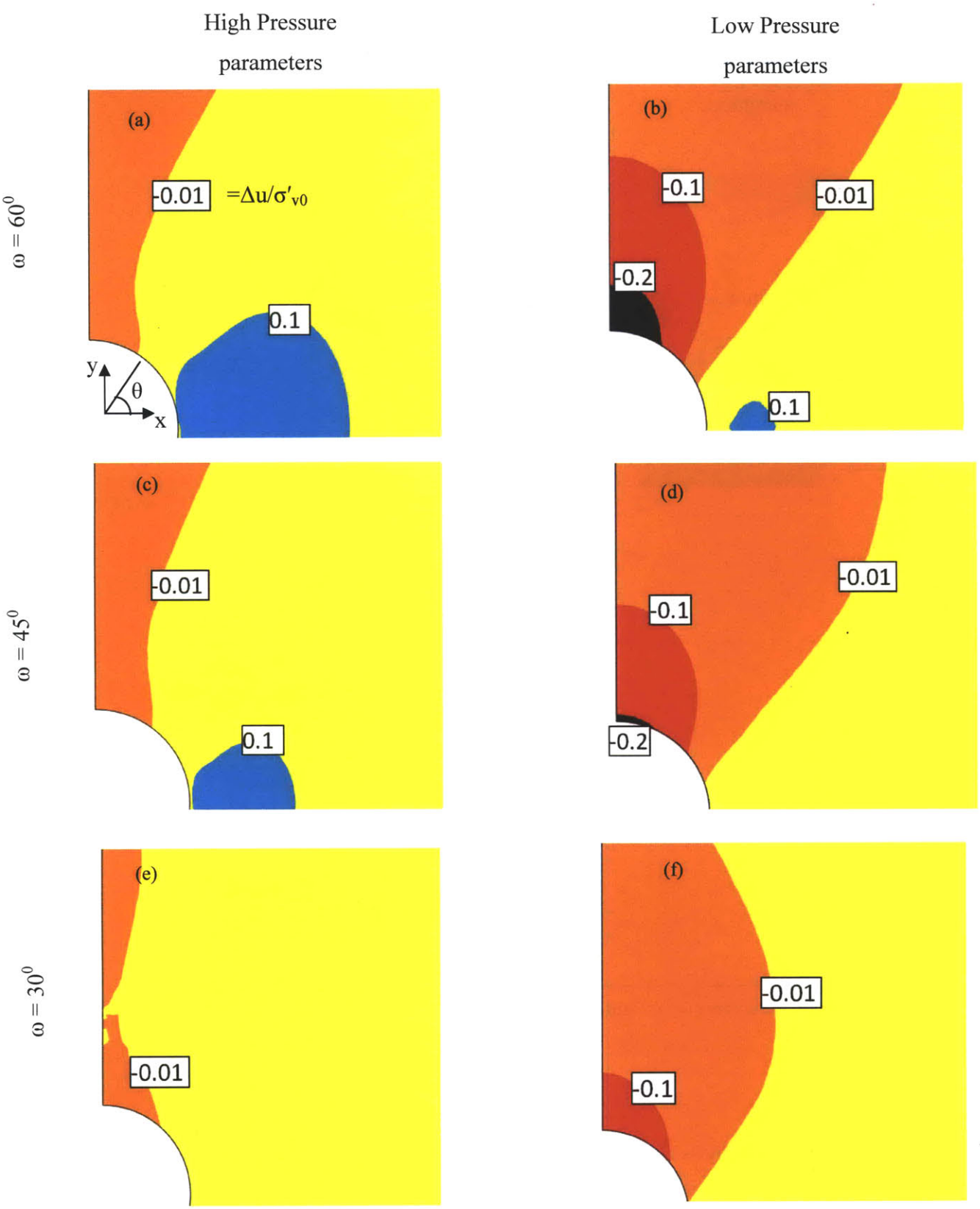

Figure 4.16 MIT-E3 predictions of normalized excess pore pressures around deviated wellbores at design mud pressure.

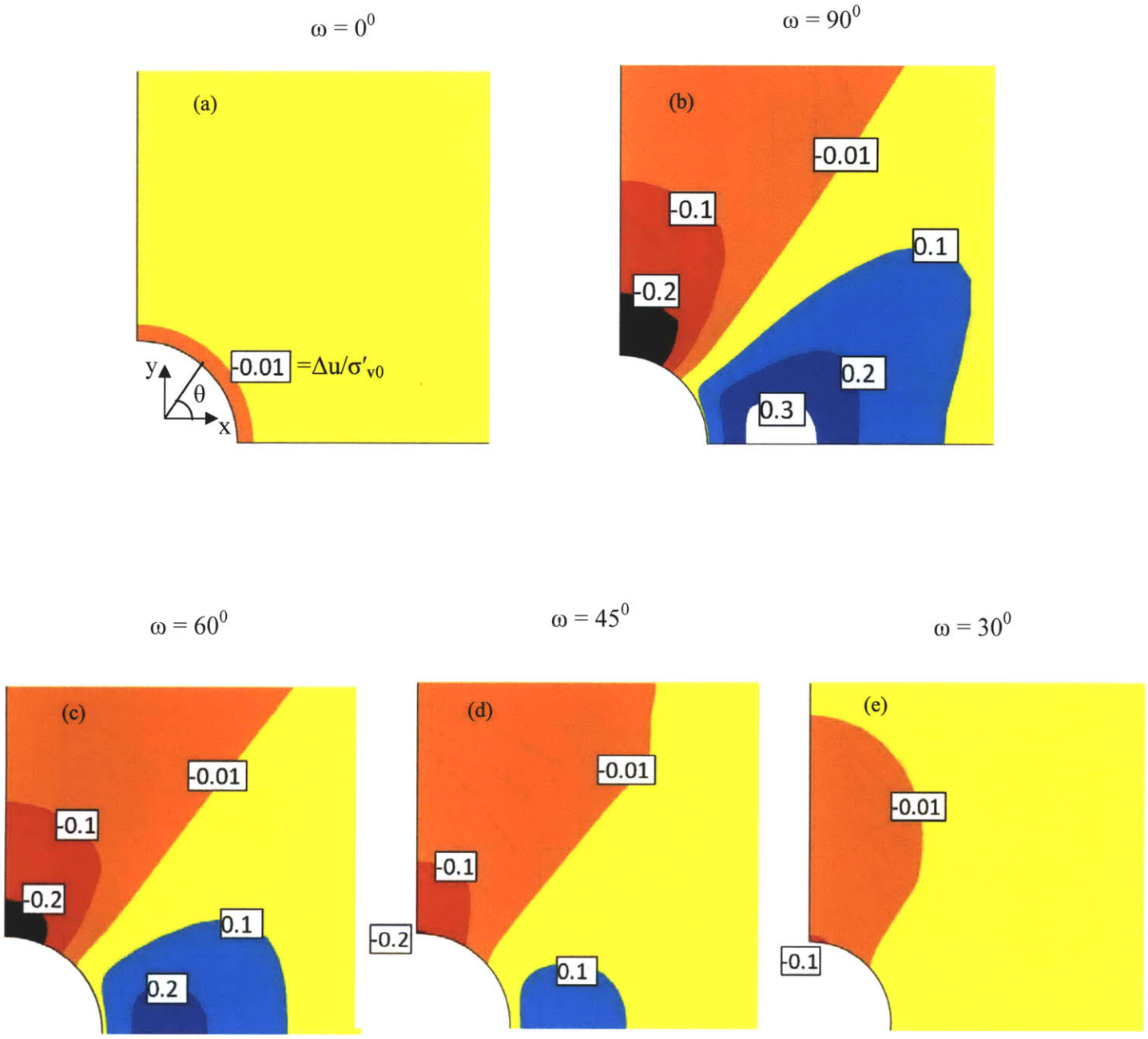

Figure 4.17 MCC predictions of normalized excess pore pressures around wellbores at design mud pressure.

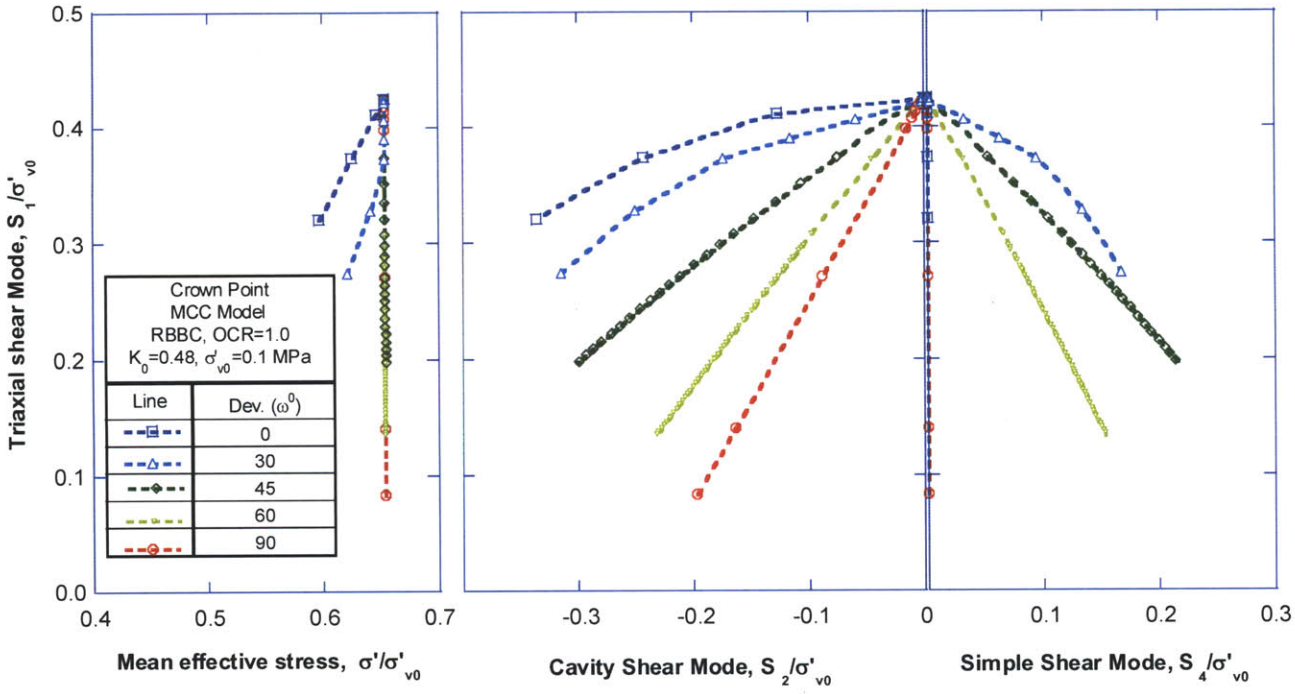

(a)

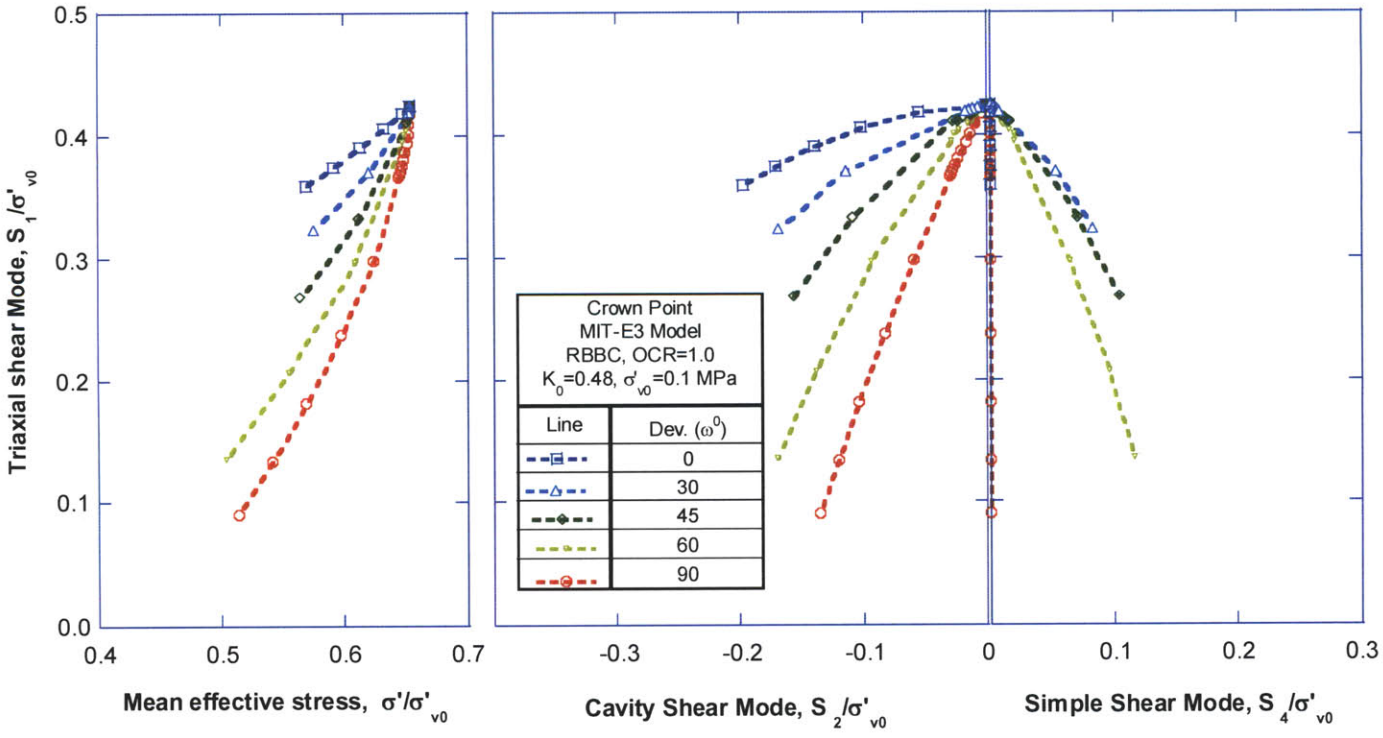

(b)

Figure 4.18 Predictions of effective stress paths at Crown Point using (a) MCC and (b) MIT-E3 soil models

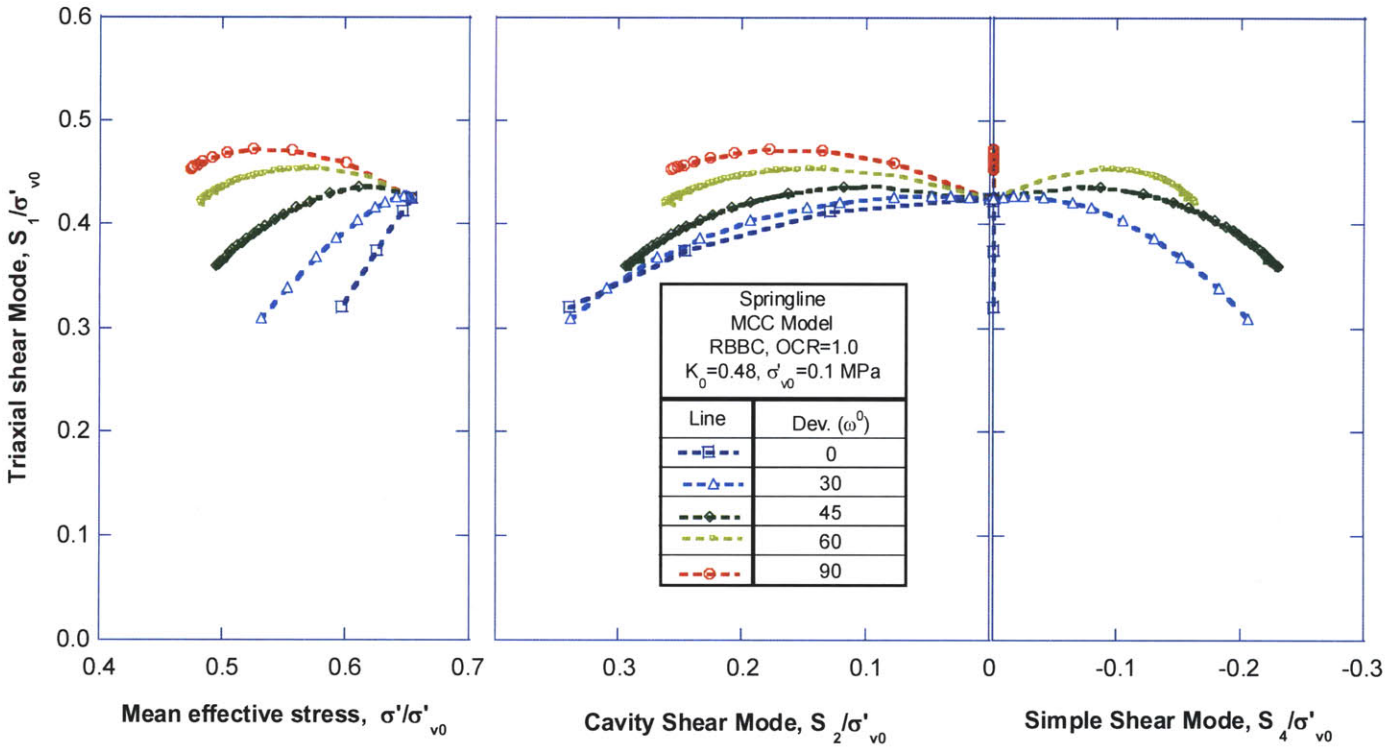

(a)

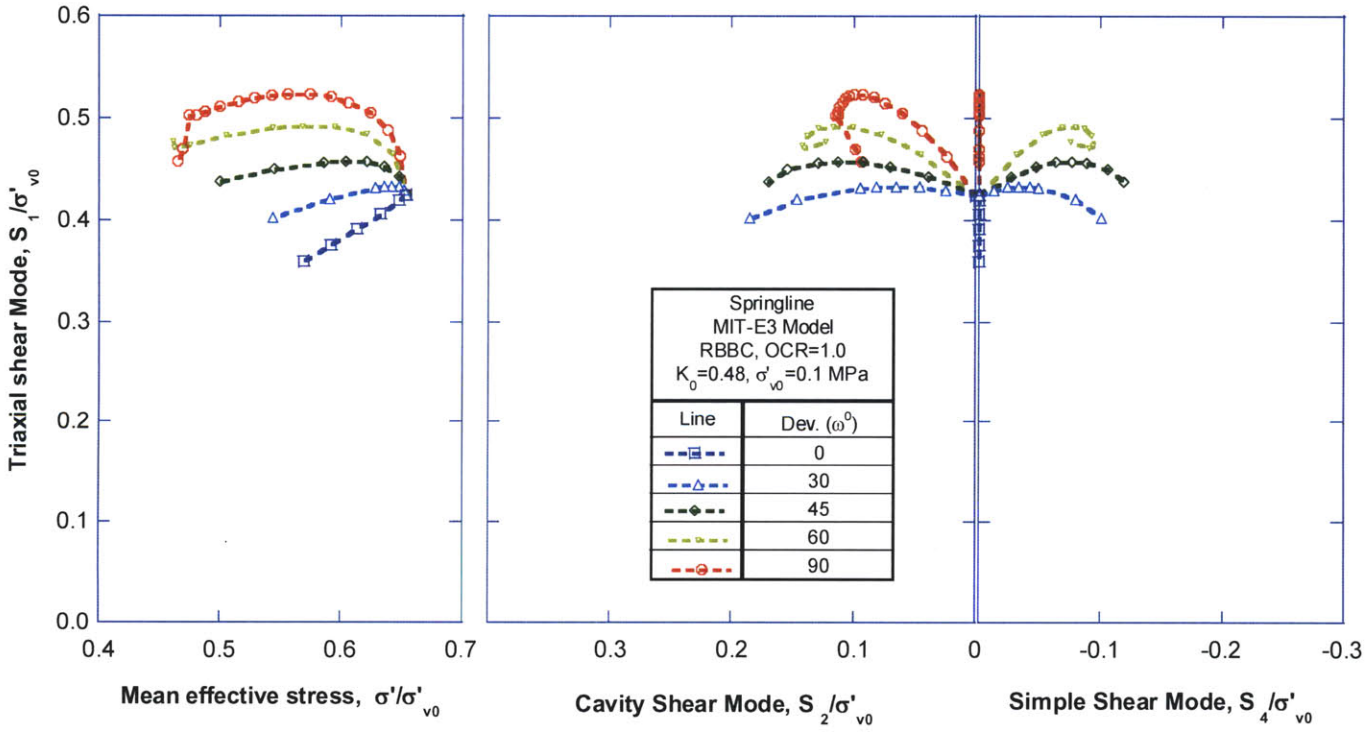

(b)

Figure 4.19 Predictions of effective stress paths at Springline using (a) MCC and (b) MIT-E3 soil models.

5 Simulation of Laboratory Model Borehole Tests

5.1 Introduction

This chapter describes the use of MCC and MIT-E3 soil models to predict and interpret model borehole tests in a Thick-Walled Cylinder (TWC) apparatus. The recent PhD thesis by Abdulhadi (2009) includes an extensive program of high pressure triaxial tests and model borehole tests in two custom-built TWC devices to test small and large specimens. The analog testing material is RBBC as discussed in Chapter 3. Abdulhadi (2009) used interpretation methods usually associated with pressuremeter tests and cavity expansion in thick-walled apparatus.

The TWC numerical model accurately depicts the boundary conditions and testing procedures in the lab. The analyses provide a complete set of data that helps to understand the soil behavior in a TWC experiment. Comparing computed and measured TWC results validates the predictions of the soil models and assesses the reliability of further analysis. In turn, comparing computed shear stress-strain behavior with that interpreted from the lab is useful to investigate the approximation of the interpretation methods.

The chapter is divided into 4 main sections. Section 5.2 describes designs of TWC devices and test procedures used to emulate stress changes around a vertical wellbore. The section also describes the finite element models used to simulate the TWC tests. Particular attention is focused on the boundary conditions needed to describe high stress gradients in these tests.

Section 5.3 compares finite element predictions with measurements from the TWC model borehole tests. The analyses include simulations with both the MCC and MIT-E3 effective stress models calibrated in low and high regions of confining stresses. The main focus is on simulations of the cavity pressure-volume relations. Section 5.4 discusses the different methods used to interpret results of the TWC experiments. The finite element model provides detailed results that help to understand stress and strain distributions around the model borehole. The analysis also provides a basis for understanding approximate interpretation methods that were evaluated by Abdulhadi (2009).

Section 5.5 considers the effects of two variables that affect the TWC results: 1) the rate of cavity pressure change; and 2) the radial dimension of the TWC specimen. More details of the large TWC simulation are provided in the form of strain distribution contours to help understand the influence of specimen size on the experiment.

5.2 Thick Walled Hollow Cylinder (TWC) Simulations

5.2.1 Description of the device

Two TWC devices were fabricated in the MIT geotechnical labs (Abdulhadi, 2009). The smaller TWC device has outer diameter D_o=7.6 cm, inner diameter D_i = 2.5cm and height, H=15 cm. These dimensions provide aspect ratios that are consistent with recommendations from prior experience using TWC tests on lithified rock (e.g. Santarelli and Brown, 1989) to eliminate boundary effects and provide a reasonable representation of the stress field around the wellbore. The large TWC model has the same boundary conditions and geometric aspect ratio with outer diameter D_o = 15.2 cm, and height, H=22.8 cm, leading to a diametric ratio of D_o/D_i = 6. Results from the large TWC illustrate the effect of sample size and are discussed in Section 5.5.2.

The design enables independent control of the axial load, cavity, cell and back pressure. The cell pressure is applied within a steel chamber that can operate at pressures up to

20MPa. The steel cell, which mates to the base, encloses a pedestal, floating top cap, top and bottom annular platens, annular porous stones, and a hollow-cylindrical test specimen sealed with internal and external custom-made latex membranes. Figure 5.1 shows a schematic of the TWC device.

The small TWC is axially loaded through the use of a 2 Ton capacity bench-top screw driven loading frame. Custom-designed pressure-volume controllers (Sheahan and Germaine, 1992) are used to regulate the pressure and measure the volume change within the external cell, internal cavity and pore water flux from the test specimen. The cell, cavity, and pore pressures are measured by pressure transducers. The system also measures the axial load and displacement using an external load cell and displacement transducer. A closed-loop automated control is carried out using a PC and a control program which is able to perform all phases of the TWC test.

All tests are performed on BBC reconstituted in the lab according to a carefully developed set of procedures (Abdulhadi, 2009). The central core of the soil specimen is formed by drilling using a succession of four metal drill bits with increasing sizes to minimize disturbances of the inner surface of the specimen. Each soil specimen is anisotropically-consolidated under stress control to a pre-defined target value, $K_0 = 0.55$ to the required vertical effective stress and is then left for a 24 hours at constant effective stress to allow for secondary compression.

The model borehole test involves a procedure of reducing the internal cavity pressure, while keeping the external cell pressure and axial stress constant. Wellbore closure is performed by drawing out cavity fluid using the pressure-volume controller at an average cavity volume strain rate of 10%/hour. The tests are terminated at 20% cavity volume strain. The drainage valves are closed to maintain constant volume conditions during cavity contraction while measuring pore pressures inside the specimen at the bottom pedestal.

5.2.2 Two-dimensional finite element model

The TWC device (Figure 5.1) is represented by a 2D axisymmetric finite element model. The model comprises three basic component parts; the soil test specimen, top cap, and bottom pedestal. The interaction between the device and the specimen dictates the boundary conditions of the model shown in Figure 5.2a. The top and bottom steel caps are not lubricated and thus, represented by solid parts continuously connected to the specimen. The caps are assumed to be elastic with very high modulus (effectively rigid material). The axial stress is applied on the surface of the top cap and thus the vertical stresses at the top of the specimen are redistributed. The pressure exerted by the top cap on the specimen is not uniform due to the large difference in rigidity.

The soil specimen is enclosed within impermeable membranes that prevent migration of pore water into the chamber. These membranes are represented by zero fluid flux boundaries but their mechanical properties are not included in the simulations[1]. The outer surface of the soil cylinder is connected hydraulically to the base and top cap of the specimen through filter paper strips. These strips act as drains that redistribute pore pressures around the boundary of the test specimen. This condition is simulated using a multi-point constraint (MPC) on the top, outer side, and bottom edges. The constraint dictates a uniform pore pressure over these edges. Since the permeability of filter paper is a much greater than that of the specimen; the model assumes instantaneous pore pressure uniformity along these edges. The filter paper is primarily intended to accelerate consolidation within the soil specimen.

The design of the TWC device allows pore water pressures to redistribute within the test specimen as cavity pressure changes within the model borehole. The test is assumed to be pressure controlled such that the soil specimen responds only to the change in cavity pressure. The finite element model simulates deformations around the cavity during this process, while TWC experiments measure the changes in cavity volume (from which an average radial deformation is inferred). Three different rates are used to control the

[1] Corrections for membrane stiffness are used to interpret the TWC test data.

change of the cavity pressure as shown in Figure 5.2b. These rates are constructed to replicate the procedures used in the experiments performed by Abdulhadi (2009).

The finite element representation for small and large TWC devices is carried out using Abaqus^{TM} as shown in Figure 5.3. The small TWC mesh uses 356 axisymmetric triangular elements and 1143 nodes, while the large TWC mesh 1708 similar elements and 5267 nodes. The elements are mixed type with 6 displacement and 3 pore pressure degrees of freedom as shown in Figure 5.3a. These elements use isoparametric quadratic expansion of the displacement field and bi-linear expansion of the pore pressure field as discussed in Chapter 3.

5.3 Comparison with TWC data

5.3.1 Cavity Volume Measurements

Figure 5.4 shows the net internal pressure inside the cavity normalized with respect to external cell cavity pressure $(p_i-u_0)/p_0$, where p_0 is the cell pressure that corresponds to the initial radial effective stress in the sample, σ'_{r0}, versus cavity volumetric strain $(\Delta V/V_0)$ from experiments using K_0-normally consolidated RBBC at vertical effective stresses, σ'_v = 0.15-10 MPa (Abdulhadi, 2009). The results show the non-linear relation between the volume strain and the cavity pressure. The bulk of the pressure drop occurs within volume strains $\Delta V/V_0$<5% volume strain before the borehole becomes unstable. Instability (deforms without further reduction in cavity pressure) occurs when net pressure ratio, $(p_i - u_0)/p_0$ = 0.25~0.35 at volume strain in the range $\Delta V/V_0$ = 8~12%, then exhibits a very slight increase with continued volume strain through the end of the test. This latter behavior might imply that the specified volume extraction rate is smaller than the specimen deformation rate. Before reaching a yield point, the specimens exhibit an initial linear cavity stiffness (up to ϵ_{cav} = 0.4%).

The effect of stress level is evident especially at small strains. The figure shows that at the same net pressure ratio, there are larger volume strains for tests at higher consolidation pressures. The initial stiffness ratio also decreases as stress level increases. There is a significant change in failure net pressure ratio from low consolidation pressure (σ'_{v0} = 0.15 MPa) to high consolidation pressure (σ'_{v0} > 2MPa). The figure shows that at high consolidation pressures, higher pressure in the cavity is needed to maintain stability in the specimen.

5.3.2 Numerical Solutions

Figure 5.5 shows the results from TWC simulations using the MIT-E3 and MCC soil models on a log scale. The input parameters are calibrated for Resedimented Boston Blue Clay (RBBC) at low consolidation pressures (Whittle et. al., 1994; σ'_{vc} <0.4 MPa) and high consolidation pressures (Chapter 3, σ'_{vc} up to 10 MPa). At low consolidation pressures, the MCC model predicts much larger cavity volume strains than MIT-E3 during the initial phase of cavity depressuring. When model parameters are adjusted for RBBC behavior at high consolidation pressure MCC shows a reduction in the amount of cavity volume strains while MIT-E3 shows the opposite trend. The small strain stiffness ratio decreases with σ'_{vc}, hence, trends for MIT-E3 are consistent with expected response in the TWC simulation.

The MCC simulations predict yielding behavior at cavity volume strains in the range $\Delta V/V_0$ = 0.1~0.5%, followed by large decrements in cavity pressures up to cavity volume changes $\approx$ 3%. The MCC does not capture failure in TWC specimen throughout the simulation following the standard cavity pressure-time profile shown in Figure 5.2b, and does not predict any increase in cavity volume strains. The MIT-E3 model predicts yield at much lower cavity strains. Failure is predicted at cavity pressure ratios $(p_i-u_0)/p_0$ = 0.22 and 0.35 for low and high confining pressure calibrations, respectively. The failure is characterized by increased cavity volume strains with no further decrement in cavity pressure, p_i. At high stress level, higher cavity pressure is needed to maintain stability in the numerical simulation, which is consistent with lab observations. However, the

analyses are terminated when large deformations and high octahedral shear strains develop in the model. This failure occurs instantaneously in the analysis and hence, the rate of cavity volume change observed in the lab is not fully captured in the FE simulations.

5.3.3 Comparison of predictions and measurements

Figure 5.6 compares the model borehole results with numerical simulation results (Figures 5.4 and 5.5). The numerical simulation using the MIT-E3 captures the initial pressure-volume response measured in the lab at low consolidation stresses, while the MCC model generally overestimates cavity volume change. Both soil models capture the normalized stiffness initially exhibited by the specimens consolidated under high stress levels using the calibrated set of input parameters.

As the cavity volume strains increases with continuous decrease in cavity pressure, the numerical simulations tend to over-estimate the change in net pressure ratio. This may be attributed to the effect of the finite rate of drawing the cavity fluid in the apparatus that is lower than the rate of by which the specimen fails. The response of the specimen in the TWC device is inevitably affected by the rate of fluid withdrawal from the cavity.

The MIT-E3 model predicts failure in the TWC specimen consolidated at σ'_{vc} = 0.15 MPa (low pressure) at $(p_i - u_0)/p_0$ = 0.22 and is in close agreement with TWC measurements. At high consolidation pressure, failure predicted by MIT-E3 is representative of net pressure ratios at failure observed in specimens consolidated under σ'_{vc} = 2, 4, 6, 8, and 10 MPa. These comparisons are true predictions of the model's responses in this mode of unloading. The MIT-E3 is independently calibrated and the input parameters are not adjusted to improve this comparison. These results validate the predictions of the MIT-E3 soil model and prove it to be reliable and realistic.

5.4 Interpretation of Simulation Results

5.4.1 Plane Strain Interpretation

To interpret the results from a TWC lab experiment, Abdulhadi (2009) used methods that were introduced for interpreting in-situ pressuremeter tests. These interpretation methods are based on assumptions of axial symmetry, plane-strain conditions, soil homogeneity, isotropy, and undrained conditions. It should be noted that cavity expansion and cavity contraction generate similar shear strain distributions, provided that all deformations are plane strain and that no volume strains occur at any point (undrained conditions), thus, the methods used to interpret cavity expansion in a model pressuremeter can be used to represent the TWC contracting cavity.

Baguelin et al. (1972), Palmer (1972), and Ladanyi (1972) proposed analytical techniques for deriving the elemental stress-strain-strength properties of the soil from pressuremeter measurements, where no prior knowledge is required for the constitutive properties of the soil. However, their analyses were limited to the case of expansion (or contraction) of a cylindrical cavity in an infinite medium. Silvestri (1998) modified these solutions to account for finite boundary conditions in a thick-walled cylinder test (such as the TWC device).

Figure 5.7 compares the elemental shear stress-strain behavior of RBBC derived from TWC according to the analytical method of Palmer (1972) and Silvestri (1998). Palmer (1972) relates the change in cavity volume to the natural strains in an infinite soil as follows:

$$\epsilon_r = -\epsilon_\theta = -\frac{1}{2}\ln\left\{1 - \frac{\Delta V}{V}\left(\frac{R}{r}\right)^2\right\} \qquad (5.1)$$

where ϵ_r and ϵ_θ are the radial and circumferential strain respectively, ΔV is the change in the volume of the cavity, V is the current volume of the cavity, R is the current radius of

the pressuremeter cavity, and r is the radial coordinate. Palmer (1972) extended the analysis to obtain an expression for the maximum shear stress in the horizontal plane in terms of the current cavity stress and the current cavity strain:

$$q_h = \frac{\sigma_{\theta\theta} - \sigma_{rr}}{2} = \frac{dp}{d\left(\ln\frac{\Delta V}{V}\right)} \tag{5.2}$$

where p is the cavity pressure.

Silvestri (1998) accounts directly for the finite radius of the thick-walled cylinder. The shear strains at the inner and outer walls of the thick walled cylinder are:

$$\gamma_a = \ln\left(\frac{a'}{a}\right)^2 \tag{5.3}$$

$$\gamma_b = \ln\left\{1 - \left(\frac{a}{b}\right)^2 + \left(\frac{a}{b}\right)^2\left(\frac{a'}{a}\right)^2\right\} \tag{5.4}$$

where γ_a and γ_b are the shear strains at the inner and the outer wall respectively, a and b are the inner and outer radii of the model pressuremeter, and a′ is the inner radius after cavity expansion/contraction takes place. The shear stresses at the inner and outer walls can then be related as follows:

$$q_h|_a = \chi(\chi - 1)\frac{dp}{d\chi} + \frac{\chi}{1 - \beta + \beta\chi} q_h|_b \tag{5.5}$$

where $\chi = \left(\frac{a'}{a}\right)^2$ and $\beta = \left(\frac{a}{b}\right)^2$.

The derivation of the stress strain curve is an iterative procedure because q_h at outer wall is not known at the beginning of the test. The iterations converge when a unique stress-strain curve is obtained at both inner and outer walls. Numerical differentiation is very sensitive to noise in the measured data. Abdulhadi (2009) used a five-point moving window to smooth out lab results. However, the initial portion of the curves is not well-defined and hence, the initial stiffness interpreted by this method is less reliable than values of the maximum shear stress deduced from the analysis.

Figure 5.7 show that the two interpretation methods imply completely different elemental behavior. The infinite disk solutions of Palmer (1972) lead to an interpreted undrained strength ratio, s_u/σ'_{vc} (USR) = 0.1 at γ= 1%, and significant post peak strain softening. The more complete analysis of Silvestri (1998) (with boundaries corresponding to the TWC geometry) generates s_u/σ'_{vc} =0.22 at γ = 2.5% and minimal post-peak change in shear resistance. The Silvestri (1998) interpretation produces a backfigured USR that is 11% higher than the USR of normally consolidated RBBC measured in undrained direct simple shear tests, s_{uDSS}/σ'_{vc} = 0.195 (Ahmed, 1990).

There are clearly approximations in applying the methods of Palmer (1972) or Silvestri (1998) to the TWC experiments. In particular, the TWC device does not achieve plane-strain shearing conditions. The axial stresses are kept constant, but axial strains can occur within the specimen during the course of the test. Similarly, though there is no drainage from the test specimen (constant volume condition), there is no restrictions on redistribution of pore pressures within the test specimen. Hence, it is possible that the value of pore pressure changes locally violating one of these key assumptions of the analytical methods.

The shear stress strain curve extracted from a point at the inner surface of the TWC simulation using MIT-E3 model with high pressure calibration parameters is also shown in Figure 5.7. The model predicts a maximum stress $q_h = (\sigma_{\theta\theta}-\sigma_{rr})/2$= 0.193 at a shear strain of 2% with slight post-peak softening. The predicted USR is very close to the elemental behavior in the DSS model. The TWC simulation is considered a more

complete representation f the true conditions of the experiment. The TWC simulation permits the pore pressures to migrate within the soil matrix during the time of the simulation. There is no assumption of plane strain conditions in the TWC simulation as top and bottom caps are included in the model. However, using the Silvestri (1998) method to interpret TWC results gives a very reasonable approximation of the specimen behavior and strength.

5.4.2 Interpretation of stress states in TWC Experiments

Finite element analyses permit a detailed diagnosis of stress conditions within the TWC model borehole tests. It is most convenient to use the transformed deviatoric stress components (Whittle and Kavvadas, 1994) for this purpose. The stress state in the TWC can be represented by the mean effective stress, σ', and three deviatoric stress components S_1, S_2, and S_3 that describe shear stress in the elemental triaxial, cavity expansion/contraction, and simple shear modes, respectively. Stress states along the mid-height of the TWC specimen have only S_1 and S_2 shear components. The space σ'-S_1 can be used to understand shear induced pore pressures, while $S_1 - S_2$ subspace indicates the magnitude and direction of shearing.

Figure 5.8a presents the yield surface and critical state cone of the MCC model in the transformed stress spaces; σ'-S_1, and S_2-S_1. The yield surface is an ellipsoid oriented along the σ' axis, while the critical state surface is a circular cone with its apex at the origin. The initial stress state for K_0-normally consolidated specimen is represented by point A[2].

Figure 5.8b shows the computed stress path, A-B for a point located at the inner wall during a TWC simulation using the MCC model at low consolidation pressure calibration parameters. The TWC produces an increase in the shear stress $\sqrt{S_1^2 + S_2^2}$ and causes

[2] Point A is located at $\sigma' = \frac{1}{3}(1 + 2K_{0NC})\sigma'_{v0}$, $S_1 = \frac{2}{\sqrt{6}}(1 - K_{0NC})\sigma'_{v0}$, and $S_2 = 0$.

hardening of the yield surface ($\Delta\alpha'>0$) in the MCC model. Figure 5.8b shows that the process involves a reduction in the triaxial shear component, S_1, as cavity shearing occurs, S_2. Loading also generates shear-induced pore pressures and hence, the effective stress decreases ($\Delta u_s = -\Delta\sigma'$). The figure shows the locations of the initial and final yield surfaces, f_A and f_B. The stress paths involve complex changes in the ordering of the principal stresses and relative magnitude of the intermediate principal stress. The latter is most commonly described by the Bishop Parameter, $b = (\sigma_2 - \sigma_3)/(\sigma_1 - \sigma_3)$. The Bishop Parameter values are indicated on the effective stress path. Initially, b=0 (triaxial compression state of stress ($\sigma_1 = \sigma_2$). During shearing, b increases to b=1 (triaxial extension, $\sigma_2 = \sigma_3$) and then decreases to b=0.8 with continued reduction in S_1. Initially, the major principal stress acts in the vertical direction. However, during shearing, this switches such that $\sigma_{\theta\theta} = \sigma_1$ by the end of the test. The final state of stress (B) has not reached the theoretical critical state for shearing to large strains (at σ_B') as shown in Figure 5.8b.

The yield surface and the critical state surface of the MIT-E3 model are shown in Figure 5.9a (using the same stress space interpretation). Initially, the stress state A is located at the top of an ellipsoid yield boundary surface that is oriented along the K_0-normal consolidation line in the σ'-S_1 space. The orientation of the yield surface is controlled by a hardening tensor *b* in the model formulation. The locus of critical state is defined by large strain friction angles measured in triaxial compression and extension modes of shear.

Figure 5.9b shows the computed stress path for a point at the inner wall of the TWC specimen in a simulation using the MIT-E3 model and the standard depressurizing rate (see figure 5.2b). Although the stress path has some features in common with the MCC predictions (reductions in S_1 and positive shear-induced pore pressures), there is smaller increase in the overall magnitude of shearing ($\sqrt{S_1^2 + S_2^2}$). The intermediate principal stress increases from b=0 to b=0.87 at the end of shearing which implies that σ'_v is always the major principal stress. The final state of stress coincides with the critical state surface (f_B) indicating that further shearing will cause no further change in effective stress state at this point. The fact that effective stress paths using MIT-E3 reach the

critical state condition is consistent with the predicted cavity volume strain vs. pressure response in which MIT-E3 soil model simulates failure in the TWC tests. In contrast there is no TWC failure predicted by the MCC simulations.

5.4.3 Stress and strain conditions within TWC specimens

The previous two sections have presented two different methods to interpret the TWC results 1) under assumptions of the plane strain shearing; and 2) based on computed stress paths for a given point at the cavity. The first considers only the in-plane shearing and ignores the out of plane shear stress component, S_1. This method assumes that the stress components governing soil behavior are the radial and circumferential stresses. The second method takes into account all three independent stress components and is affected significantly by the assumptions of yielding in the constitutive models. This section considers further the approximations inherent in the simplified plane strain interpretation of the TWC experiments. The previous section showed numerical predictions in which cavity shearing mode (S_2) is accompanied by change in the b-value at the cavity wall. To investigate this matter further, the predicted stress distributions across the thickness of the TWC specimen are plotted in Figure 5.10 to discover the effect of different shear modes on the soil specimen.

Figure 5.10 shows the stress distributions across the thick wall of the TWC specimen at the end of simulation using the MIT-E3 model and standard depressurizing rate. The results show that there are significant changes in the average effective stress, $(\sigma'_1+\sigma'_3)/2\sigma'_{v0}$ and maximum shear stress, $(\sigma'_1-\sigma'_3)/2\sigma'_{v0}$ from the values imposed at the start of shearing (0.775, 0.225 respectively). The mean effective stress decreases from 0.64 to 0.3 across the specimen at the end of simulation (p_i/σ'_{v0}= 0.3). There are smaller variations in q/σ'_{v0} (0.3 at the outer wall to 0.205 at the inner wall). The b-value changes radically across the specimen from b=0.33 (typical of plane strain conditions) to 0.92 at the inner wall. This is clear indicator of the range of shear modes involved in the device.

The presence of triaxial compression and triaxial extension shear modes is counter-intuitive because the axial stress is kept constant in the experiment. However, the constant axial stress on the surface of the top cap is redistributed in the soil specimen during cavity pressure unloading due to the interaction between the soil and the more rigid top cap. The distribution of total vertical stress across the thickness of the TWC (at $p_i/\sigma'_{v0} = 0.3$) indicates zones of unloading ($\Delta\sigma_v/\sigma'_{v0} < 0$) at the inner wall, and zones of loading ($\Delta\sigma_v/\sigma'_{v0} > 0$) at the outer wall as shown in the figure. The total vertical stress at the inner wall is reduced to 60% of the original value, while stress at the outer wall increases to 112% of its original value. The magnitudes of unloading and loading must be balanced to maintain vertical equilibrium with constant axial stress applied to the top platen. In Figure 5.10, the areas under the change in total vertical stress curve result in equal volumes of loading and unloading when integrated around the axis of the TWC.

To identify the influence of possible different shear modes on the soil behavior in a TWC experiment, stress paths from the TWC simulation using the MIT-E3 model and standard depressurizing rate are compared to that of element level test simulations. Figure 5.11 compares the stress paths at the inner and outer walls of the TWC model with predictions of element tests subjected to five different modes of undrained shear, cylindrical cavity contraction (plane strain), triaxial compression, triaxial extension, plane strain compression, and plane strain extension. The stress path at the inner wall deviates slightly from the cylindrical cavity contraction but exhibits noticeable post-peak reduction in shear resistance. The stress path at the outer follows a different stress path with net increases in both S_1 and S_2 shear components. Differences in the stress paths predicted at the inner and outer walls is a critical aspect of the model prediction that is absent from simplified interpretation methods that assume homogenous response at all points across the test specimen (e.g Silvestri, 1998).

The numerical models provide information on the stress and strain conditions everywhere within the soil matrix, so that it is possible to investigate local conditions within the TWC specimen. Because of the encouraging agreement between the results from the FE simulations and the outcome of lab experiments, the detailed set of results can provide

valuable insight in the soil behavior in a TWC experiment. Contour figures of strain distributions at different pressure levels inside the cavity; provide us with an image of the shearing mechanisms and the progression of instability mechanisms throughout the test. Two strain indicators are chosen to describe the state of strain in the soil matrix; the volumetric strain ϵ_{vol}[3], and the second invariant of the deviatoric strain tensor $|E|$[4]. The volumetric strains show the local migration of pore water pressure within the TWC specimen, while $|E|$ depicts the overall magnitudes of shear strains. Figures 5.12 to 5.15 show contours of ϵ_{vol} and $|E|$ at different cavity pressure levels indicated on the accompanied cavity pressure vs. cavity volume strains curves using standard depressurizing rate.

Figure 5.12 shows the volumetric strain and the shear strain contours from TWC simulations using the MCC model. The contours are reported at a cavity pressure p_i/p_0 = 0.1 for low pressure and high pressure calibration of RBBC. In the volumetric strain contours, the compression zones are shaded in gray and the expansion zones are left white. The compression zones are spread from the mid-height of the outer wall towards the top and bottom to cover mostly 70% of the soil's height, and towards the inner wall to cover 85% of the soil's thickness. The compression zones cover most of the area in the cross-section, but the maximum value of compression strain as indicated by on the figure is much less than the maximum expansion strain at the inner wall. At the top and bottom corners on the inner wall side, small pockets of high compression and expansion strains are found close to each other, indicating local zones of pore pressure migration associated with the boundary constraints at the top and bottom caps. The model parameters have a very small effect on the predicted patterns of volume strains. The shear strain contours indicate the influence of cavity contraction by vertical lines of equal shear strains starting at the inner wall. The contours streamlines almost throughout the height of the soil part except near the top and bottom caps. The maximum shear strain occurs at the inner wall and decreases till negligible values (<1%) in the mid-thickness of the soil part. There are

---

[3] Volumetric Strain, $\epsilon_{vol} = \epsilon_{rr} + \epsilon_{\theta\theta} + \epsilon_{zz}$

[4] Second Invariant of Deviatoric Strain Tensor, $|E| = \sqrt{E_1^2 + E_2^2 + E_3^2}$

concentrations of shear strains at the lower and upper corners (near the inner walls) due to the interaction with the boundary conditions at the top and bottom caps. The low pressure simulation exhibits larger cavity volumetric strains as shown in the accompanying cavity pressure vs. cavity strain curves. Overall the results show relatively small variations in vertical gradients of strain components within the middle 50% of the test specimen.

Figures 5.13 and 5.14 show similar volumetric and shear strain contours from simulations using the MIT-E3 constitutive model for high and low pressure calibrations. The results are shown at higher values of cavity pressure (p_i/p_0 = 0.4 and 0.35 respectively). The results at p_i/p_0 = 0.4 correspond to the onset of failure from the high pressure model calibration, while failure is fully developed at p_i/p_0 = 0.33 in Figure 5.14.

The results in Figure 5.13 are broadly consistent with trends noted for the MCC model. Shearing is dominant near the inner wall, while there is a large zone of small volumetric compression that spreads from the outer wall. However, as failure progresses, there is a volumetric expansion along the inner wall (Figure 5.14b) over the full height of the device. It should be noted that the volume strain magnitudes are relatively small which implies that the simulations are effectively undrained. Figure 5.15 (p_i/p_0 = 0.24) confirms that failure produces swelling at the inner wall where there is high variability in shear stress over the height of the specimen. These observations of failure were not found in MCC simulations as these did not reach plastic failure of the model wellbore. For MIT-E3, the shear strain reaches a value up to 7% at the mid-height of the inner wall (low pressure calibration at p_i/p_0 = 0.24 in Figure 5.15).

5.5 Variables Affecting Behavior in TWC Model Borehole Tests

5.5.1 Rate of Unloading

The rate of change of cavity pressure is reduced in the FE models are selected to match the cavity strain rates applied in the physical experiments. Abdulhadi (2009) used three different rates; fast ($\dot{\epsilon}_{cav} \cong 60\%/hr$), standard ($\dot{\epsilon}_{cav} \cong 10\%/hr$), and slow ($\dot{\epsilon}_{cav} \cong 0.5\%/hr$). The goal of using different cavity strain rates is to investigate how model wellbore stability is related to the timeframe of drilling. Slower rates of pressure reduction allow for excess pore pressures to equilibrate and pore fluid to migrate within the test specimen. The standard strain rate (10%/hr) is chosen to allow equilibration of pore pressure throughout the specimen and hence, provide more uniform conditions within the TWC device. Uniformity is important for an adequate study of the soil properties and behavior as well as for an accurate measure of the pore pressure that represents the status of the whole specimen. The current constitutive models do not include rate dependent properties; however, time dependent behavior is included due to coupled consolidation (coupled flow and deformation) within the TWC specimen. The analyses can represent undrained condition (i.e., with no local pore pressure migration), as well as effects of local pore fluid migration and hydraulic conductivity by simulating the time-dependent controls on cavity pressure (p_i vs. time; Figure 5.2b).

Figure 5.16 compares results from TWC experiments performed by Abdulhadi (2009) at three different depressurizing rates with global constant volume conditions as well as a completely drained experiment ($\dot{\epsilon}_{cav}$= 0.2%/hr, open drainage lines). Faster depressurizing of the cavity is associated with small volume strains required to reach a specified pressure (i.e. response is stiffer). The fast depressurizing test fails at p_i/p_0 = 0.25, the standard rate at p_i/p_0 = 0.27, and the slow in rate at p_i/p_0 = 0.4. In comparison, the drained experiment shows much less initial stiffness and failed at much lower cavity pressure level (p/p_0 = 0.15). At the same cavity pressure level the cavity volume strain found in the drained experiment is much higher than that of the undrained experiment with different strain rates. This can be attributed to the fact that global volume change is

allowed in the specimen by having the drainage lines opened, thus more deformations and cavity volume changes are expected.

Figure 5.16 also shows results from analogous numerical simulations using the MIT-E3 constitutive model (using high pressure parameter calibration). The simulations of the drained experiment successfully predicted the low initial stiffness and increase in the cavity volume strains. However, the simulation did not predict failure. Drained simulation is performed by treating the soil as a single phase material (no pore pressures). Failure in the experiment can occur due to development of small pore pressure that are not simulated in the numerical model. The simulation of a true undrained TWC is performed by applying the cavity pressure decrease over a very short time-frame to prevent local pore pressure migration. The true undrained simulation and the simulations using the three different cavity strain rates predict identical results except at the final stage where failure occurs. True undrained simulation showed an abrupt termination in the analysis, while in the simulations allowing local pore pressure migration, a plateau develops where relatively large cavity volume strains occur. All curves from undrained simulations gave the same stiffness as in the standard rate experiment results, and very similar cavity pressure levels at failure. The strain rate effect captured in the experiment results can not be captured by the model because the constitutive relationships are strain-independent. This suggests that volume changes due to pore fluid migration generate minor effects.

Abdulhadi (2009) used the Silvestri Interpretation Method to derive shear stress-strain properties from the TWC model wellbore tests at different cavity pressure rates. The stress strain curves for the fast, standard and slow cavity pressure rates are shown in Figure 5.17. The undrained strength ratio decreases with decreasing the strain rate, ranging from USR=0.22, 0.21, and 0.18 for fast, standard and slow cavity pressure rates respectively. The value of USR has been known to decrease with decreasing the strain rate (Sheahan et. al, 1996). In this situation, another factor comes into play which is the degree of pore pressure equilibration achieved by the specimen at different strain rates. These differences in experiment results are primarily true rate effects because the strain

independent constitutive models does not predict any change in computed USR values at these rates of strain.

The shear stress strain curves computed using the MIT-E3 model are presented in Figure 5.17 based on stress at the inner wall of the cavity using high pressure calibration parameters. The model simulations generate a maximum shear resistance USR = 0.19 for all three depressurizing rates, which is close to the values interpreted by Silvestri (1998). All curves are very similar with the exception of the final part, where post peak softening slightly increases with the decrease of the strain rate. This is an expected outcome because the strain rate is not one of the governing factors considered in the MIT-E3 constitutive model as a rate independent model. On the other hand, higher degrees of pore pressure equilibration (slower cavity pressure unloading) generate more post-peak softening.

5.5.2 Size of Specimen

Abdulhadi (2009) performed TWC experiments on larger specimens to study the sensitivity of the TWC lab results to the size of the specimen. Increasing the diametric ratio helps to explore the effect of wall thickness on the boundary conditions of the specimen and the results of the tests.

Figure 5.18 compares the cavity pressure-volume behavior measured in small and large TWC for RBBC (OCR=1.0) specimens at σ'_{vc} = 6 MPa from Abdulhadi (2009) using standard depressurizing rates. Smaller cavity volume strains occur in the large TWC tests with higher initial stiffness. There is minimal decrement in cavity pressure at cavity volume strains greater than 8% in both small and large specimens. However, the large specimen is more stable at lower cavity pressures, with failure at p_i/p_0 = 0.075 compared to p_i/p_0 = 0.24 for the small TWC specimen.

The predictions of MIT-E3 and MCC models for the large and small TWC specimens are also shown in Figure 5.18 using high pressure calibration parameters on a logarithmic

scale. Both models overestimate cavity deformations initially but the MIT-E3 model captures failure reasonably well for both specimens. The input parameters for high consolidation pressures are meant to be an average representative of a wider range of consolidation pressures. The trends observed in the computed cavity pressure-volume strain curves resemble those of the behavior observed in the lab. For large specimens, initial stiffness increases and specimen net cavity pressure ratio decreases.

Abdulhadi (2009) used the Silvestri (1998) Interpretation Method to deduce the stress strain curves from the experiments on small and large TWC specimens at the inner wall. A comparison between both stress strain curves is shown in Figure 5.19. Both curves are similar up to peak strength, USR = 0.21 and shear strain at peak, γ= 2.5% similar to data in Figure 5.7. Then, the large specimen exhibits significant post-peak softening. Evidently, the peak strength at a point on the inner wall is not affected by the specimen diameter; however, the failure propagation through the specimen is significantly affected by the size. In the large specimen, failure propagation is slower, thus more post-peak softening occurs at the inner wall.

Effective shear stress-strain curves are computed using the MIT-E3 model with high pressure calibration parameters at the inner wall of the specimen and plotted with interpretation of lab results in Figure 5.19. The curves are identical up to peak strength. The model predicts USR = 0.19 at shear strain, γ= 2%; which is lower than Silvestri (1998) interpretation but is consistent with trends observed in Figure 5.7. The solution for the large TWC device shows significant post-peak softening compared to that for the small device. The lab measurements also show some post-peak softening.

Figures 5.20 and 5.21 show contours of the volumetric and octahedral shear strains predicted by MCC model and MIT-E3 model using high pressure calibration parameters. The contours from the MIT-E3 simulation are taken at point of inflection (p/p_0 = 0.2) and at the end of simulations. The contours from the MCC simulation are only taken at the end of simulation because the slope of the curves did not change significantly through the analysis. The effect of a larger specimen size is evident because the volume strains are

much lower than the values found in the small TWC simulations. The larger drainage path inhibited volume changes in the large TWC compared to small TWC. However, these strains are spread over bigger volume in the larger TWC specimen. The shear strains are limited to the area close to the inner wall and only very small shear strains are found in the area close to the outer wall. The size of the specimen inhibits the propagation of failure significantly. As found in the small TWC simulations, the corners of the model at the inner wall near the top and bottom caps are found to be the position of local increase shear strains and adjacent compression and expansion zones.

The contour figures from the MCC simulation proved that the MCC large TWC model did not show any signs of deterioration or failure. Very low shear strains are found anywhere in the specimen. The highest value of shear strain is found at the corners of the model to be 1.37% which is lower than the MIT-E3 results. Volume strains are very low to the point that the boundary between compression zones and expansion zones is not clear. Although the MCC results are not realistic, the comparison between the contour figures from small and large TWC model showed the significant effect of specimen size in inhibiting failure propagation.

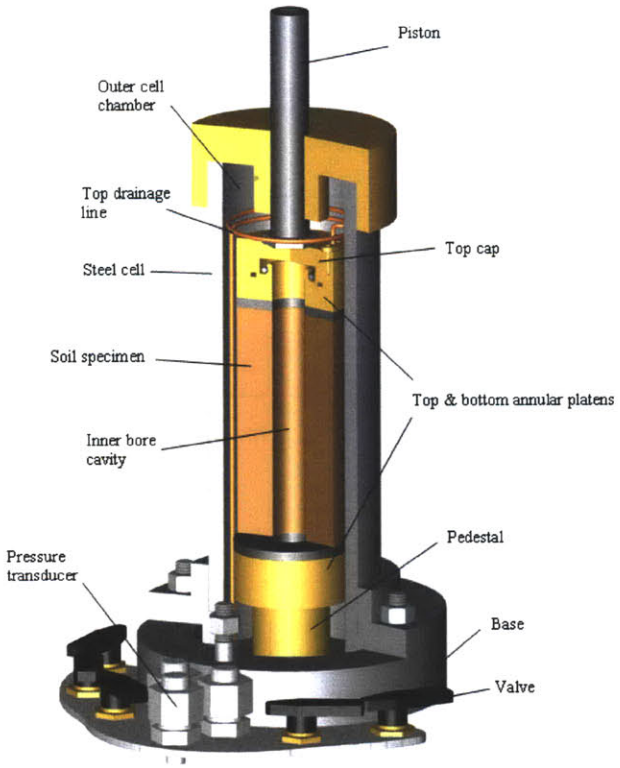

Figure 5.1 Schematic Diagram of the small TWC apparatus

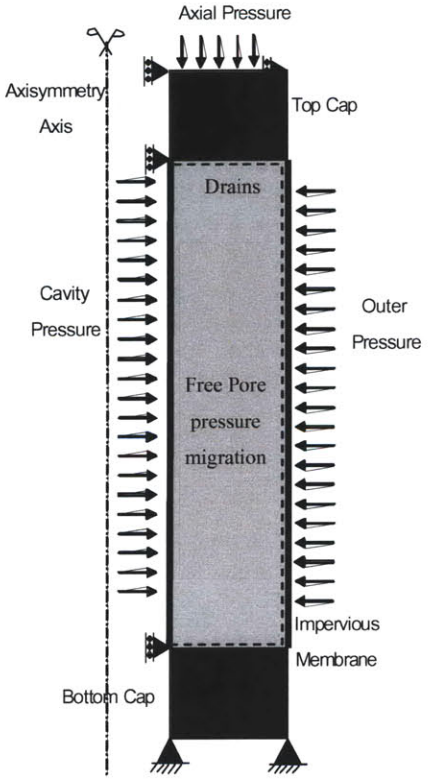

(a) 2D Axi-symmetric Model

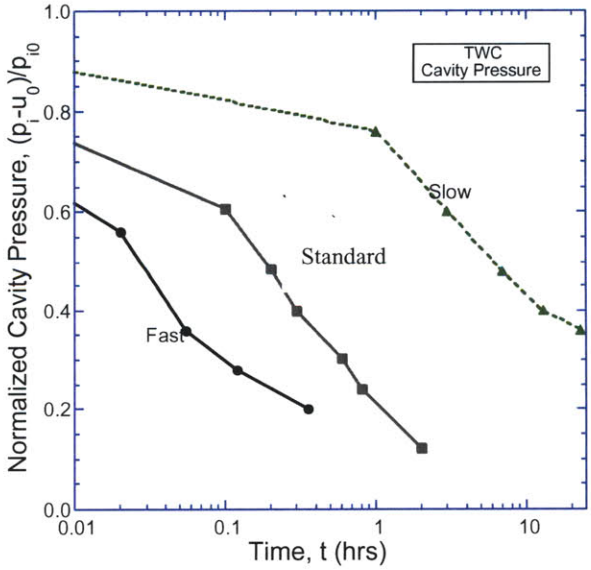

(b) Boundary Conditions within cavity

Figure 5.2 Numerical simulations of model borehole tests in laboratory TWC device.

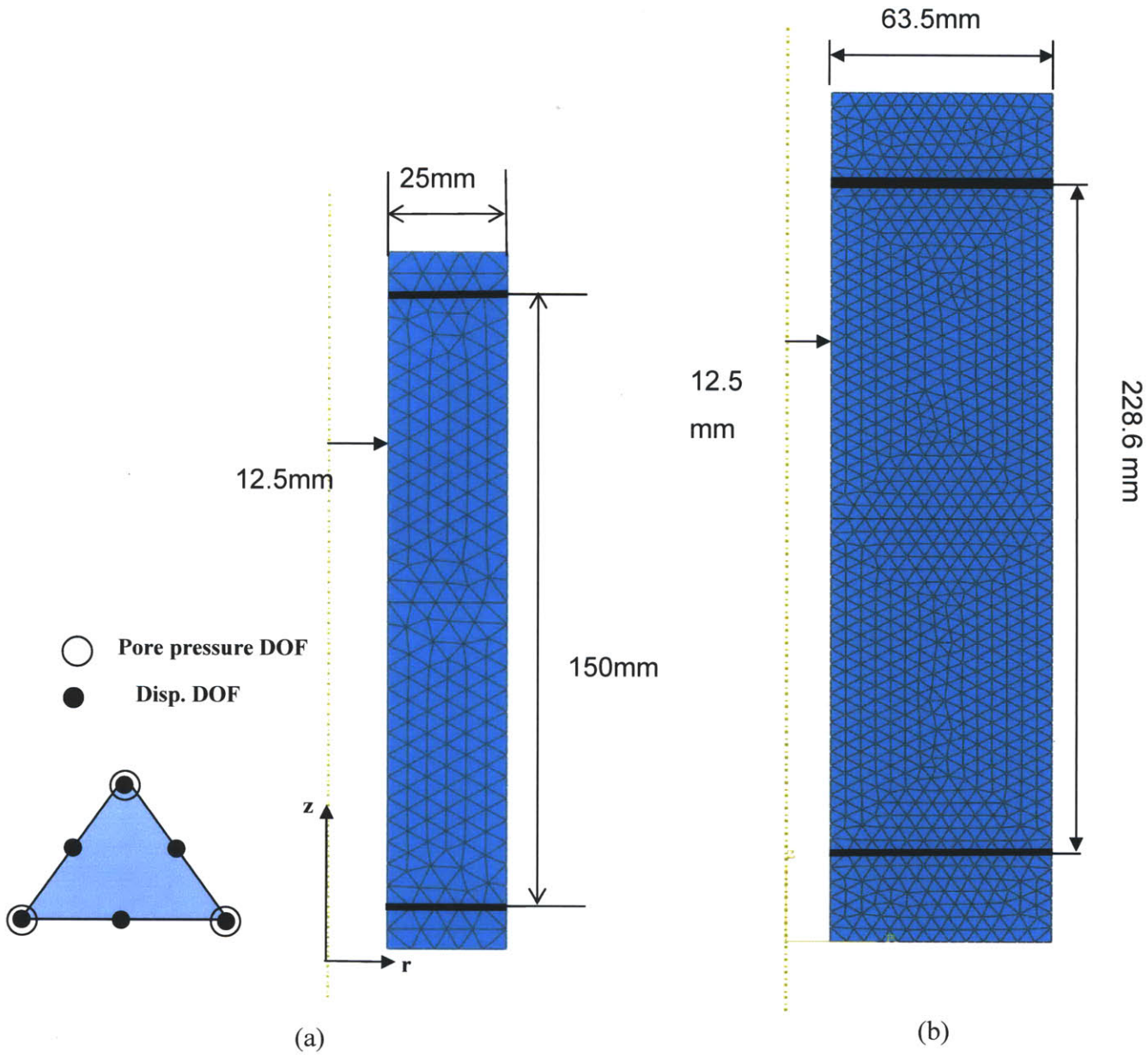

Figure 5.3 Finite element mesh used to represent the (a) small and (b) large TWC tests.

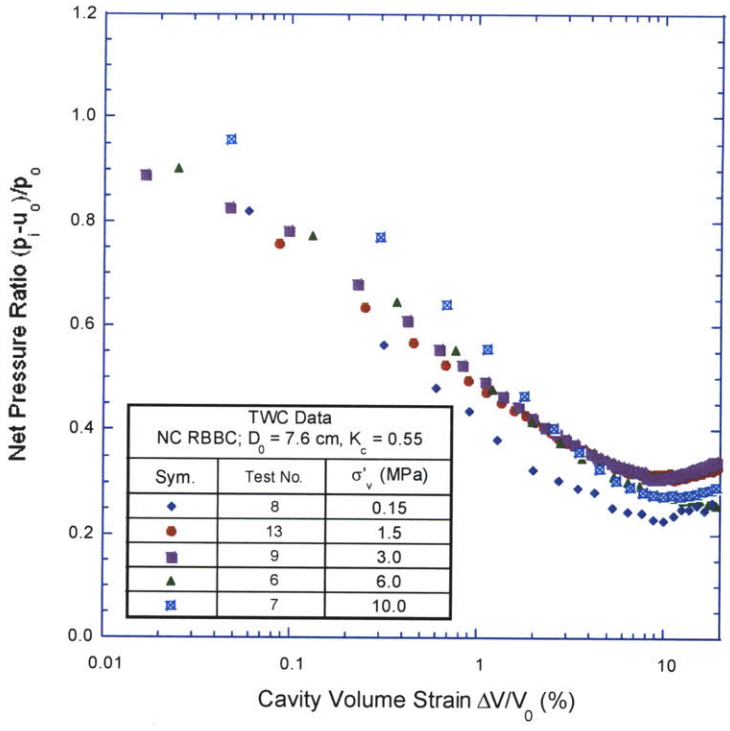

Figure 5.4 TWC lab experiments (Abdulhadi, 2009).

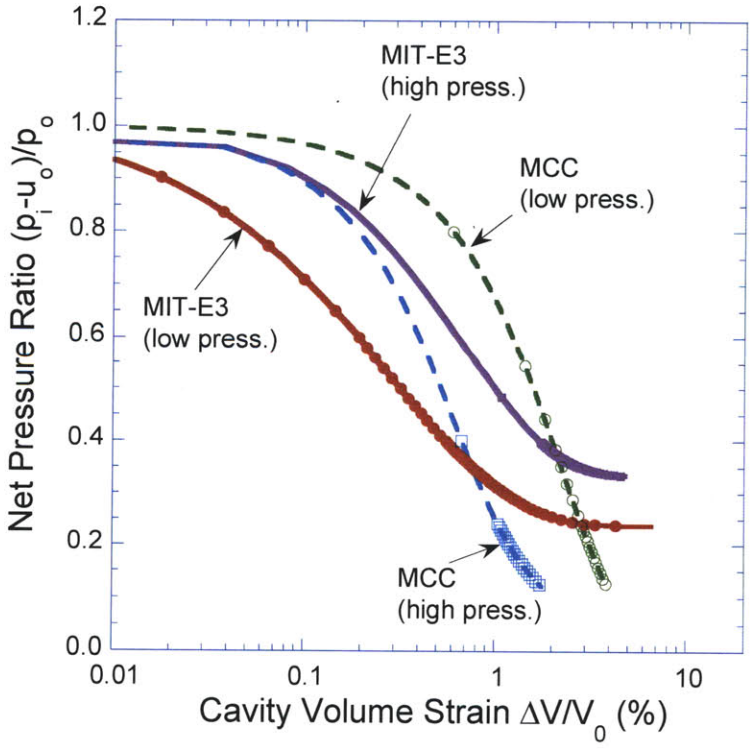

Figure 5.5 MIT-E3 and MCC predictions of the cavity volume strain as a function of the net cavity pressure.

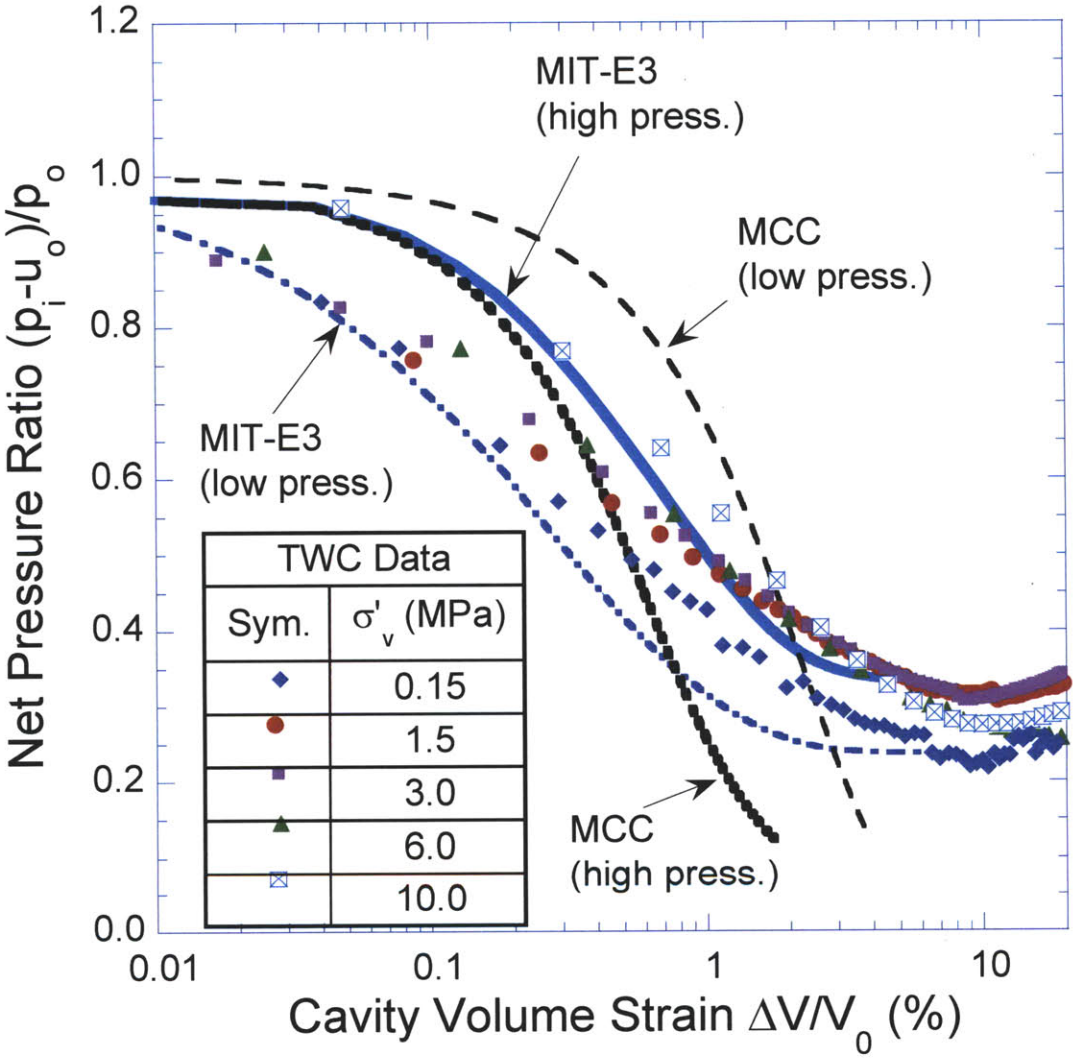

Figure 5.6 Comparison between TWC lab experiments and numerical simulations using the MIT-E3 and MCC models with input parameters calibrated for high and low consolidation pressures.

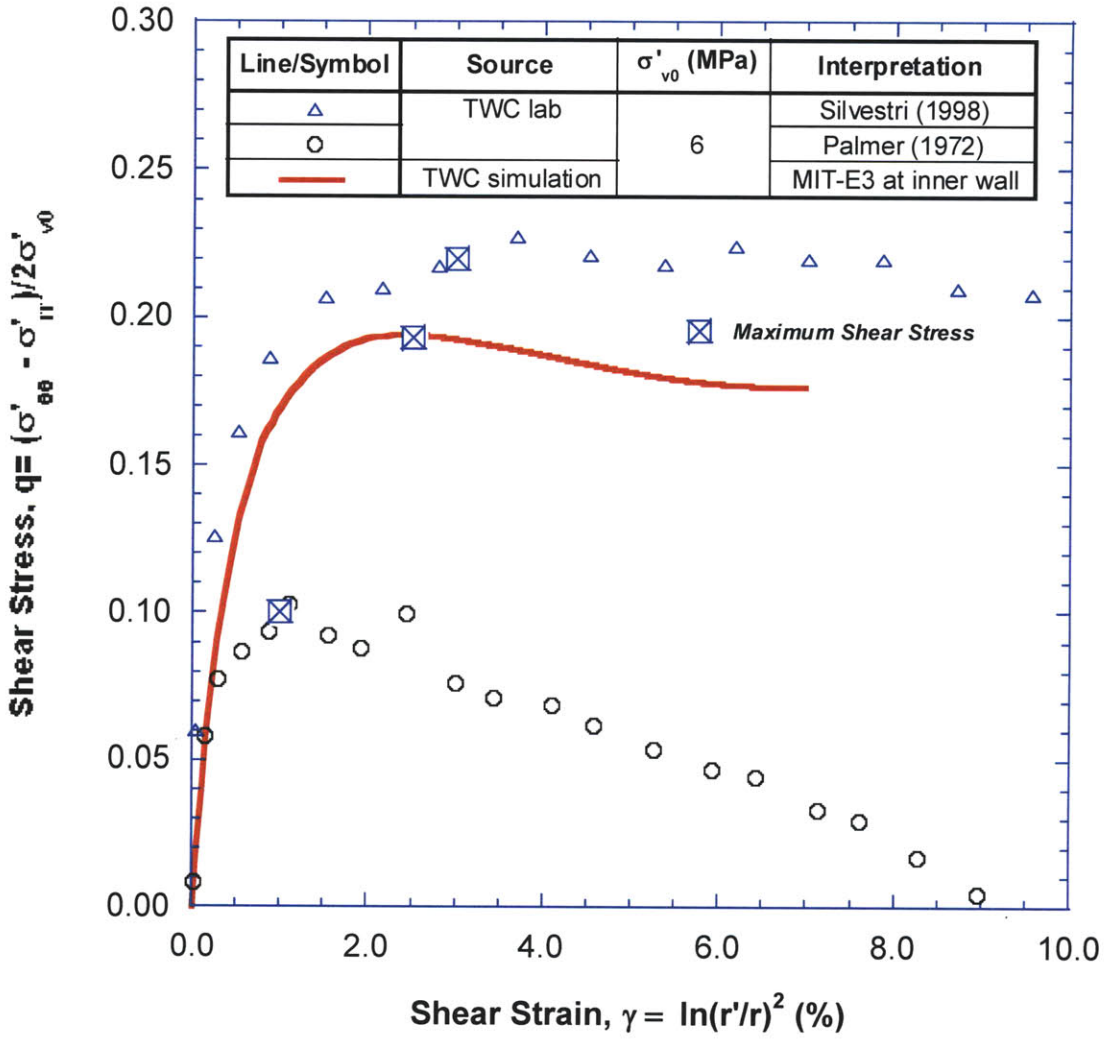

Figure 5.7 The stress strain relationships for an infinitesimal element at the inner wall of a TWC specimen. The relationships include direct interpretations of lab results (Abdulhadi, 2009) and extractions from TWC model and element simulations.

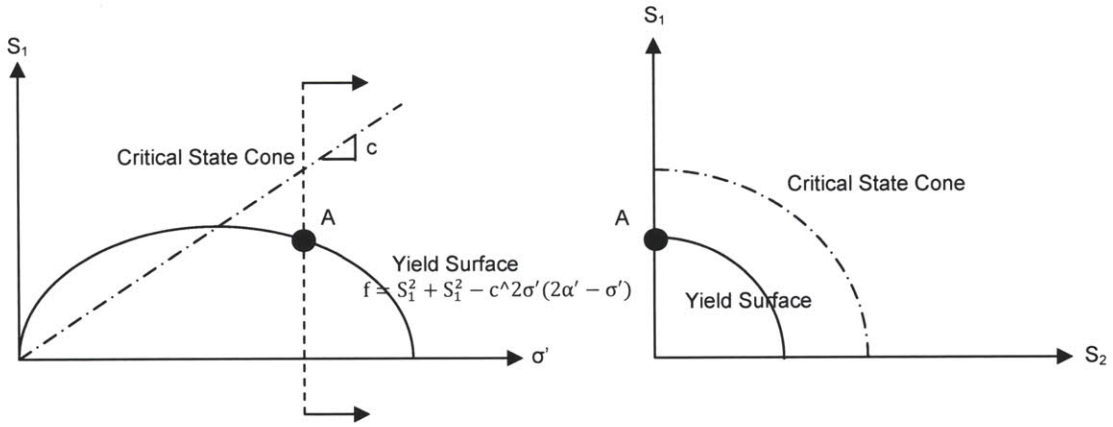

(a)

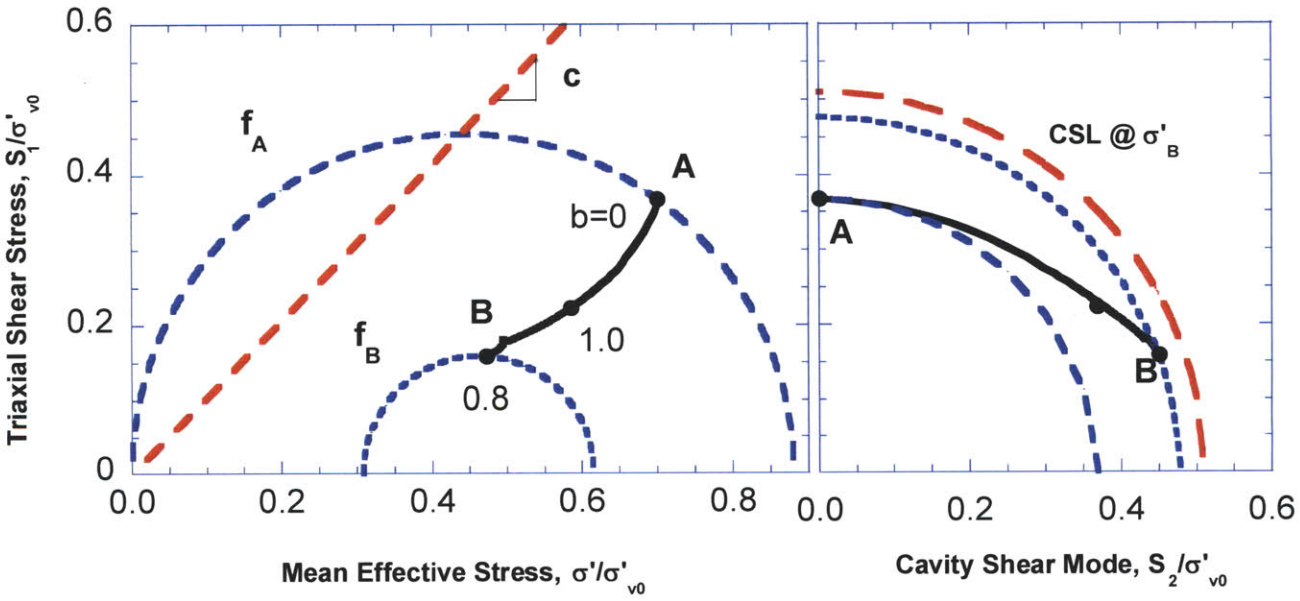

(b)

Figure 5.8 The stress path of an infinitesimal element at the inner wall of the TWC model using the MCC constitutive relations. The path is plotted in σ'-S1 space and S2-S1 space also depicting the critical state and yield surfaces.

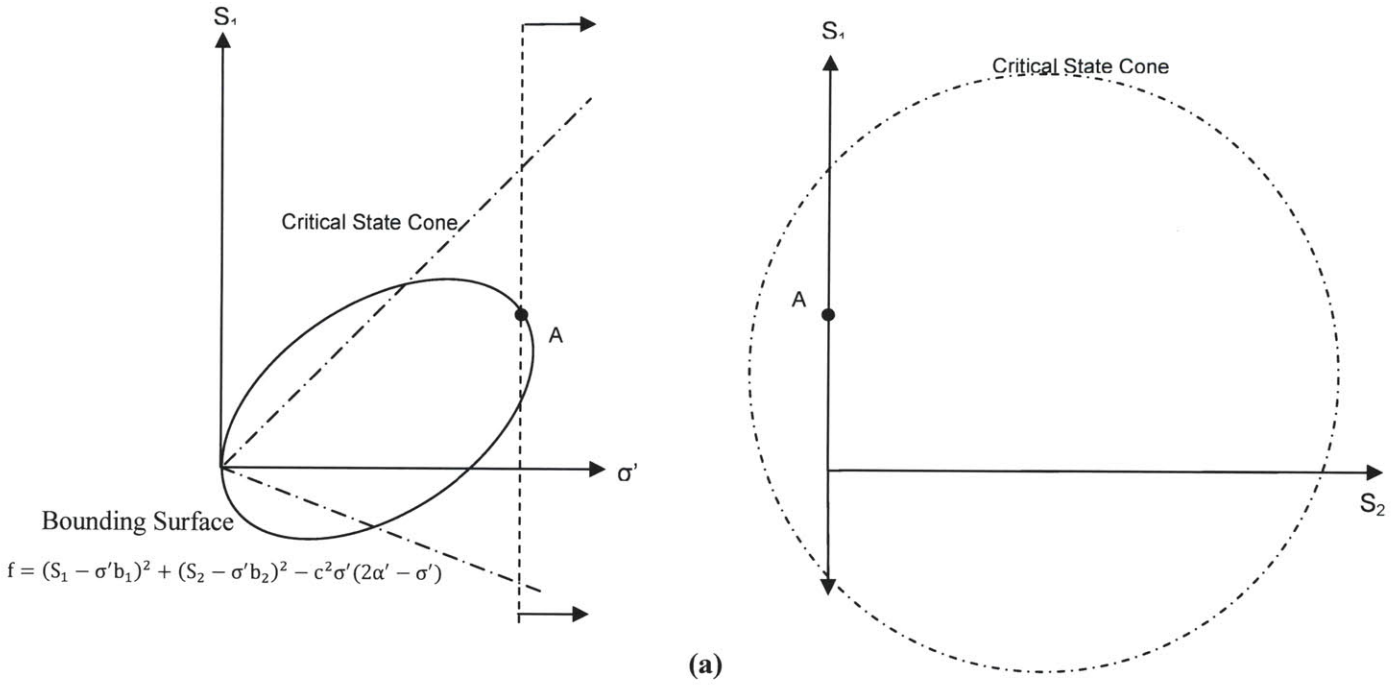

(a)

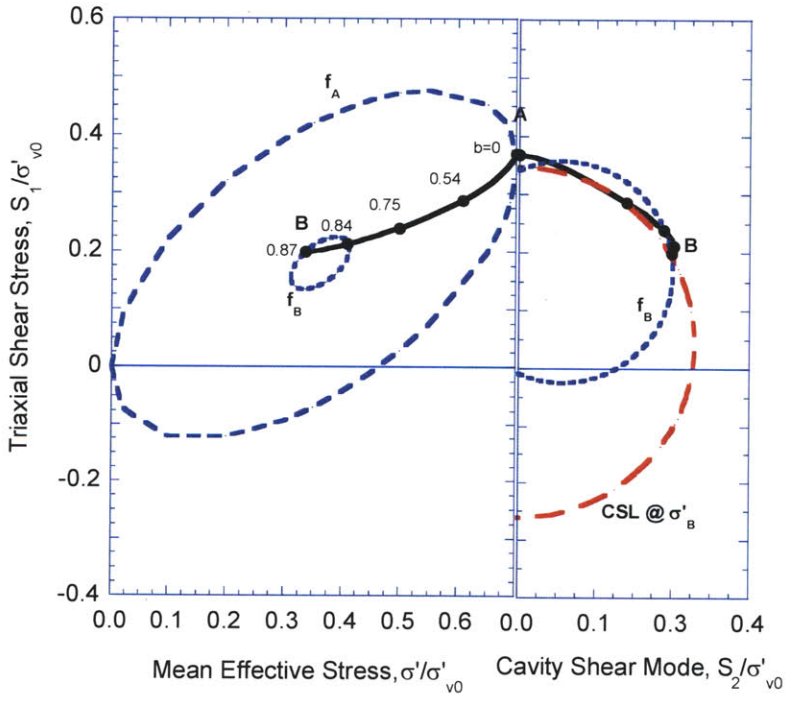

(b)

Figure 5.9 The stress path of an infinitesimal element at the inner wall of the TWC model using the MIT-E3 constitutive relations. The path is plotted in σ'-S_1 space and S_2-S_1 space also depicting the critical state and yield surfaces.

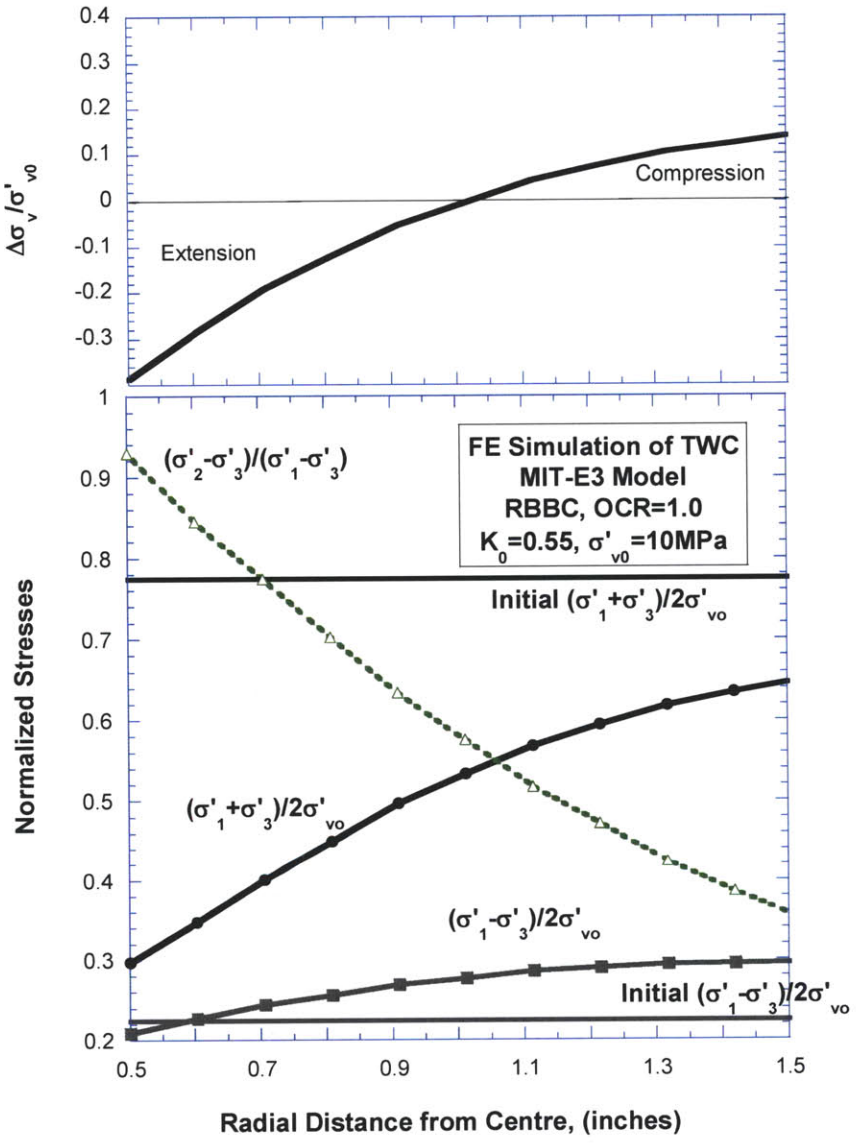

Figure 5.10 Stress distributions across the thickness of TWC model using the MIT-E3 constitutive relations.

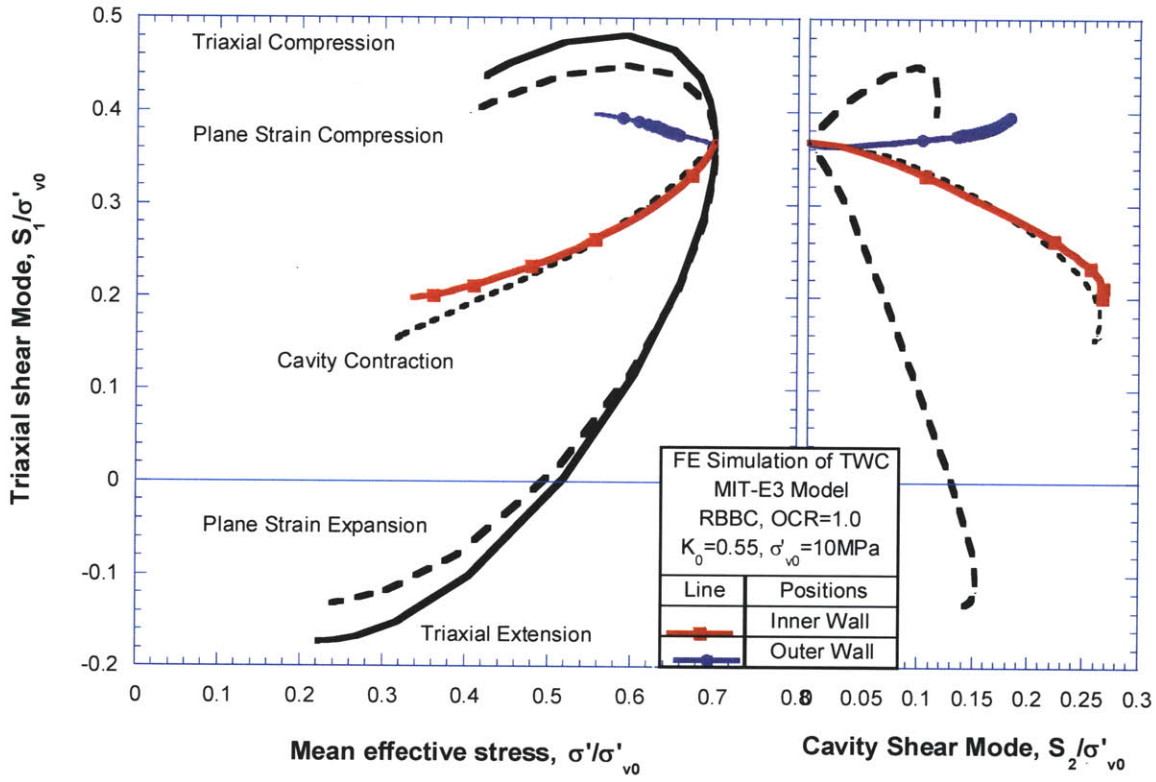

Figure 5.11 Comparison between stress paths in undrained shear element tests with simulations at inner and outer walls of TWC specimen in model borehole tests using the MIT-E3 model.

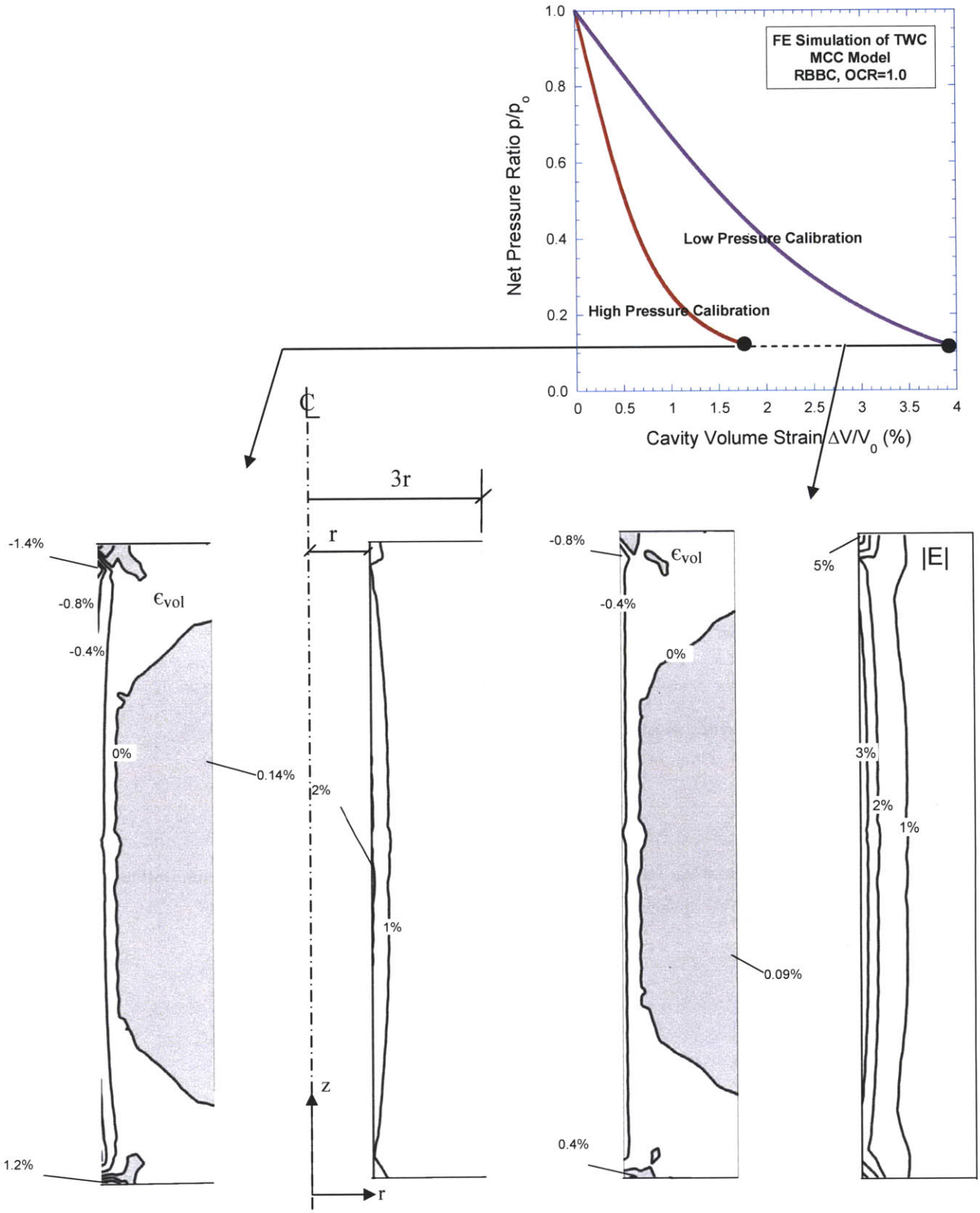

Figure 5.12 Computed Volumetric and Shear Strain Contours for simulations of TWC tests at $P_i/P_0 = 0.12$ using MCC model.

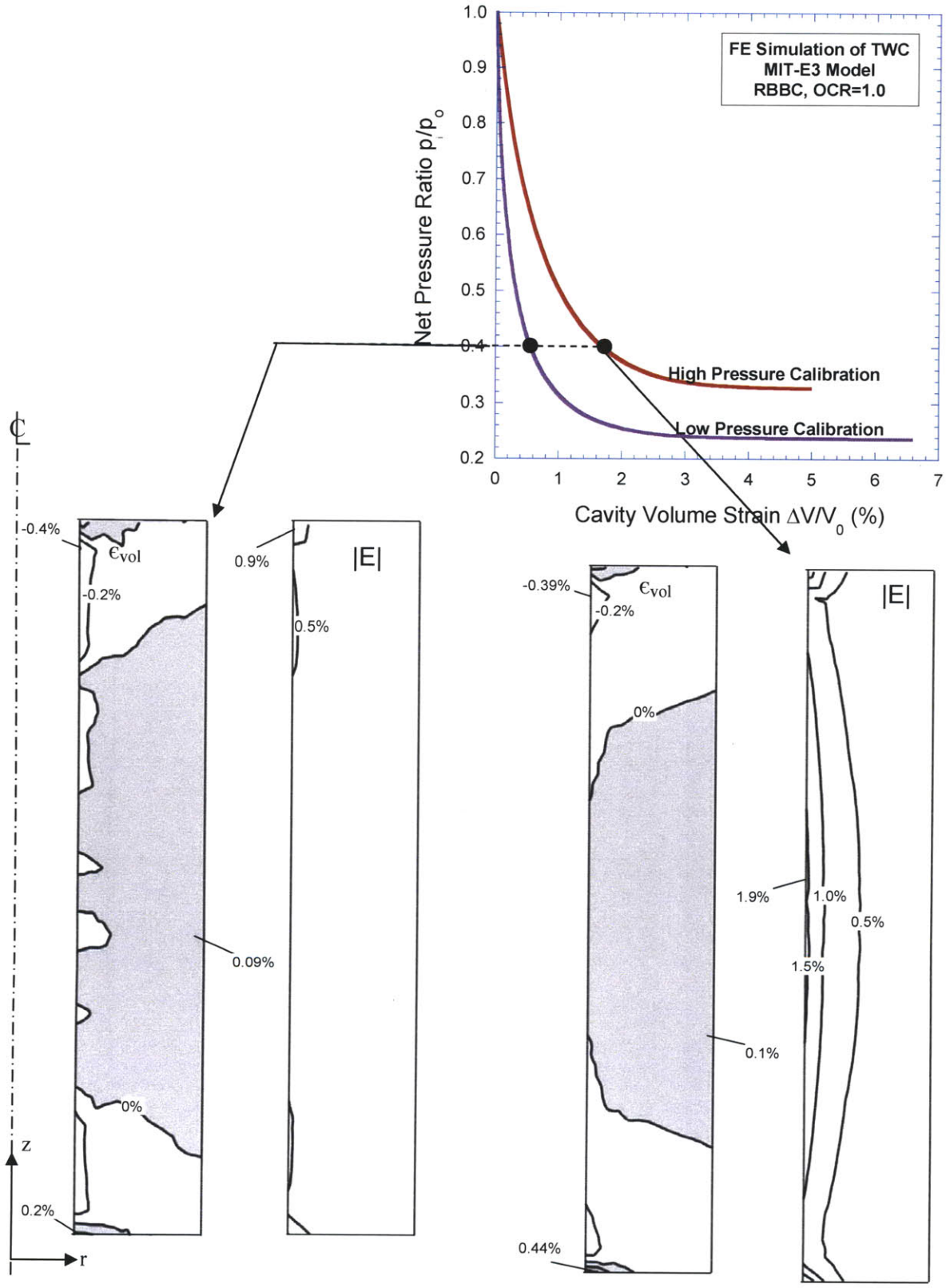

Figure 5.13 Computed volumetric Strain and Shear Strain contour predicted in TWC tests at p/p_0=0.4 using the MIT-E3 model.

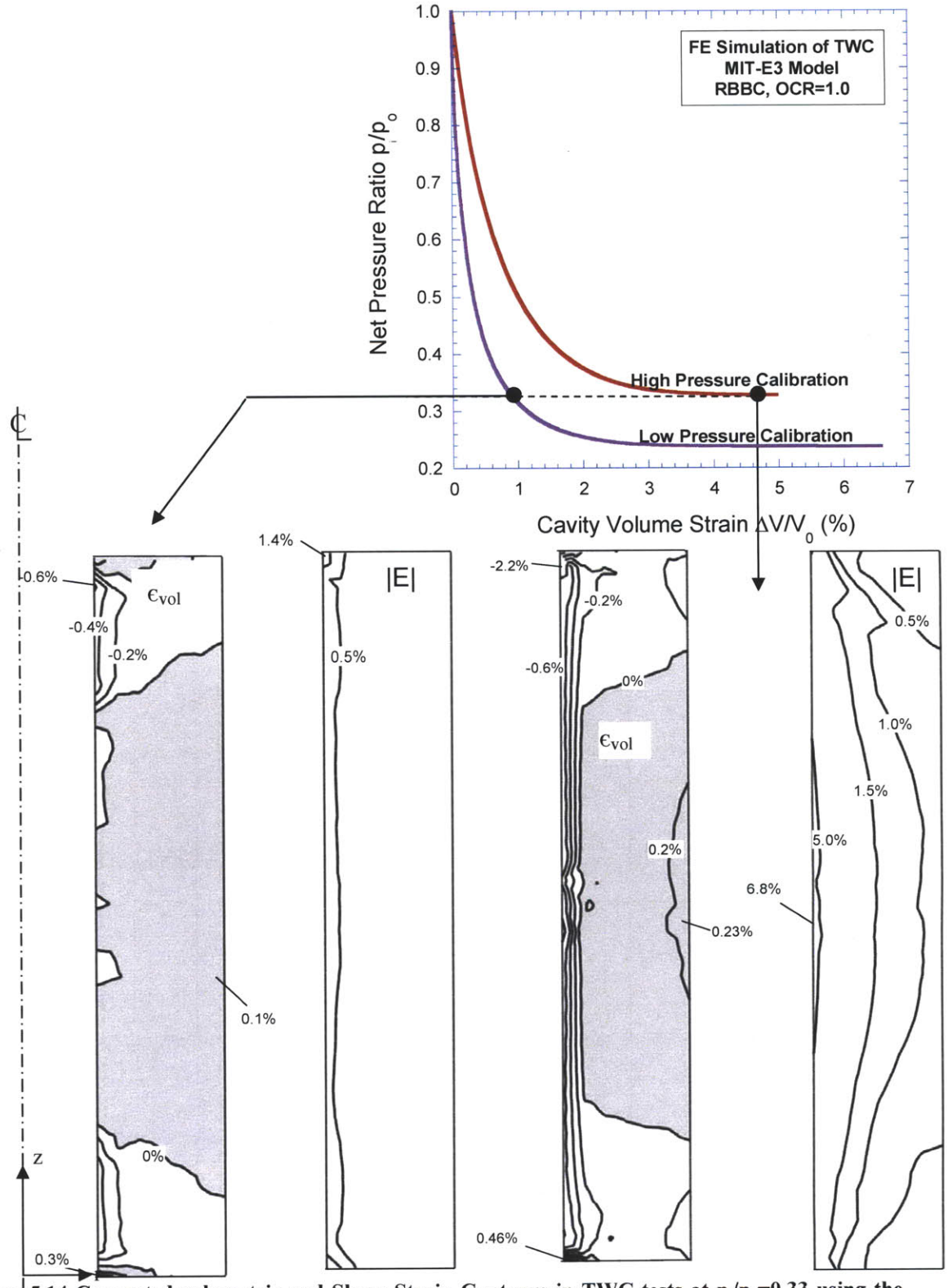

Figure 5.14 Computed volumetric and Shear Strain Contours in TWC tests at p_i/p_0=0.33 using the MIT-E3 model.

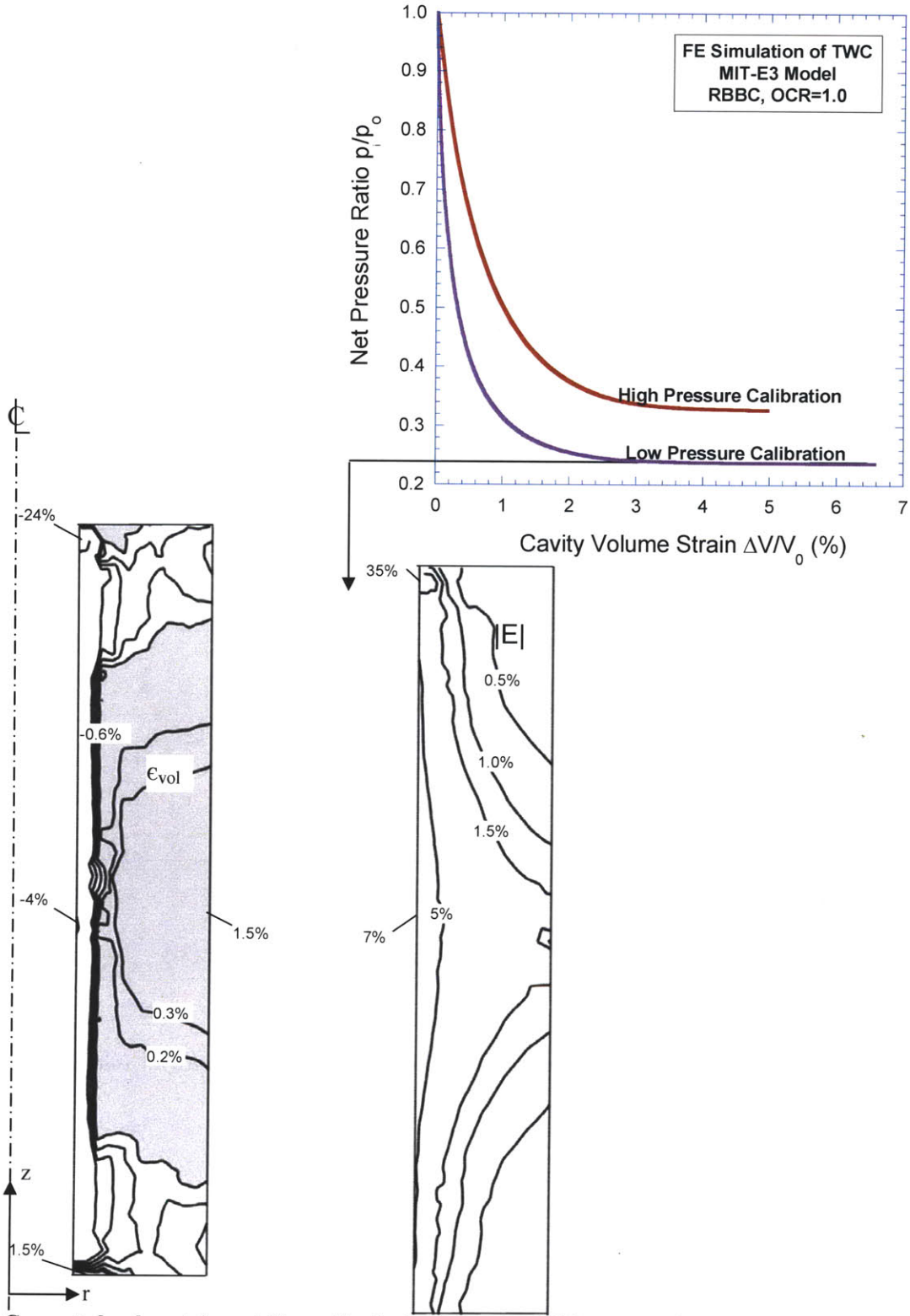

Figure 5.15 Computed volumetric and Shear Strain Contours in TWC test at p_i/p_0=0.24) using the MIT-E3 model.

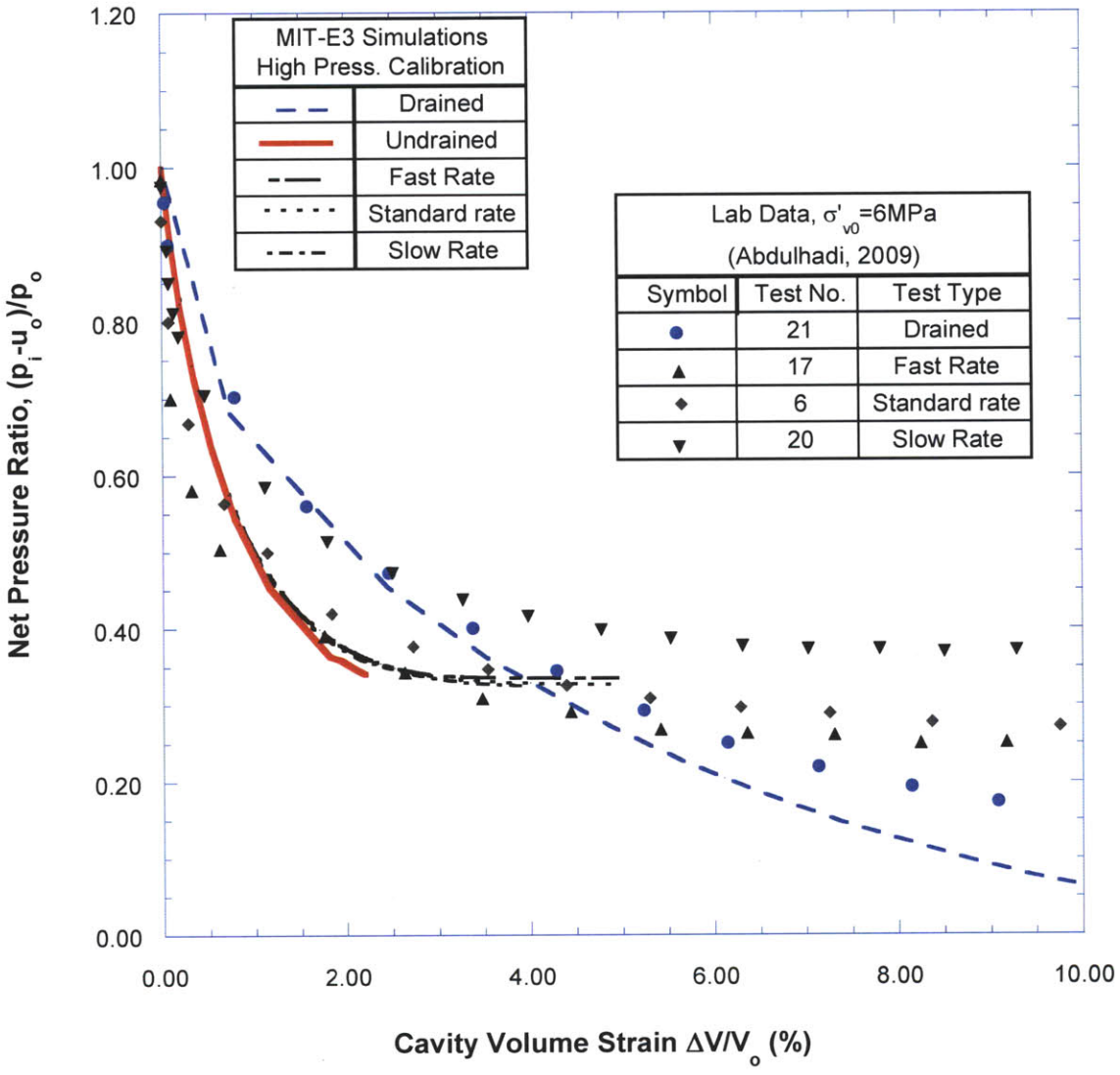

Figure 5.16 Comparison of computed and measured cavity pressure vs volume strain for TWC experiments performed at different cavity strain rates.

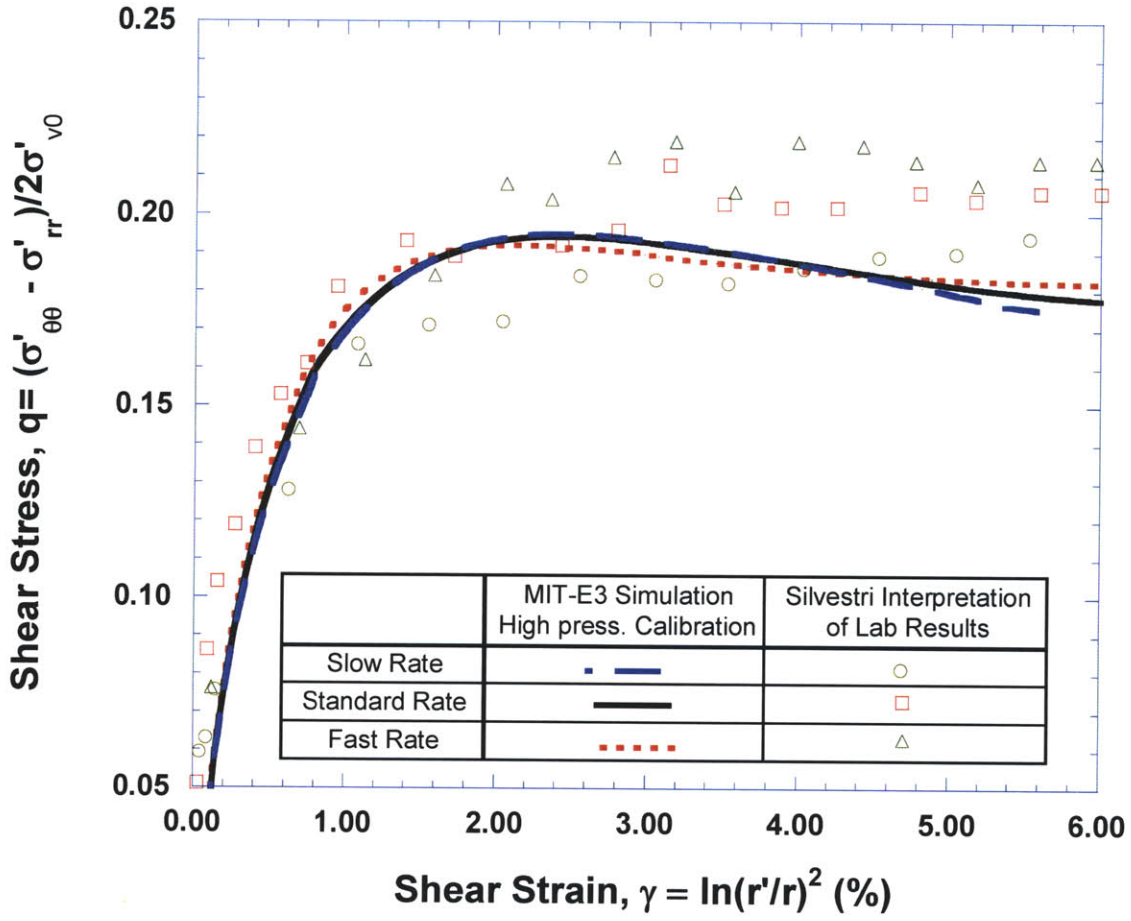

Figure 5.17 Comparison of shear stress strain behavior for TWC model borehole tests using method of Silvestri with numerical simulations at inner wall using the MIT-E3 model.

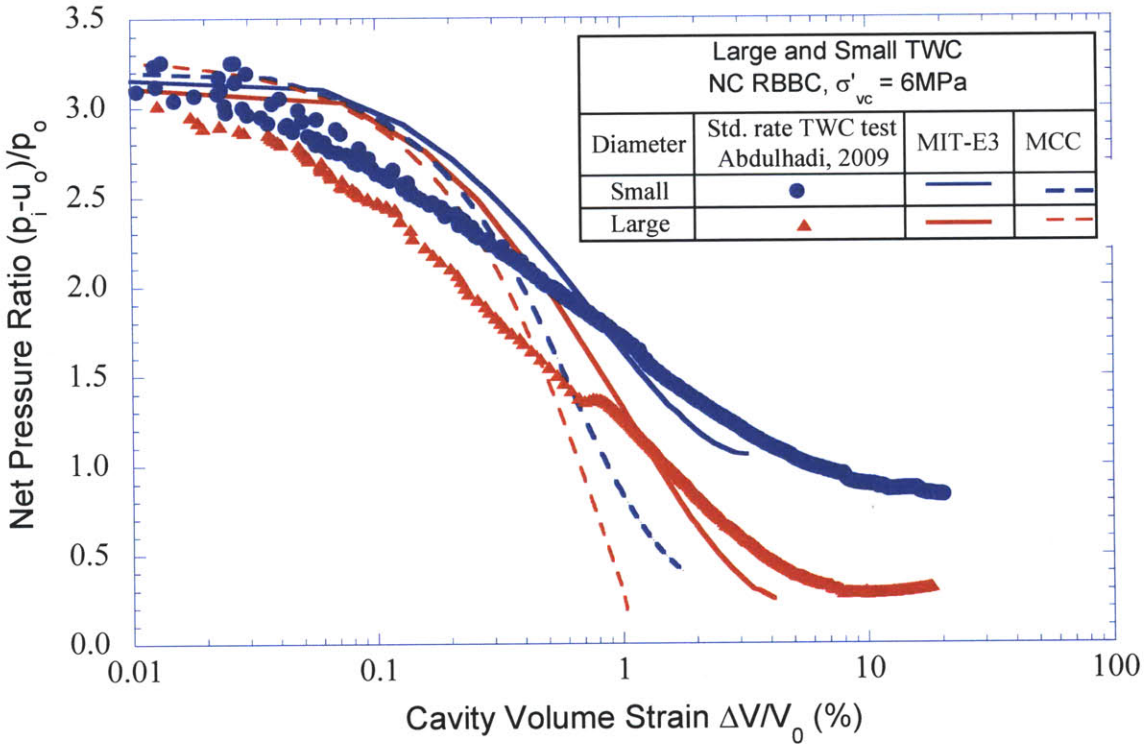

Figure 5.18 Effect of specimen size and TWC wall thickness on predicted and measured cavity pressure vs. cavity volume strain.

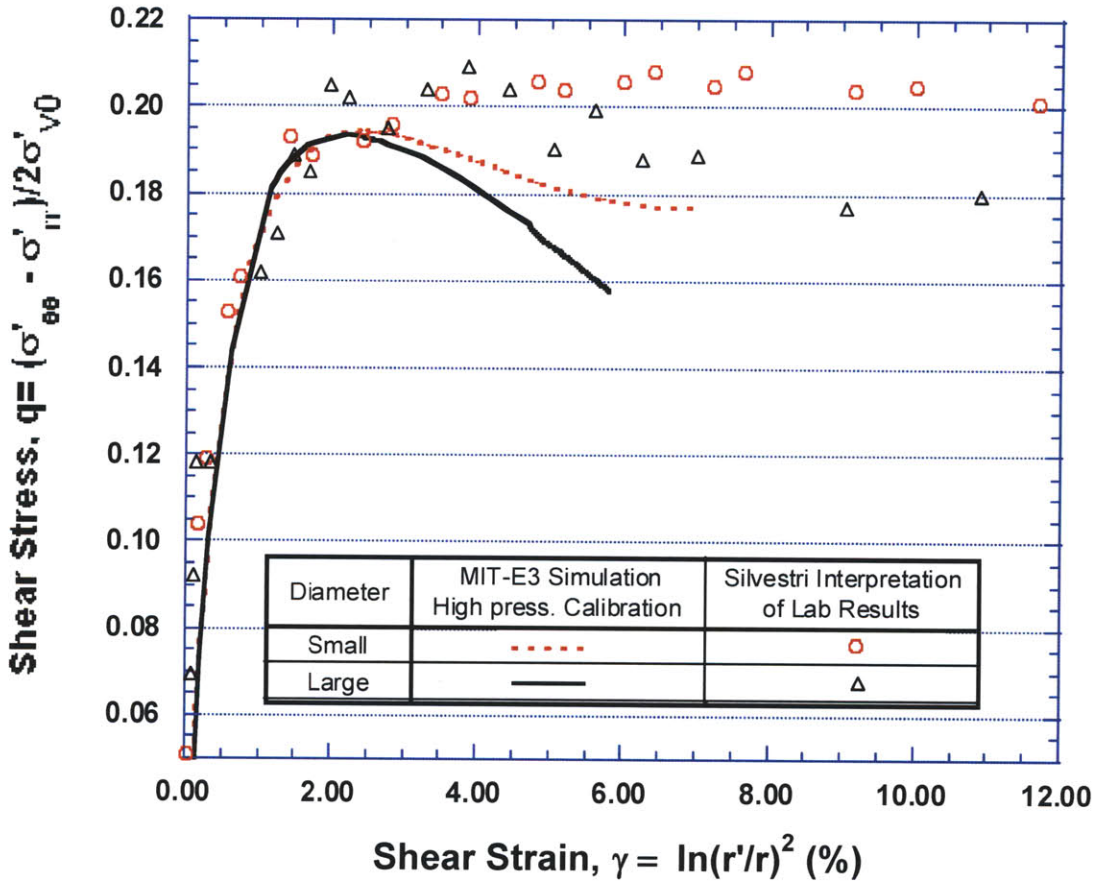

Figure 5.19 The stress strain curves for an element at the inner wall of TWC using direct interpretation of lab experiments (Abdulhadi, 2009) and using the MIT-E3 model for small and Large TWC.

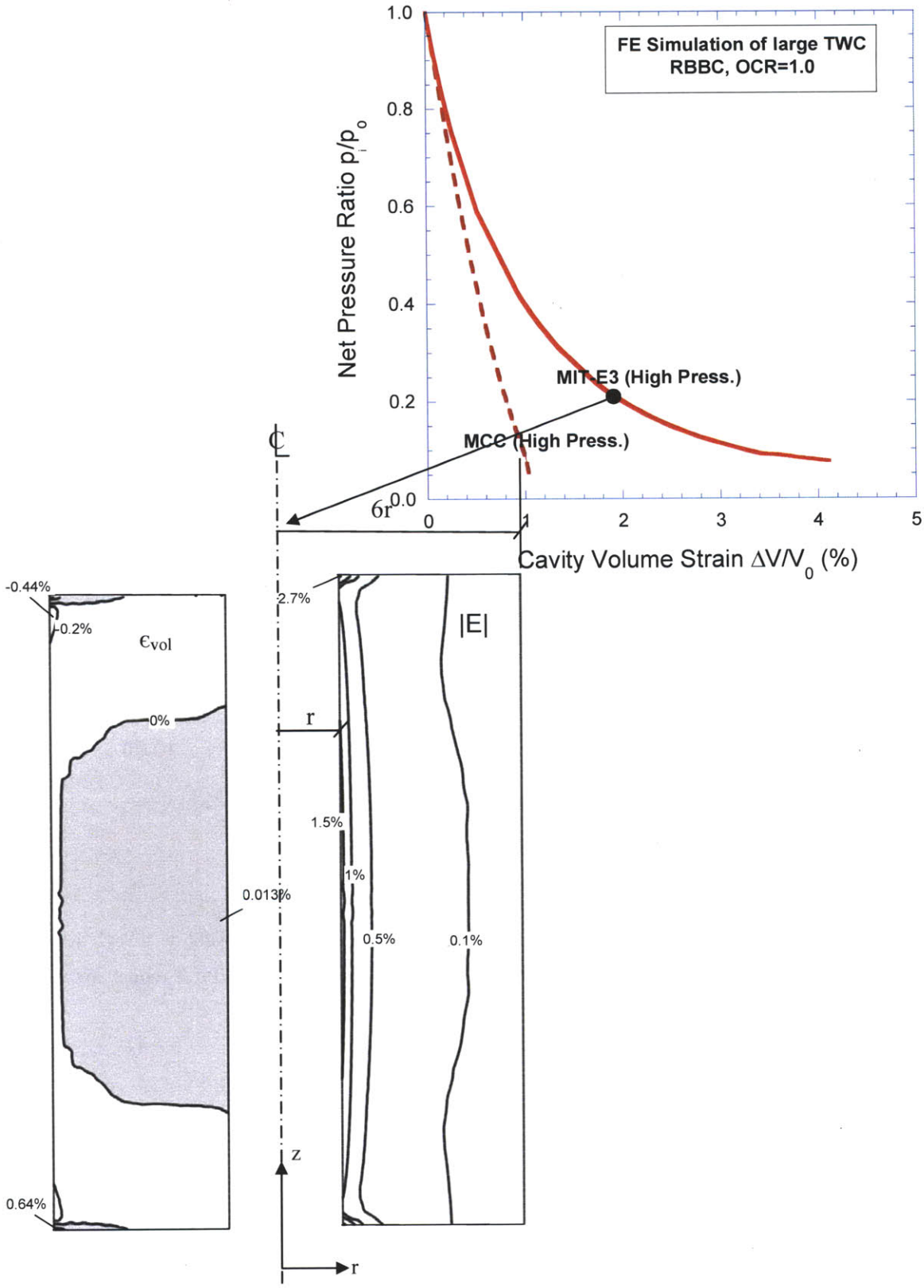

Figure 5.20 Computed volumetric and Shear Strain Contours at the p_i/p_0=0.2 predicted in Large TWC simulation using MIT-E3 model.

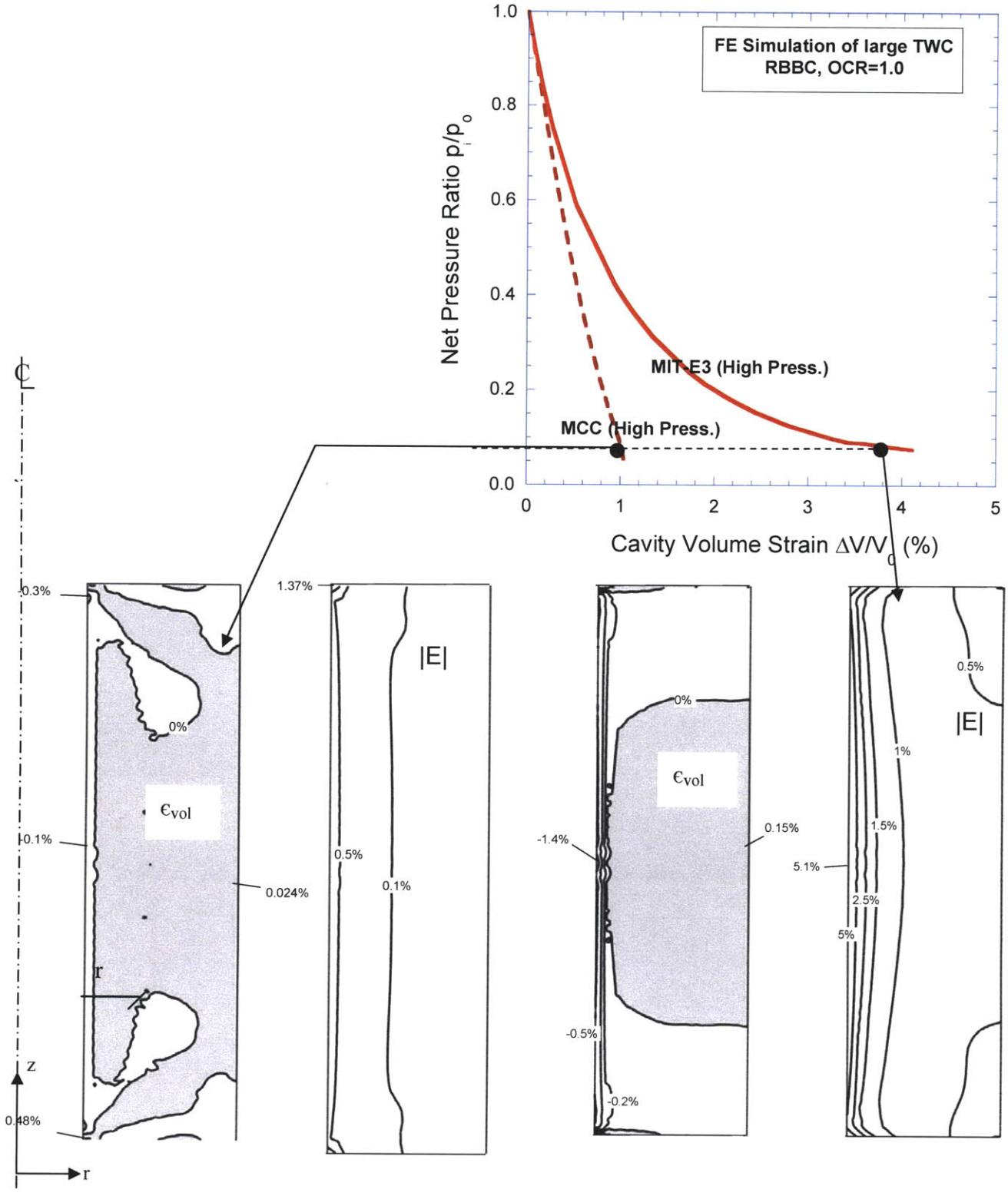

Figure 5.21 Computed volumetric and Shear Strain Contours at the p_i/p_0=0.075 predicted in Large TWC simulation using MCC and MIT-E3 models.

6 Effects of Formation Consolidation on Wellbore Stability

6.1 Introduction

In the field, wellbores are stabilized by steel casings that are installed a relatively short time after drilling. This chapter considers the effects of consolidation (i.e. migration of pore fluid) within the formation on the wellbore stability over the timeframe required for drilling and installation of wellbore casings. Numerical analyses of the coupled consolidation processes (time dependent deformations and pore pressures) are performed using the same effective stress soil models described in previous chapters, while seepage of pore water is controlled by D'Arcy's law with hydraulic conductivity controlled by the void ratio of the formation. The analyses make additional assumptions on seepage boundary conditions at the wellbore and the timeframe for wellbore installations. The results converge to the limiting case of undrained deformations for timeframes, $\Delta t \rightarrow 0$, which was assumed in Chapter 4.

Chapter 2 has presented several solutions for time-dependent behavior around circular openings in saturated rock (e.g.: Carter and Booker, 1982; Detournay and Cheng, 1988; and Charlez, 1997). However, most work on long term cavity stability has focused on analytical and semi-analytical solutions (Yu and Rowe, 1999; and Yu, 2000) using effective stress plasticity models (including Original Cam Clay and Modified Cam Clay) to describe stress-strain properties around the wellbore. These calculations assume fully drained conditions in the formation, which implicitly assumes that wellbore drilling occurs very slowly without generation of excess pore pressure. Drained analyses of this type do not consider the timeframe for consolidation and treat the formation as a single

phase medium. Such analyses provide a reference case on long term stability, but do not explain or predict wellbore deformations during drilling and casing operations.

Non-linear coupled consolidation analyses offer a more realistic representation of deformations and pore pressures within the formation. However, the analyses are affected by the boundary conditions assumed at the wellbore. Pore pressures are created due to shearing within the formation as drilling occurs and the wellbore is supported by drilling mud. The properties of the drilling mud are designed to prevent flow of water into the formation. However, overpressures within the wellbore can lead to the formation of a low permeability filter cake at the surface. Uncertainties in the boundary condition can range from conditions 1) where there is drainage of pore fluid into the wellbore (i.e. clay has lower permeability than mud cake) to 2) the mud cake forms an effectively impermeable boundary (i.e. permeability of the filter is much lower than the surrounding clay). This analysis uses Resedimented Boston Blue Clay (RBBC) as the analog formation material. Permeability properties of RBBC are discussed in Chapter 3.

The following conditions are simulated in the current analyses: Wellbore drilling is assumed to occur instantaneously under undrained conditions, such that excess pore pressures are created around the wellbore in response to the unloading process (results of this stage are presented in Chapter 4). Coupled consolidation (deformations and flow) are allowed to occur during the time frame for casing construction in the field. Two extreme cases are considered for the drainage boundary conditions in this approximate analysis: 1) the filter cake is ineffective and formation pore pressures equilibrate to wellbore mud pressures; 2) the filter cake forms an impermeable seal at the cavity wall and drainage is totally prevented at that boundary. The latter condition has been also used extensively to consider stress changes around piles and penetrometers (e.g. Whittle, 1992; Aubeny, 1992; Sutabutr, 1999).

This chapter has three sections. Section 6.2 describes the base case of unloading a vertical wellbore in undrained and drained conditions, and using different time frames. The

section presents the details of a vertical wellbore subjected to different unloading and consolidation scenarios. Four scenarios are considered: scenarios I and II are based on the assumption of full interaction between the well pressure and the pore pressure, while scenarios III and IV are based on the assumption of perfect isolation of the cavity wall. The undrained unloading is continued to the design mud pressure = $0.2\sigma'_{v0}$ in scenarios I and III, while the final value of well pressure is $-0.2\sigma'_{v0}$ in scenarios II and IV. All analyses are carried out using the MCC and MIT-E3 effective stress models, employing the high consolidation pressure calibration discussed in Chapter 3.

Section 6.3 repeats the processes in Section 6.2 but for deviated wellbores. The deviation angles used for the analyses are 30^0, 45^0, 60^0 and 90^0. Only scenarios I and III are applied to the deviated wellbores. The decrease in well pressure for deviated wellbores beyond the design mud pressure is not practical because highly deviated wellbores do not sustain further decreases in well pressure as was shown in Chapter 4. The deviated wellbores are represented by a slice model in the FE program ABAQUS as shown in Chapter 3. The numerical problems associated with using the slice model in E-C analysis[1] are presented and discussed.

Section 6.4 consolidates the results from Sections 6.2 and 6.3 and draws important conclusions on the effect of consolidation on stability. Four different criteria for comparison are used to describe behavior around wellbores: deformations at cavity wall, pore pressure distribution, volumetric strain distribution, and radial deformations. This section demonstrates that predicted behavior depends on the chosen constitutive model. More realistic models such as the MIT-E3 give a better prediction of soil behavior in a wellbore problem.

---

[1] Coupled non-linear analyses of deformations and pore water flow is described as E-C analysis by Whittle et al., 2001, as discussed in Chapter 3.

6.2 Base Case: Stress conditions around a vertical wellbore

This section describes the base case of unloading a vertical wellbore in K_0-normally consolidated BBC. The section is divided into two main subsections. First, the vertical wellbore is subjected to a typical unloading scenario where the mud pressure is decreased to the underbalanced drilling limit. In this scenario, 4 different drainage conditions are considered: 1) totally drained wellbore, 2) undrained wellbore, 3) unloading in real time as in the field with permeable cavity wall, and 4) E-C consolidation analysis.

The second subsection uses the E-C analysis to investigate 4 different scenarios of unloading the vertical wellbore. Scenario I comprises unloading a permeable vertical wellbore to a design mud pressure of $0.2\sigma'_{v0}$ and then monitor consolidation effects for 30 days. Scenario II is similar to I but the vertical wellbore is unloaded to $-0.2\sigma'_{v0}$. Scenarios III and IV are the same as I and II but applied to impermeable wellbores.

6.2.1 Unloading to underbalanced drilling limit

Stress conditions around a vertical wellbore are represented by a 2D plane strain, quarter-space models. The creation of the cavity in the field is mimicked by unloading the cavity wall in the model and gradually decreasing the net radial stresses at cavity wall to zero (underbalanced drilling limit[2]). Drained conditions are achieved by performing unloading over large time steps, while undrained conditions are approximated using an artificially short time-scale.

Figure 6.1 compares the computed ground response curves predicted by the MCC model using different drainage conditions. The ground response curves describe the pressure-deformations relationship at the cavity wall of a vertical wellbore resulting from the decrease in the well pressure. In addition to analyses with drained and undrained

[2] The underbalanced drilling is performed using mud pressures that are lower than static pore pressures within the formation, $p_w - u_0 < 0$.

conditions, a third case considers the time frame involved in drilling operations. Typical rates of drilling for oil well explorations range from 20m/hr to 60m/hr, with 30m/hr being a typical drilling rate (S. Willson pers. comm.). Assuming that a plane strain model has a thickness of unit length, the well pressure is decreased over a limited time of Δt=0.033 hours. This corresponds to a time factor comparable to undrained conditions ($T=10^{-3}$)[3]. However, it is also assumed that no excess pore pressures develop at the cavity wall during drilling. Hence, the boundary conditions resemble drainage conditions at the cavity wall.

Figure 6.1 shows that the ground response in all three cases is very similar, according to the MCC model predictions. The maximum inward deformation is 0.65% of the cavity radius in undrained conditions, 0.68% in real time drilling conditions, and 0.72% in drained conditions at the cavity wall. These results agree with intuitive expectations. Maintaining drained conditions allows volume changes to occur during the unloading procedure, leading to more inward deformations. The consolidation analysis, where partial drainage is allowed, results in intermediate values of inward deformations within the range of results provided by the extreme cases of drained and undrained conditions.

Figure 6.2 shows simulated ground response curves for the MIT-E3 model. In this case, the drained and undrained responses are very similar up to the maximum inward deformation, 1.78% at $(p_i-u_0)/\sigma'_{v0} = 0$ (consistent with Figure 4.1). The real time ground response showed less deformation than the undrained ground response, with maximum inward deformation of 1.58%.

To shed more light on the ground response curves, the in-plane effective stress paths (p-q) and shear stress-strain curves are plotted in Figure 6.3 a and b, for the MCC model and MIT-E3 models, respectively. Both the MCC and MIT-E3 models predict similar drained and undrained effective stress paths. This is attributed to the increase in circumferential

---

[3] $T = \frac{\sigma' kt}{\gamma_w R^2}$; where k=1.44E-7 m/hr, σ'=10MPa, and R=0.25m.

stresses leading to plane strain compression concurrent with expansion due to the decrease in radial stresses. The combined effect of a decrease in radial stresses and an independent increase in circumferential stresses results in quite close correspondence between drained and undrained effective stress paths in both models. It is worth noting that the critical state can not be accurately represented in the p-q space because this problem is not axi-symmetric (the out-of-plane stress is not equal to one of the in-plane stresses). However, all predictions for all drainage conditions develop significant plastic strains except for the MCC prediction of the effective stress path in undrained conditions, where underbalanced drilling limit is reached before plastic strains are generated.

E-C Analysis on Vertical Wellbores

The wellbore unloading problem can be simplified without compromising the solution by considering it as two separate problems in series: wellbore drilling as an undrained unloading problem and time to casing installation as a consolidation problem. Whittle et al. (2001) described this as the E-C analysis as discussed in Chapter 3. The drainage conditions at cavity wall depend on the quality of the filter cake formed by the drilling fluid. Two extreme cases are considered in this analysis; permeable and impermeable cavity walls. In the permeable wellbore, an intermediate step is introduced between the undrained and consolidation stages. This intermediate step starts by allowing drainage at cavity wall and ends when pore pressures at the cavity wall equilibrate with the mud pressure in the cavity. In the impermeable wellbore, the pore pressures start to redistribute around the wellbore directly after the undrained stage.

Figure 6.4 a and b illustrate the in-plane effective stress paths and the shear stress-strain curves of an element at the cavity wall for K_0-nromally consolidated RBBC using the MCC and MIT-E3 soil models, respectively. The behaviors in the permeable and impermeable wellbore are very similar. The stress path in the consolidation stage deviates abruptly toward the dry side of the critical state. Also, the consolidation phase appears as softening in the stress strain curve. The MIT-E3 predictions are capable of detecting a

sharp drop in the strength for the permeable wellbore during the intermediate stage, unlike the behavior in the impermeable wellbore. Otherwise, the stress paths and the stress strain curves are the same. This result can be attributed to the fact that whether pore pressure redistribution or pore pressure dissipation is occurring, the final value of the pore pressure at the cavity wall is zero. This means that the driving forces in the consolidation phase are the same but act at different rates. Only the MIT-E3 model, which is highly non-linear, is capable of detecting differences in behavior.

Figure 6.5a shows the pore pressure distributions in the radial direction after the undrained unloading and at different values of the dimensionless time factor[4] using the MCC model. Both the impermeable and permeable wellbores are shown. The initial pore pressure distribution for the consolidation phase is directly calculated from the undrained stage in the impermeable wellbore case. In the permeable wellbore case, the initial pore pressure distribution is adjusted for the drainage effects at the cavity wall by applying the intermediate step. The negative pore pressures are suddenly dissipated in extremely close proximity to the cavity wall (<0.1% of the radius). The initial pore pressure distribution illustrates zones of negative pore pressures ($\Delta u/\sigma'_{v0}$ = -0.15) at the cavity wall up to a radial distance of $r/R_0 = 2$, followed by a larger zone of positive pore pressures ($\Delta u/\sigma'_{v0}$ = 0.003) up to a radial distance of 8m. In the impermeable wellbore the negative and positive pore pressures dissipate gradually as the pore water migrates and the pressures redistribute. The final distribution of pore pressures shows very small magnitudes of excess pore pressures. In the permeable wellbore, the pore pressures dissipate until there is no more excess pore pressures negative or positive.

During the consolidation phase, the zones of positive pore pressures are translated into compression zones, and the zones of negative pore pressures are translated into expansion zones. Figure 6.5b shows the distribution of volumetric strains at different values of the dimensionless time factor. In the impermeable wellbore, the expansion volume strain

[4] The dimensionless time factor, $T=\frac{\sigma' kt}{\gamma_w R^2}$.

increases through time until it reaches a value of -0.2% at T=1.6. In the permeable wellbore, the expansion volume strain rises to -0.2% directly at the cavity wall, and then the expansive behavior percolates in the soil matrix up to a radial distance of $r/R_0 = 2$, similar to the final distribution in the impermeable case. Simultaneously, compression volume strains spreads with time over a wider distance and larger area because these strains occur at larger radial distance, but by very low values (~0.01%). The compression and expansion zones cancel each other as shown in Figure 6.5c. There radial deformations do not change with time, except for a slight inward increase from 0.65% of the radius to 0.68% of the radius in both the permeable and impermeable cases.

Figures 6.6 a, b, and c show similar results for the MIT-E3 model. The results indicate similar trends but quantitative differences between the impermeable and permeable wellbore cases as the MCC results. The MIT-E3 model predicts higher positive pore pressures ($\Delta u/\sigma'_{v0} = 0.015$) than the MCC model, and less negative pore pressures ($\Delta u/\sigma'_{v0} = -0.08$). However, both compressive and expansive strains predicted by the MIT-E3 model are higher than the MCC model predictions. Compressive strains reach 0.15% at radial distance of $r/R_0 = 3$, and expansive strains reach -0.4% at the cavity wall.

The inward radial deformations predicted by the MIT-E3 model are much higher than the MCC model predictions. However, the time effect predicted by the MIT-E3 is similar to that predicted by the MCC model. The radial deformations do not change with time except for a slight increase in inward deformation at the cavity wall, from 1.8% to 1.9% of the cavity radius. This increase is attributed to the simultaneous increase in compression and expansion zones that cancel each other out and amount to slight inward radial movement. Also, magnitudes of volume strains in compression and extension as well as the generated excess pore pressures are relatively small in the vertical wellbore case that eventually leads to small changes in inward radial deformations.

6.2.2 Other Scenarios for Vertical Wellbores

This section considers a variety of scenarios for stress changes caused by drilling and casing of a vertical wellbore.

Scenario I

In scenario I, the mud pressure decreases to 20% of the initial vertical effective stress in the formation, σ'_{v0}. The decrease in mud pressure is simulated over a very short time period, to mimic undrained conditions. After the undrained unloading, seepage is allowed at the cavity wall representing the possibility of a breach in the filter cake or an ineffective cake formation. Figure 6.7a shows the pore pressure distributions in the radial direction at the end of drilling and at selected time factors during consolidation.

The MCC model predicts a small zone of negative excess pore pressures at the cavity wall after drilling, extending to a distance $r/R_0 = 1.5$ from the cavity wall. The MIT-E3 model predicts small positive pore pressures for the cavity wall up to $r/R_0 = 4$. This absence of negative pore pressures is due to the fact that the MIT-E3 model predicts a higher tendency to contract as a result of the increase in circumferential stresses when the well pressure is dropped to only 20% of the initial vertical stresses.

In this scenario, the mud pressure at the cavity wall is set at $(p_i-u_0)/\sigma'_{v0} = 0.2$ such that pore water must flow from the wellbore into the formation. Through time, the pore pressures continue to increase beyond the cavity wall, as predicted by both the MCC and the MIT-E3 models. This seepage is reflected in the distributions of volumetric strains at different instants as shown in Figure 6.7b. No volumetric strains are allowed during the undrained stage because local pore pressure migration is prohibited. After drainage is allowed, expansion occurs only in close proximity to the cavity wall. This expansion zone propagates through the soil matrix with the increase in pore pressures. The value of the expansion strain at the cavity wall remains constant through consolidation time, as predicted by both constitutive models. However, the MIT-E3 model predicts larger expansion strains at the cavity wall ($\epsilon_{vol} = -0.75\%$) than MCC ($\epsilon_{vol} = -0.3\%$).

These expansive volumetric strains are translated into radial deformations as shown in Figure 6.7c. The inward deformations are considered positive; the outward deformations are considered negative. Inward deformations increase at the cavity wall and up to a distance of $0.8R_0$. Beyond $0.8R_0$, the total inward deformations that occurred at the end of the undrained stage start to decrease with the increase in pore pressures. At T=1.6, the MIT-E3 model predicts the disappearance of any radial deformations beyond the distance of $7R_0$, while the MCC model predicts outward deformations beyond $3R_0$.

Scenario II

In scenario II the well pressure is decreased to zero and tensile stresses are applied at the cavity wall at $(p_i-u_0)/\sigma'_{v0} = -0.2$. This scenario represents a case where the well pressure provided by the density of the drilling fluid is less than the initial hydrostatic pore pressures inherently present in the ground before the drilling process occurs. Then, the pore pressures are gradually changed into the same value as the well pressure allowing pore pressures from the soil matrix to dissipate into the well. This drainage boundary condition is similar to that in scenario I.

The initial pore pressure distribution in the radial direction is shown in Figure 6.8a. The final well pressure in scenario II is much lower than that in scenario I; thus, both constitutive models predicts high negative pore pressures at the cavity wall, and gradually zero excess pore pressure occurs at $r/R_0 = 3$. The MIT-E3 model predicts positive pore pressures between $2R_0$ and $10R_0$. The high negative pore pressure slightly increase toward zero in close proximity to the cavity wall (<0.5R). Beyond the distance of 0.5R, pore pressures decrease with time. There is very little change in excess pore pressure values at cavity wall because the mud pressure value is close to the negative pore pressure value at the end of the undrained unloading stage.

In Figure 6.8b, the distribution of volumetric strains is shown at different instants during the consolidation process. At the cavity wall, expansion strains occur and propagate

through time a small distance into the soil matrix ($<0.5R_0$), in the same zones where negative pore pressures increase toward zero. Beyond $0.5R_0$ compression strains occur and increase through time to cover all areas where pore pressures are decreasing. In contrast to scenario I, the radial deformations show minimal change through consolidation, as shown in Figure 6.8c, because the adjacent compression and expansion zones resulted in very little increase in radial deformations. However, the final radial deformations predicted in scenario II are much higher than those predicted in scenario I because the well pressure maintained at the cavity wall is much lower.

Scenario III

In scenario III, the well pressure is decreased to 20% of the initial vertical effective stresses, $(p_i-u_0)/\sigma'_{v0} = 0.2$, as in scenario I, maintaining undrained conditions. The consolidation analysis is performed by allowing the existing pore pressures to migrate and reallocate over a time period of 30 days (T=1.6), without allowing drainage through cavity wall. This scenario is similar to the case of impermeable wellbore previously discussed.

The initial distribution of pore pressures is similar to that in scenario I as shown in Figure 6.9a. The different drainage boundary condition at the cavity wall leads to a different redistribution of the excess pore pressure within the formation. The high positive and high negative pore pressures predicted by the MCC model are redistributed along the radial direction until the highest negative and positive pore pressures are slightly less than or more than zero. The MIT-E3 model does not predict any negative pore pressures. The peak of the distribution of positive pore pressures is smoothed out through time leading to a decrease in pore pressures up to a distance of 3R; beyond this, a minor increase in pore pressures up to a distance of 10R.

The MCC model and the MIT-E3 model predict different patterns of compression and expansion as shown in Figure 6.9b. The MCC model predicts expansion zone in close

proximity to the cavity wall followed by compression zones within $3R_0$ from the cavity wall. The MIT-E3 model predicts expansion strain at the cavity wall that turns to compression with the pore pressure continuing to decrease. Compression strains continue to increase with time up to a distance of $3R_0$, after which slight expansion strains occur with the slight increase in pore pressures. Unlike scenario I, radial deformations do not change with time because of the interaction between adjacent compression and expansion zones as shown in Figure 6.9c.

Scenario IV

In scenario IV, the well pressure is decreased to zero and tensile stresses 20% of the initial vertical stresses are applied at the cavity wall, $(p_i-u_0)/\sigma'_{v0} = -0.2$, as in scenario II. The drainage at the cavity wall remains prohibited, as in scenario III (impermeable wellbore). The consolidation process is terminated when effective radial stresses at cavity wall drop below zero i.e. when pore pressures at cavity wall is equal or higher than mud pressure.

Due to the large changes in well pressure, the generated negative pore pressures are much higher than predicted in scenario III. Although the analyses are terminated much earlier (after 10 hours of consolidation), and pore pressures did not entirely re-equilibrate as shown in Figure 6.10a, the volume strains are much higher than those in scenario III as shown in Figure 6.10b. However, the adjacent expansion and compression zones lead to negligible changes in radial deformations through time, as shown in Figure 6.10c. This case is considered unrealistic because the mud pressure is generally not permitted below the in-situ pore pressures within the formation. If such a case occurs, an adequate seal of the cavity wall (although helping with stability and minimizing radial deformations in scenario III) hastens the instability in scenario IV by allowing pore pressure redistribution, and hence a drop in effective radial stresses.

6.3 Consolidation around Non-vertical Wellbores

6.3.1 Using quasi-3D slice model

Three deviated wellbores are considered in this section: $\omega = 30^0$, 45^0, and 60^0. The quasi 3D slice model (Figure 3.2) is used to depict the deviated wellbores using the same methodology explained in Chapter 3 in detail. A single layer of elements constitutes the mesh half of the space around the wellbore. Plane strain conditions are enforced by prohibiting any out of plane deformations.

During the consolidation phase, the pore pressure migration and redistribution are supposed to be planar as the deformations are also planar. An artificial permeability tensor is assigned to the material definition to impose the condition of planar pore fluid flow. The permeability in the direction normal to the plane of the cavity (z-direction) is set to ($k_{zz}/k_{yy} = k_{zz}/k_{xx} = 10^{-10}$) of the in-plane permeability. The true permeability in the field is not isotropic and as long as only planar flow is considered, the permeability is assumed to be cross anisotropic with axes of reference coinciding with the local axes of reference of the wellbore.

Several factors contribute to the complexity of performing coupled analysis using a slice model. The non-linearity and high sophistication of the constitutive models (MCC and especially MIT-E3), the highly constrained 3D model, and the artificial cross-anisotropic permeability tensor are all factors that burden the FE solver. Some accuracy needed to be sacrificed to acquire a stable solution by using large time intervals during the consolidation phase.

Scenario I

Figure 6.11 show the MIT-E3 prediction of excess pore pressure distribution around a 30^0 deviated wellbore. The distribution of excess pore pressures is depicted at 4 different instants during the consolidation process: T=0.002, 0.02, 0.2, and 1.6. The figure shows how seepage from the permeable cavity wall dominates the distribution of the excess

pore pressures through time, and form nearly concentric hoops of gradually decreasing pore pressures around the cavity wall. Figure 6.12 show the volumetric strains around the same wellbore. Expansion zones are found around the wellbore, increase with time, and elongate in the direction of the crown. Figure 6.13 shows the radial deformations around this wellbore. The inward deformations are maximum at the Crown Point and oriented as oval shapes along $\theta=90^0$.

Similarly, Figures 6.14, 6.15, and 6.16 show the MIT-E3 predictions of excess pore pressure, volumetric strain, and radial deformation distributions around a 45^0 deviated permeable wellbore. Results of the 45^0 wellbore show lobes of positive and negative excess pore pressures are generated and oriented along radial direction, $\theta = 0^0$ and 90^0, respectively. The negative pore pressures prevail near the Crown Point where the released radial stresses are initially the major principal stresses. The positive pore pressures prevail near the Springline where the released radial stresses are the minor principal stresses. With larger deviation angle, higher positive pore pressures are generated near the springline and negative pore pressures are generated near the crown. This leads to more expansion and inward deformations near the crown. The results from the 60^0 wellbore are very similar to those 45^0 wellbore as shown in Figures 6.17, 6.18, and 6.19.

Figures 6.20 through 6.29 show the MCC predictions of excess pore pressures, volumetric strains, and radial deformations for the 30^0, 45^0, and 60^0 wellbores. The MCC results have similar trends to those of the MIT-E3 model. However, the MCC model predicts smaller deformations at cavity wall and within the formation. At high deviation angles ($\omega=60^0$), using the MCC model generates larger magnitudes of positive and negative pore pressures than using the MIT-E3. Pore pressures along $\theta=0^0$ equilibrate with seepage from the wellbore and high positive peaks dissipates. Compression zones ($\epsilon_{vol} = 0.1\%$) are created behind the cavity wall along $\theta=0^0$ concurrent with dissipation of the high positive pore pressure peaks. This leads to slight outward deformations (<0.1% of the cavity radius) along $\theta=0^0$ generated from the compressions zones. These expansion

strains predicted by the MCC model are smaller than those predicted by the MIT-E3 model.

Scenario III

Figure 6.29 shows the distribution of excess pore pressures around an impermeable wellbore deviated by 30^0 as predicted by the MIT-E3 model. The peaks of positive and negative pore pressures are smoothed out through time due to reallocation and redistribution, rather than being dominated by seepage from the cavity as in scenario I. The negative pore pressures near the Crown Point increase with time until all negative pore pressures around the cavity wall are diffused. The high positive pore pressures near the Springline decrease with time and diffuse into larger areas in the soil matrix, rendering the excess pore pressures around the cavity wall of negligible value. Figure 6.30 show the MIT-E3 predictions of the volumetric strain distributions around the same wellbore. Relatively small expansion strains are found at the crown area. Unlike the results in scenario I, compression zones occur at the springline area. Figure 6.31 shows the radial deformations around the wellbore. Maximum inward deformations occur at the crown and the area around it close to the cavity wall is dominated by inward deformations. Through time, distribution of radial deformations does not change significantly because volumetric strains are small.

Figures 6.32 through 6.34 and Figures 6.35 through 6.37 show similar MIT-E3 predictions for the 45^0 wellbore and the 60^0 wellbore, respectively. The magnitude of expansion and compression volume strains increase with deviation angle and magnitudes of positive and negative excess pore pressures. In Figure 6.36, the distribution of compression strains around the 60^0 wellbore is shown to be erratic toward the end of the consolidation phase. This erratic distribution indicates a tendency toward instability, similar to the behavior of a horizontal wellbore predicted by the MIT-E3 model shown in the next section.

Figures 6.38 through 6.46 show the MCC predictions of excess pore pressures, volumetric strains, and radial deformations for the 30^0, 45^0, and 60^0 wellbores. Trends similar to the results in scenario I are found such that the expansion zones and inward deformations are in the form of lobes at $\theta=90^0$. Predicted pore pressures by the MCC model are higher than those predicted by MIT-E3, while lower expansion strains and inward deformations are found. Unlike scenario I results, compression zones are found in all wellbores, oriented in lobes along $\theta=0^0$. Also, outward deformations do not occur for the 45^0 and 60^0 wellbores. There is no flow from the cavity into the soil; hence, observed outward deformations are negligible.

6.3.2 Using 2D model

The procedure of modeling a horizontal wellbore is explained in Chapter 3 in detail. The wellbore is modeled using a 2-dimensional plane strain quarter-space model. The far field stresses are in equilibrium with the initial distribution of stresses in the soil matrix. The unloading process is performed in stages, maintaining undrained conditions by keeping extremely short time intervals. First, the deviator component of the supporting stresses at the cavity wall is removed. Then, the uniform well pressure at the cavity wall is decreased to 20% of the value of the initial vertical stresses as in unloading scenarios I and III.

In this section, the MCC and MIT-E3 predictions are presented simultaneously for each scenario (I and III). The contour figures presented in this section describe the pore pressure distributions, the volumetric strain distributions, and the radial deformations, as predicted by both models. Figure 6.47 shows the MIT-E3 predictions of excess pore pressures distribution around a horizontal wellbore, while Figure 6.48 shows the MCC predictions. The negative pore pressures prevail near the Crown Point, while positive pore pressures prevail near the Springline. Through time, the seepage source at the cavity wall ($p_i/\sigma'_{v0} = 0.2$) affects the soil formation and pore pressures redistribute such that the fluid distribution at T =1.6 approaches an axisymmetric field. The MIT-E3 model

estimates failure at high mud pressure, close to the chosen reference mud pressure. Hence, the excess pore pressure distribution is irregular near the Springline. On the other hand, the MCC model generates higher magnitudes of positive and negative excess pore pressures.

Figures 6.49 and 6.50 show the zone of volumetric expansion and compression generated within the formation as seepage occurs from the wellbore as predicted by the MIT-E3 and MCC models, respectively. These strains are linked with inward radial deformation and squeezing of the cavity wall a shown in Figures 6.51 and 6.52. The MIT-E3 predicted irregular distributions of expansion and compression zones in the same way positive and negative excess pore pressures are distributed. Very high expansion strains (10%) are found at angular dimension $\theta=15^0$, where local increase in radial deformations exists. The MCC model predicts more regular patterns of volume strains. The expansion zones in Figure 6.50 match the inward radial deformations in Figure 6.52. Near the crown, the inward radial deformations occurring at the end of the undrained stage increase slightly where expansion occurs and decrease behind the cavity wall near the springline where compression occurs. Outward deformations occur after some time in the consolidation stage.

Figures 6.53 through 6.58 show similar MIT-E3 and MCC predictions for the impermeable horizontal wellbore. Pore pressure redistributes through time and the peaks of high positive and negative pore pressures get smoothed out as shown in Figures 6.53 and 6.54. Expansion strains initially occur around the springline and the crown points where the pore pressure increases at the beginning of the consolidation process. Through time, the pore pressures continue to increase at the Crown Point and the area around. With the pore pressure increase, the expansion strain increases as shown in Figures 6.55 and 6.56. The pore pressure at the springline point and the area around it eventually decreases after a slight preliminary increase; the expansion strains are transformed into compression strains at the end of the consolidation stage. The distribution of radial deformation shown in Figures 6.57 and 6.58 shows a very similar behavior to that found in scenario I. The MCC model predicts maximum inward radial deformation occurs at the

Crown Point and the minimum inward radial deformation occurs at the springline point. The Outward deformation also occurs behind the cavity wall in the radial direction starting from the springline point. The MIT-E3 model predicts large inward deformations at Crown and at $\theta=15^0$, and no outward deformations.

Effect of Consolidation on stability

The MIT-E3 model predicts failure occuring in horizontal wellbores at mud pressure= $\sim 0.18\sigma'_{v0}$ as discussed in Chapter 4. This is indicated by zones of high octahedral shear strains at angular dimension, $\theta=15^0$. Figure 6.59 depicts the distribution of the octahedral shear strains (second invariant of the deviatoric strain tensor) to show the effect consolidation on shear strains during unloading scenarios I and III. Failure occurs in the form of a breakout shape around the springline point of the wellbore. Shear strains increase through time up to a value of 40% at T=1.6, indicating the chance of localized failure during scenario I. In scenario III, the maximum strain at T=1.6 occurs near the springline point and is 27%. The increase in shear strains occurs at points where small excess pore pressures are generated during the undrained stage. During consolidation, pore water migrates to these areas causing high expansion strains and local increase in inward deformations. Lower shear strains in scenario III indicate the benefit of sealing the cavity wall and preventing seepage; however, allowing long consolidation times is still a threat to the stability of horizontal wellbores and facilitates localized failure.

6.4 Summary and Conclusions

The results in this chapter show that pore pressure equilibration (permeable wellbore) or redistribution (impermeable wellbore) lead to some increase in cavity deformations at cavity wall but more importantly significant volume change and radial deformations behind the cavity wall and around the wellbore. Consolidation around wellbores is highly dependent on the deviation angle of the wellbore and drainage conditions at cavity wall. However, the results are also significantly affected by the chosen constitutive model. The

more realistic MIT-E3 model gives more reliable predictions of wellbore stability during consolidation.

Three main observations can be made from the presented results:

1- With increase in deviation angle, the deviatoric component of geostatic stresses generate higher negative pore pressure near the Crown Point and higher positive pore pressures near the Springline of the wellbore. During consolidation, higher pore pressure gradients lead to more deformations around wellbore. In a horizontal wellbore, the MIT-E3 model even predicts instability mechanisms during consolidation due to a local increase in octahedral shear strains.

2- The MIT-E3 soil model predicts larger deformations than the MCC model in all deviation angles. The sophisticated formulation of MIT-E3 discussed in Chapter 3 (anisotropic yield surface, bounding surface plasticity, kinematic hardening) enables a more realistic depiction of the effects of deviation angle. The model is capable of illustrating the onset of localized failure in contours of octahedral shear strains. On the other hand, the MCC model predicts higher positive pore pressures. The positive pore pressures near the Springline generate significant compression zones during consolidation behind the cavity wall. Adjacent compression and extension zones result in relatively small increase in cavity deformations.

3- Unloading scenario I allows drainage at cavity wall and permits pore fluid flow in and out of the wellbore. This scenario generates more deformations at cavity wall and more volume change and radial deformations around the cavity. This becomes more significant with increase in deviation of wellbores and more obvious in MIT-E3 predictions. Scenario III generates more compression volume strains resulting in less inward deformations at the cavity.

These conclusions are illustrated in the following two subsections where results from the previous section are summarized. The first subsection discusses deformation at cavity

wall and cavity distortions. The second subsection describes the behavior around wellbores by presenting radial distributions of pore pressure, volume strains, and radial deformations at $\theta=0^0$ (Springline direction) and 90^0 (Crown direction).

6.4.1 Cavity Deformations

The distortion of the wellbore cavity is indicated by the ratio of the inward deformations at springline, δ_{sp} to those at the crown, δ_{cr} (Distortion ratio). Increase in distortion is indicated by change in distortion ratio further from unity (i.e. higher than or lower than 1). Maximum deformations occur at the crown at the end of the undrained unloading. Thus, the cavity distortion ratio (δ_{sp}/δ_{cr}) at the beginning of the consolidation stage starts with a value less than unity. Figures 6.60 a and b show the evolution of the cavity distortion ratio through time, as predicted by the MCC model and the MIT-E3 model for the permeable (scenario I) and the impermeable (scenario III) respectively.

The MCC model predicts that the distortion increases with time during the consolidation phase. The inward deformations at the crown increase at more rapid rates than at the springline in scenario I. The compression zones along $\theta=0^0$, predicted by the MCC model, inhibits the radial deformations at the springline relative to the deformations at the crown. The MIT-E3 model does not predict any compression in scenario I; thus, the springline point deforms freely and the cavity distortion ratio approaches unity. The MIT-E3 results for the inclined wellbores show some irregularities at later stages of consolidation due to increase in local deformations.

The MCC model and the MIT-E3 model predict compression zones in all non-vertical wellbores subjected to unloading scenario III. The inward deformation at the springline is inhibited relative to the inward deformation at the crown. The cavity distortion ratio continues to be less than unity during consolidation as shown in Figure 6.60b. The MCC predicts higher degrees of distortion in scenario III than in scenario I because higher

compression strains are predicted. The MIT-E3 predicts that the distortion remains relatively the same throughout the consolidation process.

In highly deviated wells and after significant time in the consolidation phase, deformations tend to increase locally near the Springline or near the Crown Point. In this case the distortion ratio is not sufficient to describe cavity deformations. Figure 6.61 a and c show MCC predictions of cavity deformations for vertical and horizontal wellbores, respectively. Figure 6.61 b and d show the MIT-E3 predictions for the same wellbore. In the figure, the three basic conclusions previously mentioned are obvious. Cavity deformations are larger in horizontal wells. The MIT-E3 model predicts larger deformations than MCC. In the MCC predictions, there is significant difference between inward deformations at Crown Point and that at the Springline. Also, scenario I generated more deformation in deviated wells than scenario III. This difference is more obvious in horizontal wells.

6.4.2 Consolidation behind cavity wall

The excess pore pressures along $\theta=0^0$ (Springline direction) increase with the deviation angle, and the peaks of positive pore pressures behind the cavity wall get smoothed out, as shown in Figure 6.62. The pore pressure values increase at the cavity wall and decrease behind it in scenario I. In scenario III, the pore pressures decrease through consolidation along the springline direction. Figure 6.63 shows the excess pore pressure distribution along $\theta=90^0$ (Crown direction). The generated pore pressures are negative and increase in value (toward zero) with the decrease in deviation angle. During consolidation, the negative pore pressures are diffused into the soil in scenario III while in scenario I, pore pressures are dominated by seepage from the cavity wall. The MIT-E3 predicts lower pore pressures than the MCC, but maintains similar trends. Excess pore pressure distribution from the horizontal wellbore predicted by the MIT-E3 model is erratic along $\theta=0^0$ because of the high shear strains shown in Figure 6.59 and the tendency for localized failure.

In scenario I, expansion strains occur in close proximity to the cavity wall where the pore pressures increase to $0.2\sigma'_{v0}$ by seepage as shown in Figures 6.64. Behind the cavity wall, compression zones occur along $\theta=0^0$ with decreasing values as the deviation angle decreases. In scenario III, compression strains dominate the direction for all wellbore deviations because the drop in pore pressures is higher in this scenario. Along the Crown direction, only expansion strains occur with the highest value at the cavity wall as shown in Figure 6.65. The expansion strains found in scenario I are higher than those found in scenario III. The MIT-E3 predictions of volumetric strain distributions, show that the results for different wellbores are very close. In the horizontal wellbore, volumetric strains are also erratic in the same way the pore pressures are.

Radial deformations are plotted along $\theta=0^0$ in Figure 6.66 and along $\theta=90^0$ in Figure 6.67. In the springline direction, the inward deformations at the cavity wall and outward deformations behind the cavity wall increase with deviation angles. During consolidation, inward deformations increase at the cavity wall and outward deformations increase behind the cavity wall. In scenario I, more outward deformations occur because of the seepage effects. In the crown direction, only inward deformations occur, which increase with deviation angles. The MIT-E3 predictions are affected by wellbore deviation in close proximity to the cavity wall. Beyond a radial distance of $1R_0$, deformations of different wellbores are very similar. The results from the horizontal wellbore show the effect of the plastic hinge where radial deformations increase abruptly at radial distance of $1R_0$. The MIT-E3 does not predict any outward deformations except for deformations of very small values in scenario I due to outward seepage. The effect of wellbore deviation is more significant along the Crown direction.

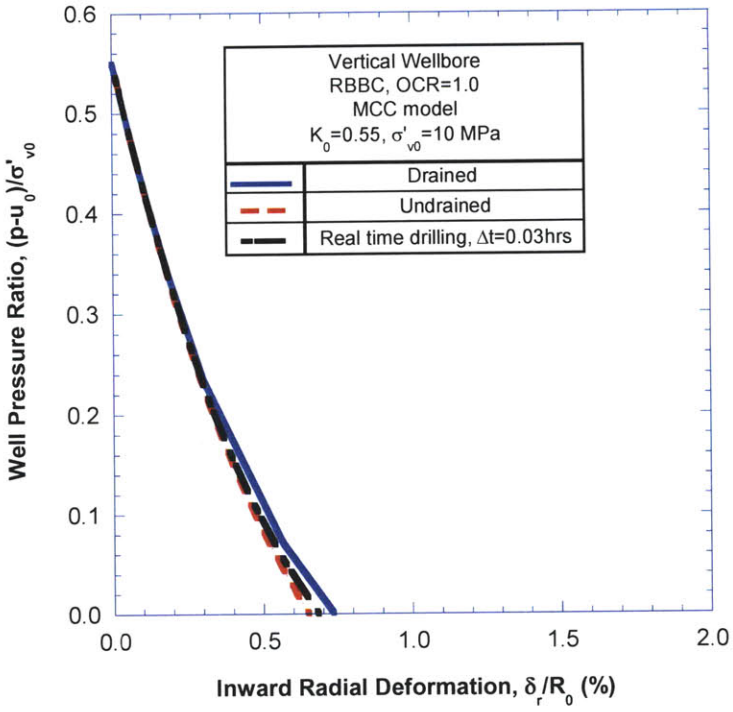

Figure 6.1 MCC predictions of uniform inward deformations of a vertical well in RBBC under different drainage conditions.

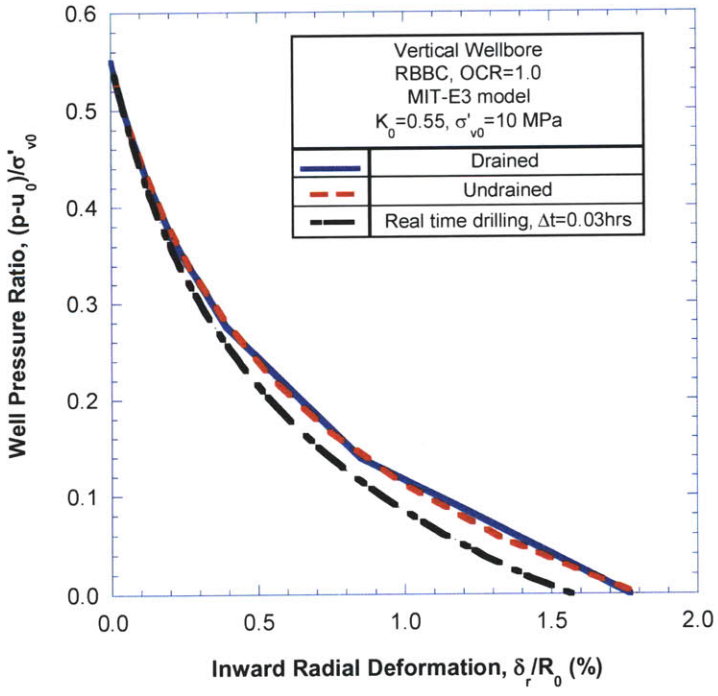

Figure 6.2 MIT-E3 predictions of uniform inward deformations of a vertical well in RBBC under different drainage conditions.

(a)

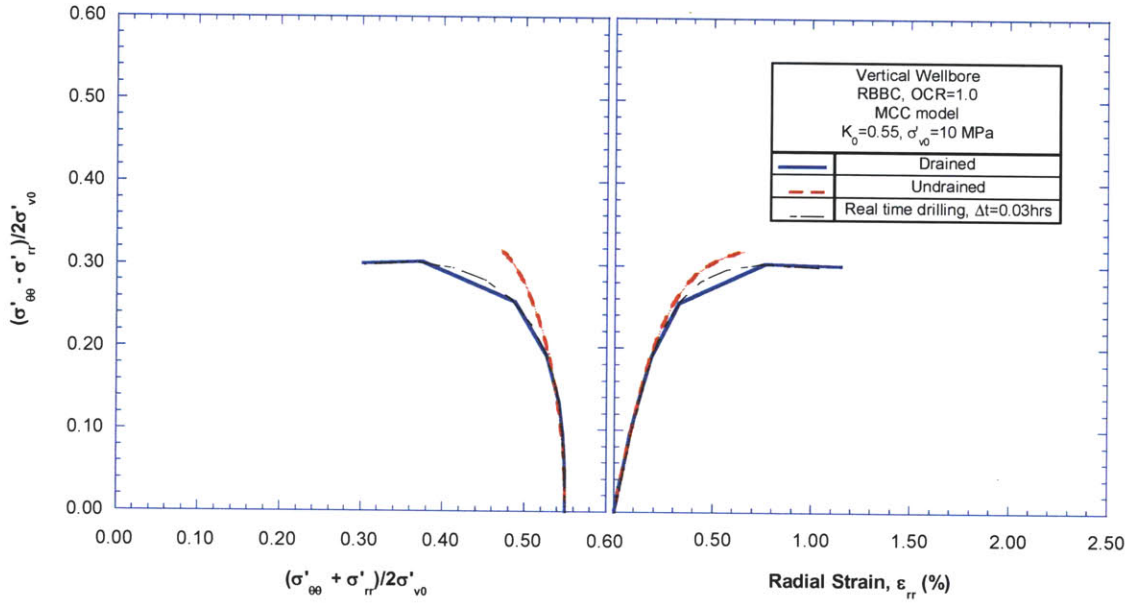

(b)

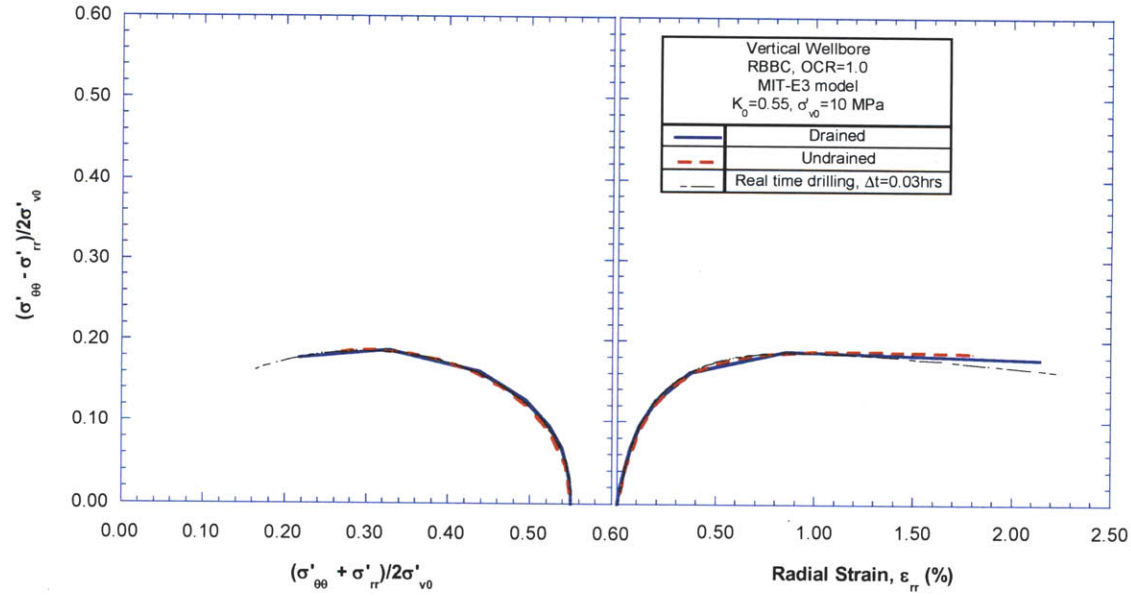

Figure 6.3 Effective stress paths and shear stress-strain behavior at cavity wall in a vertical wellbore in RBBC using (a) MCC and (b) MIT-E3 models under different drainage conditions.

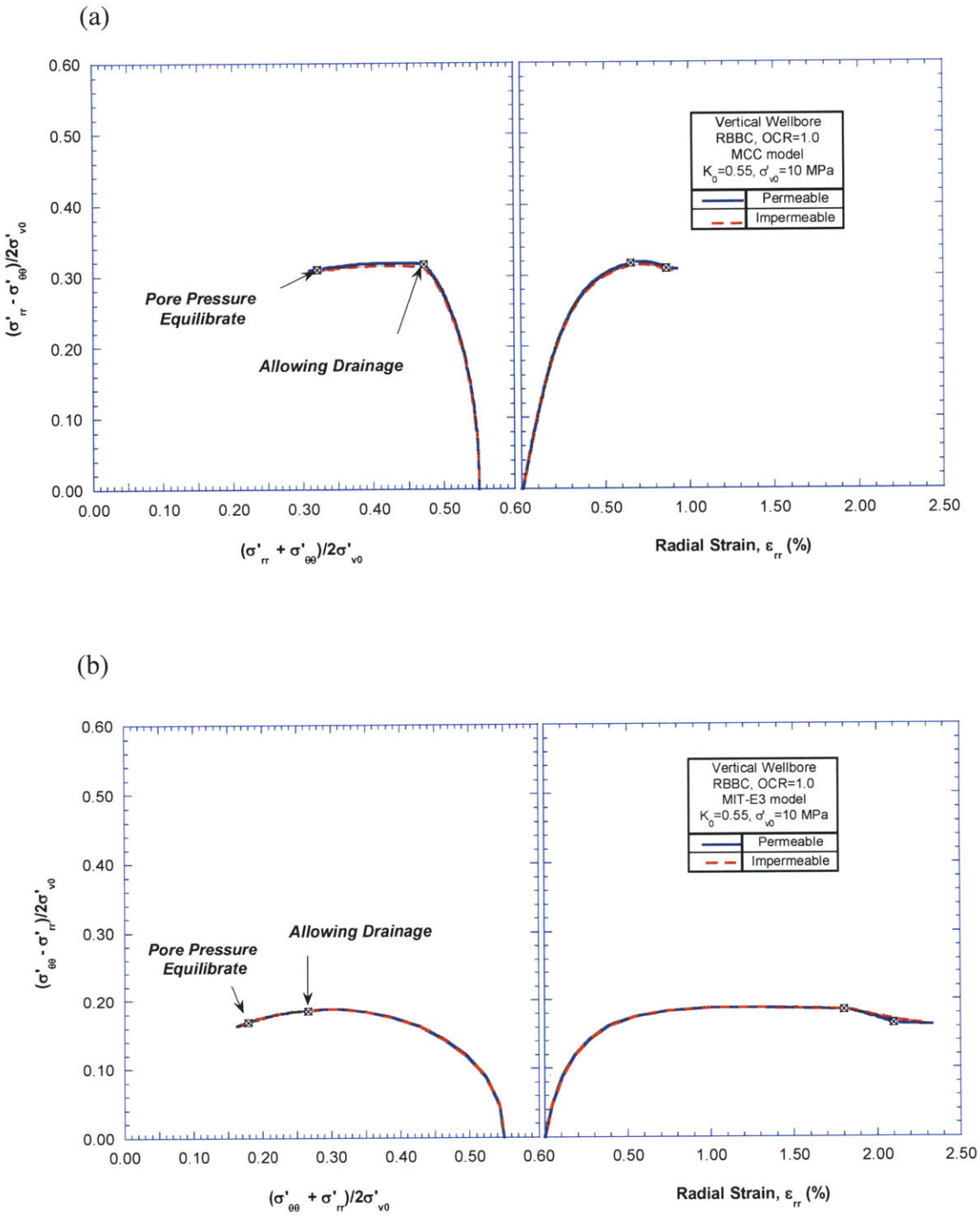

Figure 6.4 Effective stress paths and shear stress-strain behavior at cavity wall in a vertical wellbore in RBBC using (a) MCC and (b) MIT-E3 models with permeable and impermeable cavity walls.

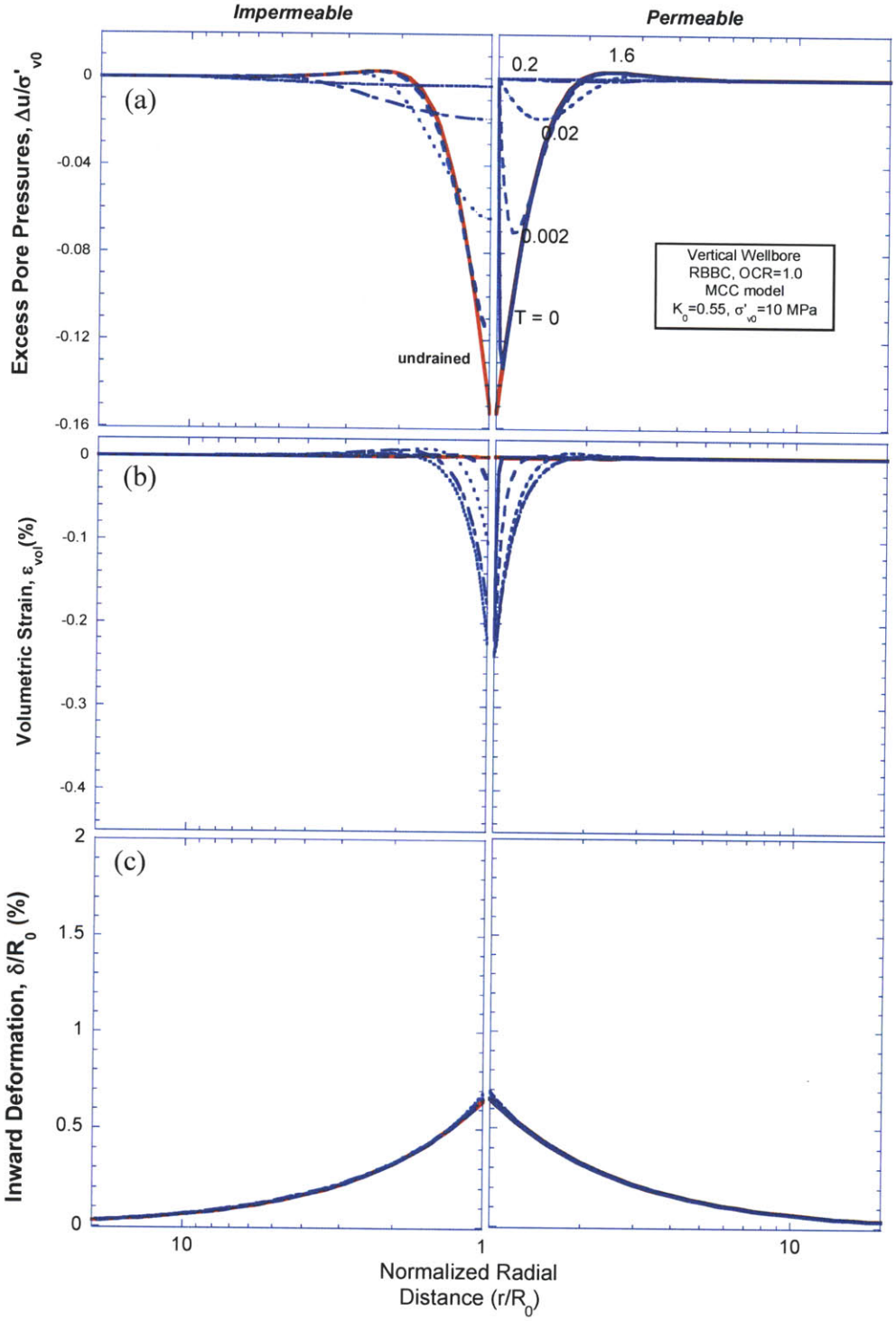

Figure 6.5 Radial distribution of (a) excess pore pressures, (b) volumetric strains, and (c) inward radial deformations around vertical wellbores with permeable and impermeable cavity wall using MCC model.

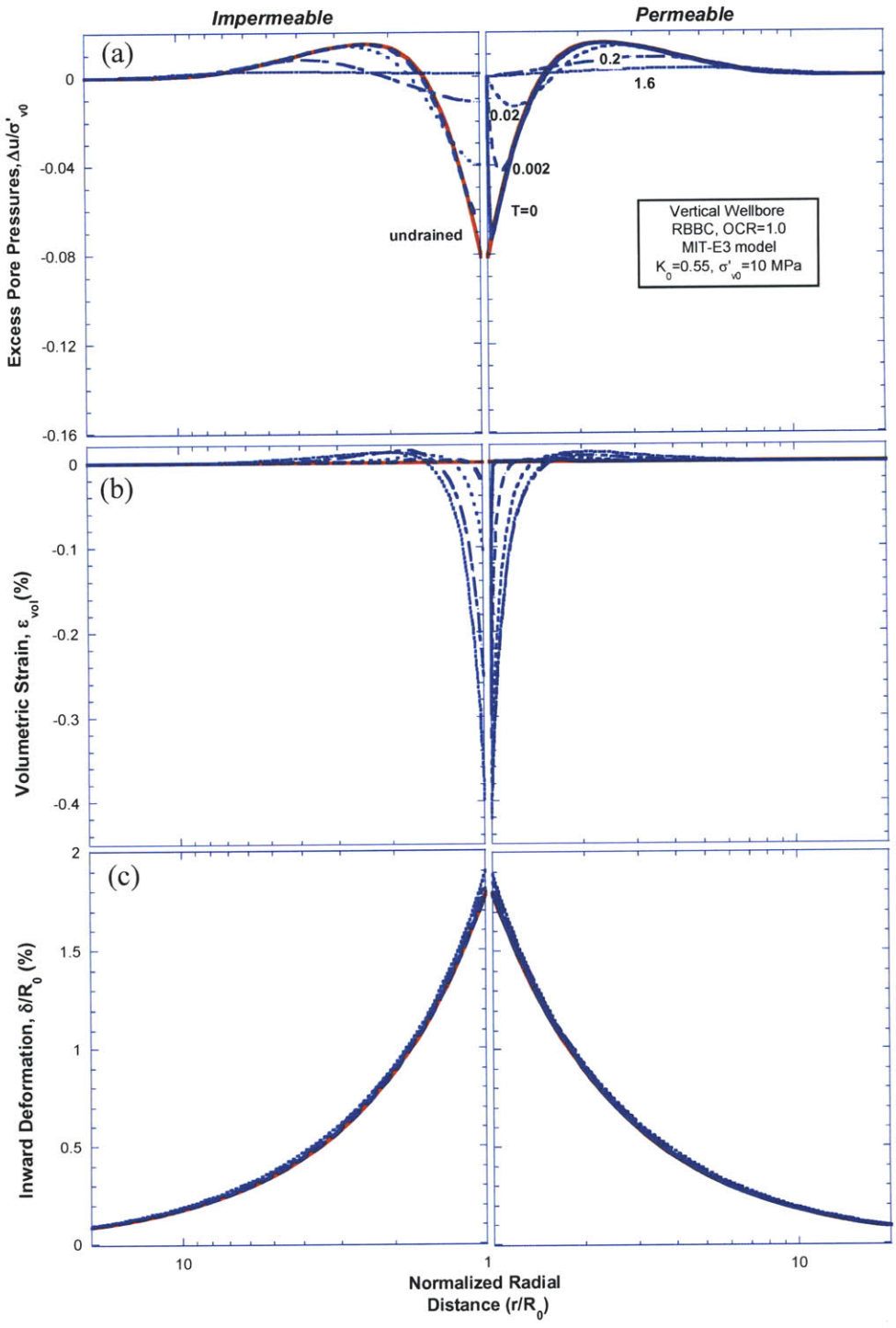

Figure 6.6 Radial distribution of (a) excess pore pressures, (b) volumetric strains, and (c) inward radial deformations around vertical wellbores with permeable and impermeable cavity wall using MIT-E3 model.

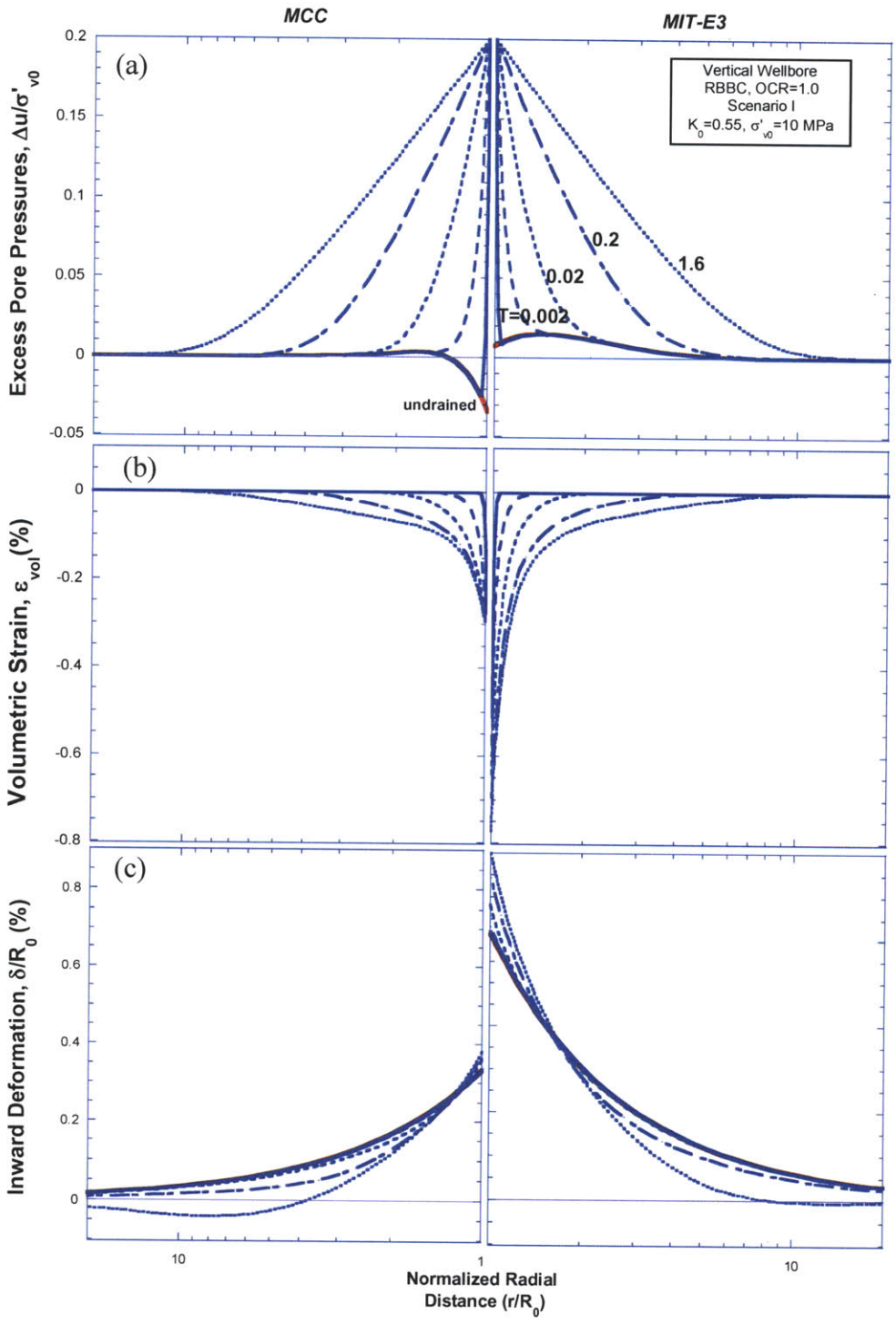

Figure 6.7 Radial distribution of (a) excess pore pressures, (b) volumetric strains, and (c) inward radial deformations around vertical wellbores during Scenario I wellbore unloading using MCC MIT-E3 models.

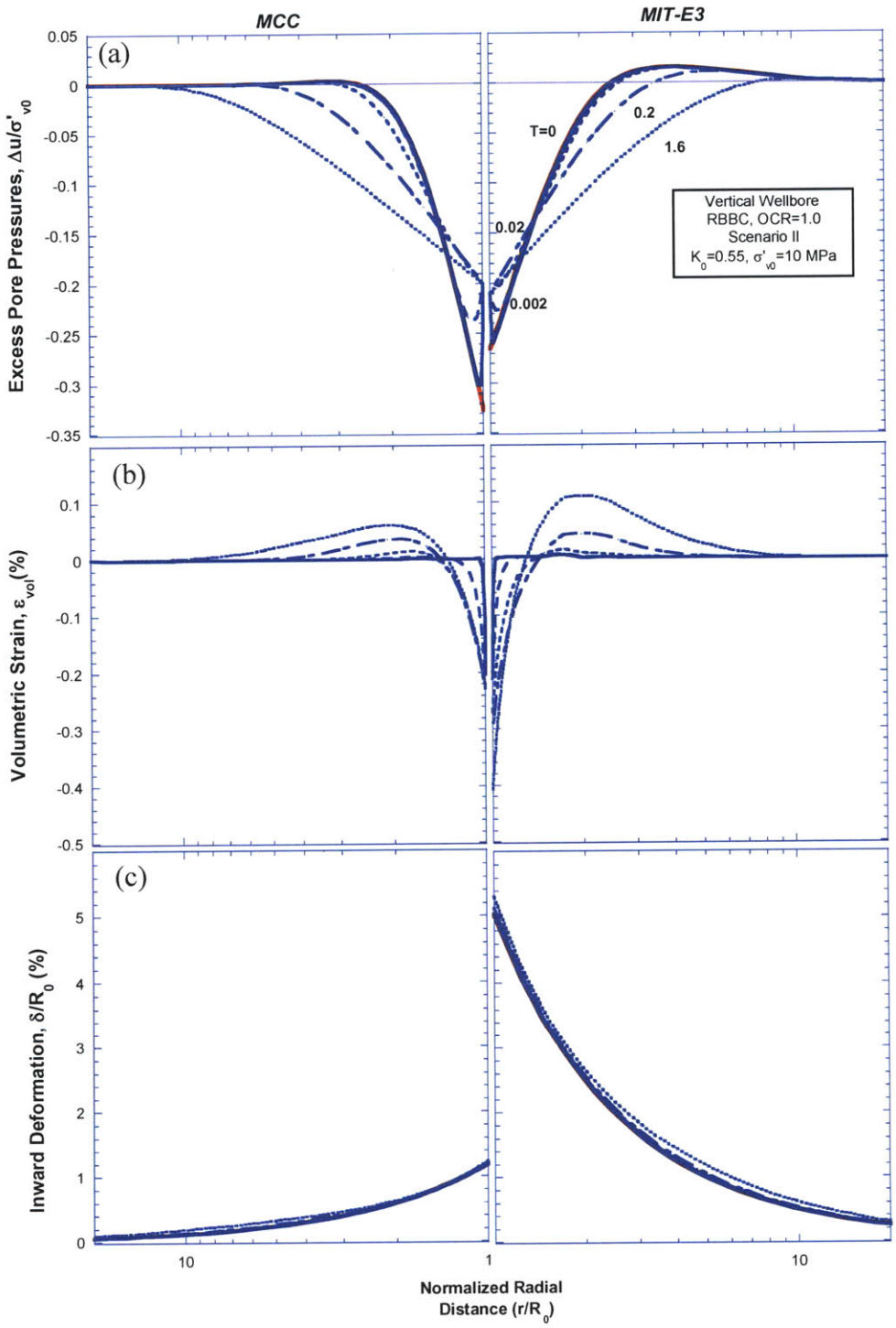

Figure 6.8 Radial distribution of (a) excess pore pressures, (b) volumetric strains, and (c) inward radial deformations around vertical wellbores during Scenario II wellbore unloading using MCC MIT-E3 models.

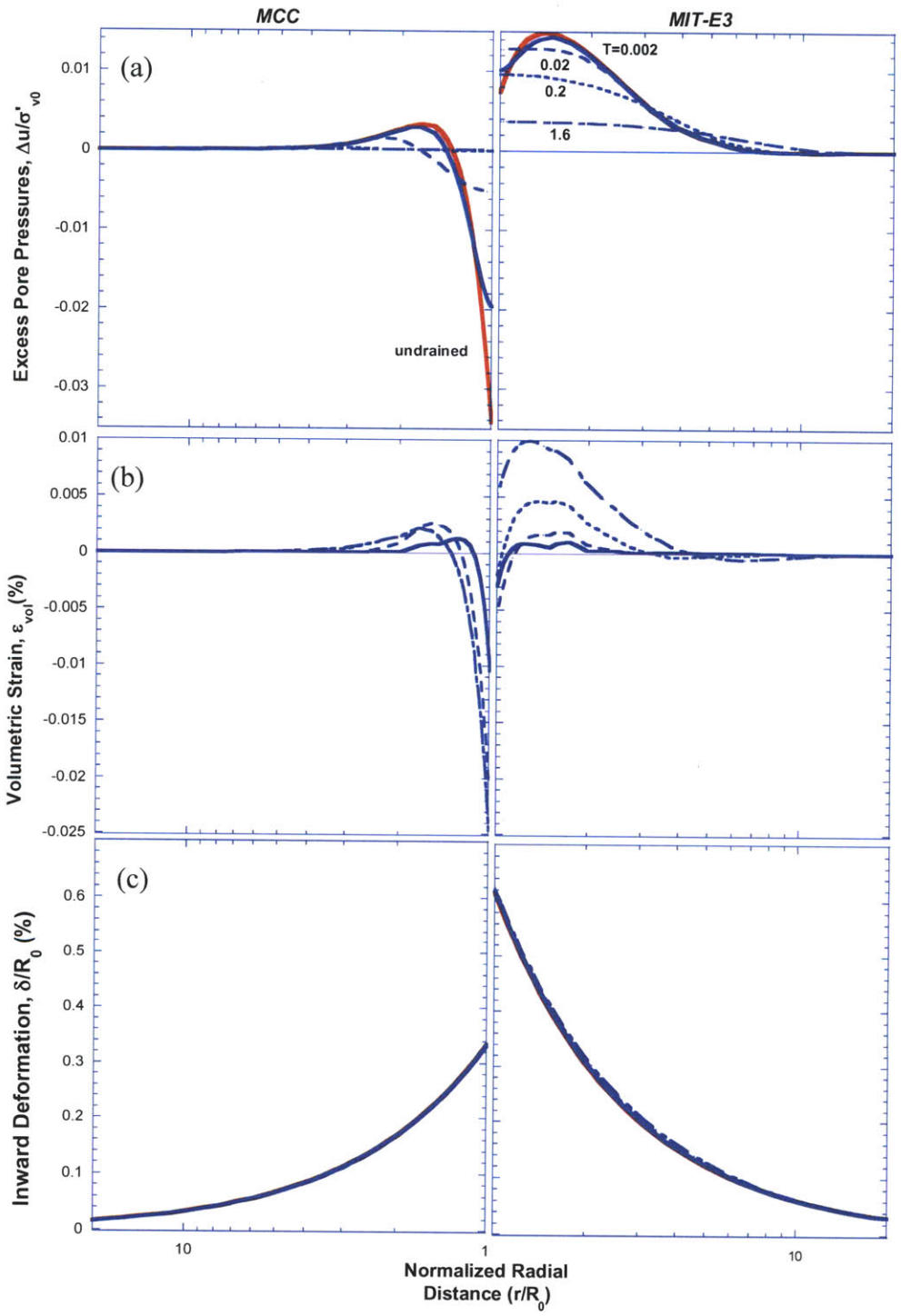

Figure 6.9 Radial distribution of (a) excess pore pressures, (b) volumetric strains, and (c) inward radial deformations around vertical wellbores during Scenario III wellbore unloading using MCC MIT-E3 models.

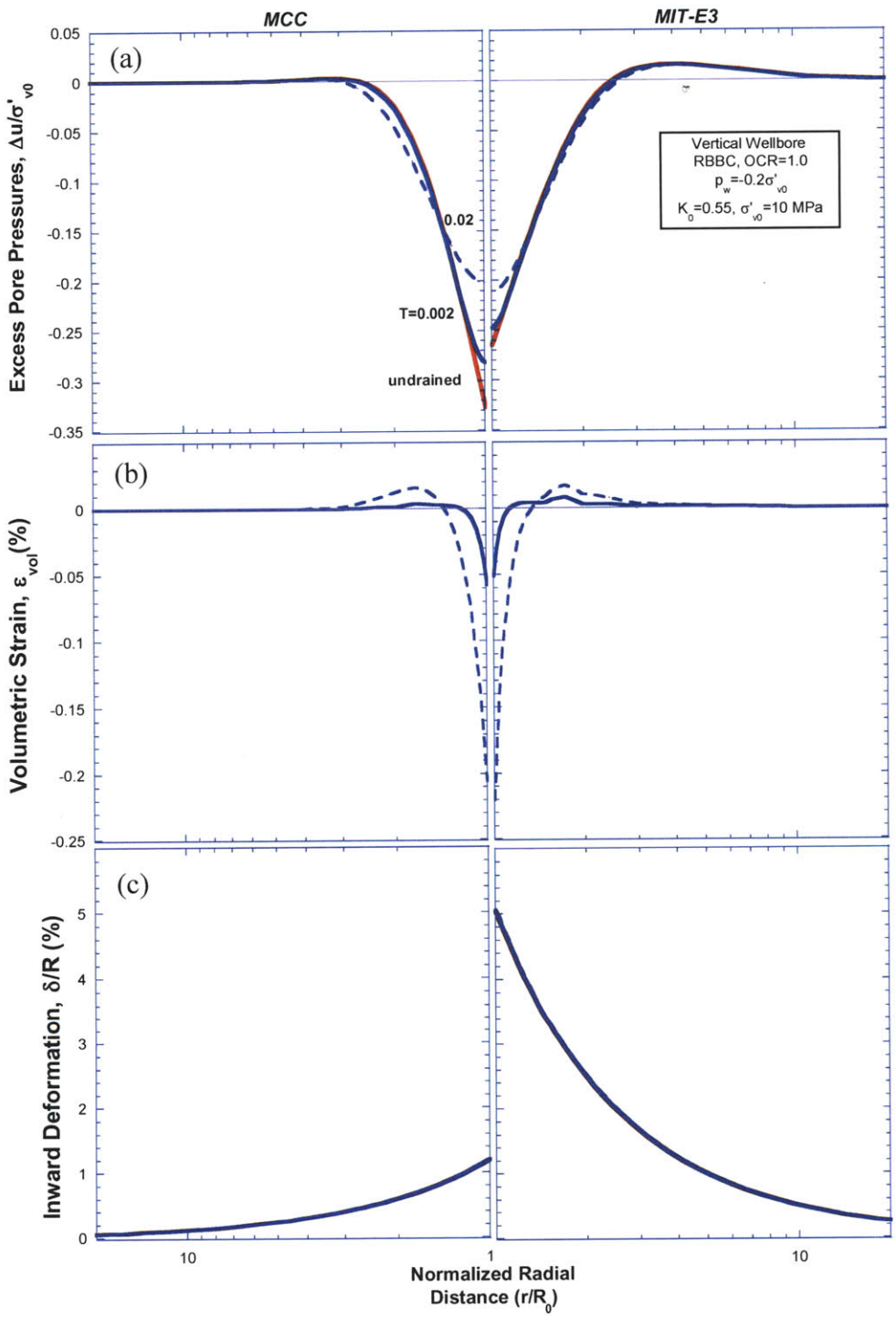

Figure 6.10 Radial distribution of (a) excess pore pressures, (b) volumetric strains, and (c) inward radial deformations around vertical wellbores during Scenario IV wellbore unloading using MCC MIT-E3 models.

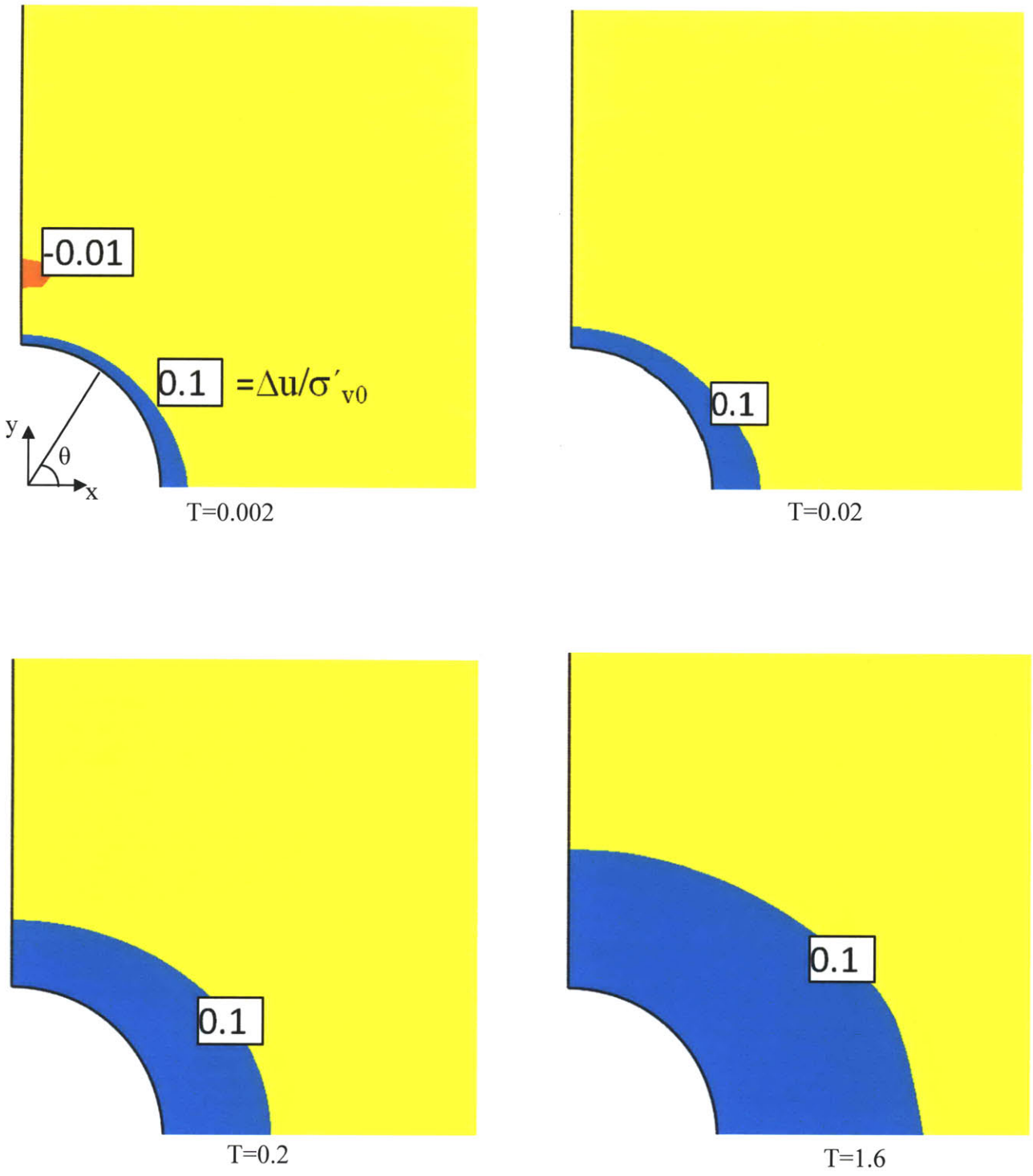

Figure 6.11 MIT-E3 predictions of excess pore pressure distributions around a 30^0 deviated wellbore during unloading scenario I.

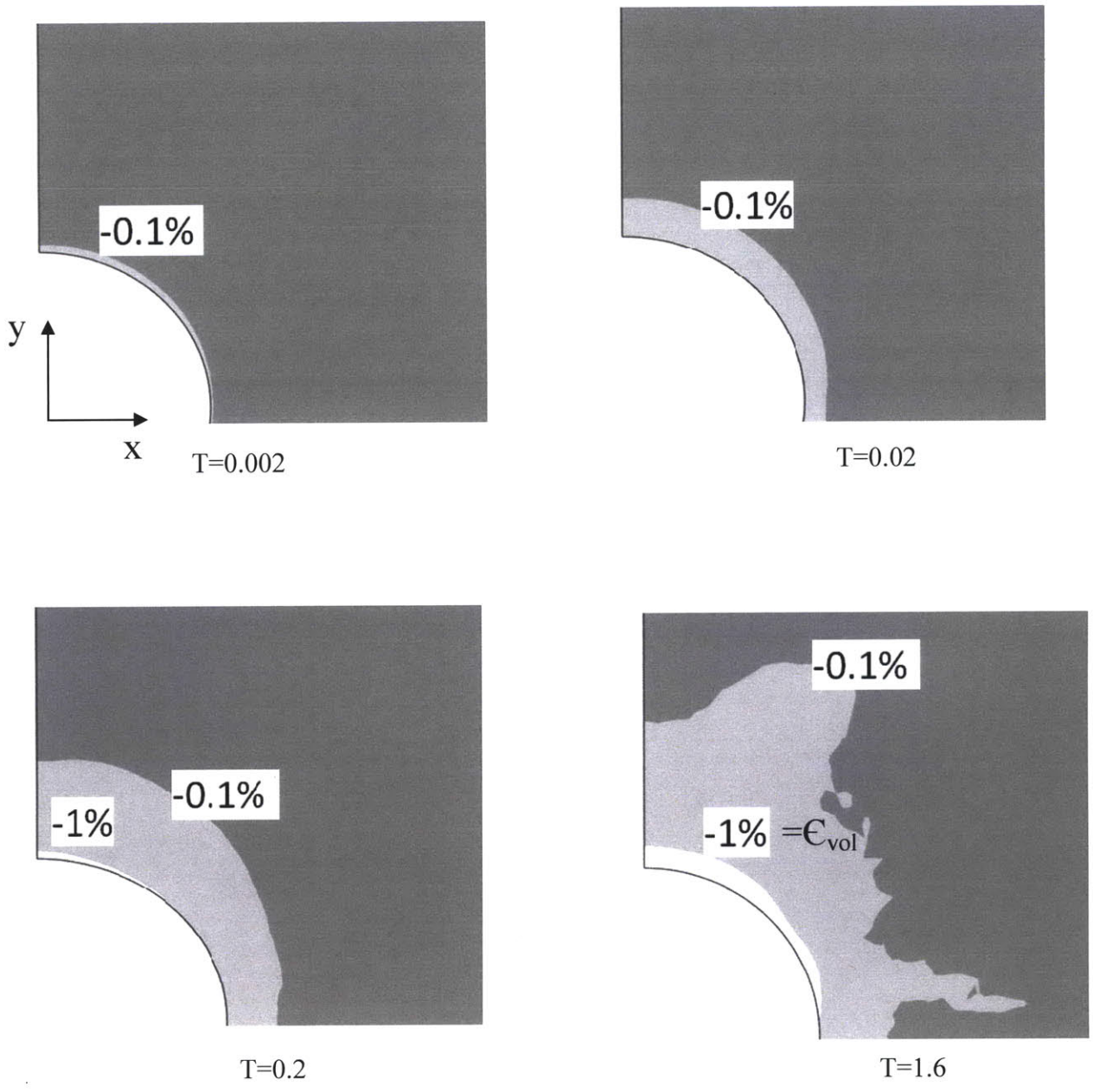

Figure 6.12 MIT-E3 predictions of the volumetric strain distributions around a 30^0 deviated wellbore during unloading scenario I.

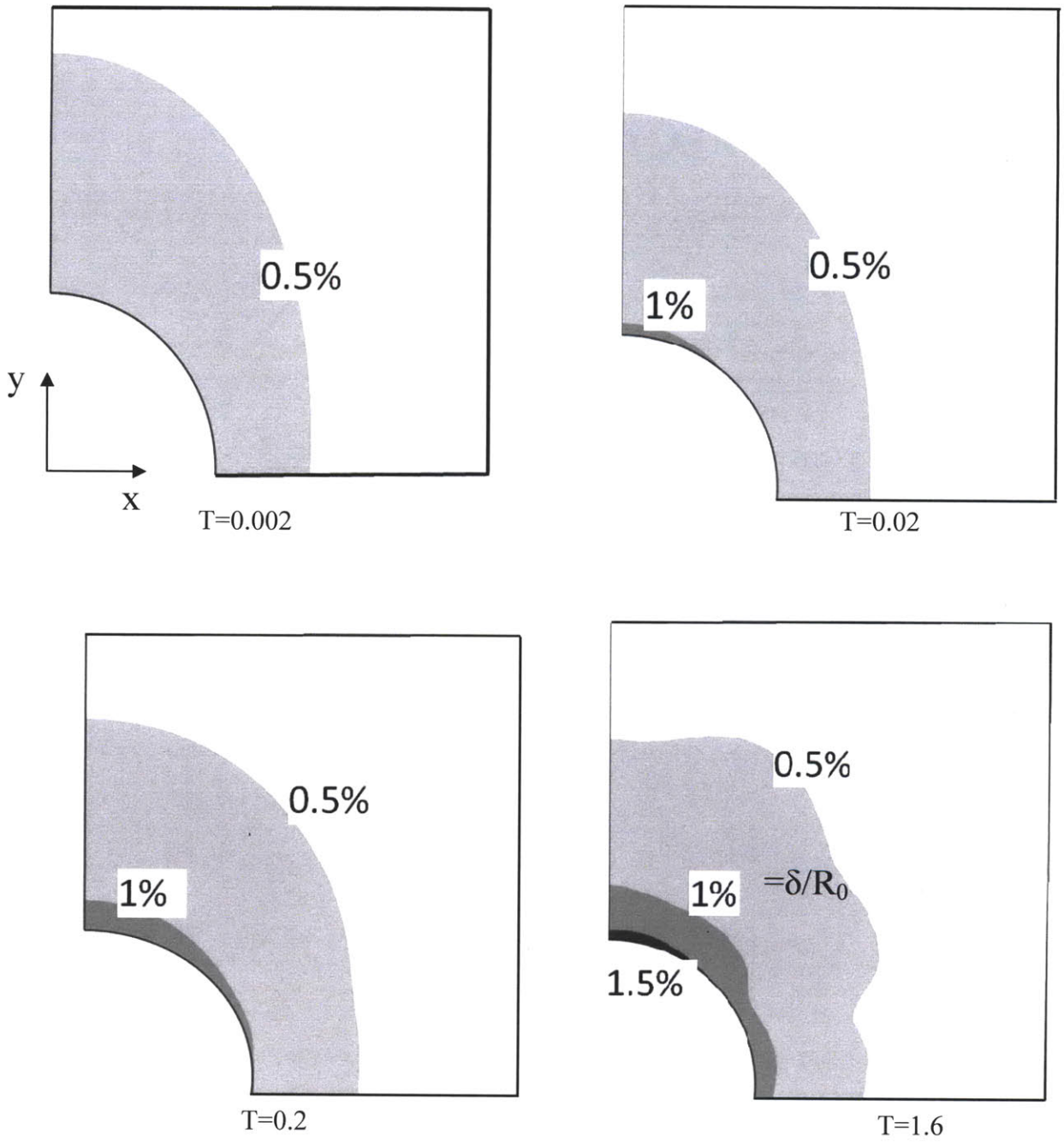

Figure 6.13 MIT-E3 predictions of the radial deformations around a 30^0 deviated wellbore during unloading scenario I.

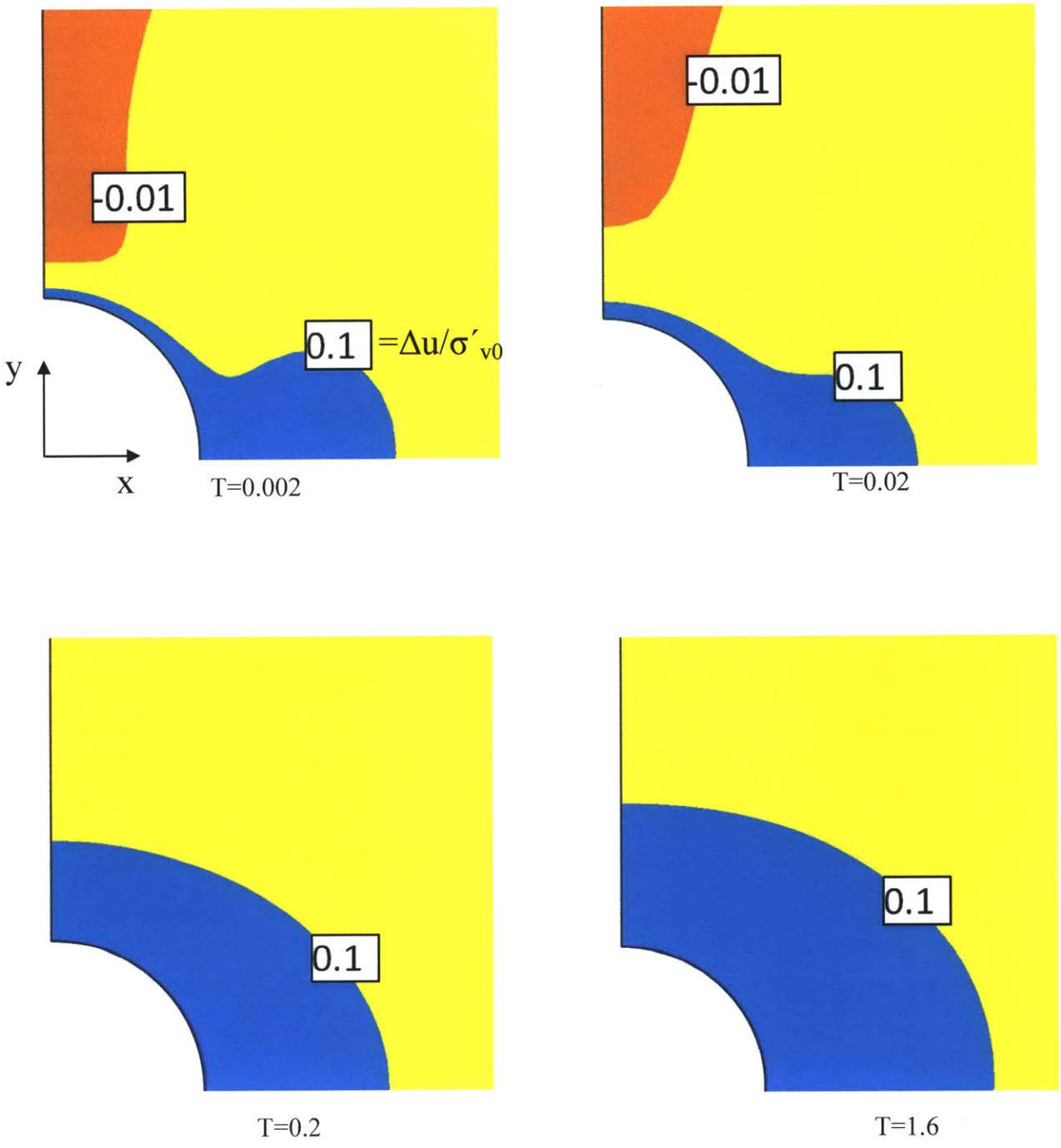

Figure 6.14 MIT-E3 predictions of excess pore pressure distributions around a 45^0 deviated wellbore during unloading scenario I.

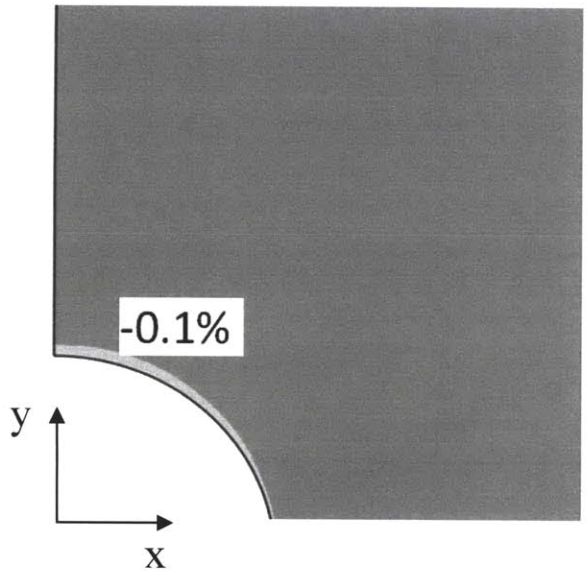

T=0.002

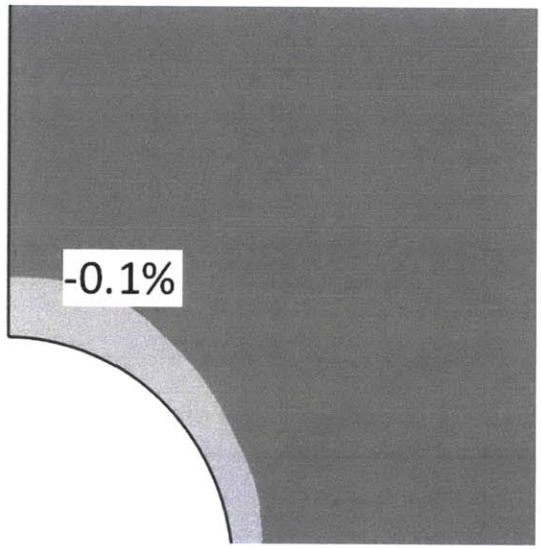

T=0.02

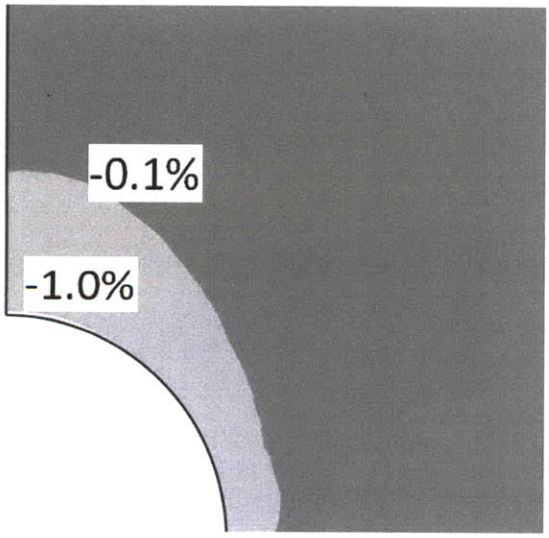

T=0.2

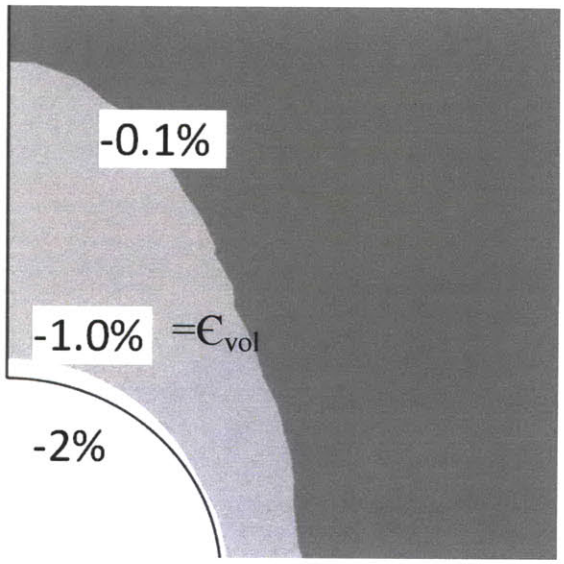

T=1.6

Figure 6.15 MIT-E3 predictions of the volumetric strain distributions around a 45^0 deviated wellbore during unloading scenario I.

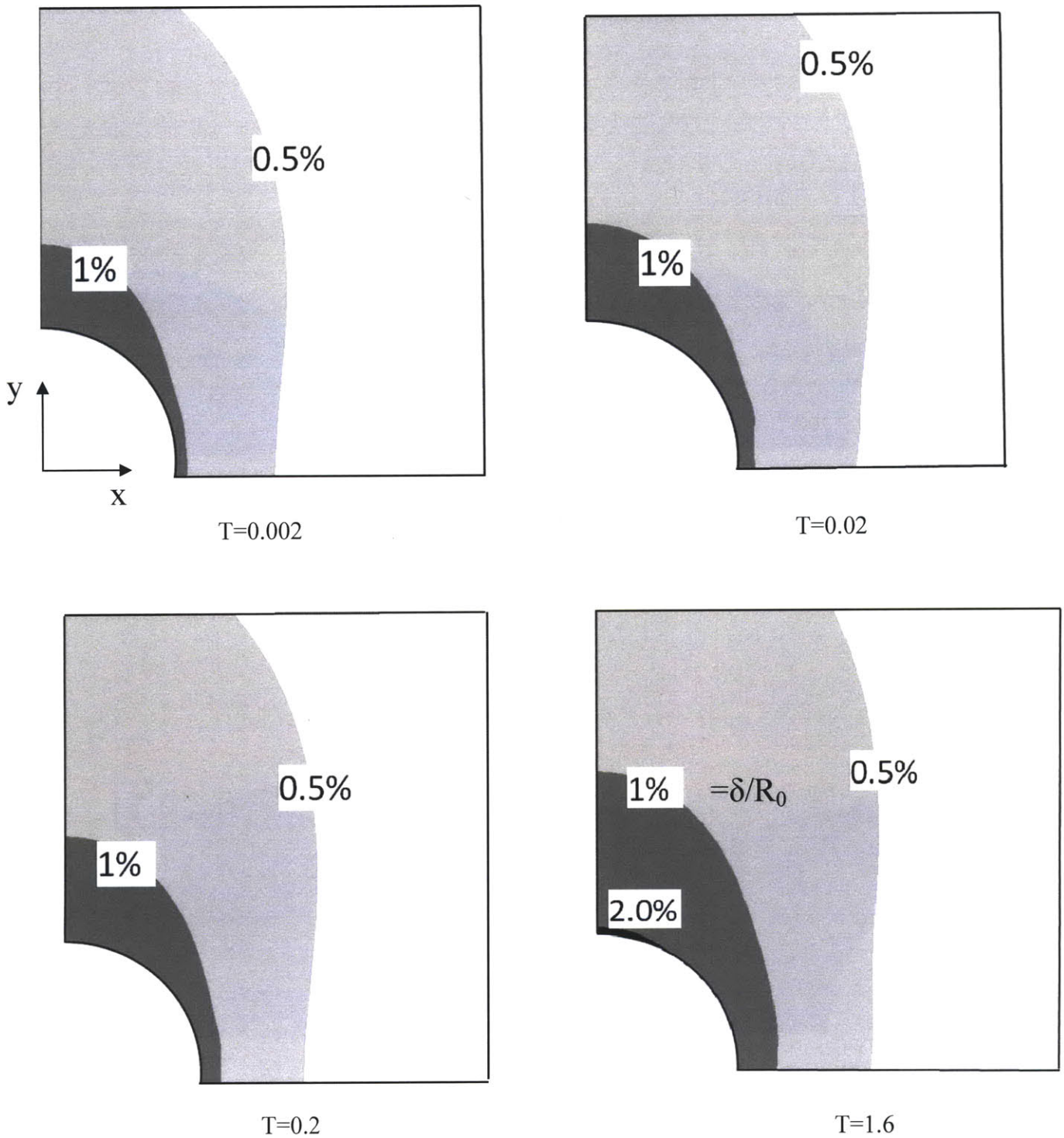

Figure 6.16 MIT-E3 predictions of the radial deformations around a 45^0 deviated wellbore during unloading scenario I.

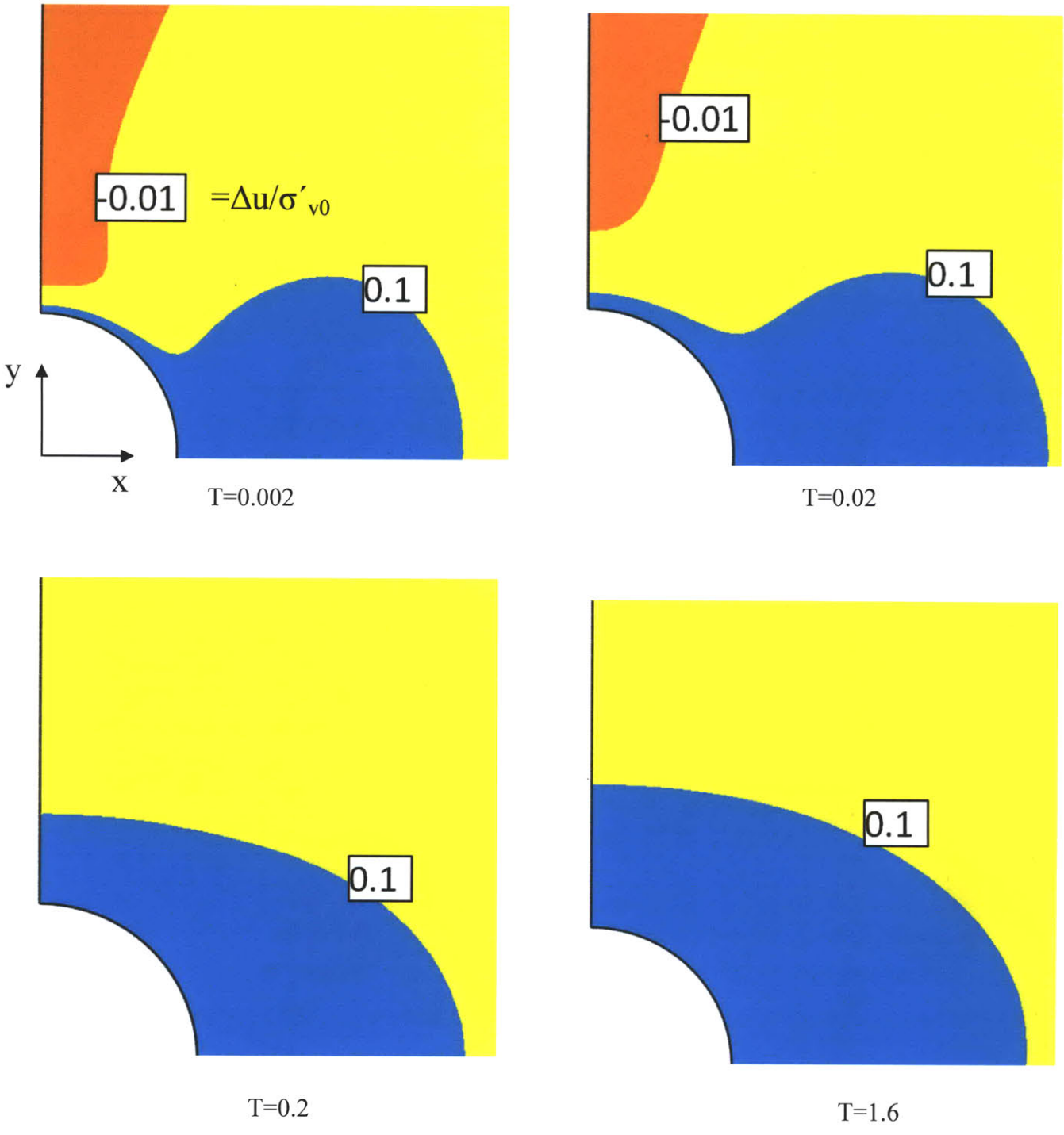

Figure 6.17 MIT-E3 predictions of excess pore pressure distributions around a 60^0 deviated wellbore during unloading scenario I.

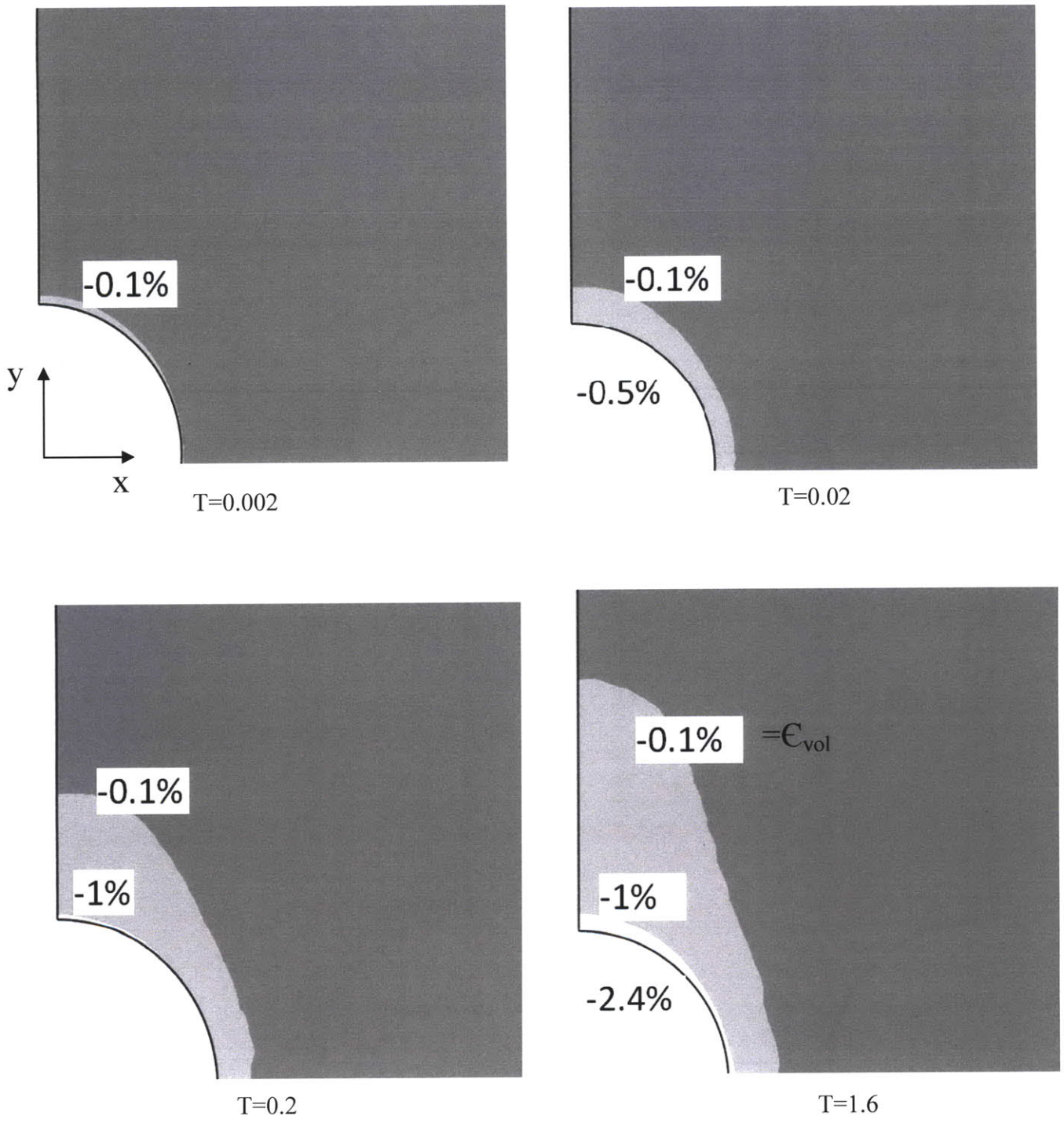

Figure 6.18 MIT-E3 predictions of the volumetric strains distributions around a 60^0 deviated wellbore during unloading scenario I.

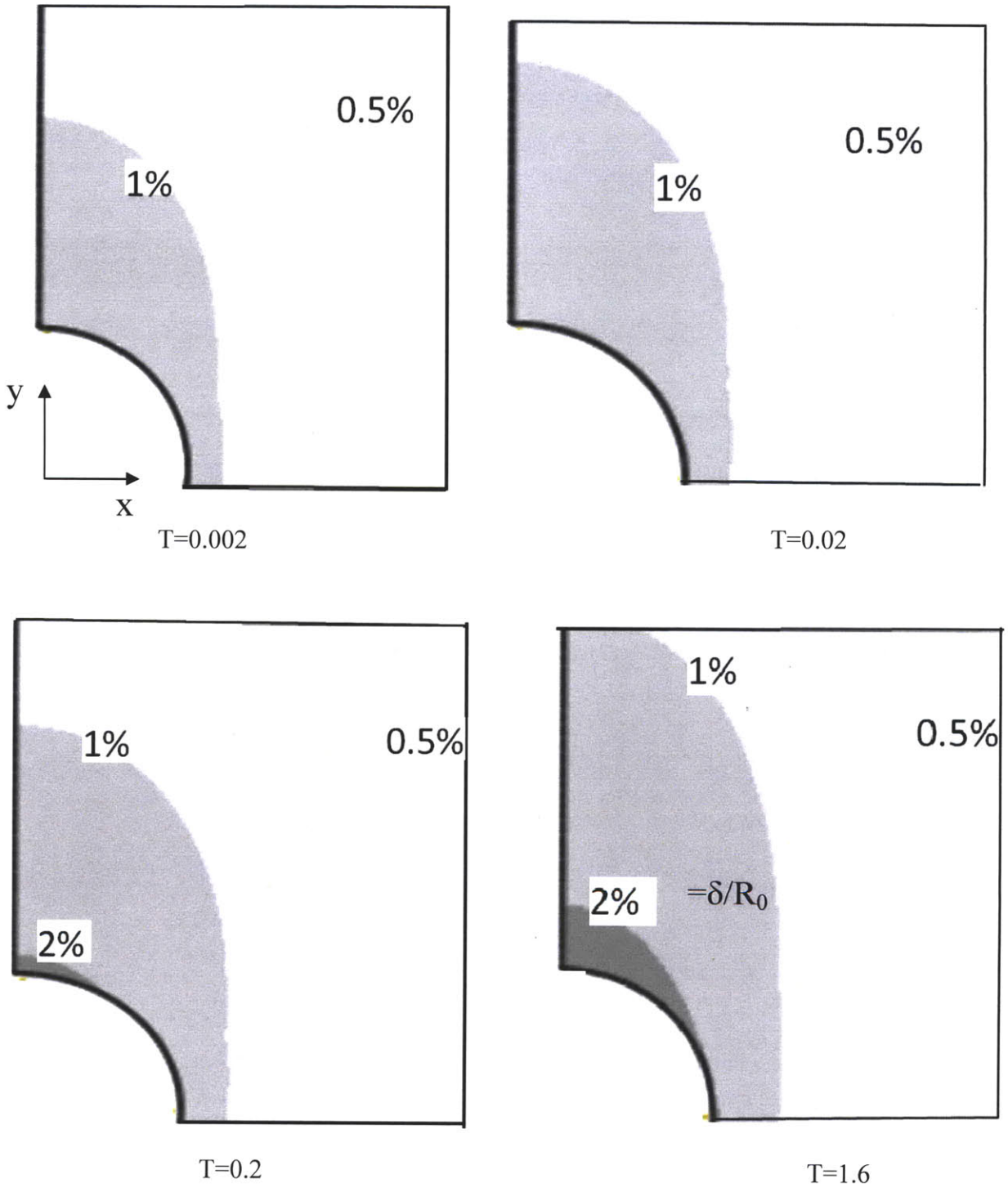

Figure 6.19 MIT-E3 predictions of the radial deformations around a 60^0 deviated wellbore during unloading scenario I.

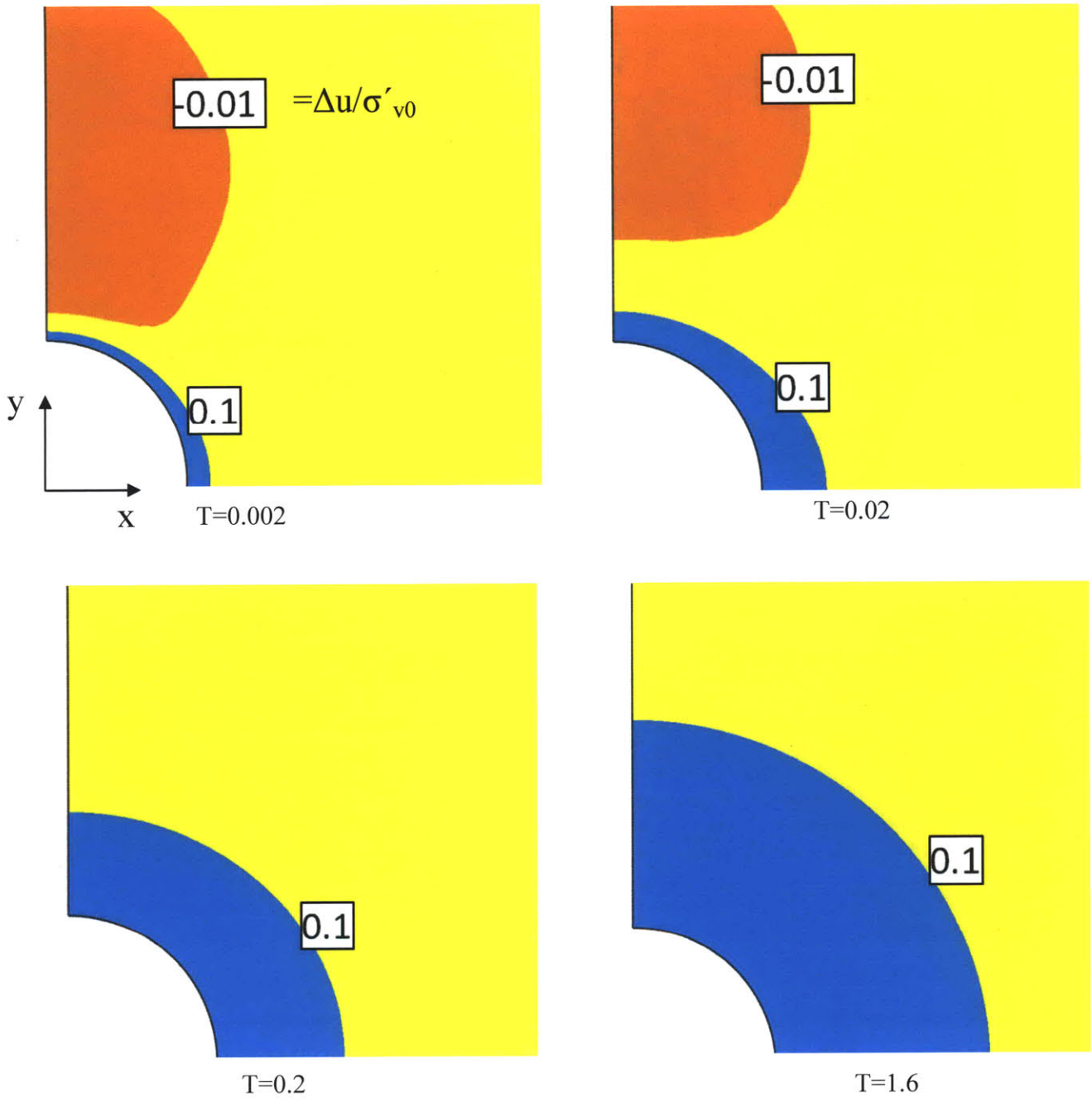

Figure 6.20 MCC predictions of excess pore pressure distributions around a 30^0 deviated wellbore during unloading scenario I.

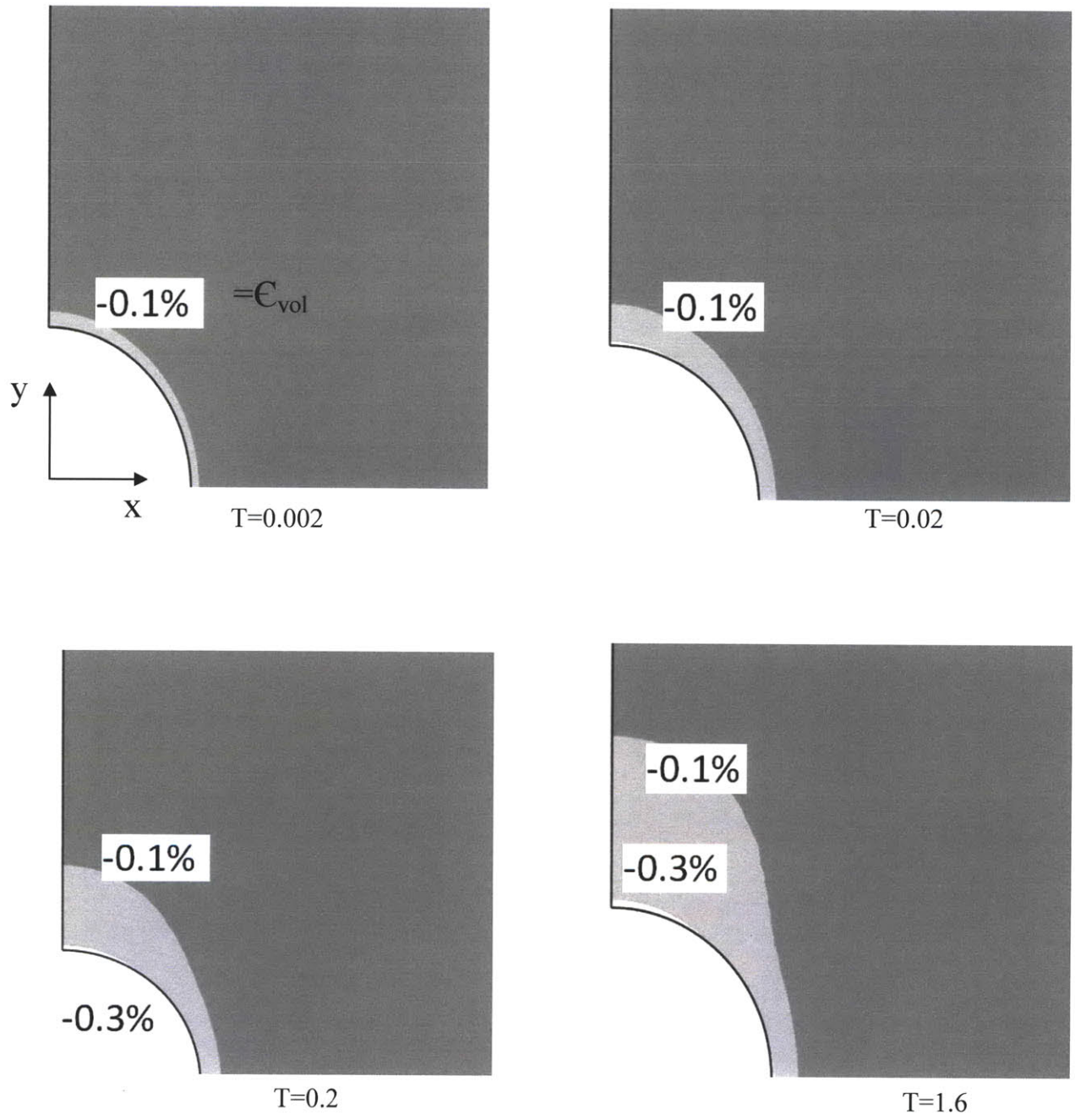

Figure 6.21 MCC predictions of the volumetric strain distributions around a 30^0 deviated wellbore during unloading scenario I.

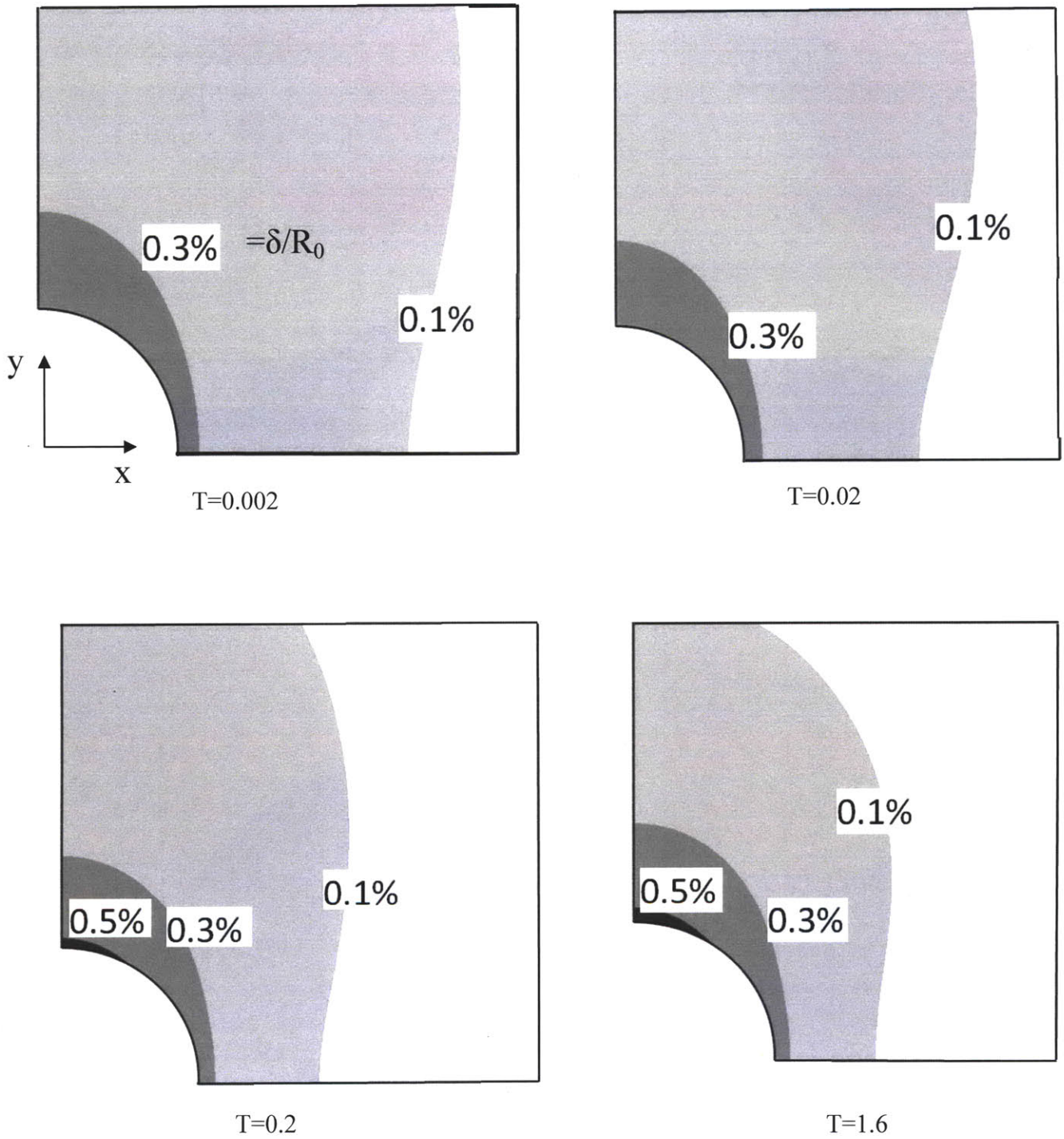

Figure 6.22 MCC predictions of the radial deformations around a 30^0 deviated wellbore during unloading scenario I.

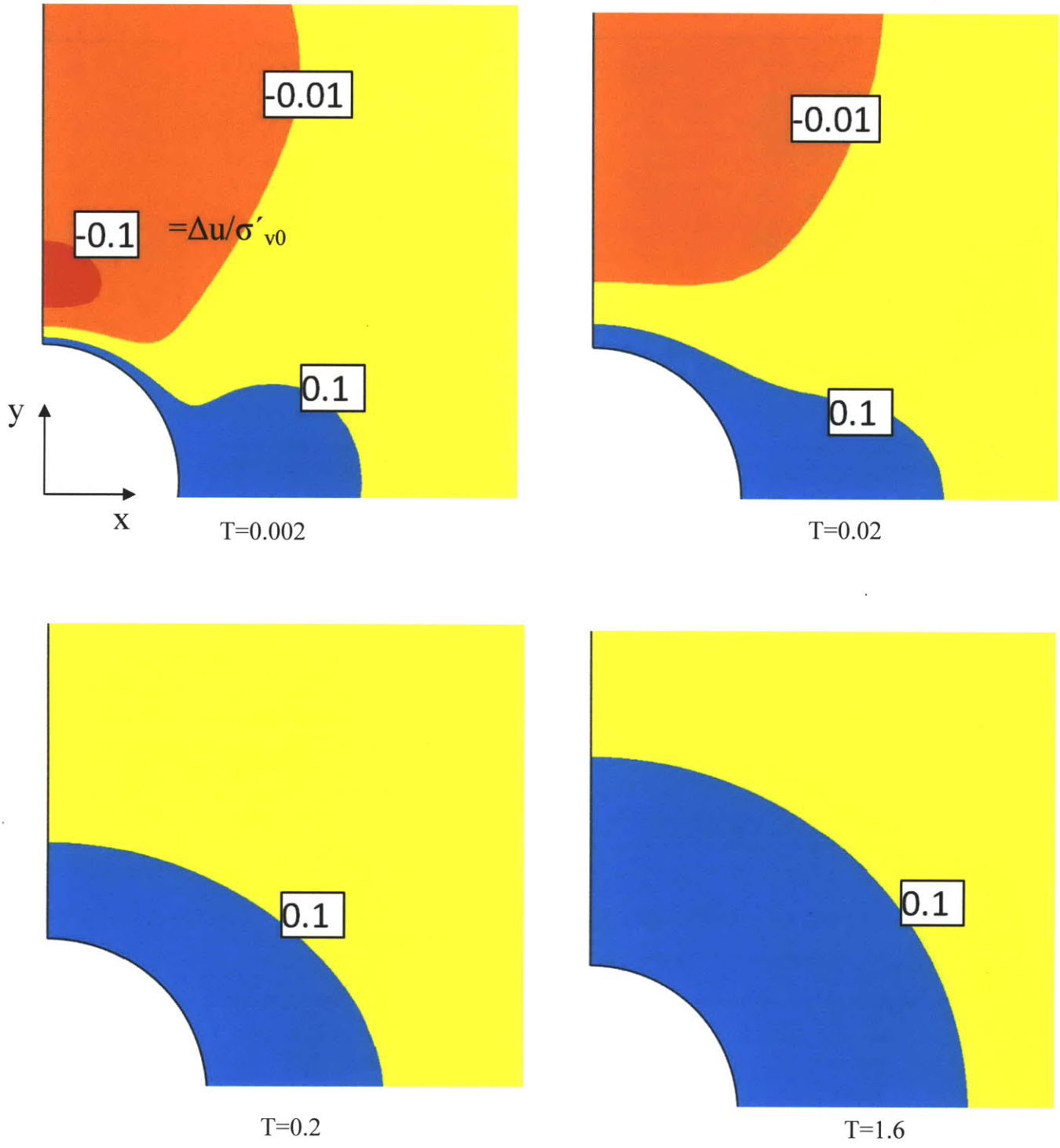

Figure 6.23 MCC predictions of excess pore pressure distributions around a 45^0 deviated wellbore during unloading scenario I.

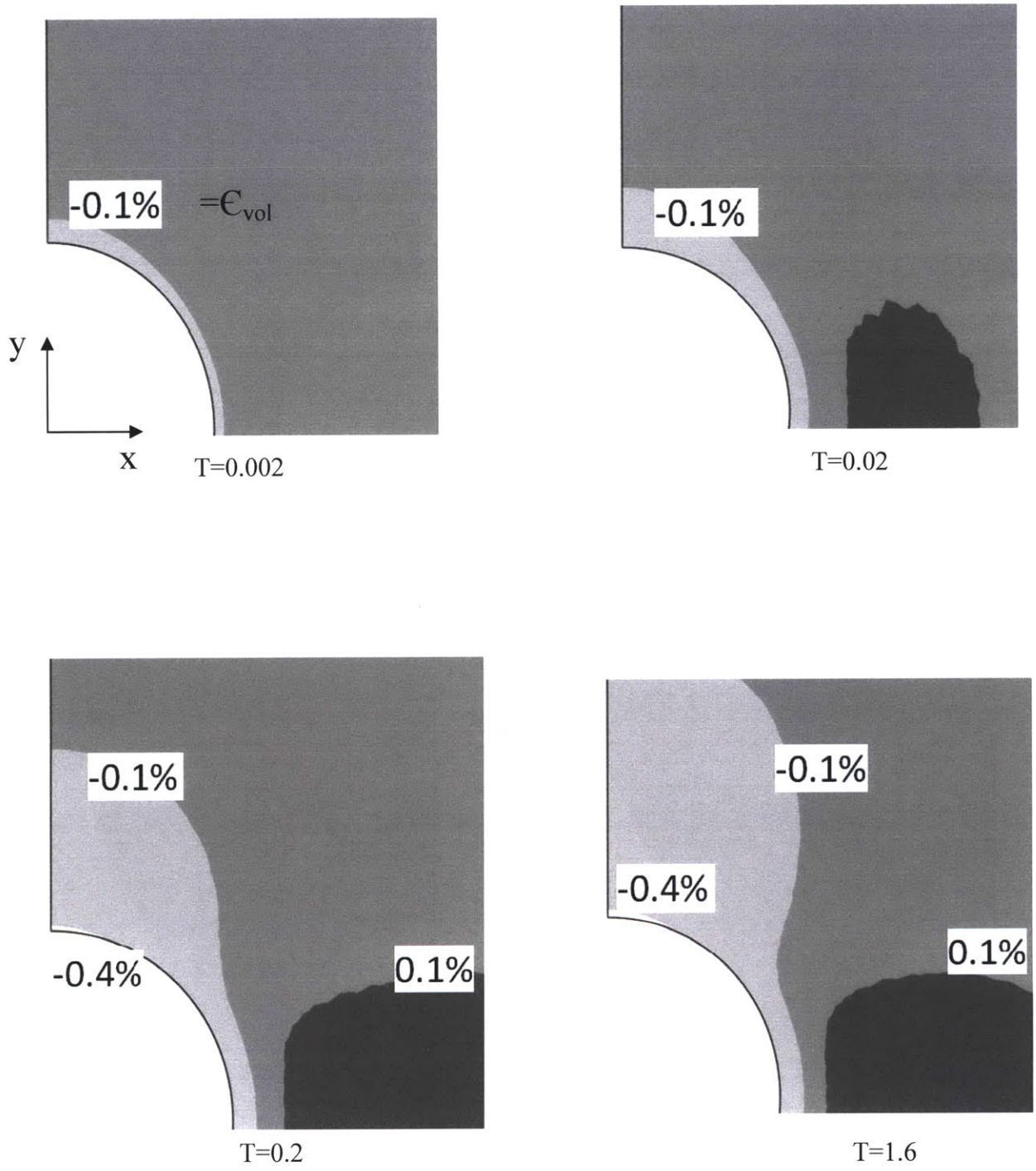

Figure 6.24 MCC predictions of the volumetric strain distributions around a 45^0 deviated wellbore during unloading scenario I.

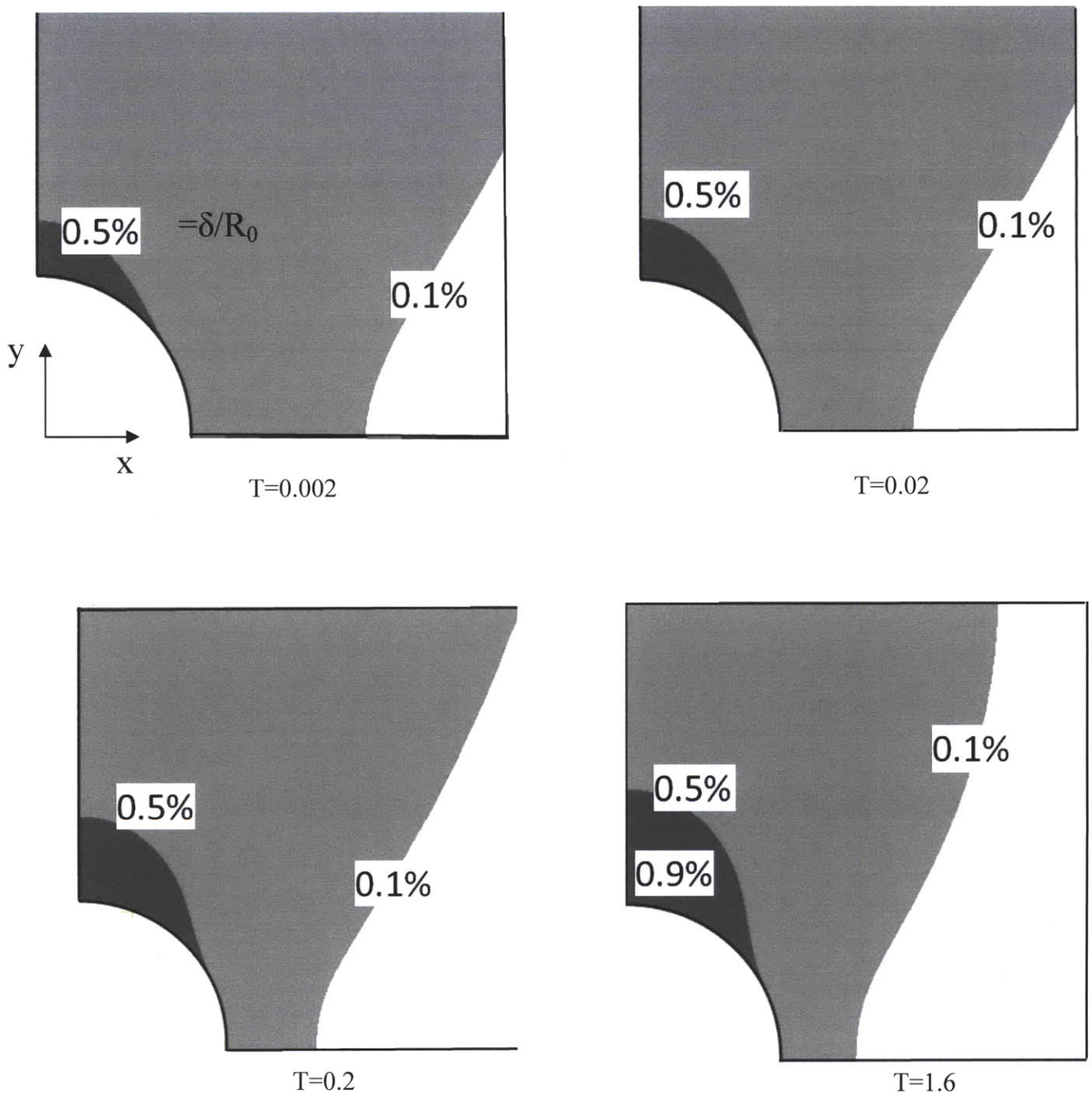

Figure 6.25 MCC predictions of the radial deformations around a 45^0 deviated wellbore during unloading scenario I.

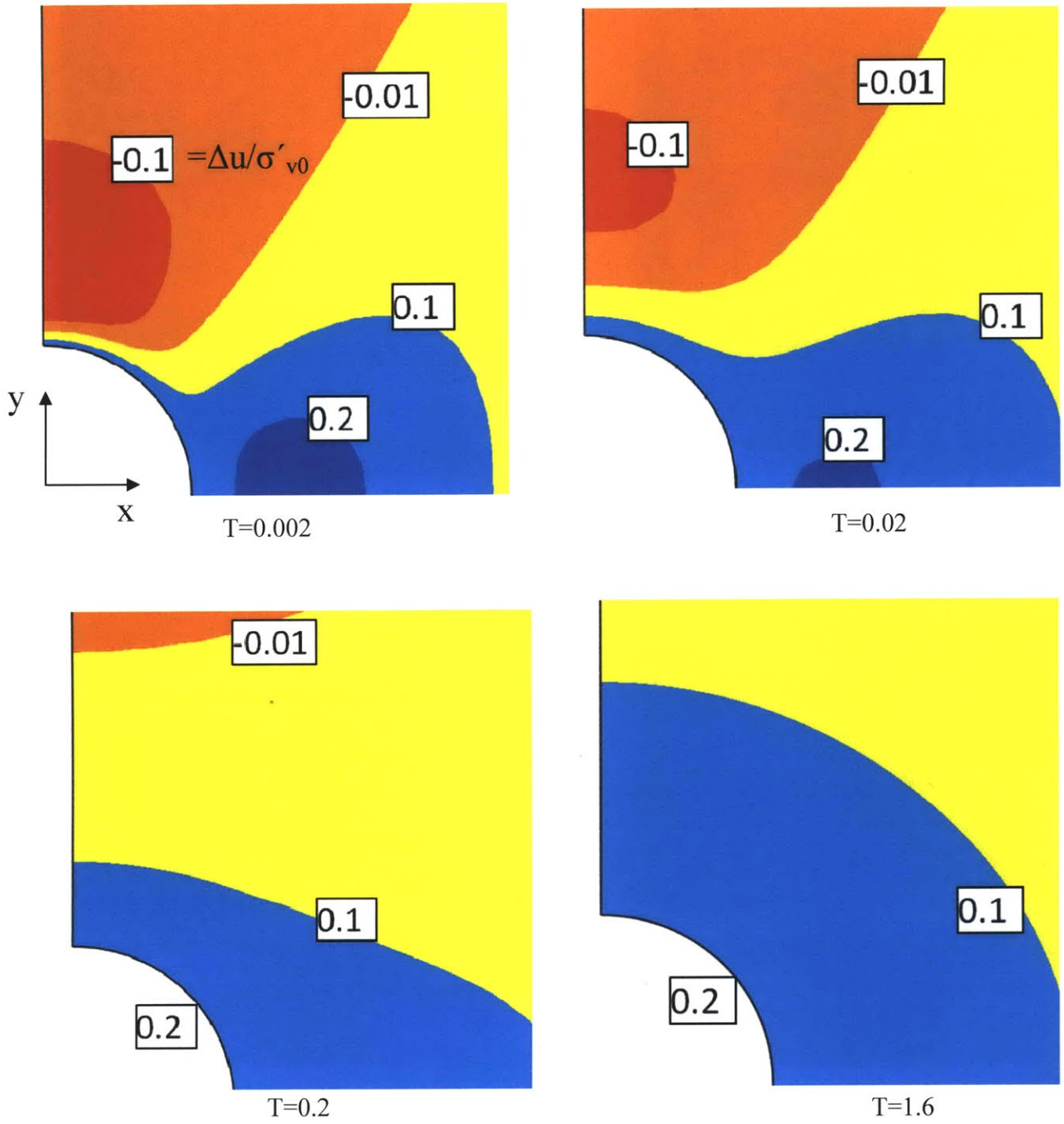

Figure 6.26 MCC predictions of excess pore pressure distributions around a 60^0 deviated wellbore during unloading scenario I.

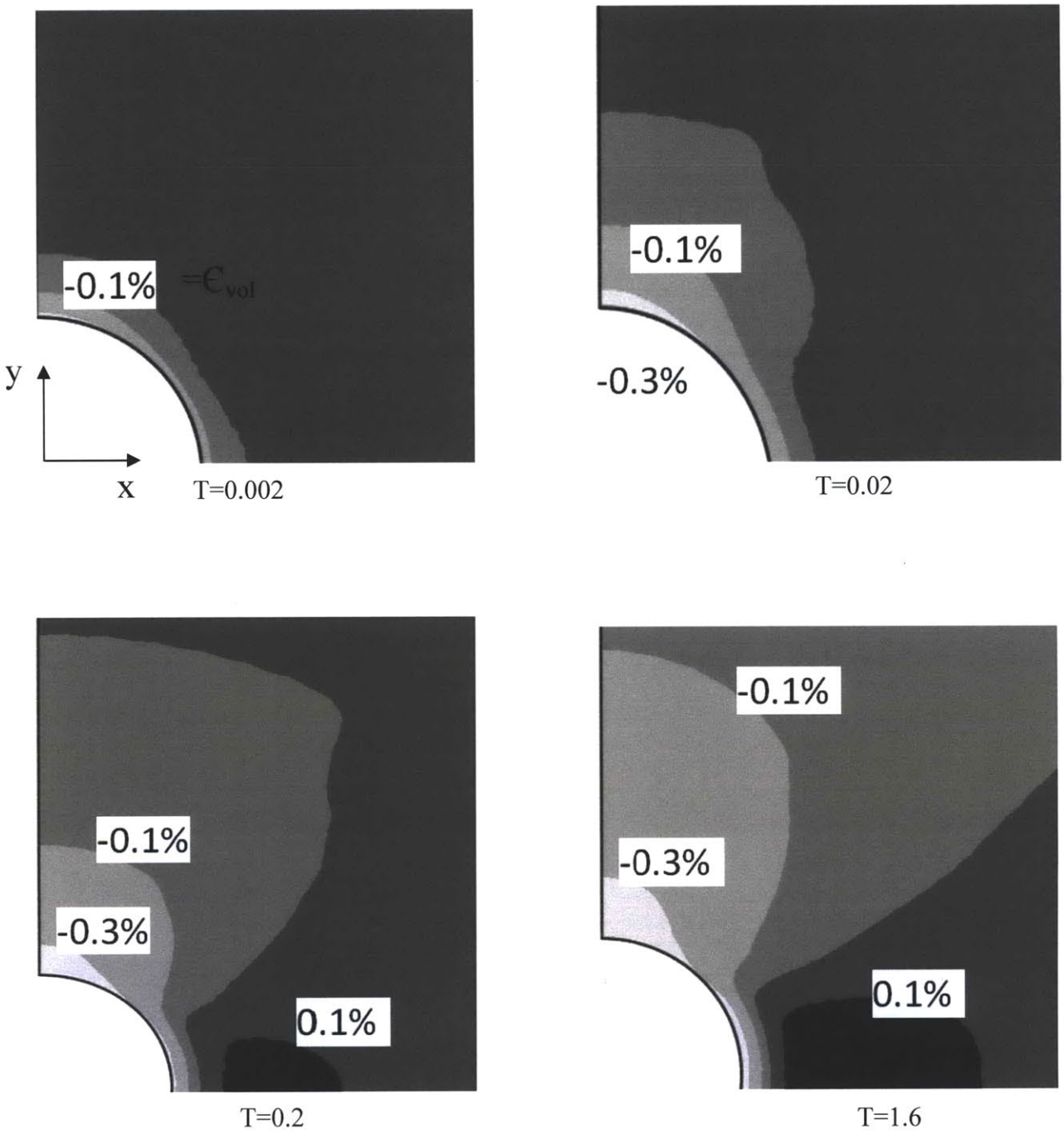

Figure 6.27 MCC predictions of the volumetric strain distributions around a 60^0 deviated wellbore during unloading scenario I.

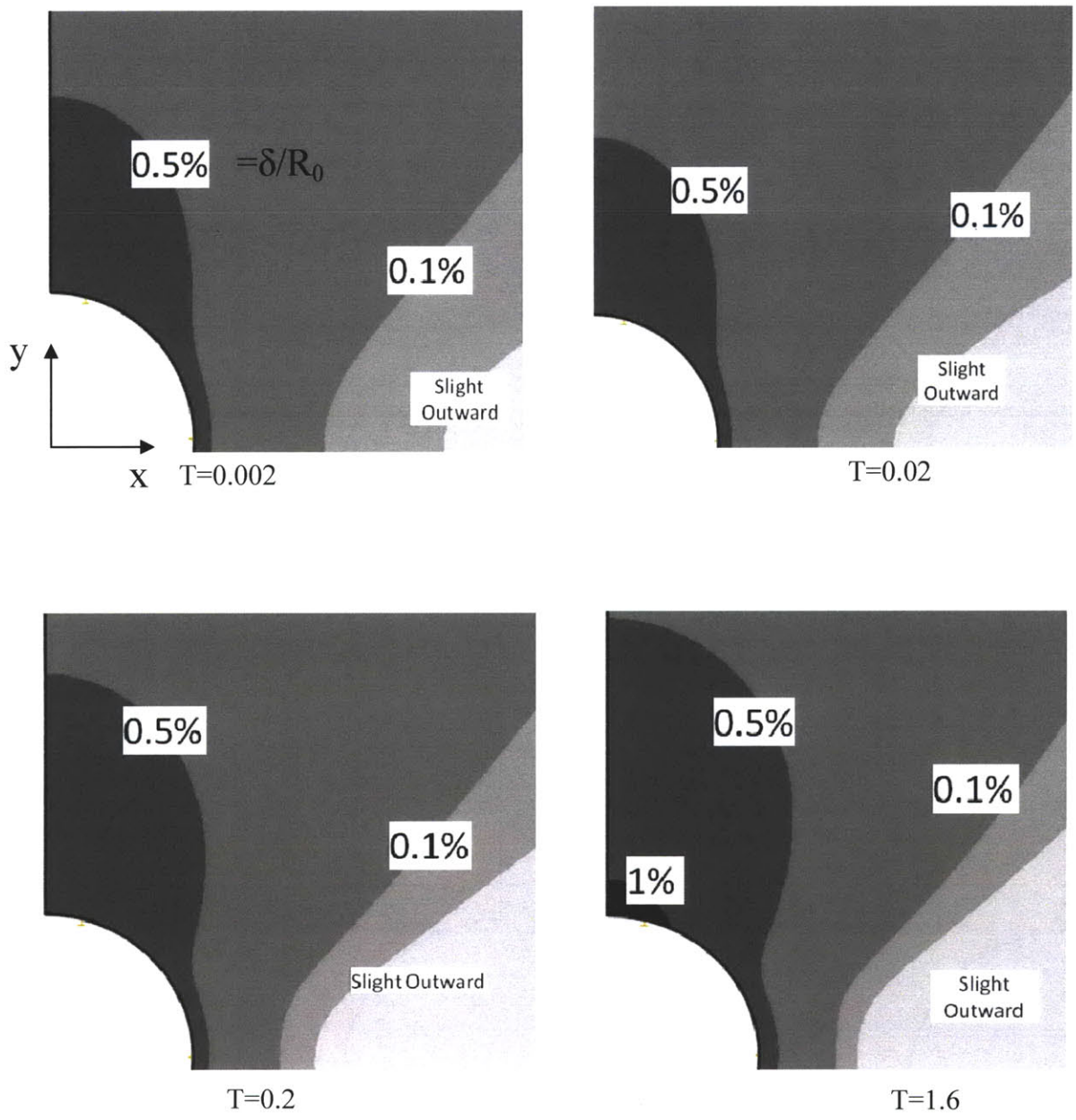

Figure 6.28 MCC predictions of the radial deformations around a 60^0 deviated wellbore during unloading scenario I.

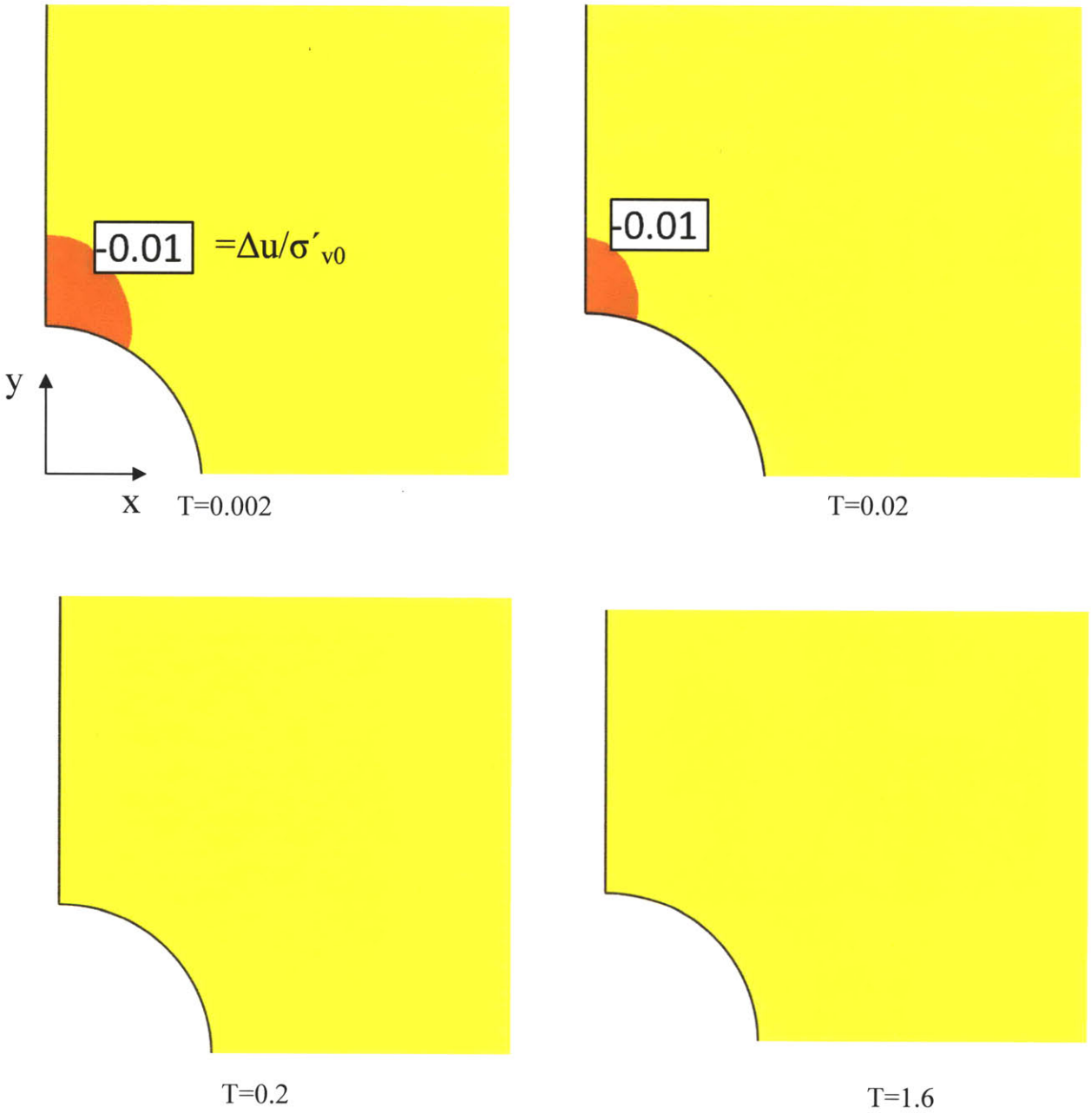

Figure 6.29 MIT-E3 predictions of excess pore pressure distributions around a 30^0 deviated wellbore during unloading scenario III.

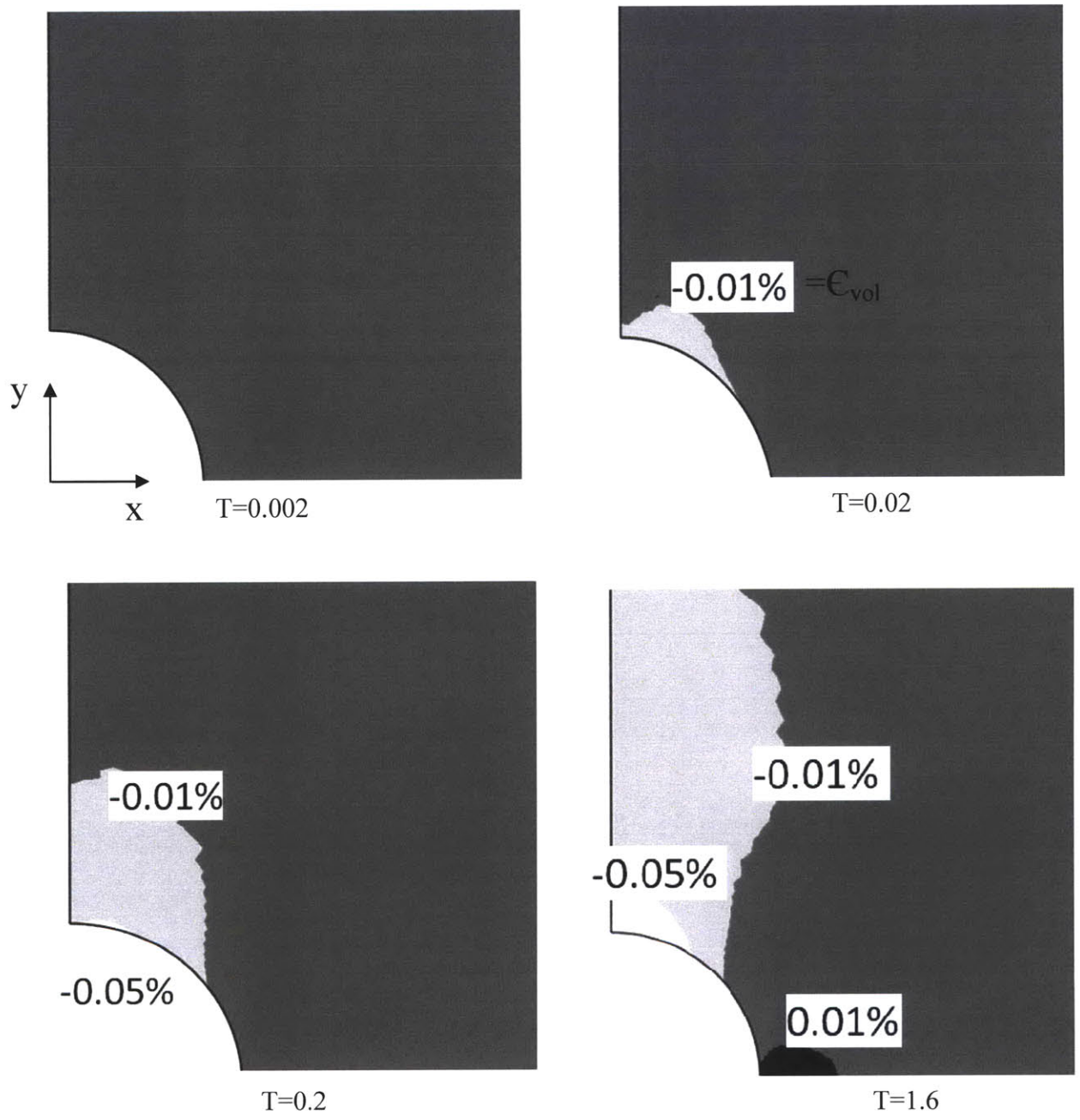

Figure 6.30 MIT-E3 predictions of volumetric strain distributions around a 30^0 deviated wellbore during unloading scenario III.

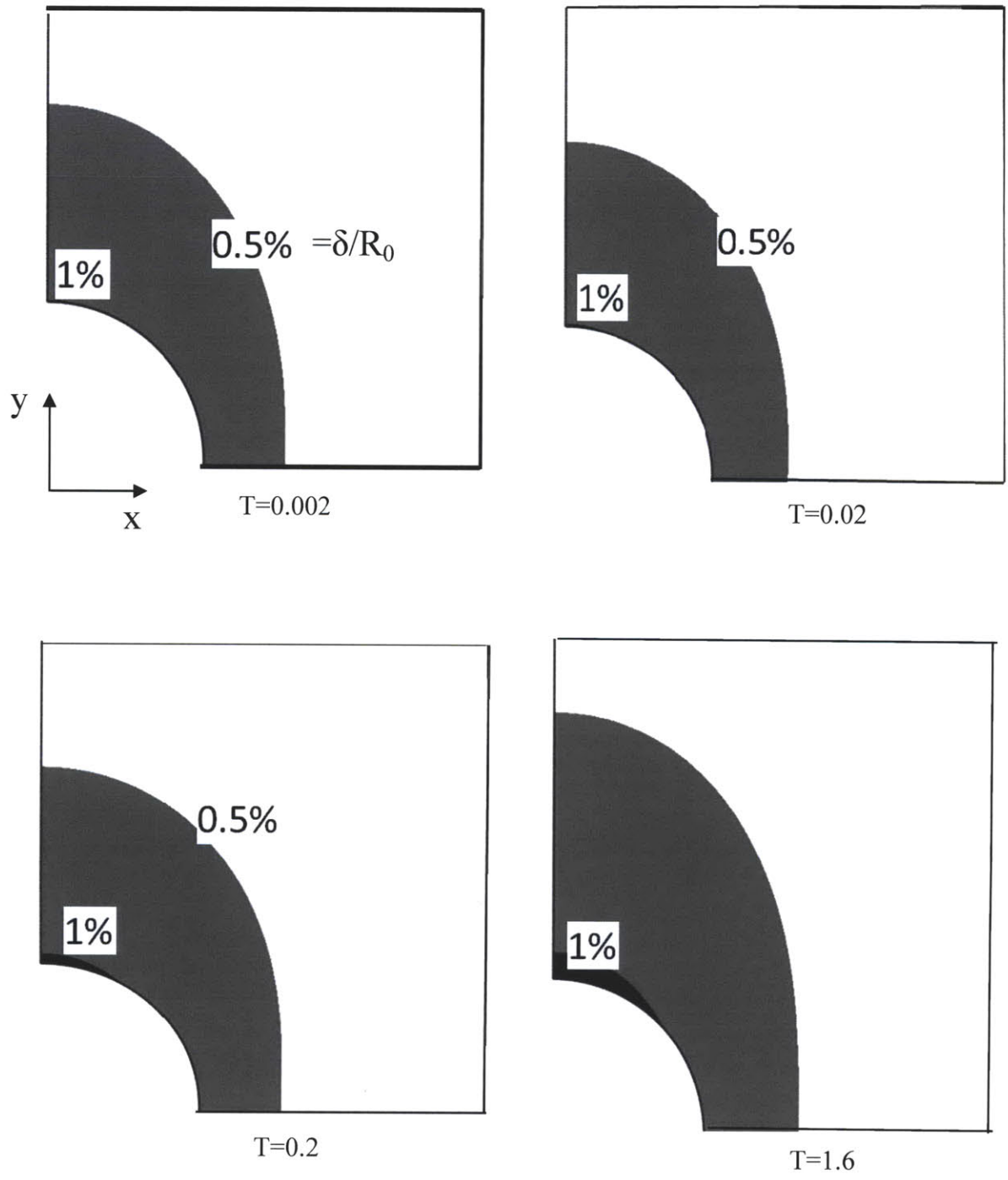

Figure 6.31 MIT-E3 predictions of radial deformations around a 30^0 deviated wellbore during unloading scenario III.

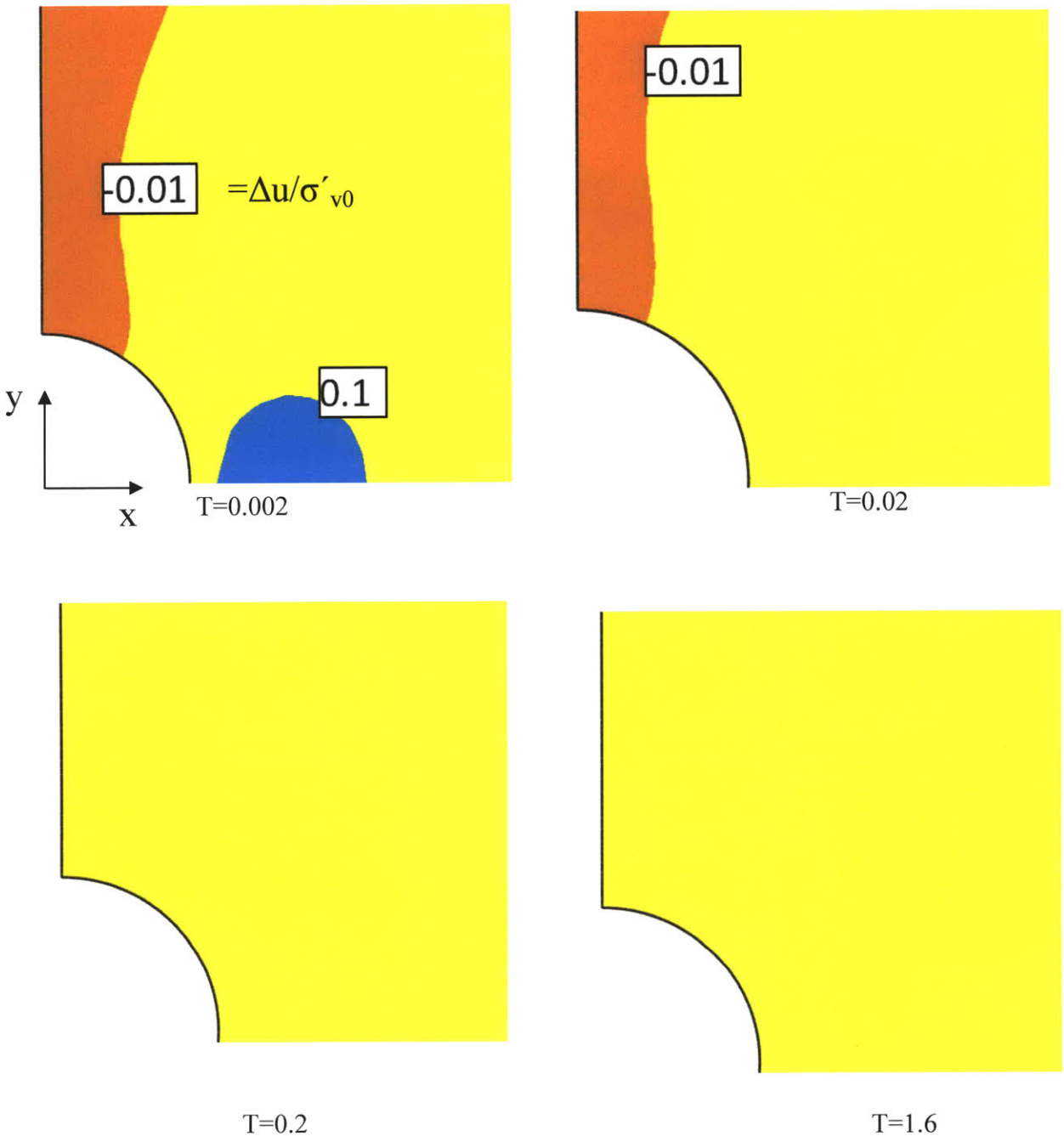

Figure 6.32 MIT-E3 predictions of excess pore pressure distributions around a 45^0 deviated wellbore during unloading scenario III.

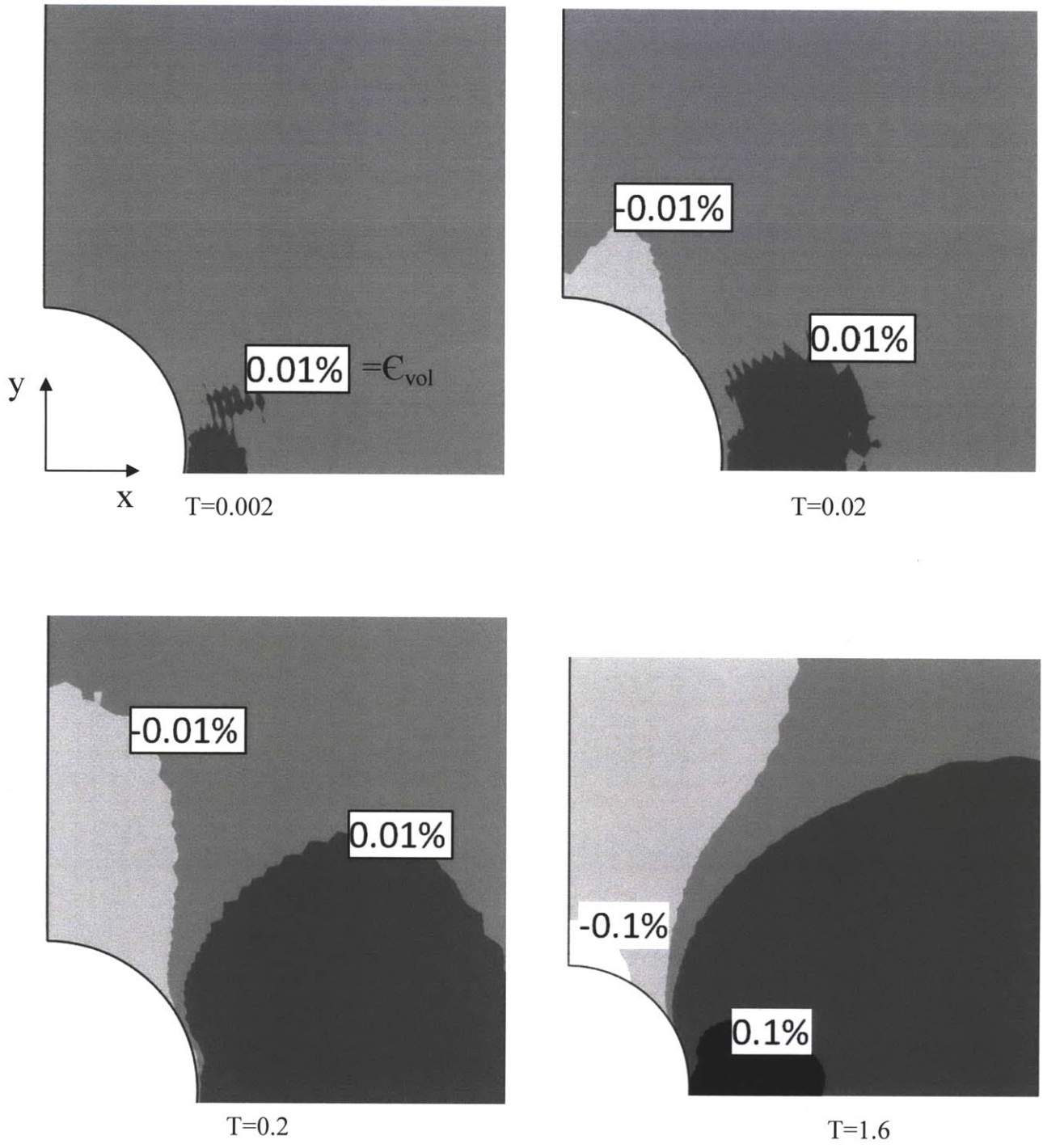

Figure 6.33 MIT-E3 predictions of volumetric strain distributions around a 45^0 deviated wellbore during unloading scenario III.

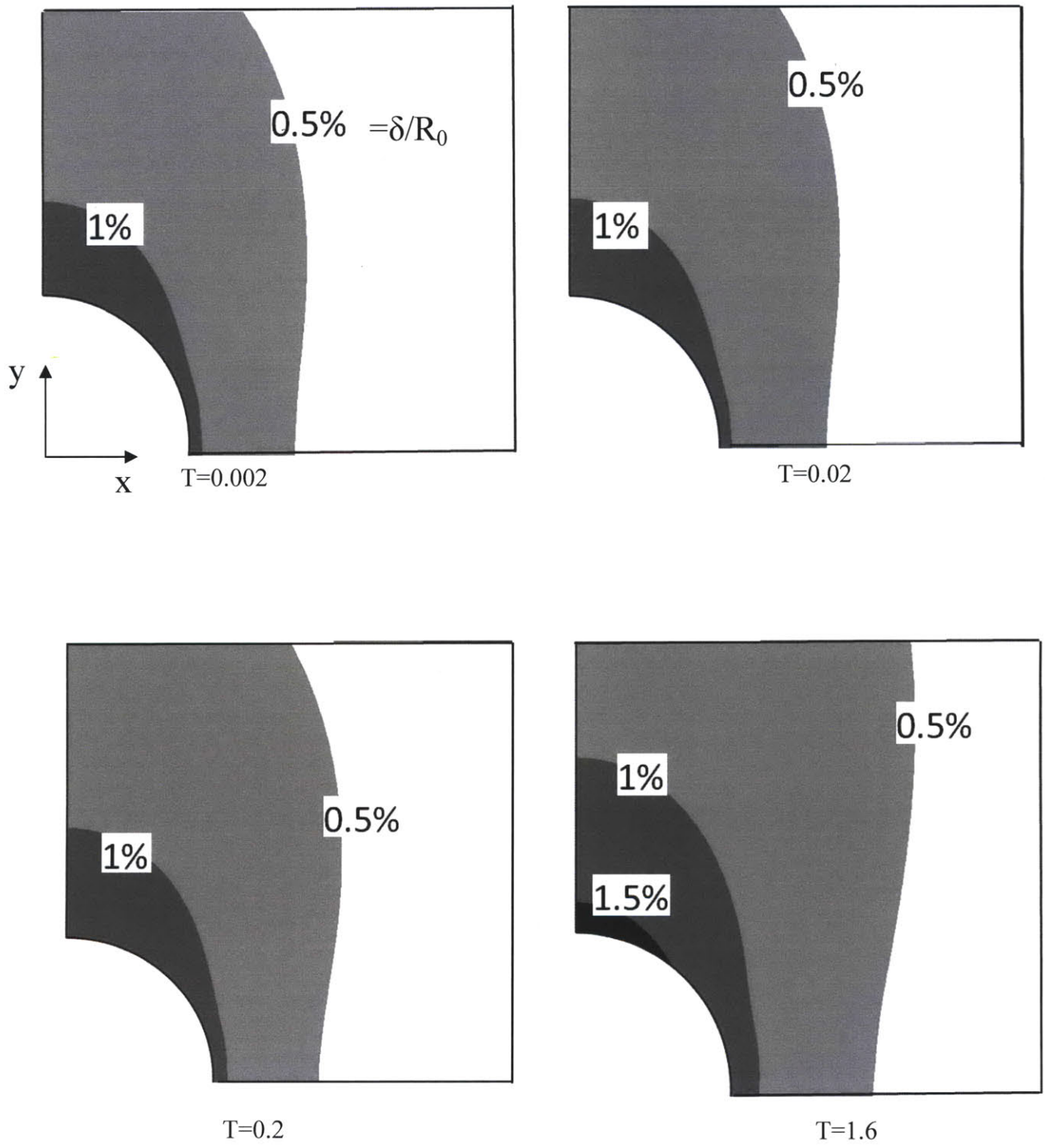

Figure 6.34 MIT-E3 predictions of radial deformations around a 45^0 deviated wellbore during unloading scenario III.

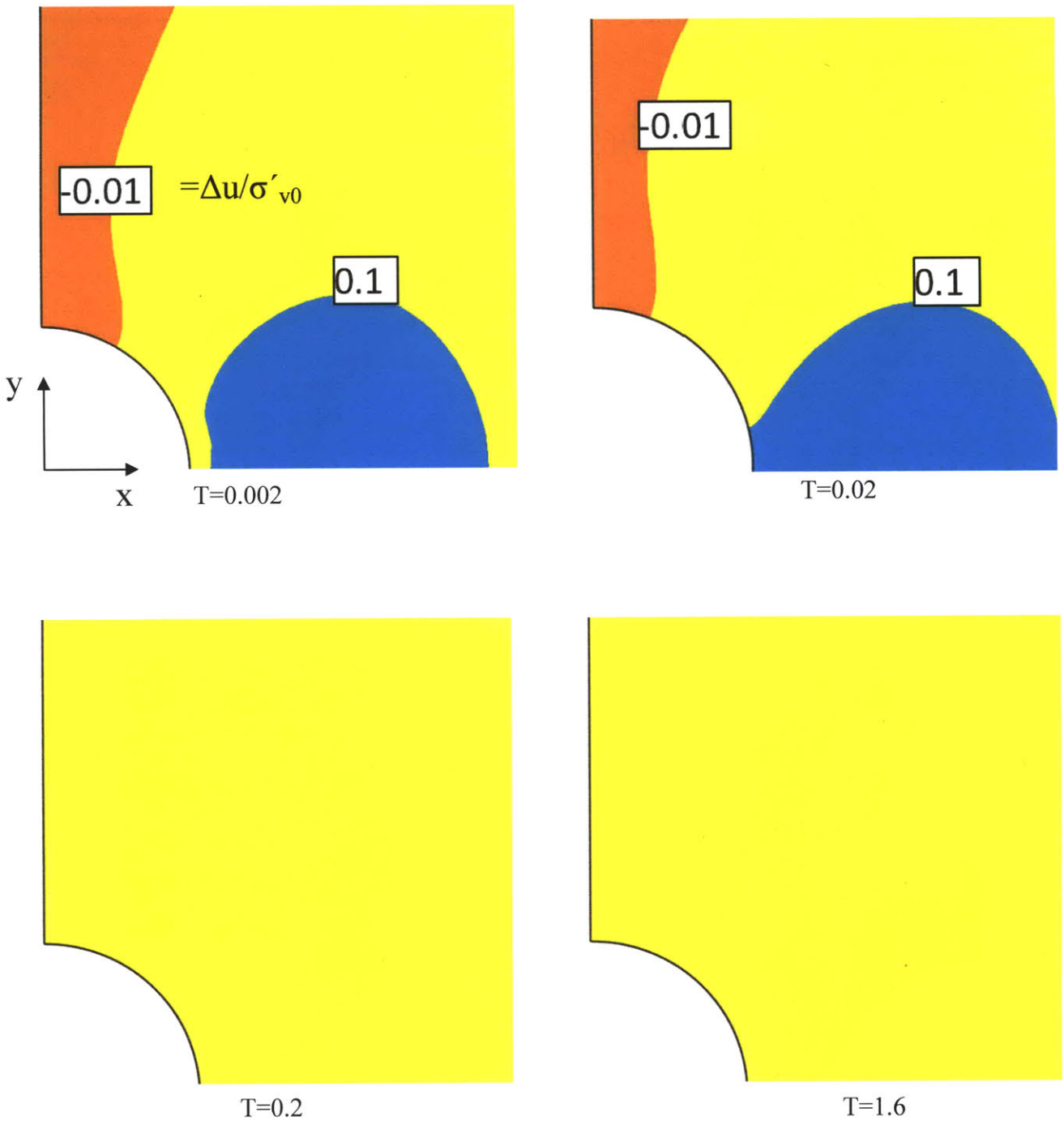

Figure 6.35 MIT-E3 predictions of excess pore pressure distributions around a 60^0 deviated wellbore during unloading scenario III.

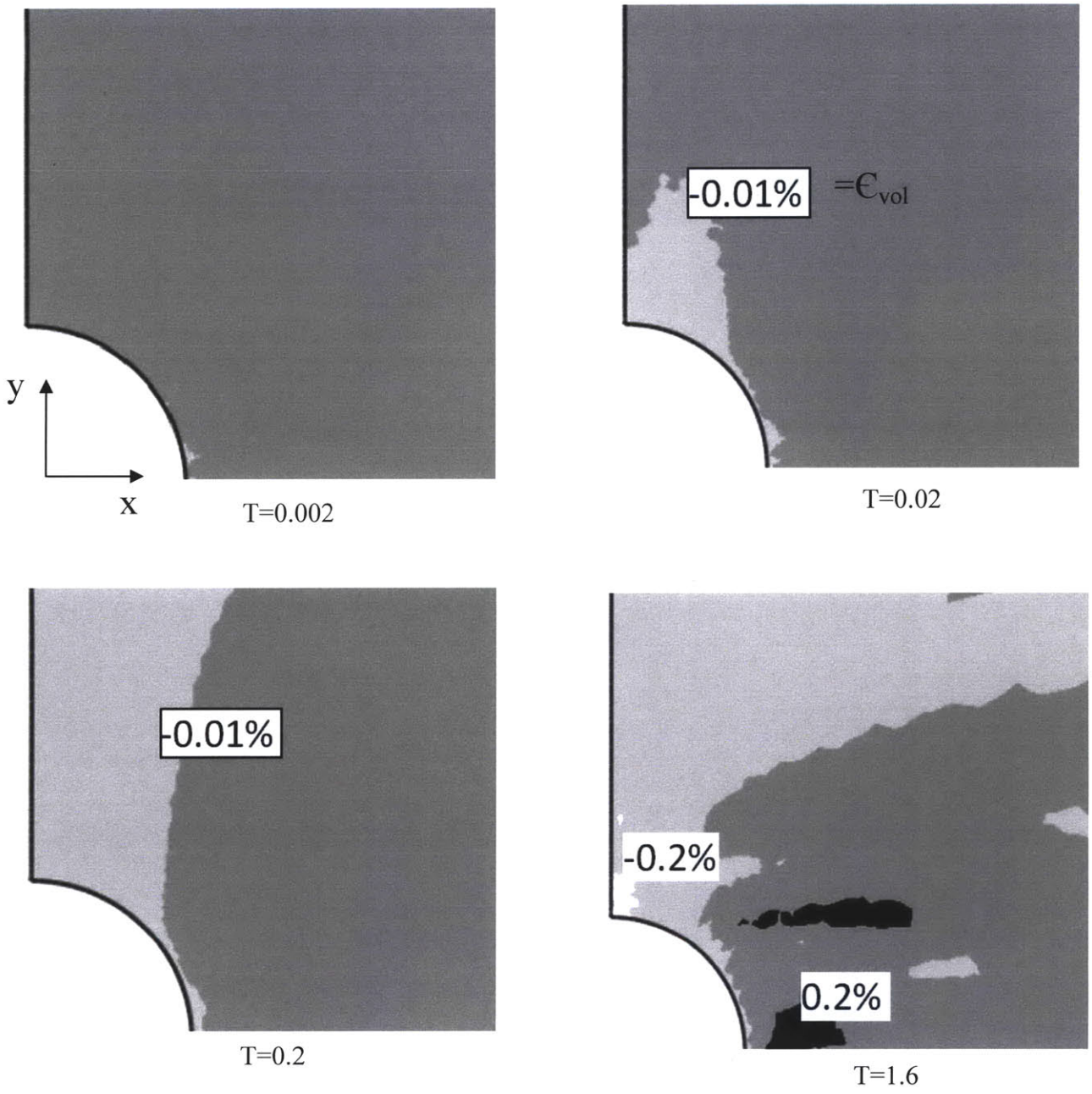

Figure 6.36 MIT-E3 predictions of volumetric strain distributions around a 60^0 deviated wellbore during unloading scenario III.

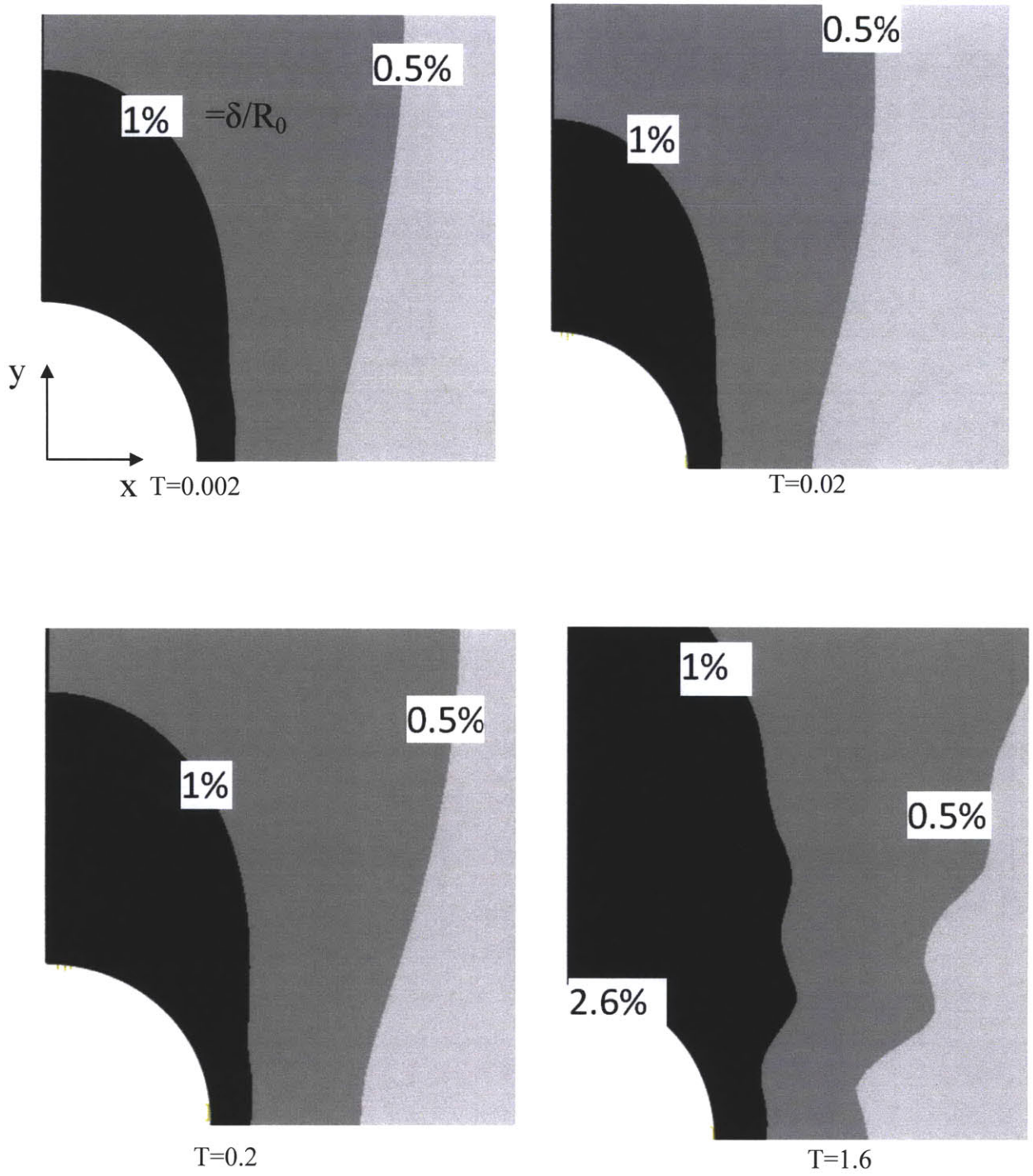

Figure 6.37 MIT-E3 predictions of radial deformations around a 60^0 deviated wellbore during unloading scenario III.

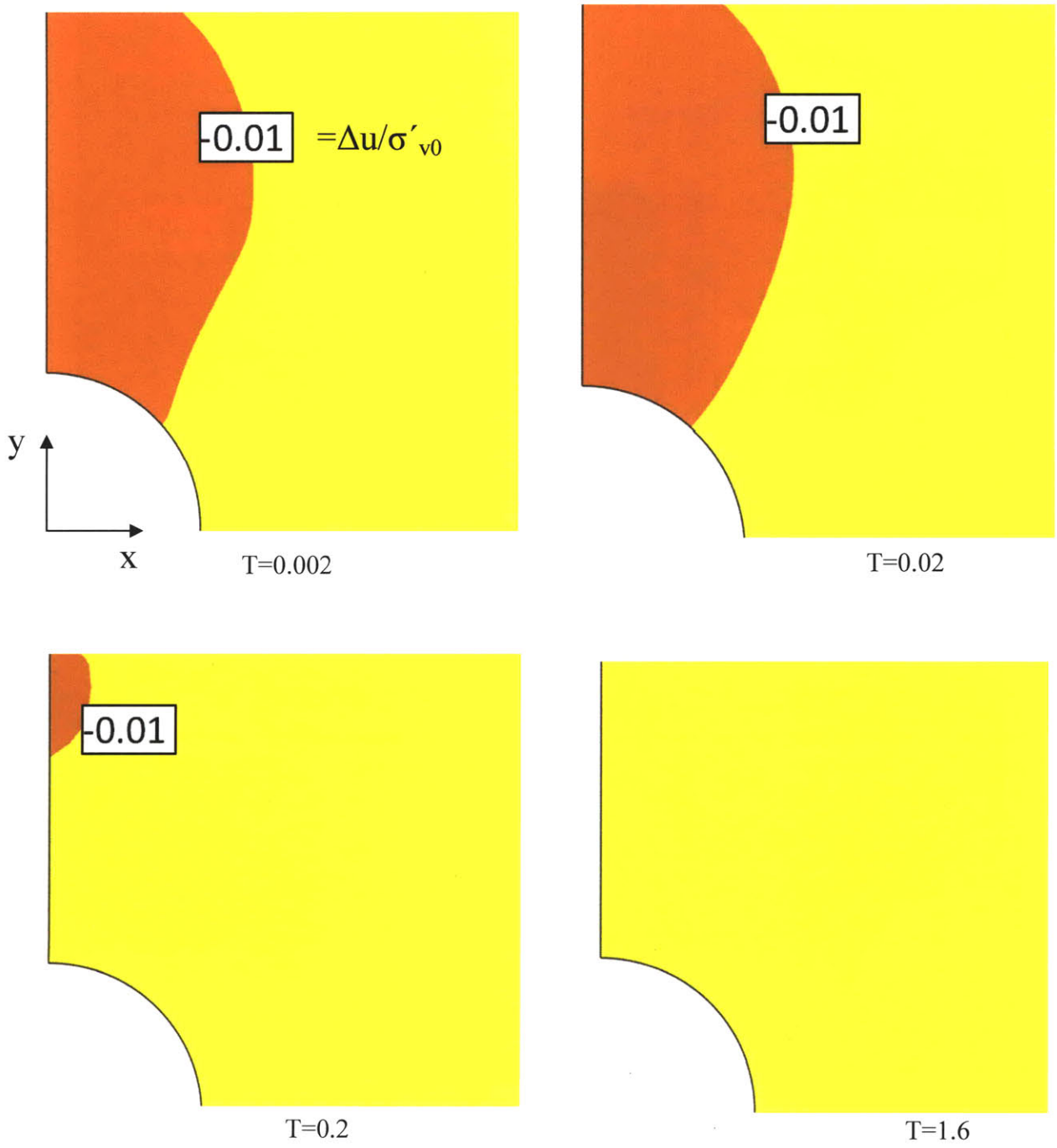

Figure 6.38 MCC predictions of excess pore pressure distributions around a 30^0 deviated wellbore during unloading scenario III.

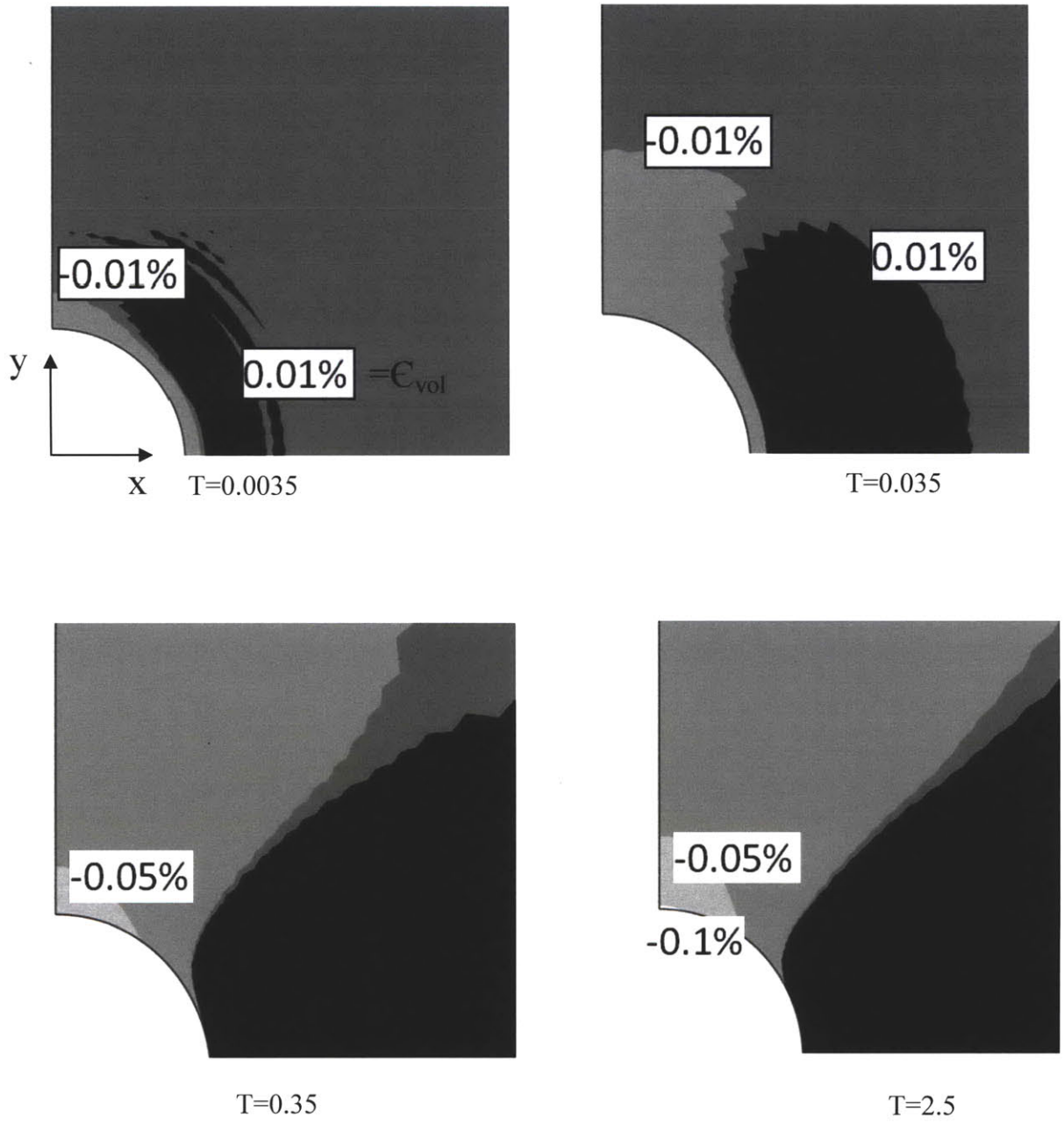

Figure 6.39 MCC predictions of the volumetric strain distributions around a 30^0 deviated wellbore during unloading scenario III.

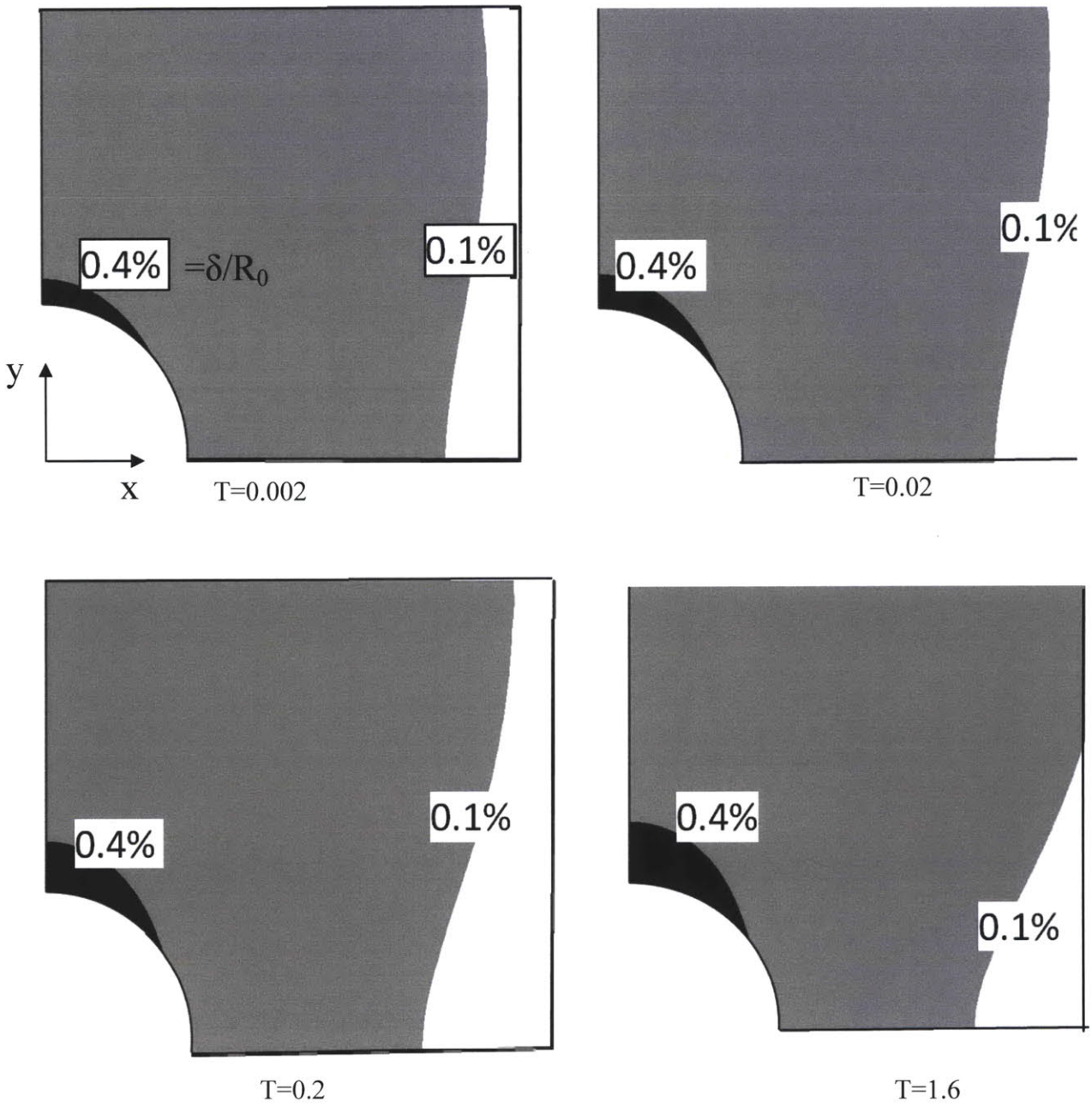

Figure 6.40 MCC predictions of the radial deformations around a 30^0 deviated wellbore during unloading scenario III.

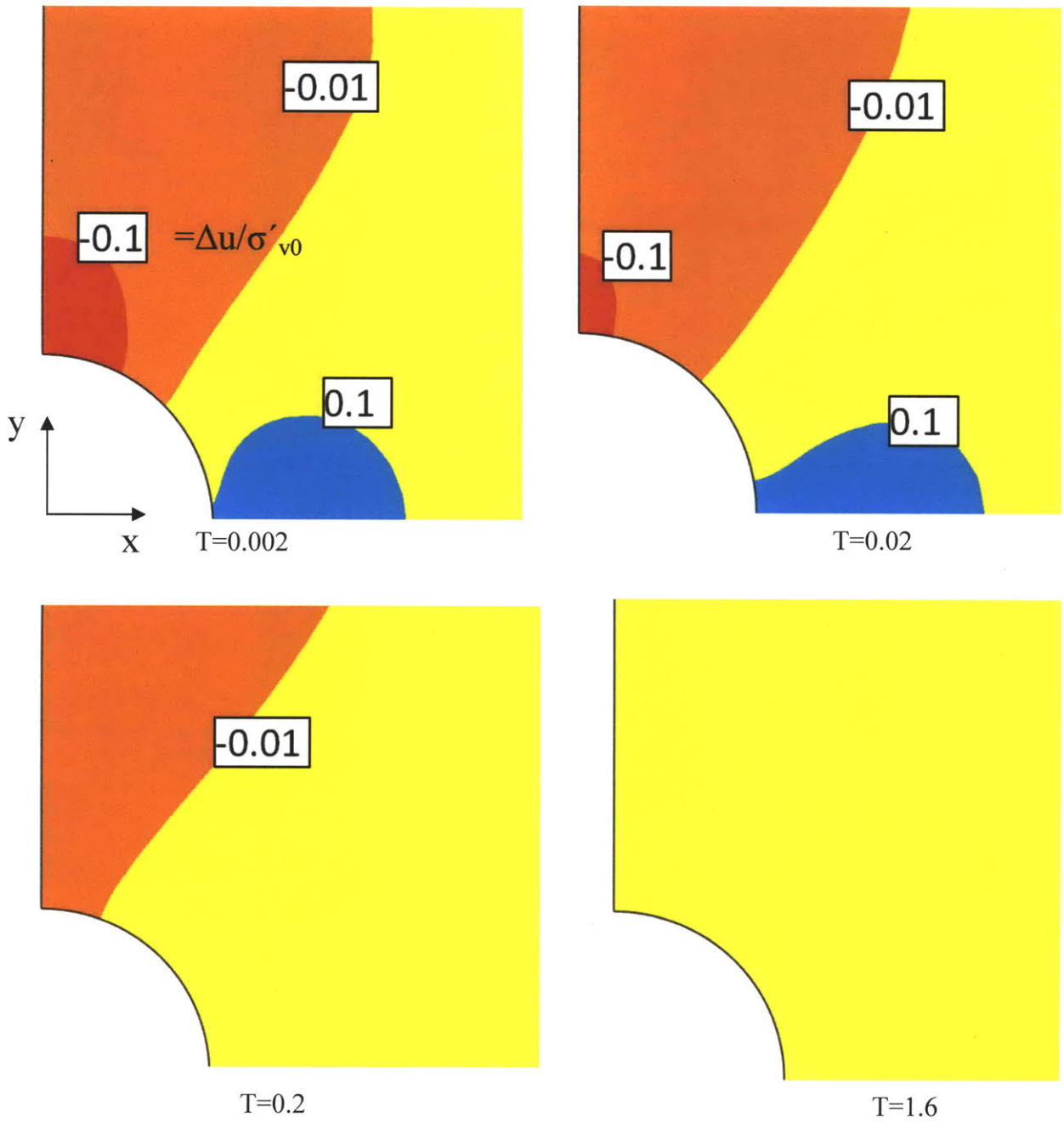

Figure 6.41 MCC predictions of excess pore pressure distributions around a 45^0 deviated wellbore during unloading scenario III.

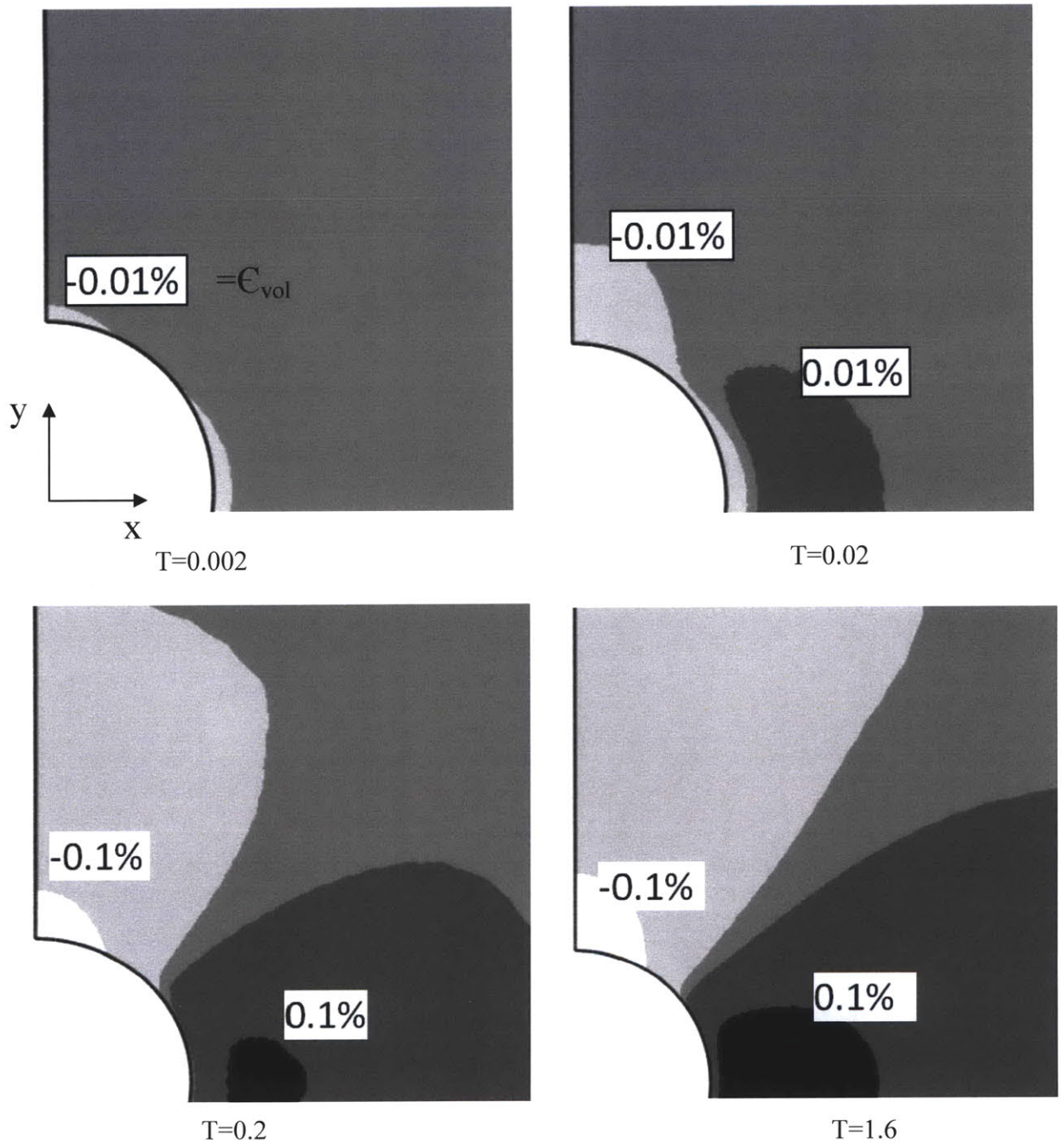

Figure 6.42 MCC predictions of the volumetric strain distributions around a 45^0 deviated wellbore during unloading scenario III.

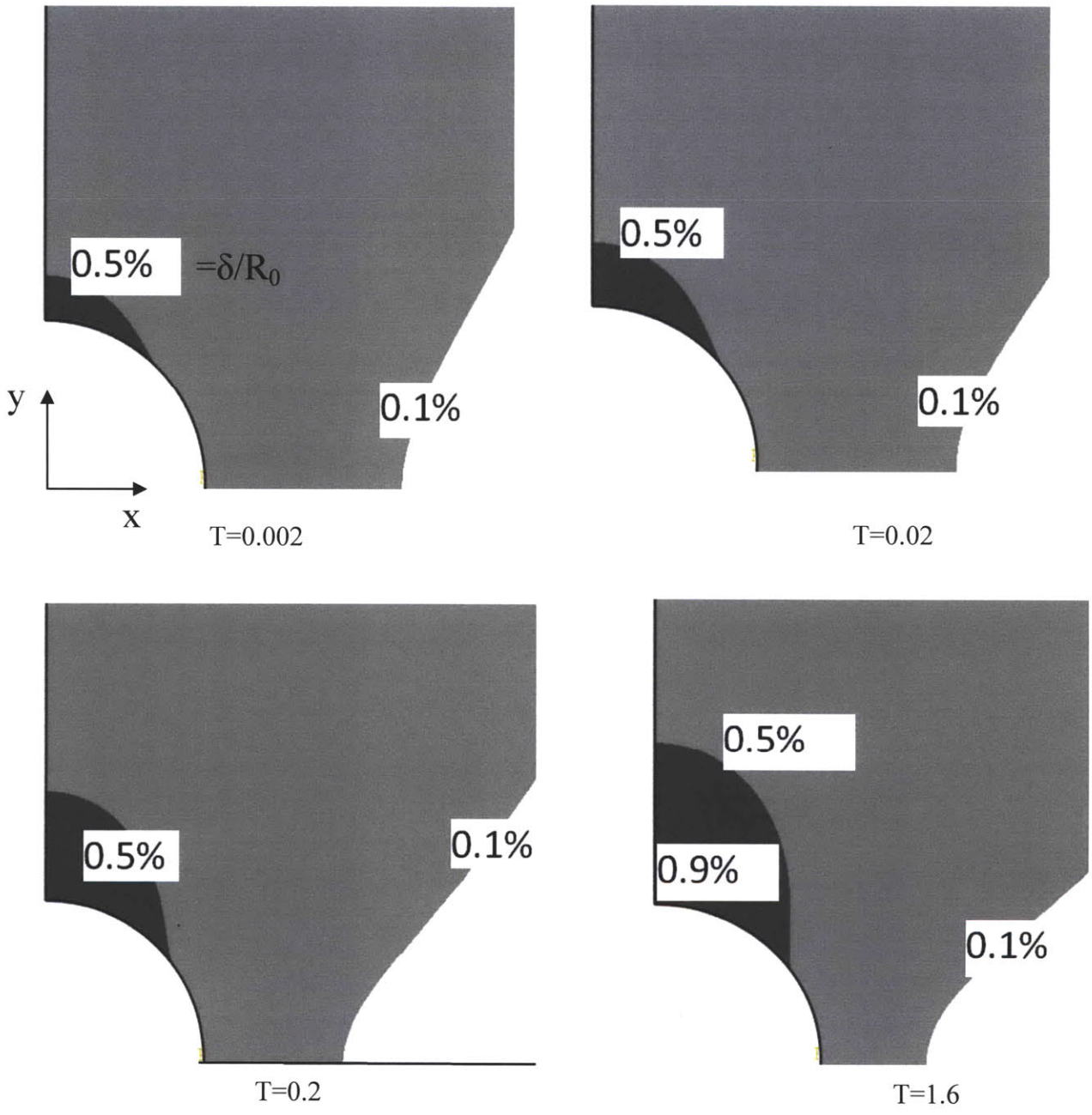

Figure 6.43 MCC predictions of the radial deformations around a 45^0 deviated wellbore during unloading scenario III.

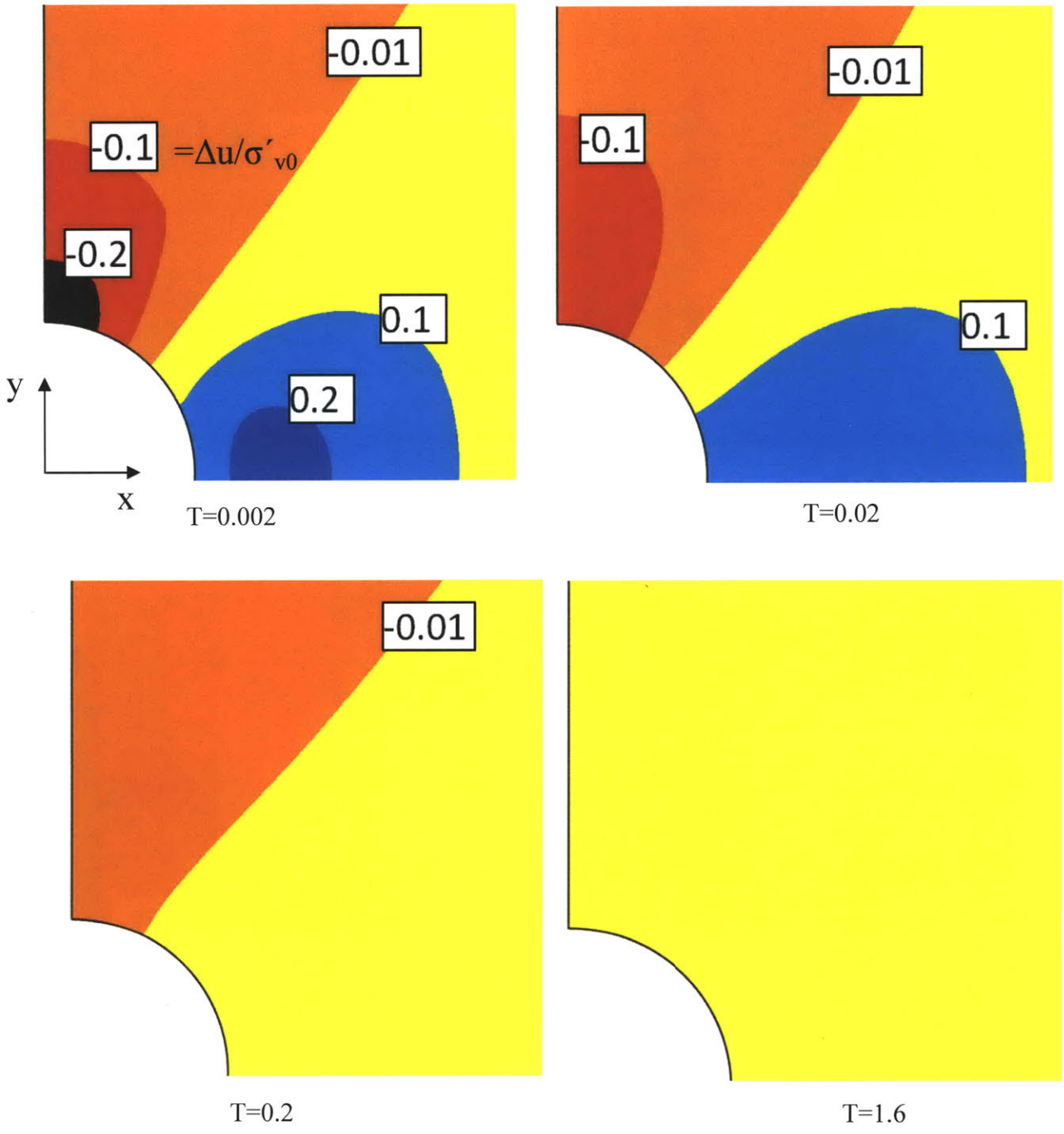

Figure 6.44 MCC predictions of excess pore pressure distributions around a 60^0 deviated wellbore during unloading scenario III.

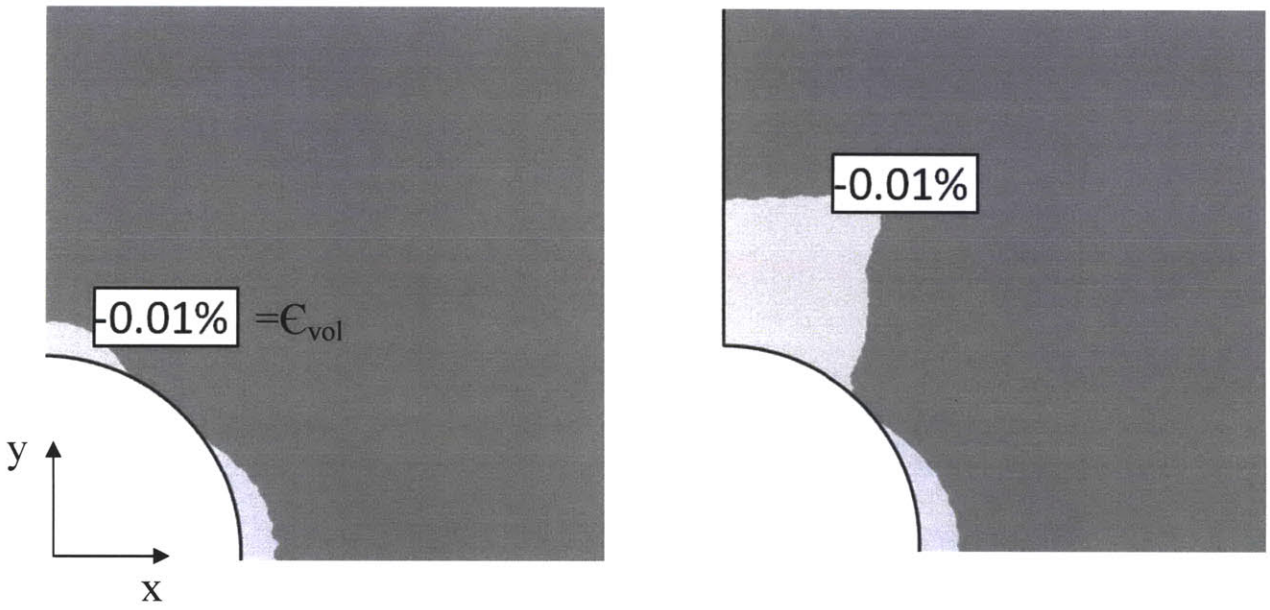

T=0.002 T=0.02

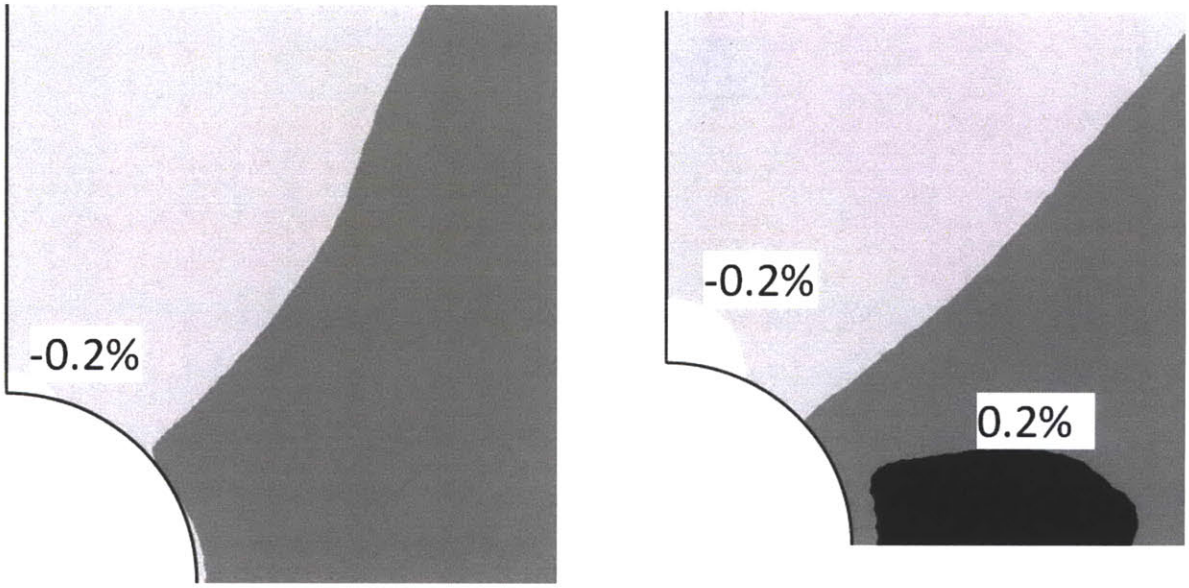

T=0.2 T=1.6

Figure 6.45 MCC predictions of the volumetric strain distributions around a 60^0 deviated wellbore during unloading scenario III.

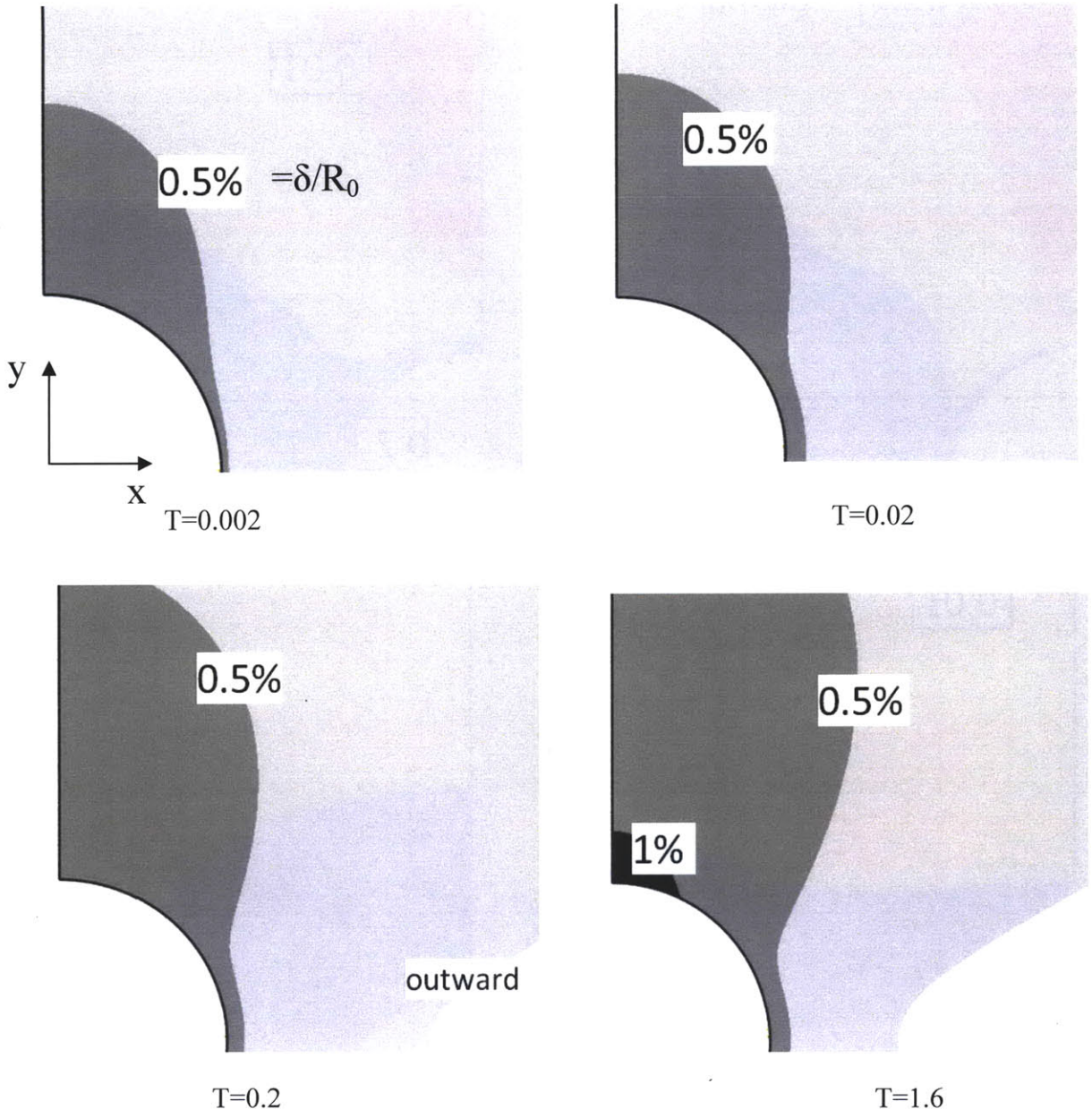

Figure 6.46 MCC predictions of the radial deformations around a 60^0 deviated wellbore during unloading scenario III.

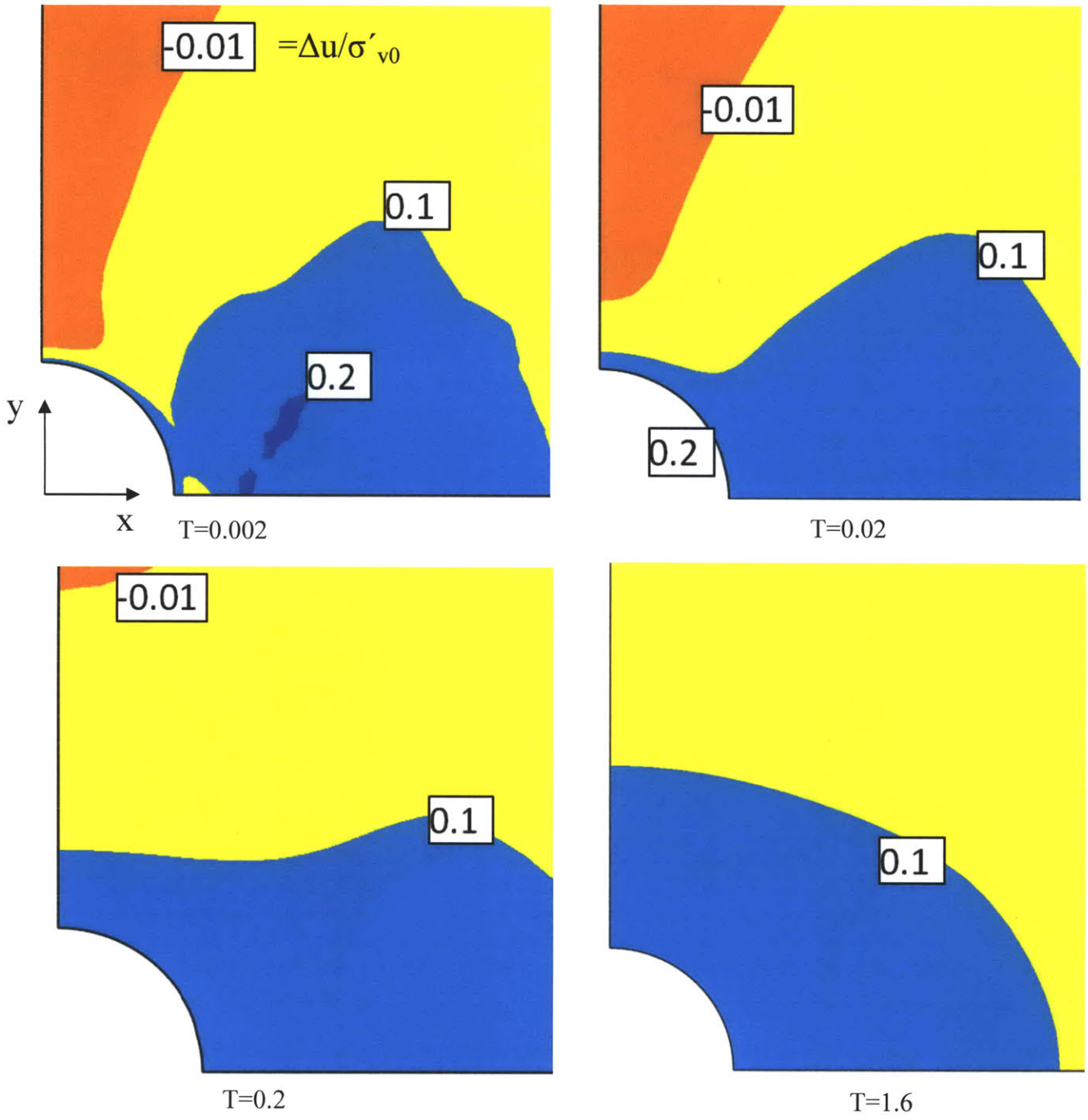

Figure 6.47 MIT-E3 predictions of excess pore pressure around a horizontal wellbore during unloading scenario I.

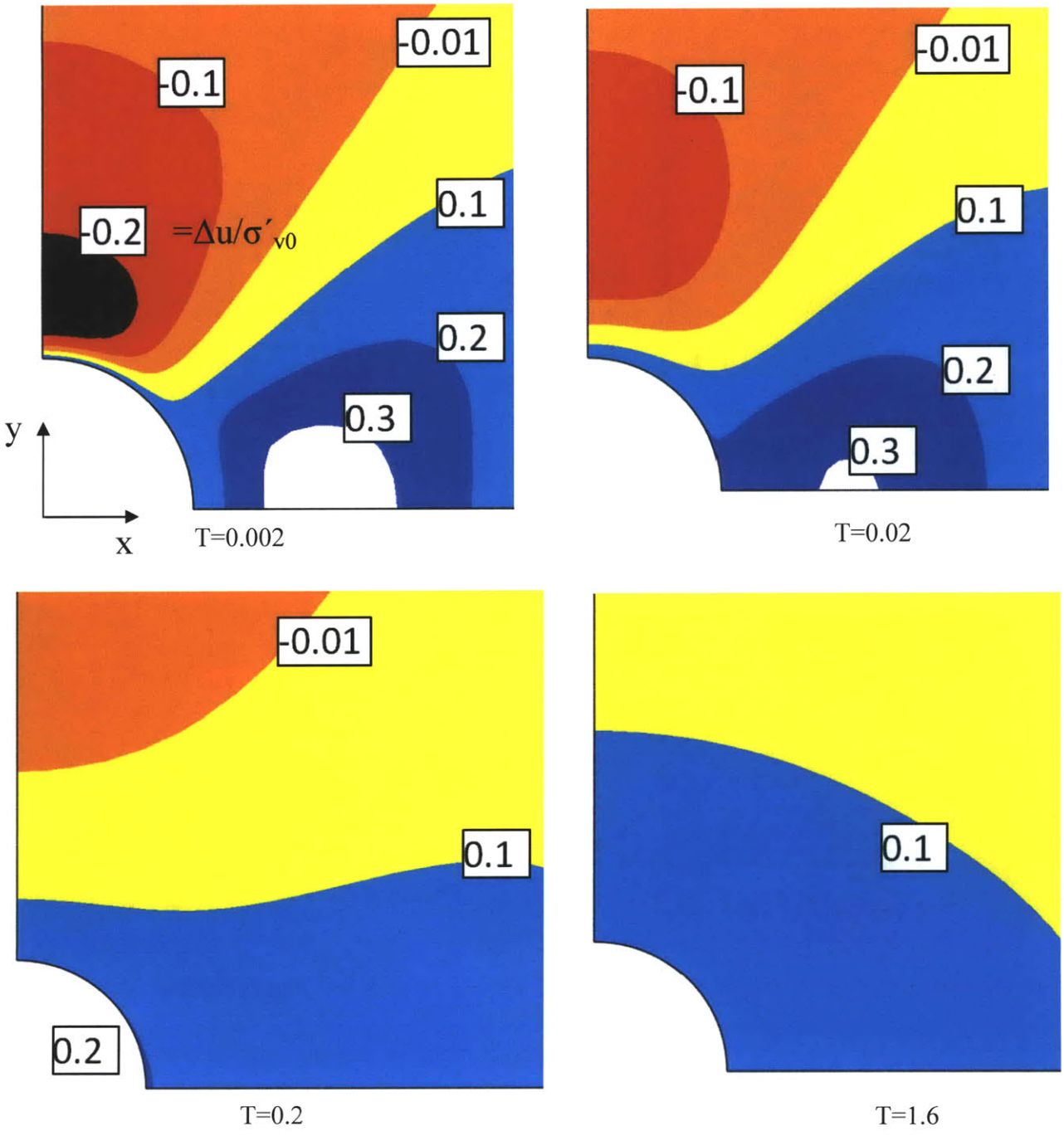

Figure 6.48 MCC predictions of excess pore pressure around a horizontal wellbore during unloading scenario I.

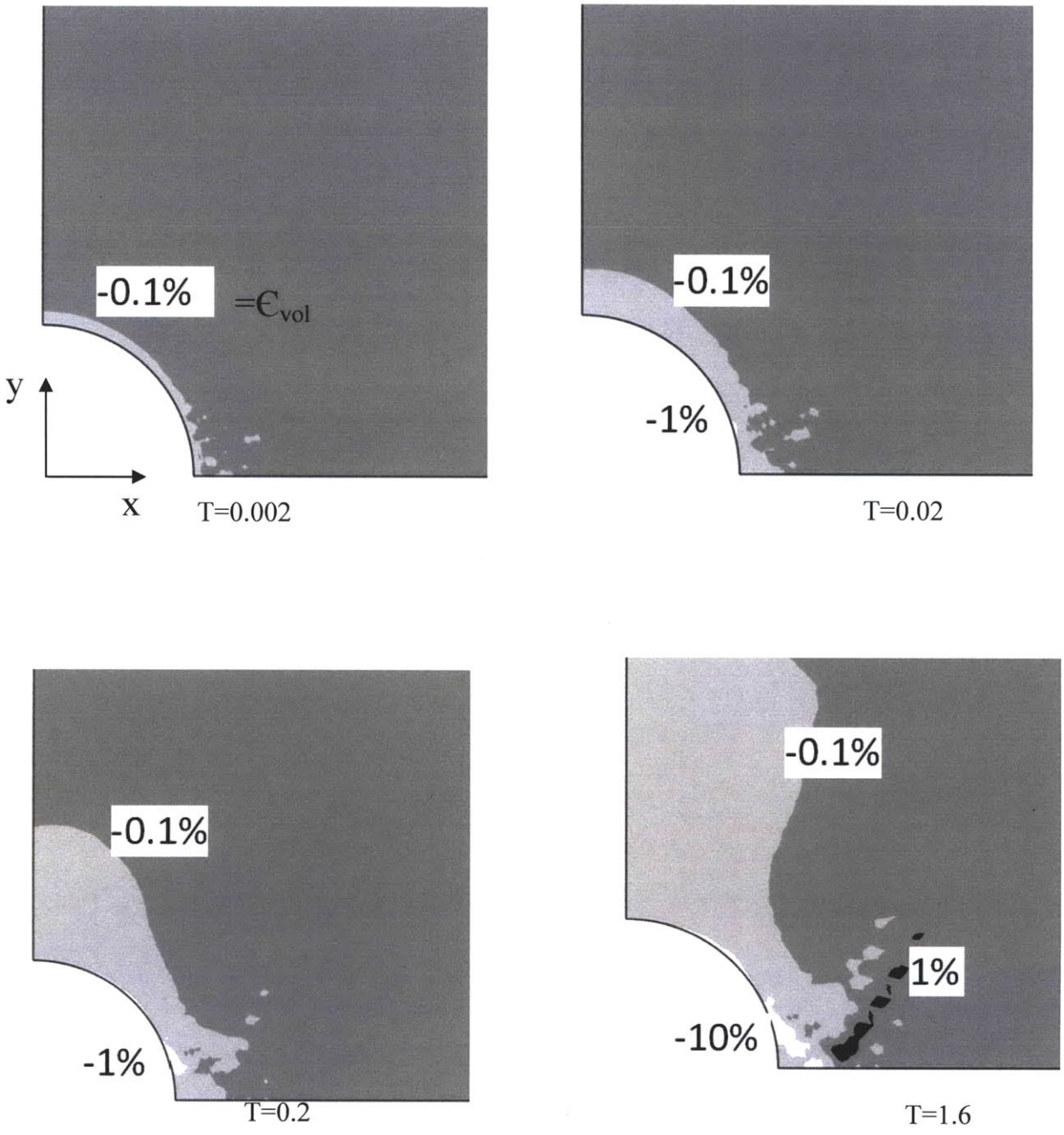

Figure 6.49 MIT-E3 predictions of volumetric strain distributions around a horizontal wellbore during unloading scenario I.

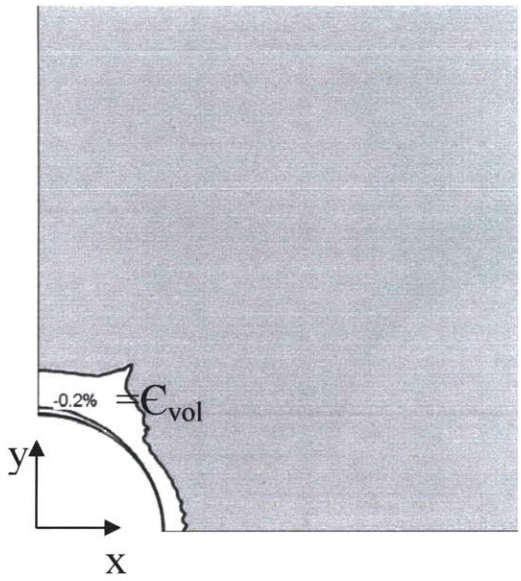

T=0.002

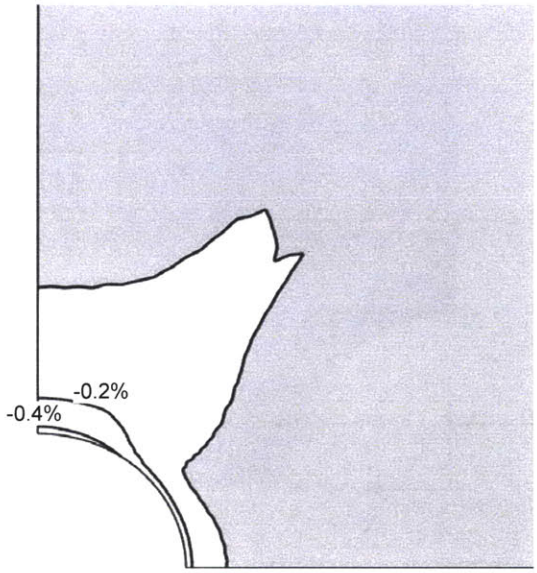

T=0.02

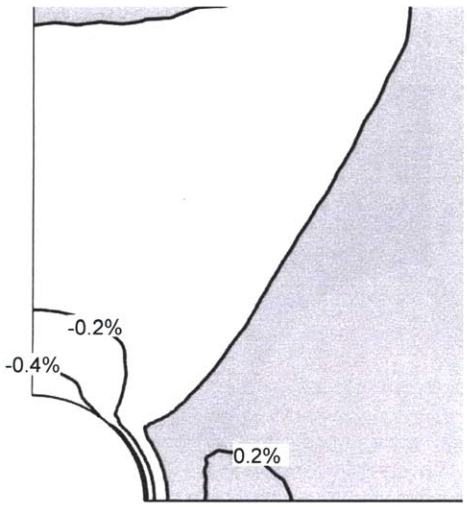

T=0.2

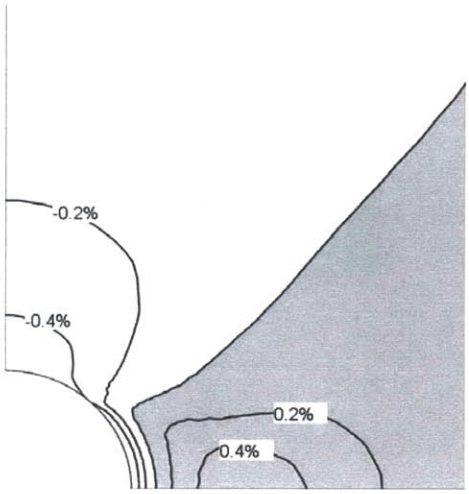

T=1.6

Figure 6.50 MCC predictions of volumetric strain distributions around a horizontal wellbore during unloading scenario I.

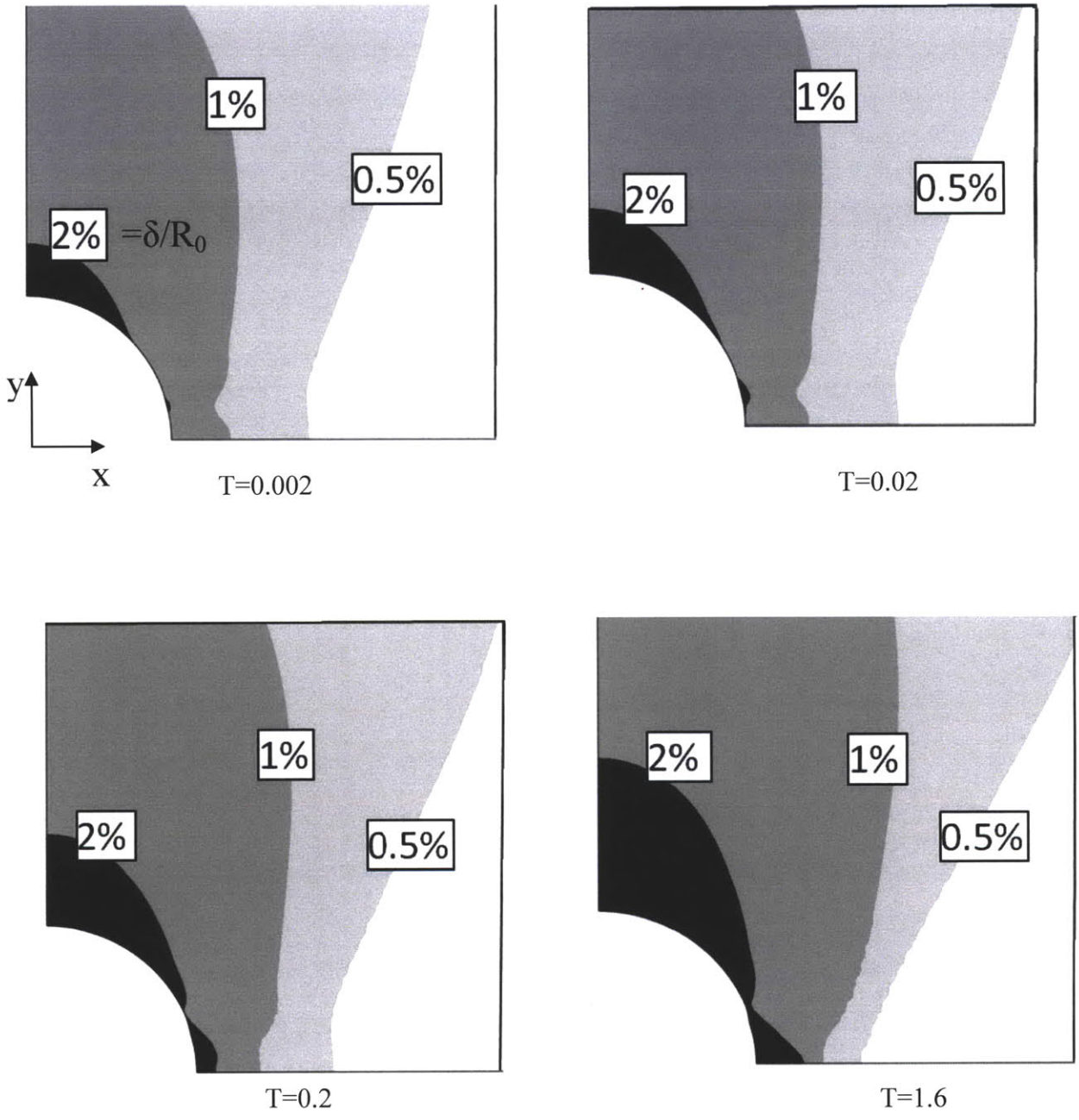

Figure 6.51 MIT-E3 predictions of radial deformations around a horizontal wellbore during unloading scenario I.

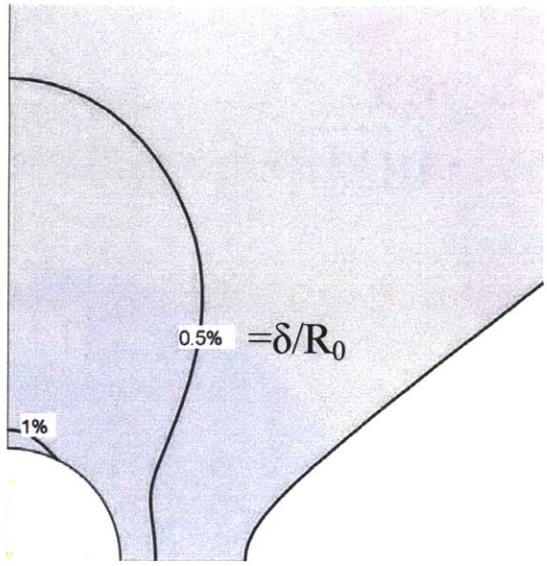

T=0.002

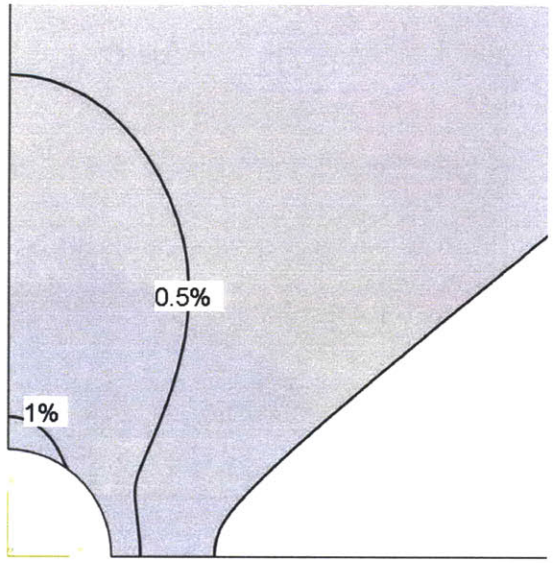

T=0.02

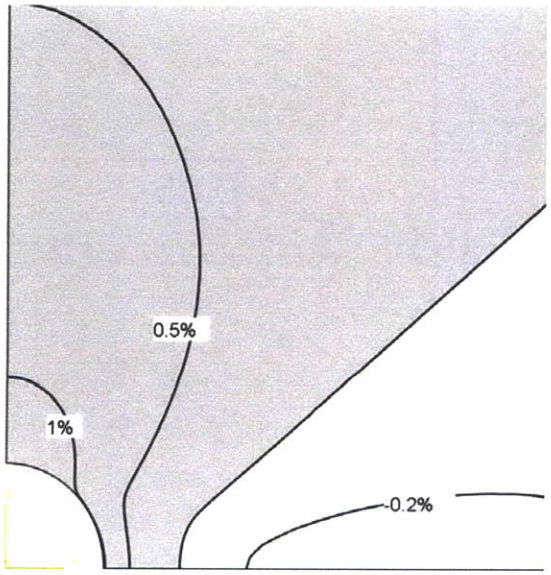

T=0.2

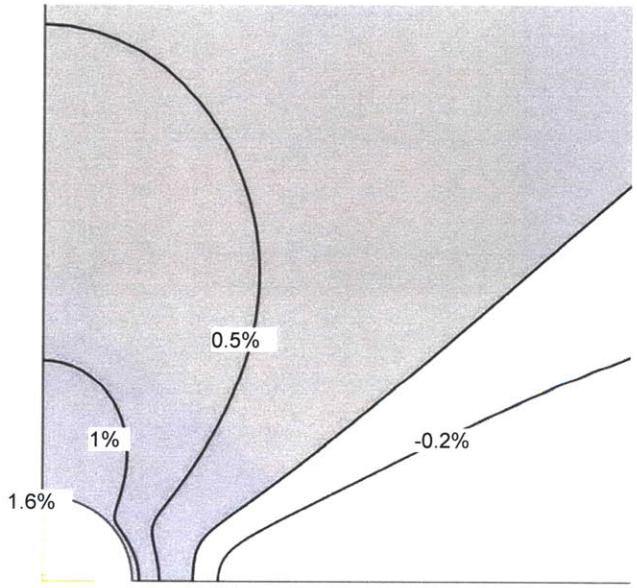

T=1.6

Figure 6.52 MCC predictions of radial deformations around a horizontal wellbore during unloading scenario I.

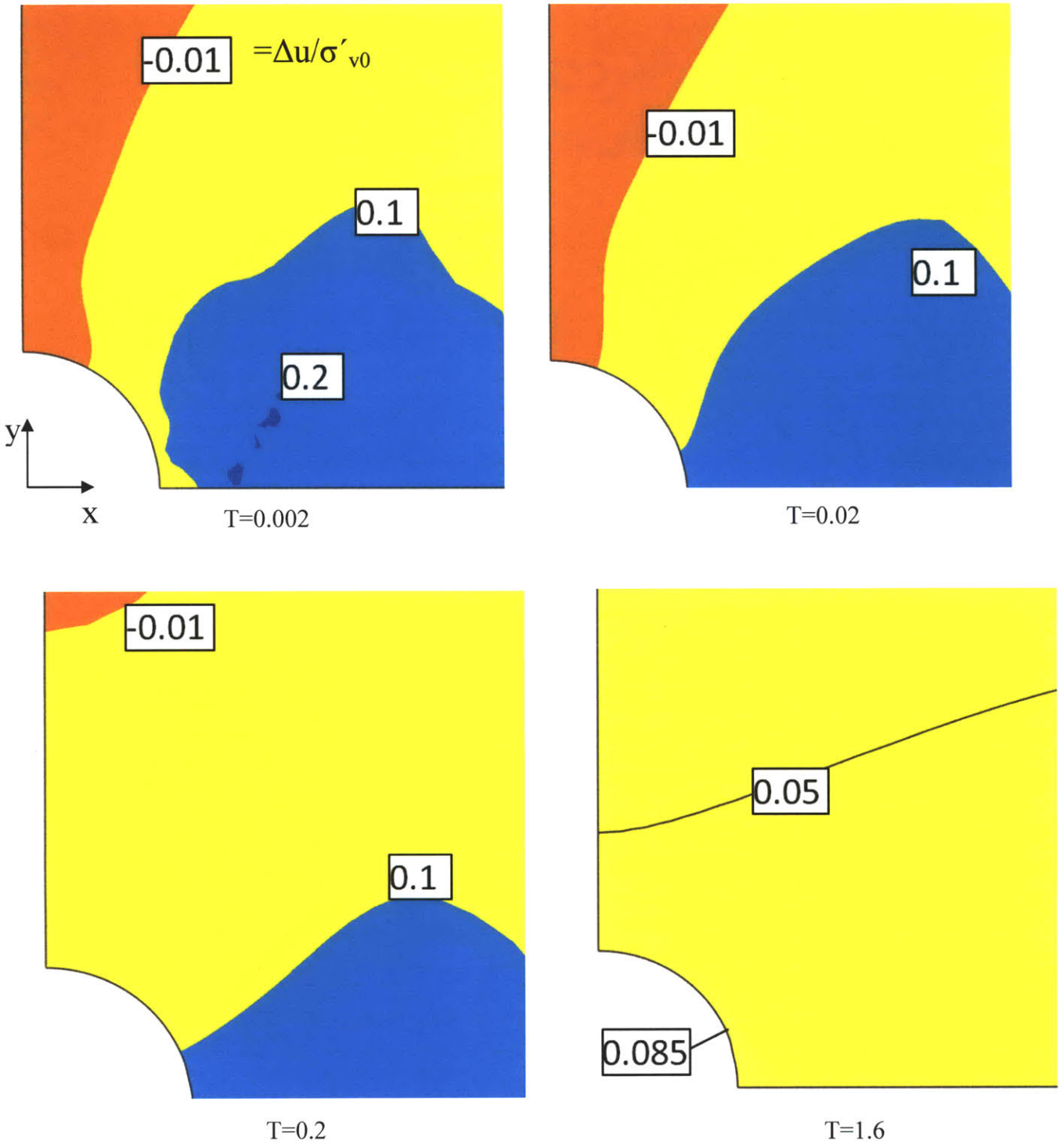

Figure 6.53 MIT-E3 predictions of excess pore pressure distributions around a horizontal wellbore during unloading scenario III.

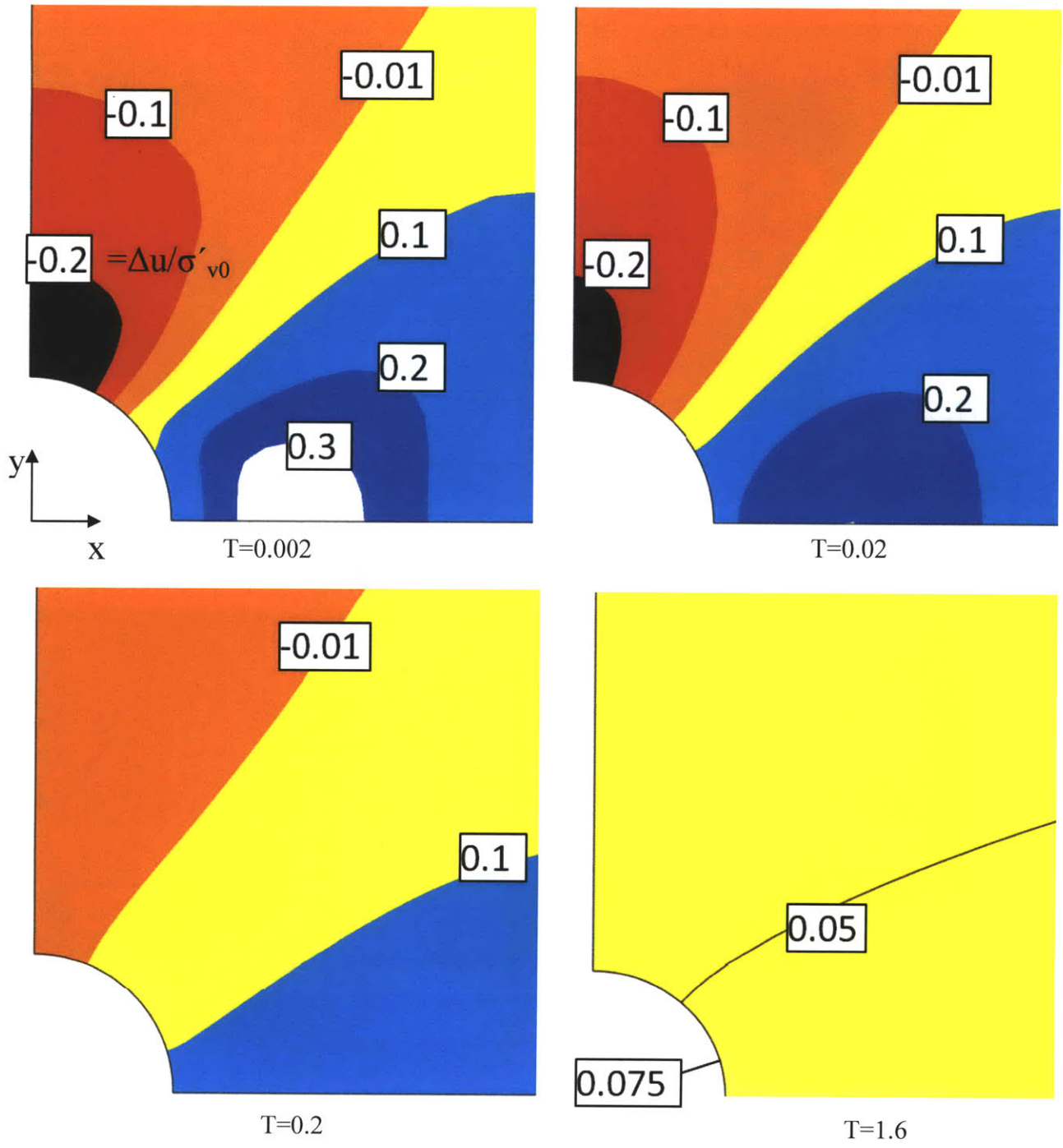

Figure 6.54 MCC predictions of excess pore pressure distributions around a horizontal wellbore during unloading scenario III.

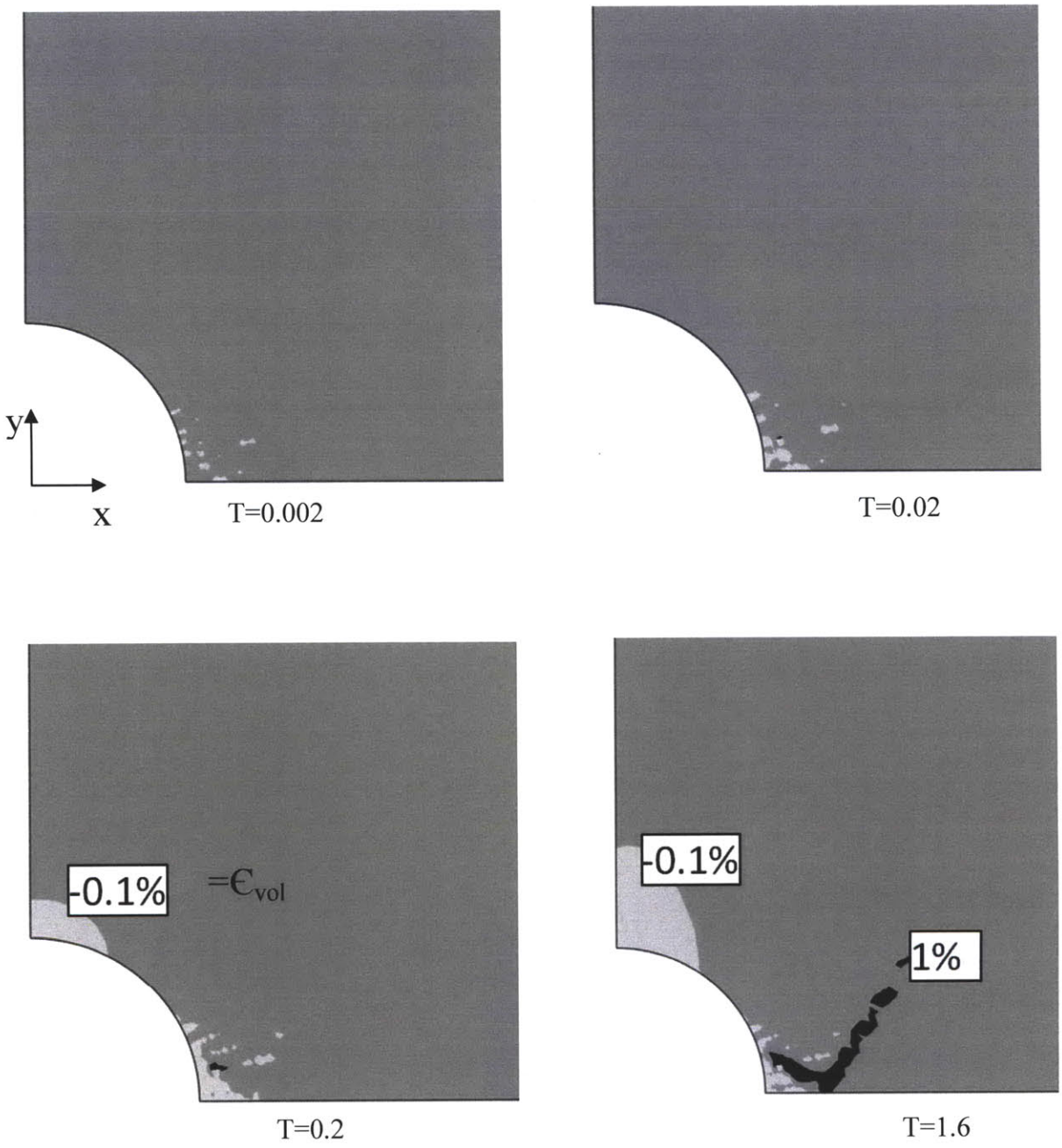

Figure 6.55 MIT-E3 predictions of volumetric strain distributions around a horizontal wellbore during unloading scenario III.

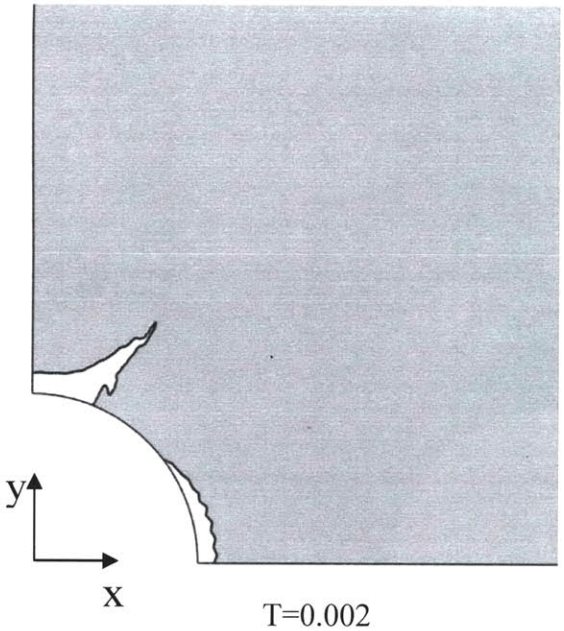

T=0.002

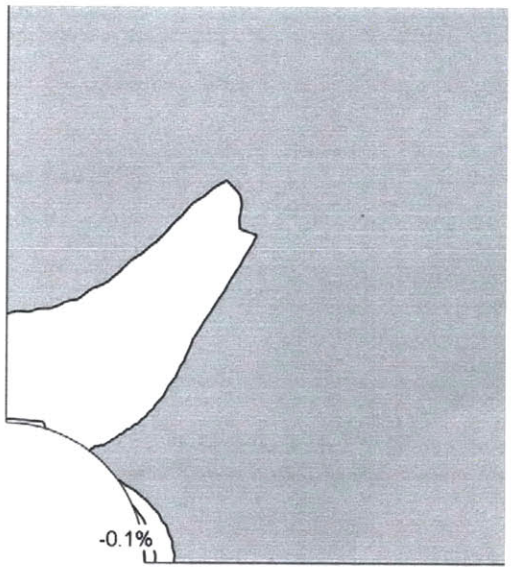

T=0.02

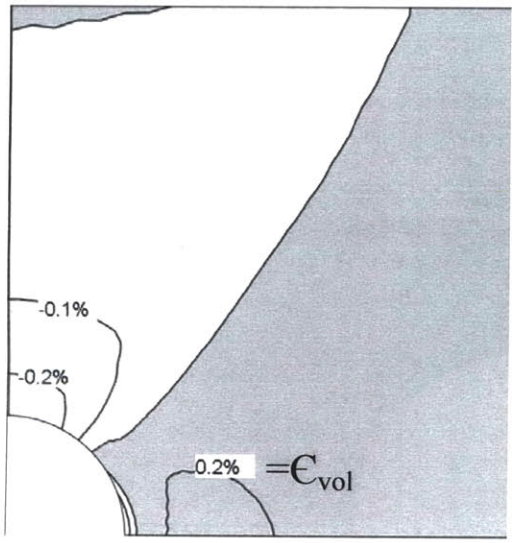

T=0.2

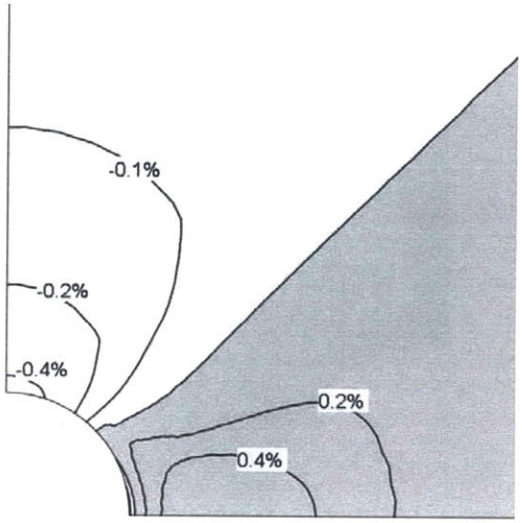

T=1.6

Figure 6.56 MCC predictions of volumetric strain distributions around a horizontal wellbore during unloading scenario III.

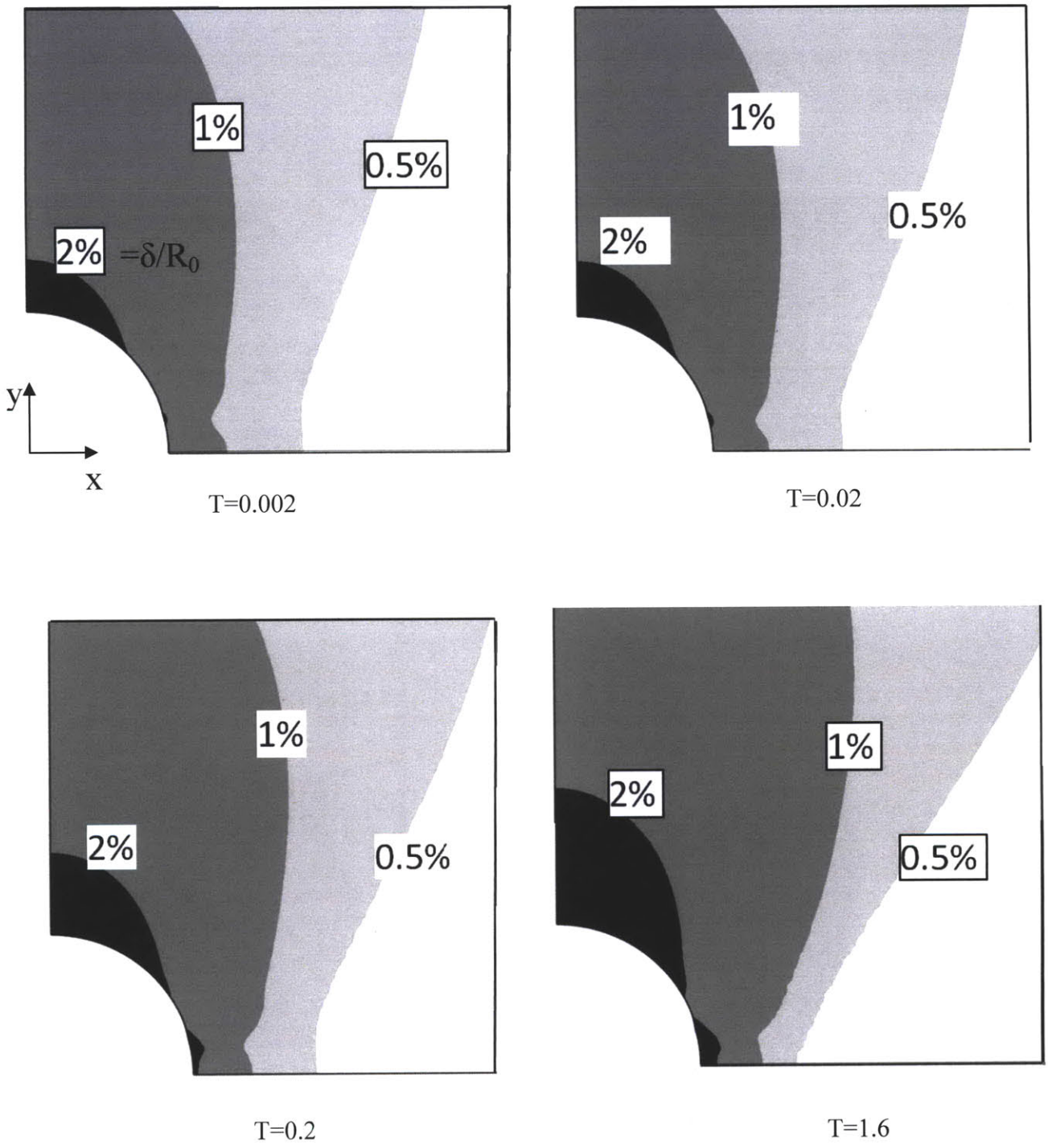

Figure 6.57 MIT-E3 predictions of radial deformations around a horizontal wellbore during unloading scenario III.

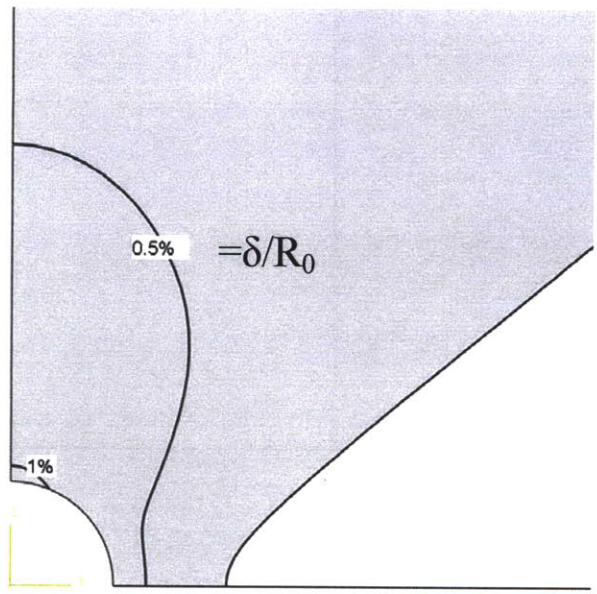

T=0.002

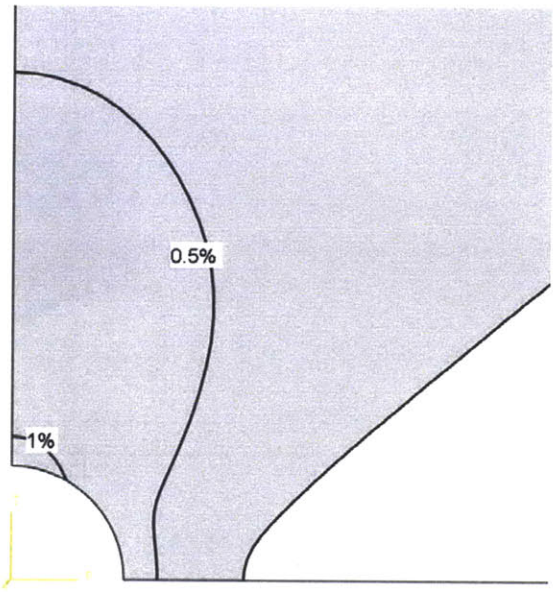

T=0.02

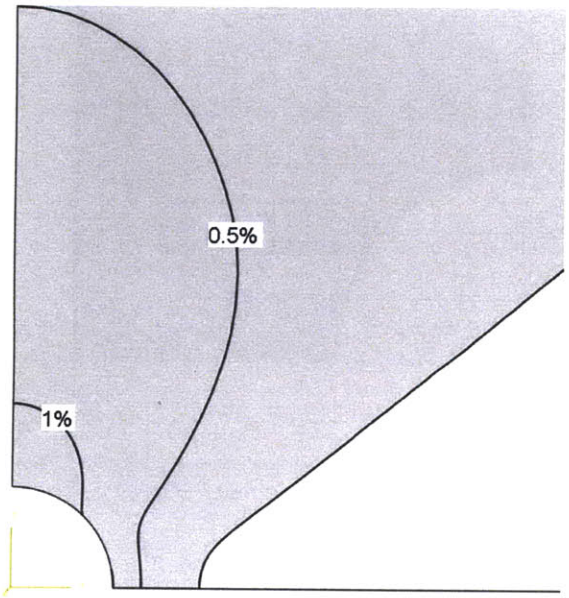

T=0.2

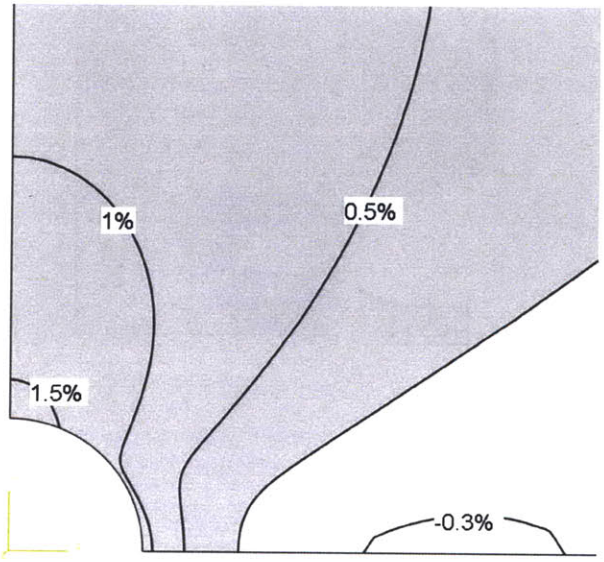

T=1.6

Figure 6.58 MCC predictions of radial deformations around a horizontal wellbore during unloading scenario III.

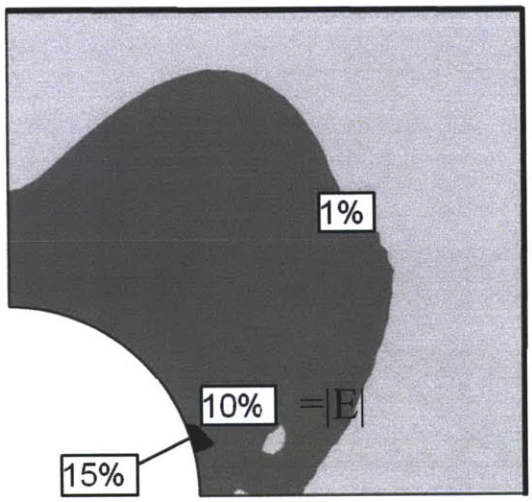

Scenario I

T=1.6

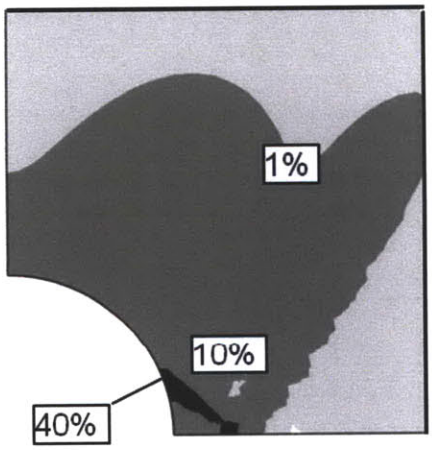

Scenario III

T=1.6

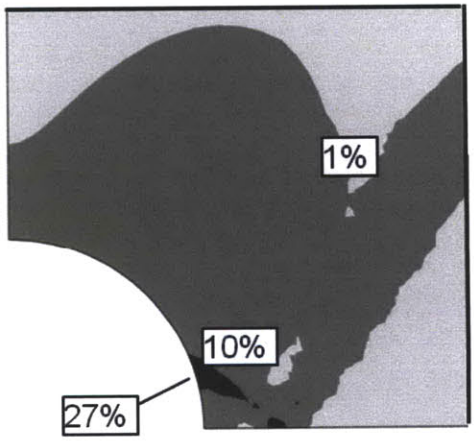

Figure 6.59 MIT-E3 predictions of the second invariant of the deviatoric strain tensor around a horizontal wellbore for permeable and impermeable cavity walls.

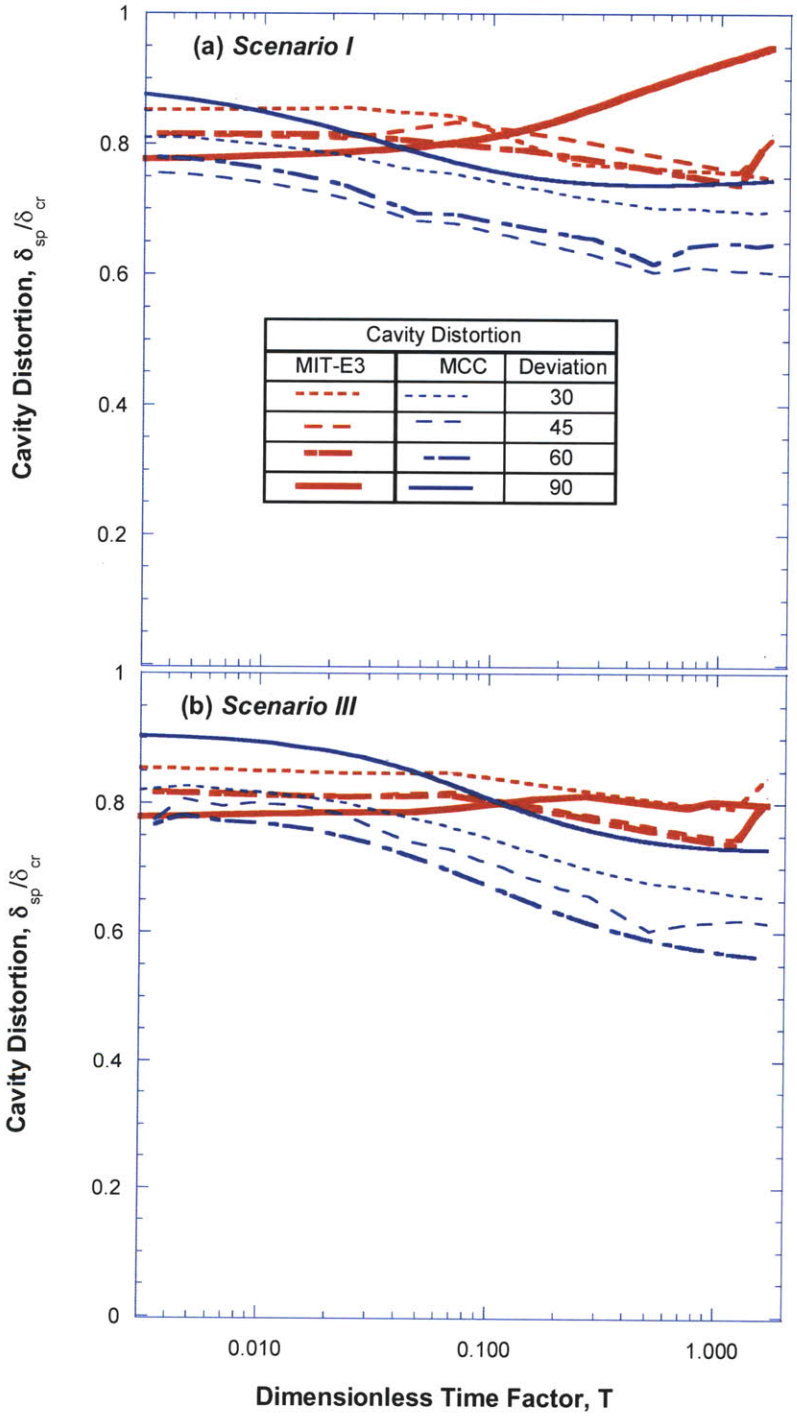

Figure 6.60 Effect of Consolidation on cavity distortion of deviated wellbores during unloading scenario (a) I and (b) III.

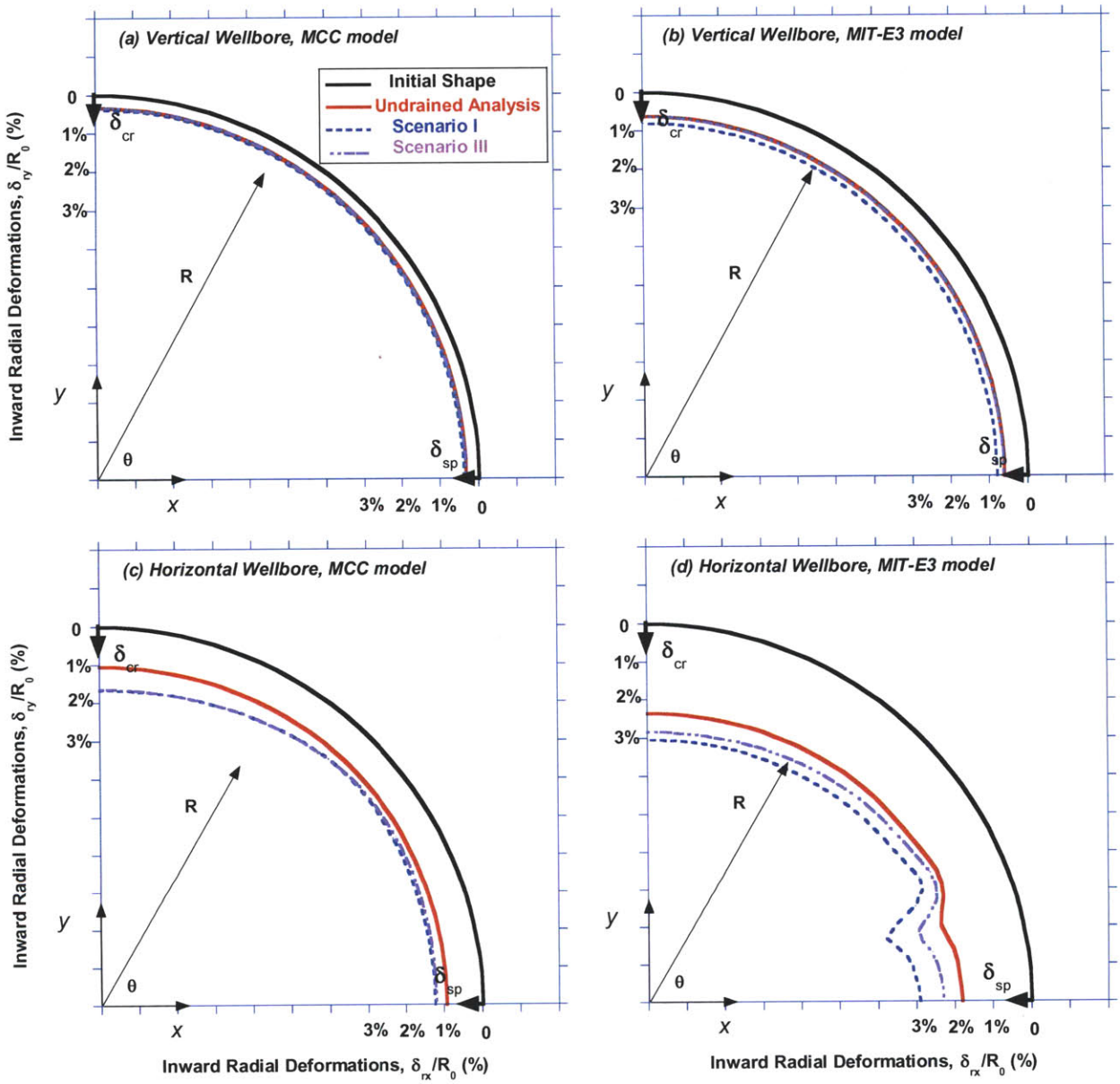

Figure 6.61 MIT-E3 and MCC predictions of cavity deformations in vertical and horizontal wellbores. (Deformations are scaled 10:1)

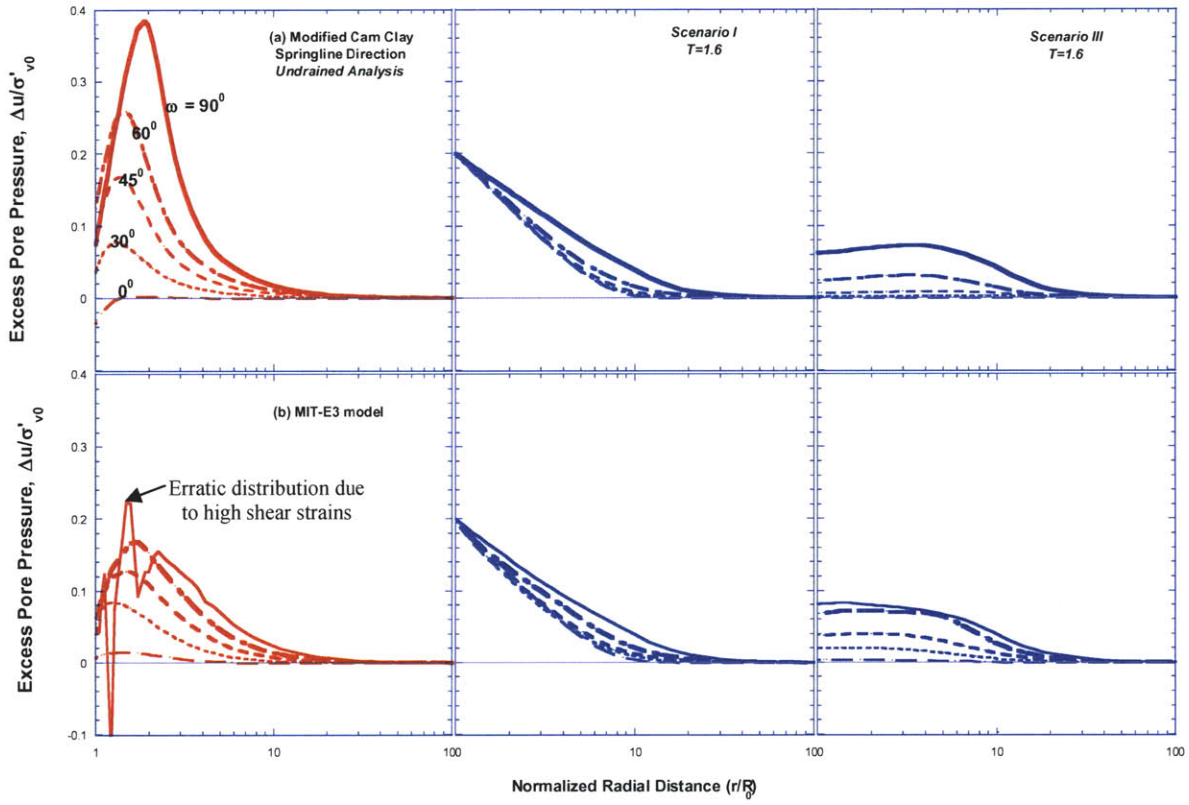

Figure 6.62 Effect of consolidation on pore pressure distribution in the radial direction $\theta=0^0$ around deviated wells during unloading scenarios I and III using (a) MCC and (b) MIT-E3 models.

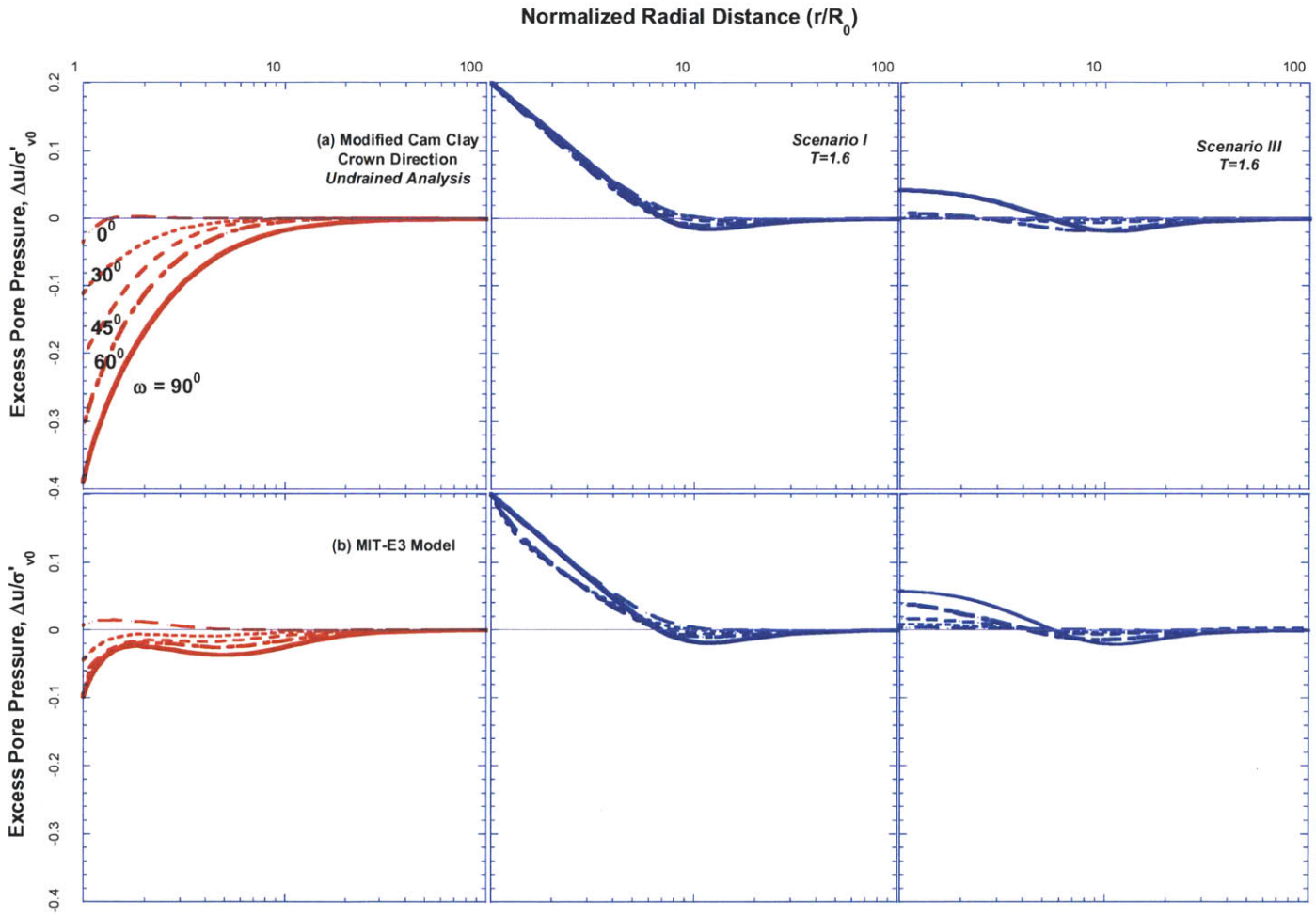

Figure 6.63 Effect of consolidation on pore pressure distribution in the radial direction θ=90^0 around deviated wells during unloading scenarios I and III using (a) MCC and (b) MIT-E3 models.

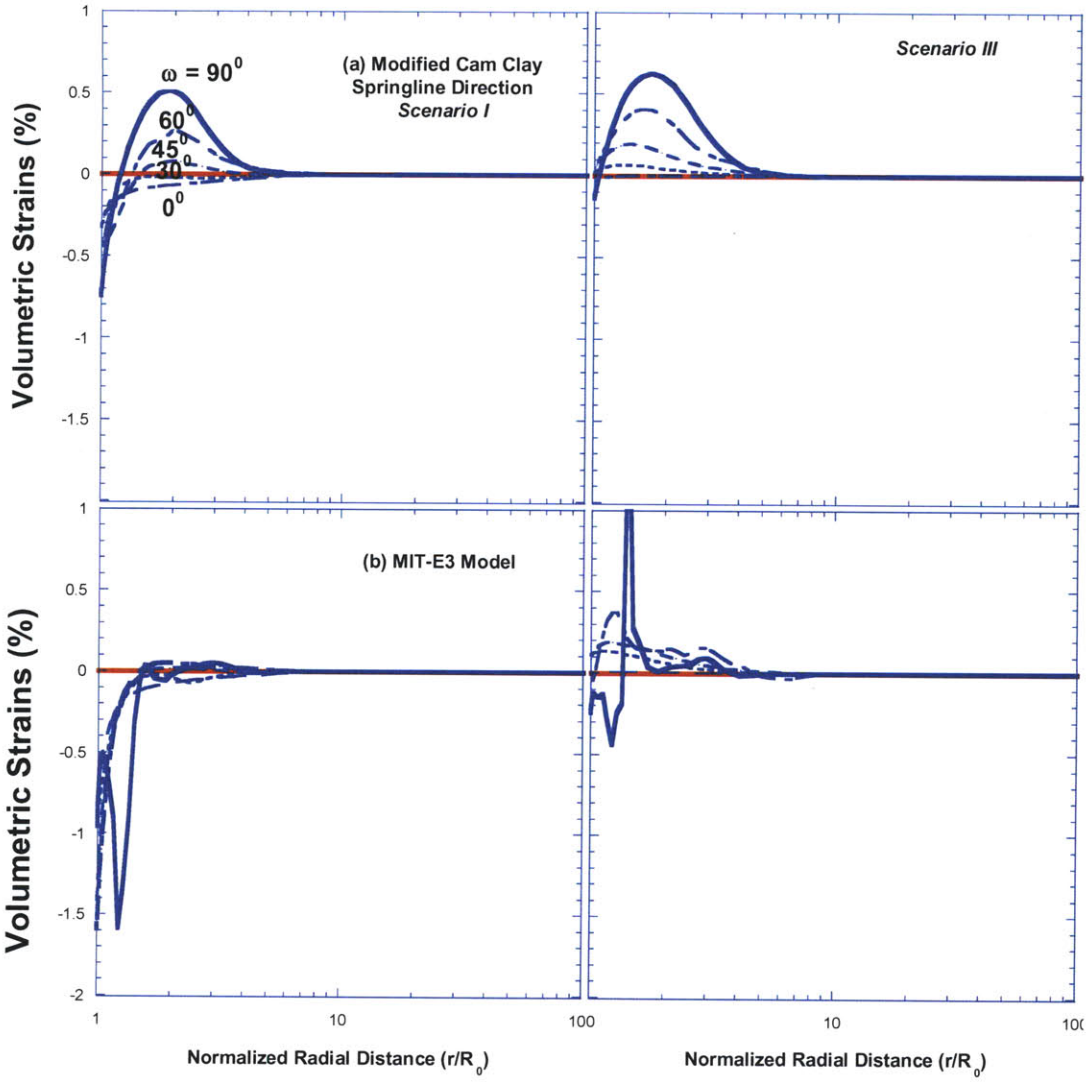

Figure 6.64 Effect of consolidation on volumetric strain distribution in the radial direction $\theta=0^0$ around deviated wells during unloading scenarios I and III using (a) MCC and (b) MIT-E3 models.

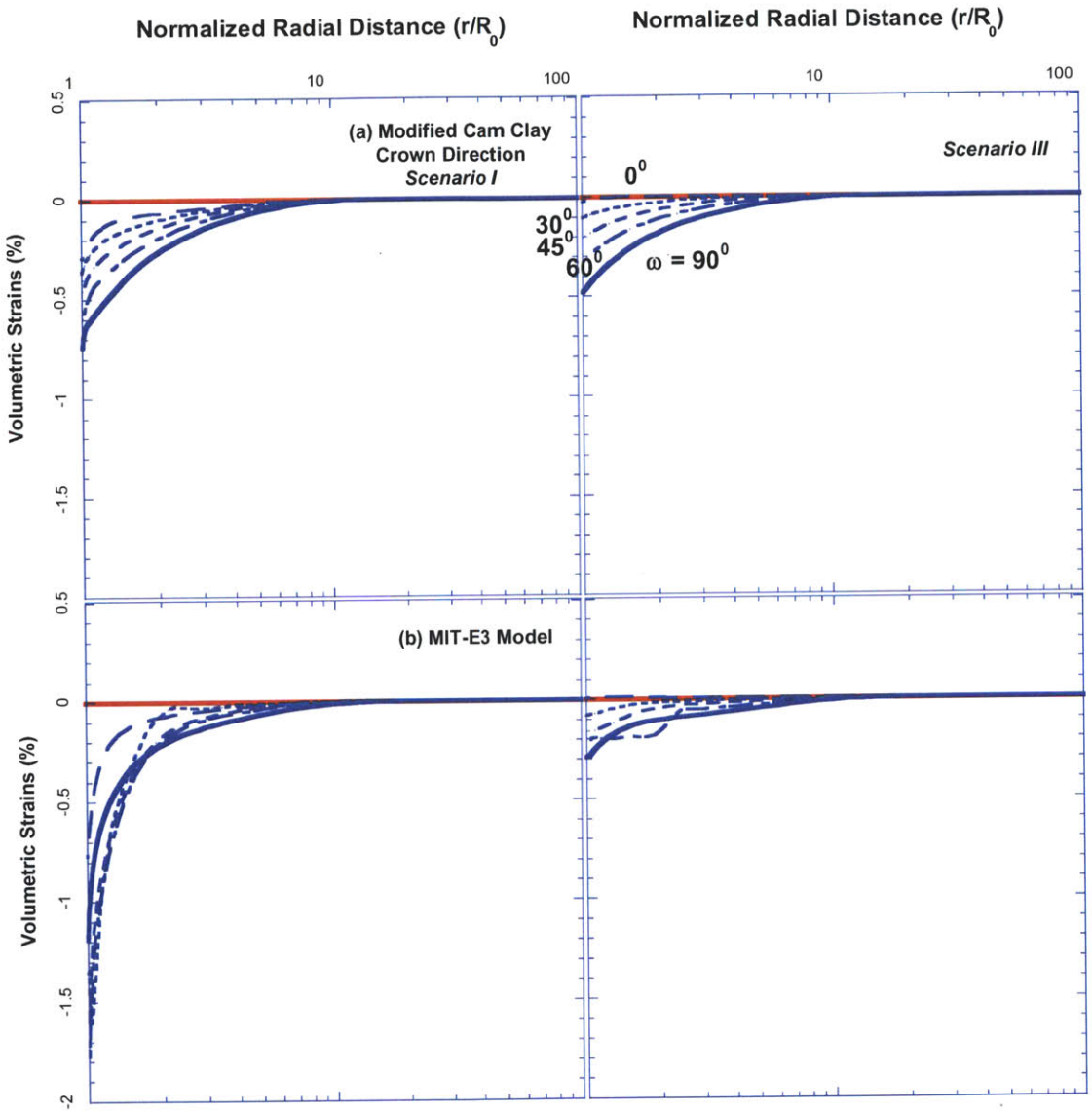

Figure 6.65 Effect of consolidation on volume strain distribution in the radial direction $\theta=90^0$ around deviated wells during unloading scenarios I and III using (a) MCC and (b) MIT-E3 models.

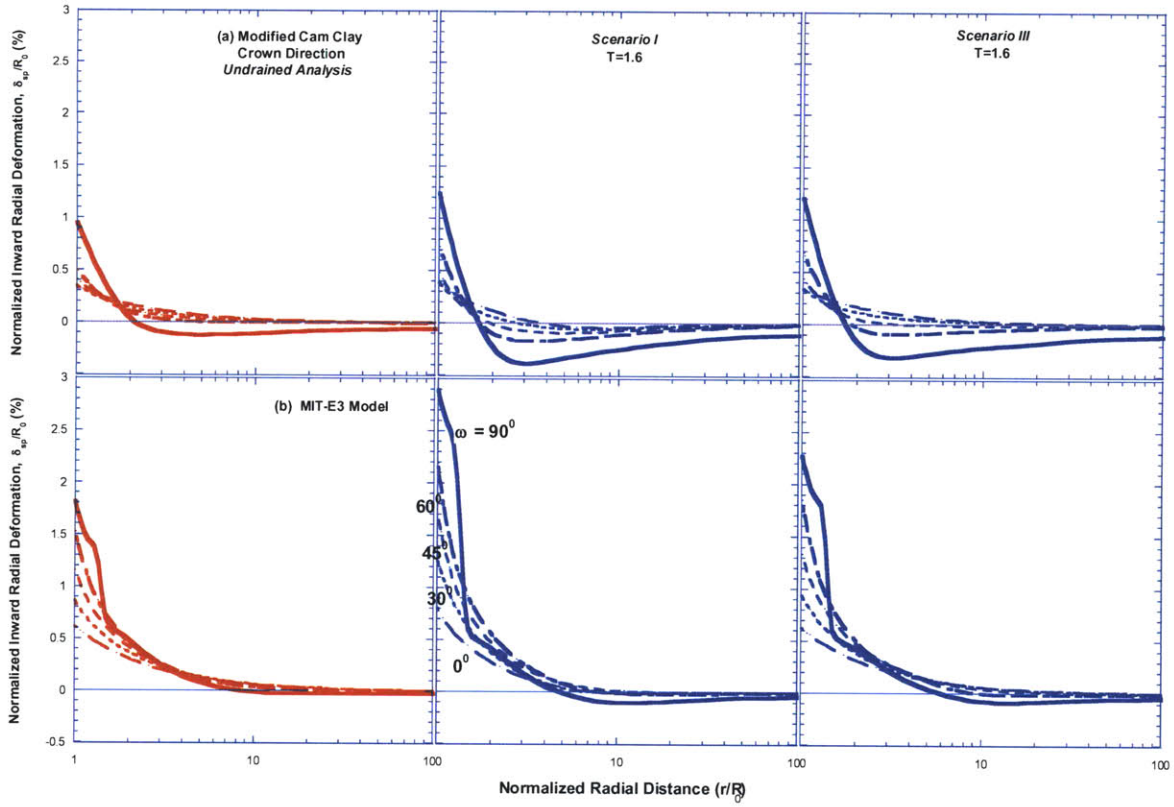

Figure 6.66 Effect of consolidation on radial deformations distribution in the radial direction $\theta=0^0$ around deviated wells during unloading scenarios I and III using (a) MCC and (b) MIT-E3 models.

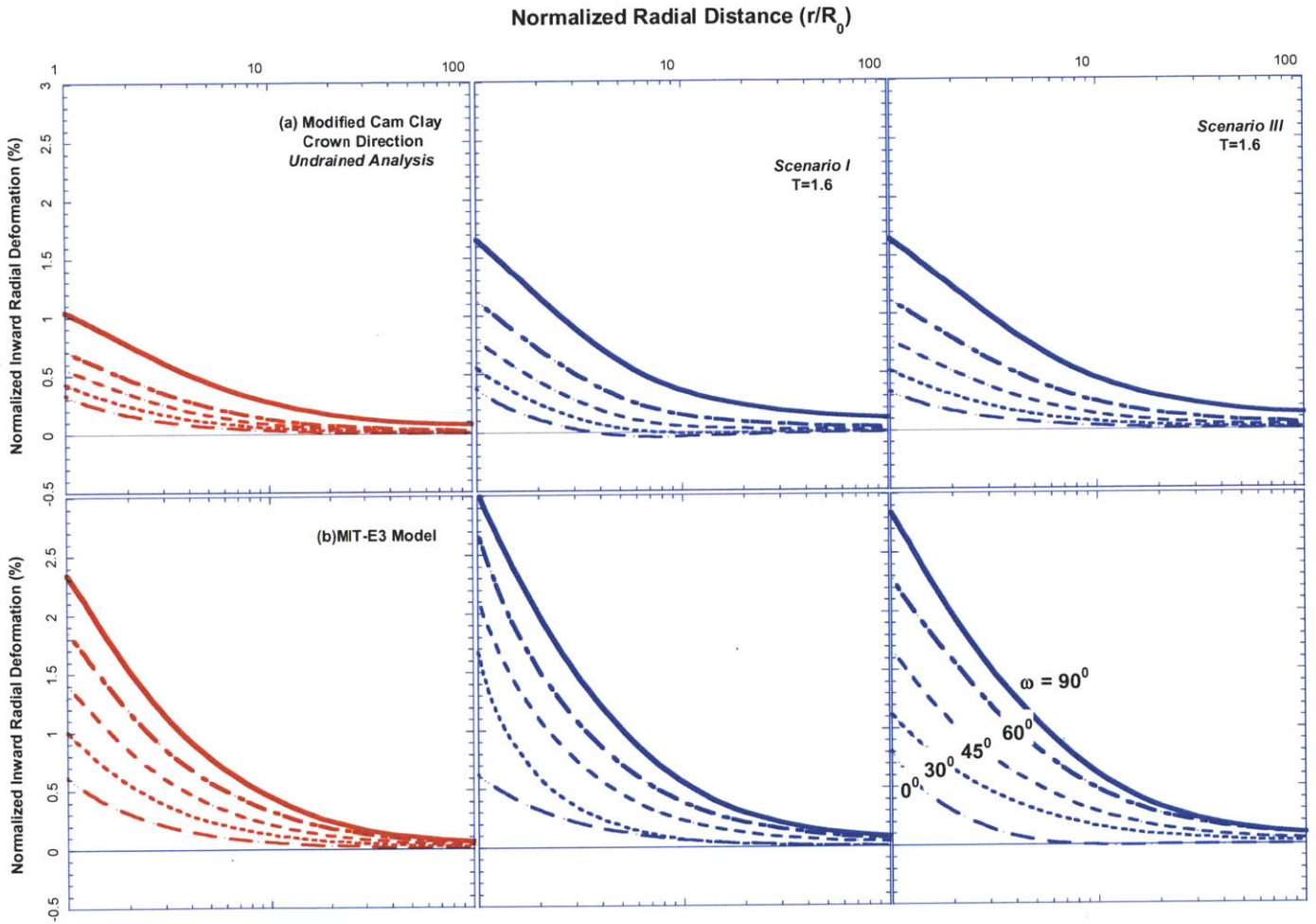

Figure 6.67 Effect of consolidation on radial deformation distribution in the radial direction $\theta=90^0$ around deviated wells during unloading scenarios I and III using (a) MCC and (b) MIT-E3 models.

7 Summary, Conclusions and Recommendations

7.1 Overview

Borehole stability is a key issue for the oil industry. The wellbore stability analysis depends on a proper determination of the drilling fluid density that provides the pressure inside the cavity of the wellbore. Most wellbore instability problems occur in soft or ductile formations because of the complex behavior they exhibit. Oil production at very shallow depths has motivated this research on stability of vertical and deviated wellbores in soft low permeability formations. This research contributes towards the use of more realistic constitutive models and extensive numerical analyses in predicting soil behavior around wellbores, and the understanding of the fundamental mechanisms controlling stability of wellbores. Numerical analyses employed an advanced constitutive model (MIT-E3) and a non-linear finite element program (ABAQUS^{TM}) to capture the complex behavior of soft formations around the wellbores.

This thesis is part of a larger project that also comprises experimental measurements of element and model-borehole lab tests (Abdulhadi, 2009) performed on an analog testing material (RBBC). Soil models parameters are calibrated to the behavior of the analog material consolidated to a wide range of stress levels (0.15MPa ~ 10MPa). The numerical analyses results are validated by comparing them to measurements from model borehole experiments in Thick-Walled Cylinder (TWC) devices.

The research includes developing finite element models to simulate vertical and deviated wellbores and calibrating effective stress models to the behavior of analog testing material to perform the following main tasks:

1. Simulating lab experiments on model-boreholes using the TWC apparatus (Abdulhadi, 2009). A comparison between simulation results and experiment measurements validated numerical simulations and proved the benefits of using more realistic soil models such as the MIT-E3 model. The numerical simulations provided a better understanding of soil behavior in TWC mode of shearing.

2. Investigating the relationship between mud pressure and wellbore deformations under undrained conditions. The values of critical mud pressures are discussed. The critical mud pressure is the lowest possible pressure inside the cavity where failure of wellbores occurs. Failure of wellbores is detected in two cases: 1) the onset of localized failure and large localized deformations, 2) very large uniform deformations at cavity wall (reference value at Crown Point is $\delta_{cr} > 10\%$).

3. Studying the effect of consolidation on wellbore stability and behavior of the surrounding formation. The well pressure is held constant at the value of the reference mud pressure, while changes in pore pressures and radial deformations are computed around the wellbore up to a reference time interval of 30days.

7.2 Summary of numerical analyses

Wellbore failures are separated into three different categories; brittle compressive failure, ductile compressive failure, and tensile failure. Chapter 2 described each failure category, discussed the concept of safe mud weight as a key input to the wellbore design procedure, and presented previous solutions for the wellbore problem and the factors affecting these solutions. This research focused on the ductile failure of wellbores in K_0-consolidated formations. Chapter 3 describes the mechanical model of the wellbore (wellbore unloading problem) formed by taking a plane strain section orthogonal to the wellbore axis (i.e. slice model). This slice model only represents half of the space around the wellbore cavity due to symmetry and is of a finite thickness to accommodate out-of-plane

traction forces. Plane strain conditions are imposed by preventing any out-of-plane deformations. Far field stresses are determined by transforming geostatic stresses in the rock mass into the analysis plane. Drilling is simulated by reducing a set of stresses around the wellbore cavity to a hydrostatic condition defined by the weight of the drilling mud.

Two effective stress soil models are used to define the behavior of the formation, Modified Cam Clay (MCC, Roscoe and Burland, 1968) and MIT-E3 (Whittle and Kavvadas, 1994). These soil models are based on previous studies of RBBC which have established normalized engineering properties of soil (following the SHANSEP framework; Ladd and Foott, 1974) such that the undrained shear strength and stiffness of K_0-normally consolidated clay are proportional to the vertical effective stress at the end of consolidation. However, Abdulhadi (2009) has found that there are significant changes in the effective stress-strain-strength properties at high confining stresses (1~10 MPa). The behavior at high consolidation pressures is more ductile with lower Undrained Strength Ratio (USR= s_{uTC}/σ'_{vc} = 0.28 vs. 0.33 at σ'_{vc} = 0.15 MPa), and larger required strains to mobilize peak shear (ε_{ap} = 1.4% vs. 0.2% at σ'_{vc} = 0.15 MPa). There is also a surprising decrease in the friction angle measured at large strain, i.e. critical state conditions ($\phi'_{TC} = 31.5^0$ vs. 33.7^0 at 0.15 respectively). Chapter 3 describes how a new set of input parameters for the soil models are computed to represent the RBBC behavior at high consolidation pressures.

The models are integrated within Finite Element program ABAQUS™ via user material subroutines (Hashash, 1992). This finite element program enables simulation of coupled consolidation (time dependent deformations and pore pressures). Two-dimensional and quasi-3D finite element models are used to simulate wellbores in the field while axi-symmetric finite element models are used to simulate the TWC experiment numerically. Two types of analyses are performed in this research, undrained analysis and consolidation analysis. Undrained analyses are used to simulate drilling of wellbores and to examine critical mud pressures at which failure during drilling occurs. Consolidation analyses are used to investigate the effects of time on wellbore stability when an adequate

mud pressure is present. The finite element meshes use mixed interpolation elements (displacement and pore pressure degrees of freedom) to perform the analysis.

Undrained analysis is performed in three stages. First, the initial conditions and geostatic stresses are assigned to the model. Then, the deviatoric stresses are relieved at the cavity wall by reducing a set of stresses around the wellbore cavity to a hydrostatic condition defined by the weight of the drilling mud. Finally, the mud pressures (radial pressures on cavity wall) are reduced to a target value. This target value is either the critical mud pressure at which failure is initiated or a reference mud pressure that maintains wellbore stability and reasonable inward deformations at cavity wall.

Chapter 4 presents the results from stages two and three in the analysis that simulates the drilling of the wellbore. In the field, drilling of wellbores usually occurs at a rate from 20 to 60 m/hr (Willson, pers. comm.). Due to the low permeability of the encountered clay formations ($k=1.44 \times 10^{-7}$ m/hr at reference pressure 4MPa), drilling is assumed to occur under undrained conditions. A unit depth is drilled in 0.05 hours. This corresponds to a dimensionless time factor, $T= 1.44 \times 10^{-4}$. Therefore, it is reasonable to assume negligible migration of pore fluid within the formation during drilling. Two criteria used to detect failure in wellbore: the incipient of localized failure recognized by large localized deformations at certain points on the wellbore cavity, and if this did not occur then, large uniform deformations of cavity wall recognized by inward deformations at the crown of the cavity wall up to 10% of initial radius. The relationship between well pressure and inward deformations is presented for five different deviation angles: 0^0, 30^0, 45^0, 60^0, and 90^0.

If the target value is the reference mud pressure, consolidation analysis is performed to monitor the effect of time on wellbore stability before casing installation as described in Chapter 6. A reference time interval of 30 days is assumed between end of drilling and casing. Non-linear coupled consolidation analyses offer a more realistic representation of deformations and pore pressures within the formation. However, the analyses are affected by the boundary conditions assumed at the wellbore. Two drainage conditions are

assumed at the cavity wall: 1) there is drainage of pore fluid into the wellbore (i.e. clay has lower permeability than mud cake) 2) the mud cake forms an effectively impermeable boundary (i.e. permeability of the filter is much lower than the surrounding clay).

Four unloading scenarios are considered for the vertical wellbore: scenarios I and II are based on the assumption of full interaction between the well pressure and the pore pressure, while scenarios III and IV are based on the assumption of perfect isolation of the cavity wall. The undrained unloading is continued to the reference mud pressure = $0.2\sigma'_{v0}$ in scenarios I and III, while the final value of well pressure is $-0.2\sigma'_{v0}$ in scenarios II and IV (underbalanced drilling). Only scenarios I and III are applied to the deviated wellbores.

Chapter 5 presents the results of another set of numerical analyses to validate numerical models by comparing their results to measurements from model borehole tests in a Thick-Walled Cylinder (TWC) apparatus (Abdulhadi, 2009). The analyses are also used to evaluate TWC interpretation methods that are usually associated with pressure meter tests and cavity expansion in thick walled apparatus. The finite element model provided detailed results that help to understand stress and strain distributions around the model borehole.

7.3 Results and Conclusions

Examination of the results from the numerical simulations described in the previous section lead to the following main conclusions:

1. More realistic soil models are needed to achieve accurate predictions of soil response to wellbore drilling and a more reliable assessment of wellbore stability. The MIT-E3 model has an anisotropic yield surface and hardening rules that capture the evolution of anisotropy with changes in stress state, and hence is

considered a more realistic representation of natural deposits behavior. The results of TWC simulations using the MIT-E3 model predicted failure in the specimens at the same cavity pressures observed in the lab experiments. Also, using the MIT-E3 model, the onset of localized failure in deviated wellbores can be predicted.

2. Using the hydrostatic pore pressure value as a design mud pressure value is not always a safe choice in soft formations, especially for deviated wellbores. Localized failures may initiate even if higher mud pressures are provided in the cavity. Moreover, due to the low permeability of the soft formations around wellbores at shallow depths, significant volume changes occur after drilling and before casing. These volume changes can cause delayed localized failure at pockets with low excess pore pressures at cavity wall, if the reference mud pressure is relatively close to the critical mud pressure.

These conclusions are based on the following more specific observations.

7.3.1 Model Borehole Tests

TWC lab experiments are adequately simulated numerically by axi-symmetric finite element model that take into account the top and bottom caps, filter drains and rates of cavity pressure change. The more advanced constitutive model, MIT-E3 was capable of capturing the change in initial stiffness and net cavity pressure ratio with consolidation stress level. However, the analyses are terminated when large deformations and high octahedral shear strains develop in the model. This failure occurs instantaneously in the analysis and hence, the rates of cavity volume change observed in the lab are not fully simulated.

The finite element model provided detailed results that helped to understand stress and strain distributions around the model borehole. The data provided a basis to evaluate the approximate method (Silvestri, 1998) used to interpret TWC results. This method is

originally developed for interpreting pressuremeter results and is based on assuming plane strain and undrained conditions. The full set of simulation results showed that the TWC specimen is affected by the top cap (redistribution of axial stress) and internal redistribution of pore pressures (presence of compression and extension volume strains). However, both sources computed closely an undrained strength ratio of $s_u/\sigma'_{v0} \sim 0.2$, and hence the Silvestri (1998) is considered a reasonable approximation of the TWC specimen shear stress strain response. The shear stress-strain behavior at inner wall of the TWC is shown to be very close to that at cavity wall of vertical wellbores.

The constitutive models representing soil behavior are not strain dependent, hence the difference in cavity depressurizing rates allowing more time for pore pressure re-equilibration is the only factor that would cause different results. However, simulations using different depressurizing rates gave similar strength ratios and that of a truly undrained simulation (using short time frames to prevent pore pressure migration) was also very similar. The simulation results using the MIT-E3 soil model were also consistent with lab results in depicting the effect of TWC specimen size on improving stability and decreasing critical cavity pressure.

7.3.2 Undrained analysis of wellbores

Chapter 4 described the prediction of failure in the performed numerical analysis and the relationship between mud pressure and cavity deformations for vertical and deviated wellbores. Wellbore failure was defined by two different criteria: 1) incipient localized failure due to local increase in inward deformations and high octahedral shear strains; 2) or large cavity deformations up to $0.1R_0$ at Crown Point. The MCC did not capture the first criteria of failure and thus generally overestimates wellbore stability. MIT-E3 predicted localized deformations in deviated wellbores at locations where zones of high octahedral shear strains are generated. The highest critical state mud pressure was for the horizontal wellbore ($0.18\sigma'_{v0}$). Wellbores deviated by 30^0, 45^0, and 60^0 fail at mud pressures equal to $-0.177\sigma'_{v0}$, $-0.013\sigma'_{v0}$, and $0.055\sigma'_{v0}$, respectively. Only the vertical

wellbore fails due to excessive cavity deformations (δ_{cr}/R_0 = 10%) at mud pressure equal to -0.34σ'_{v0} (underbalanced).

At the reference mud pressure (0.2σ'_{v0}), wellbore deformations and magnitudes of excess pore pressures increased with deviation angle. In general, MCC predicted larger magnitudes of positive excess pore pressures around Springline and negative excess pore pressures at Crown which affected results of consolidation analysis.

7.3.3 Effect of Consolidation on Borehole Stability

Drilling is assumed to occur under undrained conditions. However, the generated shear induced pore pressures around the cavity of the wellbore during drilling re-equilibrate with mud pressure (permeable wellbore) or redistribute around cavity (impermeable wellbore) within the time frame before casing installation leading to further cavity deformations and more importantly significant volume change and radial deformations behind the cavity wall and around the wellbore. Consolidation around wellbores is highly dependent on the deviation angle of the wellbore and drainage conditions at cavity wall.

With increase in deviation angle, the deviatoric component of geostatic stresses generate higher negative pore pressure near the Crown Point and higher positive pore pressures near the Springline of the wellbore. During consolidation, higher pore pressure gradients lead to more deformations around wellbore. In a horizontal wellbore, the MIT-E3 model even predicts further development of localized deformations and local increase in octahedral shear strains.

Radial deformations generated during consolidation analysis are less than that generated in the undrained drilling of the wellbore. The MIT-E3 soil model predicts larger deformations than the MCC model in all deviation angles. On the other hand, the MCC model predicts higher positive pore pressures. The positive pore pressures near the Springline generate significant compression zones during consolidation behind the cavity wall. Adjacent compression and extension zones result in relatively small increase in cavity deformations.

Consolidation around permeable wellbores generated more deformations at cavity wall and more volume change and radial deformations around the cavity. This became more obvious with increase in deviation of wellbores and in MIT-E3 predictions. Consolidation around impermeable wellbores generated more compression volume strains resulting in less inward deformations at the cavity.

7.4 Impact

Results have significant practical implications that should be considered in the analysis of wellbore stability:

1. Using sophisticated soil models that give more realistic prediction of soft formations behavior and stress history effects is essential for a safe assessment of required densities of drilling fluids.

2. Localized failure may occur in deviated wellbores during drilling or within the time between drilling and casing due to redistribution of excess pore pressures and volume changes. The value of hydrostatic pore pressure is not always a safe mud pressure for wellbore design. A careful analysis of the state of stability of the wellbore through time should be made before choosing the design mud pressure.

3. Maintaining an impermeable cavity wall and casing wellbores shortly after drilling is most important in soft formations. Due to the low permeability of soft formations, time dependent behavior may lead to delayed localized failure in deviated permeable wellbores.

7.5 Recommendations for future work

This research has applied sophisticated constitutive models and non-linear finite element analysis to the wellbore unloading problem to capture a more realistic prediction of the formations response to mud pressure changes. Results demonstrated the advantage of using the MIT-E3 soil model in describing failure in wellbores and the effects of consolidation on wellbore stability. The analyses pertain to wellbores drilled K_0-consolidated (cross-anisotropic) clays and assumed plane strain conditions and isotropic permeability. Further work to extend the understanding of wellbore instability to more generalized cases should focus on the following areas:

1- Repeating the simulations presented in this research using different constitutive properties calibrated to shallow formations where actual oil production is taking place (e.g. Gulf of Mexico and North Slope of Alaska). The results of simulations can be validated by comparison with measurements from the field rather than lab measurements.

2- The effect of fully anisotropic far field geostatic stresses (i.e. $\sigma'_{xx} \neq \sigma'_{zz}$). Ewy (1993) predicted out-of-plane deformations for deviated wellbores in such formations. The deviated wellbores were also simulated using the slice model, as explained in Chapter 2; and the results demonstrated significant warping near the cavity. Using a 3D finite element model rather than a quasi-3D one is a more accurate approach to investigate the wellbore stability in anisotropic conditions. A 3D finite element model is also useful to incorporate effects of anisotropic permeability on consolidation around vertical and deviated wellbores. Investigating the interplay between wellbore orientation and anisotropy in permeability as well as the interplay between anisotropy in geostatic stresses and in permeability enables a more generalized depiction of field cases. However, careful determination of constitutive models and properties is required to realistically depict the behavior of anisotropic materials.

3- Failure mechanisms of wellbores are indicated by local and concentrated increases in octahedral shear strains (Chapter 4). A more accurate approach to simulate failure is to capture post-localization response. This will require procedures to evaluate localization of deformations (shear and compaction bands; Rudnicki, 2004) and a regularization strategy (e.g. Crook et. al., 2003).

4- The constitutive equations of soil models should include effects of consolidation stress level and strain rates. Elemental laboratory experiments (Abdulhadi, 2009) demonstrated significant influence of consolidation stress level over the strength and stiffness of BBC. On the other hand, research by Sheahan et al. (1992) concluded that increasing strain rates are associated with an increase in strength for normally consolidated BBC. There is a class of rate dependent soil models that can be used to investigate rate of drilling effects on wellbore stability.

References

1) Abdulhadi, N. O., Akl, S. A., Germaine, J. T., and Whittle, A. J., 2008, "Wellbore Instability Mechanisms is Soil: Progress Report June 2006 – September 2008," Report submitted to BP America Inc., Cambridge, MA.
2) Abdulhadi, N. O., Akl, S. A., Germaine, J. T., and Whittle, A. J., 2009, "Wellbore Instability Mechanisms in Very hard Clay," 17th International Conference on Soil Mechanics and Geotechnical Engineering, Egypt, October 2009.
3) Abdulhadi, N. O., 2009, "An experimental investigation into the stress-dependent mechanical behavior of cohesive soil with application to wellbore instability," PhD Thesis, Department of Civil and Environmental Engineering at MIT, Cambridge, MA.
4) Ahmed, I., 1990, "Investigation of Normalized Behavior of Resedimented Boston Blue Clay using Geonor Direct Simple Shear," SM Thesis, Department of Civil and Environmental Civil Engineering, MIT, Cambridge, MA.
5) Amadei, B. 1983, "Rock Anisotropy and the Theory of Stress Measurements" (Lecture notes).
6) Arthur, J. R. F., Chua, K. S., and Dunstan, T., 1977, "Induced anisotropy in a sand." Geotechnique, London, England, 27(1), 13-36.
7) Aubeny, C. P., 1992, "Rational Interpretations of in-situ tests in cohesive soils," PhD thesis, Department of Civil Engineering, MIT, Cambridge, MA.
8) Aubeny, C. P., Whittle, A. J., and Ladd, C. C. 1998, "Effects of Disturbance on Undrained Strengths Interpreted from Pressuremeter Tests," ASCE Journal of Geotechnical and Geoenvironmental Engineering. Volume 126, No. 12, pp. 1133-1145.
9) Baguelin, F., J. F. Jezequel, E. L. Mee, and A. L. Mehaute, 1972, "Expansion of Cylinderical Probes in Cohesive Soils." Journal of Soil Mechanics and Foundation Division, ASCE, pp. 1129-1142.

10) Bell, J. S. 1989, "Investigating stress regimes in sedimentary basins using information from oil industry wireline logs and drilling records." Geological Applications of Wireline Logs. Special Publication 48 (Geological Society of London), 305-325.

11) Bell, J. S., and Gough, D. I. 1983, "The use of borehole breakouts in the study of crustal stress, in Hydraulic Fracturing stress measurements." D. C., National Academy Press, Washington.

12) Bogobowicz, A. D., Rothenburg, L. and Dusseault, M. B. 1991 "Solutions for non-newtonian flow into elliptical openings." J. App. Mech. 58(3), 820-825.

13) Bol, G.M., Wong, S.-W., Davidson, C.J., Woodland, D.C. 1994 "Borehole stability in shales." SPE Drilling & Completion 9, 87-94.

14) Bradley, W.B. 1979 "Failure of Inclined Boreholes". Journal of Energy Resource and Technology. Transactions of ASME, 101, 232-239.

15) Bratli, R. K. and Risnes, R. 1981, "Stability and failure of sand arches." Soc. of Petroleum Engineers Journal, (April), 236-248.

16) Brown, E. T., Bray, J. W. Ladanyi, B. and Hoek, E. 1983, "Ground response curves for rock tunnels." Journal of Geotechnical Engineering, ASCE, 109(1), 15-39.

17) Brudy, M. and Zoback, M. D. 1993, "Compressive and tensile failure of boreholes arbitrarily-inclined to principal stress axes: Application to the KTB boreholes, Germany." International Journal Rock Mechanics Mining Sciences, 30, 1035-1038.

18) Brudy, M. and Zoback, M. D. 1999, "Drilling induced tensile wall fractures: implications for the determination of in situ stress orientation and magnitude." International Journal Rock Mechanics Mining Sciences, 136, 191-215.

19) Carter, J. P., Booker, J. R., and Small, J. C., 1979, "The analysis of finite elasto-plastic consolidation," International Journal for Numerical and Analytical Methods in Geomechanics.

20) Carter, J. P., and Booker, J. R. 1982, "Elastic Consolidation around a deep circular Tunnel." International Journal of Solids Structures. Volume 18, page 1059-1074.

21) Castillo, D. A. and Zoback, M. D. 1994, "Systematic variations in stress state in the Southern San Joaquin Valley: Inferences based on wellbore data and contemporary seismicity." American association Petroleum Geologists Bulletin, 78(8), 1257-1275.

22) Charlez, Ph., and Heugas, O., 1991, "Evaluation of Optimal Mud Weight in soft shale levels", Rock Mechanics as a Multidisciplinary Science (Editor: Roegiers), Balkema, pp. 1005-1014

23) Charlez, Ph. 1997. **Rock Mechanics**. Vol. 2: Petroleum Applications. Editions Technip.

24) Collins, I. F. and Yu, H. S. 1996, "Undrained cavity Expansion in critical state soil." Int. J. Numer. Anal. Meth. Geomech., 20, 485-516.

25) Davis, E. H. 1968, **Theories of plasticity and the failure of soil masses. Soil Mechanics: Selected Topic**s (Editor: I.K. Lee), Butterworths, Sydney.

26) Detournay, E. 1986, "Elastoplastic model of a deep tunnel for a rock with variable dilatancy." Rock Mech Rock Eng. 19:99-108.

27) Detournay, E. and A. Cheng, 1988, "Poroelastic response of a borehole in a non-hydrostatic stress fields", International journal of Rock Mechanics and Mining sciences and Geomechanics Abstracts. Vol. 25, pp. 255-266.

28) Detournay, E. and Cheng, A.H.D. 1993, "Fundamentals of poroelasticity. In: Comprehensive Rock Engineering" (Editor: J. A. Hudson), Pergamon Press, Oxford, Vol. 2, 113-171.

29) Donath, F. A. 1966, "Experimental study of shear failure in anisotropic rock." Bulletin of Geological Soc. America, 72, 985-990.

30) Drucker, D. C. and prager, W. 1952," Soil Mechanics and plastic analysis or limit design." Quart. Appl. Math 10: 157-165.

31) Dusseault, M. B., and Gray, K. E. 1994, "Mechanism of stress-induced wellbore damage." SPE#23825.

32) Duveau, G., Shao, J. F., and Henry J. P. 1998, "Assesment of some failure criteria for strongly anisotropic geomaterials." Mech. Cohes.-Frict. Mater., Vol. 3, 1-26.

33) Euverte, C., Allemandou, X. and Dusseault, M. B. 1994 "Simulations of openings in viscoelastoplastic media using a discrete element method." Proc. 8th IACMAG Conf., West Virg, 6pp.

34) Ewy, R. T. 1991, "3-D Stress Effects in Elastoplastic Wellbore Failure Models", Proc. 32nd US Rock Mechanics Symposium. Balkema, Rotterdam, 951-960.

35) Ewy, R. T. 1993, "Yield and Closure of Directional and Horizontal Wells", International Journal of Rock Mechanics, Mining Sciences, and Geomechanics Abstracts. Vol. 30, No.7, pp.1061-1067.

36) Faruque, M. O. and Desai, C. S., 1985, "Implementation of a General Constitutive Model for geological material." Int'l J. for Numerical and Analytical Methods in Geomechanics, Vol. 9, pp 415-436.

37) Fjaer, E., Holt, R.M., Horsrud, R., Raaen, A.M., & Risnes, R. (2008) Petroleum Related Rock Mechanics, 2nd Edition, Elsevier.

38) Florence, A. L. and Schwer, L. E. 1978, "Axisymmteric Compression of a Mohr-Coulomb medium around a circular hole." Int. J. Num. Anal. Meth. Geomech. 2: 367-379.

39) Gaziaol, D., Forsans, T., Boisson, M.J.F., Piau, J.-M. 1995 "Wellbore failure mechanisms in shale: Prediction and prevention." J. Petr. Tech. 47, 589-595.

40) Germaine, J. T., 1982, "Development of the directional shear cell for measuring cross anisotropic clay properties, " ScD Thesis, Department of Civil and Environmental Engineering at MIT, Cambridge, MA.

41) Guenot, A., Santarelli, F. J., 1989, "Influence of mud temperature on deep borehole behavior." In: Maury, V., Formaintaux, D. (Eds.), **Rock at Great Depth**. Balkema, Rotterdam, pp.809-817.

42) Guenot, A., 1990 "Instability problems at great depth, drilling boreholes and wells." In: Maury, V., Formaintaux, D. (Eds.), **Rock at Great Depth**. Balkema, Rotterdam, pp.1199-1208.

43) Guenot, A., 1998 "Contraintes et ruptures autour des forages petroliers." Proc. 6th Int. Congr. Rock Mech. Montreal, Balkema, Rotterdam, 951-960.

44) Hashash, Y. M. A., 1992, "Analysis of deep excavations in clay," PhD Thesis, Department of Civil and Environmental Engineering, MIT, Cambridge, MA.

45) Hashash, Y. M. A. and Whittle, A. J., 1992, "Integration of the Modified Cam-Clay Model in Non-Linear Finite Element Analysis," Computers and Geotechnics, 14, pp 59-83.

46) Herrman, L. R., Kaliakin, V., Shen, C. K. Mish, K. and Zhu, Z-Y., 1987, "Numerical Implementation of Plasticity Model for Cohesive soils," ASCE, J. Engrg Mech., Vol. 113, No.4, pp. 500-519.

47) Hojka, K., Dusseault, M. B., and Bogobowicz, A. D. 1993. "An analytical solution for transient thermo-elastic stress fields around a borehole during fluid injection into permeable medium." J. Can. Petroleum Tech., 32(4), 49-57.

48) Hughes, T. J. R., 2000, **The Finite Element Method**, Dover Publications, Mineola, New York.

49) Jaeger, J. C. and Cook, N. G. W. 1979, **Fundamentals of Rock Mechanics**, 2nd edn. New York, Chapman and Hall.

50) Jen, L., 1998, "The Design and performance of Deep Excavations in Clay," PhD thesis, Department of civil and Environmental Engineering, MIT, Cambridge, MA.

51) Kavvadas, M. J., 1982, "Non-linear consolidation around driven piles in clays," ScD Thesis, Department of Civil Engineering, MIT, Cambridge, MA.

52) Kavvadas, M. J., 1993, "Implementation of a class of higher-order elements for the non-linear analysis of soils in the finite element program ABAQUS," Draft Report, Department of Civil and Environmental Engineering, MIT, Cambridge, MA.

53) Kullhawy, F. H. 1975, "Stress deformation properties of rock and rock discontinuities." Engineering Geology, 9, 325-350.

54) Labenski, F., Reid, P. et al. 2003, "Drilling fluids approaches for control of wellbore instability in fractured formations." SPE/IADC 85304. SPE/IADC Middle East Drilling Technology Conference and Exhibition, Abu Dhabi, UAE, Society of Petroleum Engineers.

55) Ladanyi, B., 1972, "In-Situ Determination of Undrained Stress-Strain Behavior of Sensitive Clays with the Pressuremeter." Canadian Geotechnical Journal, pp. 313-319.

56) Ladd, C. C. and Foott, R., 1974, "New Design Procedure for stability of soft clays, "Journal of the geotechnical Engineering Division 100(GT7), 763-786.

57) Ladd, C. C. and Varallyay, J., 1965, "The influence of stress system on the behavior of saturated clays during undrained shear," Research Report R65-11, Soil Publication No. 1777, Department of Civil Engineering, MIT, Cambridge, MA.

58) Legaspi, D. E., 1996, "Finite analyses to predict performance of shallow foundations of clay," PhD thesis, Department of Civil and Environmental Engineering, MIT, Cambridge, MA.

59) Lekhnitskii, S. G. 1963, **Theory of Elasticity of an Anisotropic Elastic Body**, Holden-Day, Inc.

60) Levadoux, J. L. 1980, "Pore Pressures due to Cone Penetration Analysis of deep excavations in clay," Ph.D. Thesis, Department of Civil Engineering, MIT, Cambridge, MA.

61) Lo, K. Y., Ng, M. C., and Rowe R. K., 1984, "Predicting settlement due to tunneling in clays', Tunneling in Soil and Rock, ASCE Geotech III Conf. Atlanta, GA, pp48-76.

62) McLean, M. R. 1987, "Wellbore Stability Analysis." PhD Thesis, university of London, England.

63) McLean, M. R. and Addis, M. A. 1990, "Wellbore Stability analysis: a review of current methods of analysis and their field application." Paper IADC/SPE 19941, Proc. 1990 IADC/SPE Drilling Conference: 261-274.

64) Moniz, S. R., 2009, "The influence of effective consolidation stress on the normalized extension strength properties of resedimented boston blue clay," MEng Thesis, Department of Civil and Environmental Engineering, MIT, Cambridge, MA.

65) Moos, D., and Zoback, M. D. 1990, "Utilization of Observations of Well Bore failure to Constrain the Orientation and Magnitude of Crustal Stresses: Application to Continental Deep Sea Drilling Project and Ocean Drilling Program Boreholes." J. Geophys. Res., 95, 9305-9325.

66) Moos, D., Peska, P. et al. 2003, "Comprehensive wellbore stabiltiy analysis using quantitative risk assessment." Journal Petr. Sci. and Eng., Spec. Issue on wellbore Stability, 38. B. S. Aadnoy and S. Ong, 97-109.

67) Nagtegaal, J. C., 1982, "On the implementation of inelastic constitutive equations with special reference to large deformation problems," Computer Methods in Applied Mechanics and Engineering, 33, pp 469-484.

68) Nawrocki P. and Dusseault, M. B. 1993, "Stability of a circular tunnel in non-linear rock." Geot. Eng. of Hard Soils, Soft Rocks, Athens, Balkema, 1541-1548.

69) Nawrocki P. and Dusseault, M. B. 1994, "Effect of material nonlinearity on deformations around openings in geomaterials." Computer Methods and Advances in Geomechanics, (Editors: Siriwardane and Zaman), Balkema, 2119-2124.

70) Nayak, G. C., and Zienkiewiczs, O. C., 1972, "Elasto-plastic Stress Analysis. A Generalization for Various Constitutive Relations including Strain Softening." Int. J. Numerical Methods in Geomechanics, Vol. 5, No. 1, pp. 113-135.

71) Oden, J. T. and Carey, G. F., 1984, **Finite Elements: Mathematical Aspects**, Vol IV. Englewood Cliffs, N. J.: Prentice-Hall.

72) Ogawa, T., and K. Y. Lo (1987), "Effects of dilatancy and yield criteria on displacements around tunnels", Canadian Geotech Journal, Volume 24, pp 100-113.

73) Ottensen, S., Zheng, R. H. Et al. 1999, "Wellbore Stability Assessment Using Quantitative Risk Analysis." SPE/IADC 52864. SPE/IADC Drilling Conference, Amesterdam, The Netherlands, Society of Petroleum Engineers.

74) Palmer, A. C., 1972, "Undrained Plane Strain Expansion of Cylinderical Cavity in Clay: A simple Interpretation of the Pressuremeter Test." Geotechnique, pp. 451-457.

75) Pasternack, S. C. and Timmerman, D. H., 1987, "Numerical Implementation of a two surface elasto-plastic constitutive relations." Int. J. for Numerical Methods in Engineering, vol. 23, pp 353-366.

76) Pei, J., 2006, "Strength of Transversely Isotropic Rocks," PhD Thesis, Department of Civil and Environmental Engineering, MIT, Cambridge, MA.

77) Peska, P. and Zoback, M. D. 1995, "Compressive and tensile failure of inclined wellbores and determination of in situ stressesand rock strength." Journal of Geophysical Research, 100(B7), 12791-12811.

78) Plumb, R. A. and Cox, J. W. 1987." Stress directions in eastern North America determined to 4.5km from borehole elongation measurements." Journal of geophysical Research, 92, 4805-4816.

79) Potts, D. M. and Gens, A., 1985, "A Critical Assessment of Methods of Correcting for Drifft from Yield Surface in Elasto-plastic Finite Element Analysis." Int'l J. for Numerical and Analytical Methods in Geomechanics, Vol. 9, pp. 149-159.

80) Randolph, M. F., Carter, J. P. and Worth, C. P. 1979, "Driven piles in clay – the effects of installation and subsequent consolidation", Geotechnique, 29, 361-393.

81) Risnes, R. Bratli, R. K. and Horsrud, P. 1982, "Sand stresses around a wellbore." Soc. Pet. Eng. J. 22: 883-898.

82) Roscoe, K.H. & Burland, J.B. 1968 "On the generalised stress-strain behavior of 'Wet' clay." in *Engineering Plasticity*, Ed. J. Heyman & F.A.Leckie, Cambridge University Press, 535- 609.

83) Santarelli, F. J., Brown, E.T. and Maury, V. 1986, "Analysis of borehole stressing using pressure-dependent, linear elasticity." International Journal for Rock Mechanics and Mining Sciences, 23(6), 445-449.

84) Santarelli, F. J., Brown, E.T., 1989, "Failure of three sedimentary rocks in triaxial and hollow cylinder tests." International Journal of Rock Mech. Min. Sci, and Geotech. Abstracts.

85) Schofield, A. N., and Worth, C. P. 1968," Critical State Soil Mechanics" McGraw-Hill, New York.

86) Seah, T. H., 1990, "Anisotropy of normally consolidated Boston blue clay," ScD thesis, Department of Civil Engineering, MIT, Cambridge, MA.

87) Sheahan, T. C., 1991, "An experimental study of the time-dependent undrained shear behavior of resedimented clay using automated stress path triaxial equipment," ScD Thesis, Department of Civil Engineering, MIT, Cambridge, MA.

88) Sheahan, T. C. and Germaine, J. T., 1992, "Computer Automation of Conventional Triaxial Equipment." Geotechnical Testing Journal, ASTM. 311-322.

89) Sheahan, T. C., C. C. Ladd, and J. T. Germaine, 1992, "Rate-Dependent Undrained Shear Behavior of Saturated Clay." Journal of Geotechnical Engineering, ASCE, pp. 99-108.

90) Silvestri, V., 1998, "On the Determination of the Stress-Strain Curve of Clay from Undrained Plane-Strain Expansion of Hollow Cylinders: A Long Forgotten Method." Canadian Geotechnical Journal, pp. 360-363.

91) Simo, J. C., and Hughes, T. J. R., 1987, "General Return Mapping Algorithms for Rate-Independent Plasticity." Constitutive laws for engineering Materials: Theory and Applications, pp 221-231.

92) Simo, J. C., and Taylor, R. L., 1985, "Consistent Tangent Operator for Rate-independent Elastoplasticity." Computer Methods in Applied Mechanics and Engineering, 48, pp 101-118.

93) Small, J. C., Booker, J. R. and Davis, E. H., 1976, "Elasto-plastic consolidation of soil," International J. Solids Structures, 12, 431-448.

94) Sutabutr, T., 1999, "Analysis and Interpretation of Tapered Piezoprobe and Application to Offshore pile design," ScD Thesis, Department of Civil and Environmental Engineering, MIT, Cambridge, MA.

95) Van Cauwelaert, F. 1977, "Coefficients of deformations of an anisotropic body." Journal of the engineering mechanics division, ASCE, 103(EM5), 823-835.

96) Wang, Y. and Dusseault, M. B. 1991a&b "Borehole yield and hydraulic fracture initiation in poorly consolidated rock strata." Part 1- impermeable media. Part II-permeable media. Int. Jour. R. M., Min. Sci. and Geomech. Abs., 28(4), 235-258.

97) Whittle, A. J. 1987 "A constitutive model for over consolidated clays with application to the cyclic loading of friction piles." Ph.D. Thesis, Department of Civil Engineering, MIT, Cambridge, MA.

98) Whittle, A. J. 1992, "Assessment of an effective stress analysis for predicting the performance of driven piles." Advances in Underwater Technology, Ocean science and Offshore Engineering Volume 28, Offshore Site Investigation and Foundation Behavior, Society for Underwater Technology, London, 607-643.

99) Whittle, A. J., DeGroot, D. J., Ladd, C. C., and Seah, T-H, 1994, "Model prediction of the anisotropic behavior of Boston Blue Clay, " ASCE journal of Geotechnical Engineering, 120(1), 199-225.

100) Willson, S. M., Last, N. C. et al. 1999, "Drilling in South America: A wellbore stability approach for complex geologic conditions." SPE 53940. 6th LACPEC Conference, Caracas, Venezuela, Society of Petroleum Engineers.

101) Willson, S., Edwards, S., Kristiansen, T., and Li, X. 2004 "Best Practices and Workflow for Wellbore Stability Prediction," BP document.

102) Wiprut, D., Zoback, M. et al. 2000, "Constraining the full stress tensor from observations of drilling induced tensile fractures and leak-off tests: Application to borehole stability and sand production on the Norwegian margin." Int. J. Rock Mecha. & Min. Sci., 37, 317-336.

103) Wu, B. and Hudson, J. A., 1991, "Stress-induced anisotropy in rock and its influence on wellbore stability." Rock Mechanics as a Multidisciplinary Science, (Editor: Rogiers), Balkema, 941-950.

104) Wu, B., King, M. S., and Hudson, J. A. 1991, "Stress-induced ultrasonic wave velocity anisotropy in a sandstone." International Journal for Rock Mechanics and Mining Sciences, 28(1), 101-107.

105) Yu, H., and R. K. Rowe 1999, "Plasticity Solutions for Soil Behavior around Contracting Cavities and Tunnels." International Journal for Numerical and Analytical Methods in Geomechanics, Volume 23, pp 1245-1279.

106) Yu, H. 2000, **Cavity Expansion methods in Geomechanics**, Kluwer Academic Publishers.

107) Zervos, A., P. Papanastasiou, and J. Cook 1996,"Elastoplastic finite element analysis of inclined wellbores". Society of Petroleum Engineers, SPE/ISRM, Trondheim, Norway.

108)Zoback, M. D., Moos, D. et al. 1985, "Wellbore breakouts and In situ stress." Journal of Geophysical Research, 90 (B7), 5523-5530.

109)Zoback, M. L. 1992, "First and second ore=der patterns of tectonic stress: The World Stress Map Project." Journal of Geophysical Research, 97, 11703-11728.

110)Zoback, M. D. 2007, **Reservoir Geomechanics,** Cambridge University Press.

111)Zoback, M. L., and Zoback, M. D. 1980, "State of stress in the conterminous United States." J. Geophys. Res., 85, 6113-6156.

112)Zoback, M. L., and Zoback, M. D. 1989, "Tectonic stress field of the conterminous United States." Geol. Soc. Am. Memoir., 172, 523-539.